Interdisciplinary Studies on Rock Varnish

Dissertation

zur Erlangung des Grades eines
‘Doktor rerum naturalium (Dr. rer. nat.)‘ der Fachbereiche:
08 – Physik, Mathematik und Informatik,
09 – Chemie, Pharmazie und Geowissenschaften,
10 – Biologie,
Universitätsmedizin
der Johannes Gutenberg-Universität

verfasst und vorgelegt von
Dorothea Sabine Macholdt

Geb. 08.03.1986
in Seeheim-Jugenheim

Max Planck Graduate Center mit der Johannes Gutenberg-Universität Mainz
angefertigt am Max-Planck-Institut für Chemie

Mainz, 2017

Tag der mündlichen Prüfung: 29. Mai 2017

I hereby declare that I wrote the dissertation submitted without any unauthorized external assistance and used only sources acknowledged in the work. All textual passages which are appropriated verbatim or paraphrased from published and unpublished texts as well as all information obtained from oral sources are duly indicated and listed in accordance with bibliographical rules. In carrying out this research, I complied with the rules of standard scientific practice as formulated in the statutes of Johannes Gutenberg-University Mainz to insure standard scientific practice.

Mainz, 30/03/2017, Dorothea S. Macholdt

Abstract

This work is a study of rock varnishes collected from different locations worldwide and from several environments. The focus was set on the microanalytical investigation of i) the geochemistry of different varnishes and adjacent collected mineral dust, ii) the structures of different varnishes, and iii) signs for a definite proof for a biogenic compound necessary for the formation of rock varnish. To this end, a combination of different cutting-edge analytical techniques was utilized to investigate the rock varnishes.

Rock varnish is a black, micrometer thin, sedimentary crust on top of rock surfaces. It occurs on almost all lithologies and can be found for instance in deserts, in caves, on mountains and plateaus, in large cities, Antarctica, at waterfronts, and possibly even on Mars. Rock varnish consists of a mixture of dust grains as its main component, and a Mn-rich matrix material as cement component. A biogenic contribution to the genesis has been suggested. Rock varnish is a phenomenon that has defied more than 200 years of intermittent scientific examination.

Methods and instruments used in this study were amongst others fs/ns LA-ICP-MS, fs LA-MC-ICP-MS, solution ICP-MS, portable XRF, stationary XRF, EPMA, NanoSIMS, FIB- and Microtome-slicing, STXM-NEXAFS, SEM, Raman spectroscopy, EDX, XRD, and TEM. More than 150 individual rock samples were investigated for their chemical composition by fs LA-ICP-MS, and on each sample about 10-30 measurements were conducted to obtain enough statistical accuracy since the crusts are very inhomogeneous. On the basis of the results, several samples were selected that were additionally investigated by other methods mentioned above, to receive further information about, e.g., nano- and microstructures, element distributions, in-situ oxidation state distributions, and isotope ratios. Mineral dust samples were collected and investigated by fs LA-ICP-MS and XRD, due to their role as potential element and material source for rock varnish. Additionally, STXM-NEXAFS measurements, Raman spectroscopy, extensive PCR, qPCR, and NGS studies, EPR measurements, light microscopic investigations, $\delta^{13}C$ measurements, as well as fluorescence microscopy analyses on DAPI, DRAQ5, and OsO_4 fixed thin sections were performed in the search for proof of a biogenic genesis of rock varnish.

It was found that rock varnishes from disparate environments differ, and that the term rock varnish can thus be subdivided and categorized. It was possible to analyze the trace element composition of the microstructure of varnish without contamination from the host rock. Images of nano- and microstructures were obtained for a large set of varnishes and for varnishes from different environments. It was furthermore possible to determine and locate Mn oxidation states at the nanometer scale within single samples and by this show the reduction of the manganese matrix around cavities, a sign for previous redox reactions. The results indicate that the airborne dust is the major contributor to the genesis of varnishes found in deserts, vehicle emissions the main source of varnish on facades in urban areas, and water the source of crusts within river splash zones. No indicator for a possible biogenic origin was found in any varnish sample, even though a large variety of tests was performed. However, one would expect to find organisms capable of oxidizing Mn, at least in the most recently formed layers, or on the surface of rock varnish. Thus, an abiogenic genesis of rock varnish seems most plausible. In addition to the measurements, technical developments were made, such as the development of a new microanalytical reference material for Mn-rich rocks, a calibration for portable XRF measurements of thin Mn-rich coatings, and a measurement technique that allows the measurement of femtogram amounts of powdered material (such as dust) with high precision and accuracy. By providing these technical developments and a broad variety of information about different varnish types, as well as details about individual samples, significant cornerstones are now given on the basis of which future investigations can proceed with the aim to disclose the secret of the genesis of rock varnish.

Zusammenfassung

In dieser Arbeit wurden Wüstenlackproben von verschiedenen Gebieten dieser Erde und aus unterschiedlichen Umgebungen untersucht. Der Schwerpunkt lag auf der mikroanalytischen Erforschung der i) Geochemie der Wüstenlacke und des unter den Gesteinen gesammelten Mineralstaubs, ii) Strukturen innerhalb der Wüstenlacke und iii) der Suche nach einem eindeutigen Beweis für eine biogene Komponente die zur Entstehung von Wüstenlack beiträgt. Um dieses Ziel zu erreichen, wurden mehrere Methoden, die dem neuesten Stand der Technik entsprechen, miteinander kombiniert, um die weltweit gesammelten Wüstenlacke zu untersuchen.

Wüstenlack ist eine schwarze, Mikrometer dünne, sedimentäre Kruste auf Gesteinsoberflächen. Sie kann auf nahezu allen Gesteinstypen beobachtet werden und ist beispielsweise in Wüsten, in Höhlen, auf Bergen und Plateaus, sowie in größeren Städten, der Antarktis, in der Spritzwasserzone von Flüssen und vermutlich selbst auf dem Mars zu finden. Wüstenlack besteht aus einer Mischung von Mineralstaub als Hauptkomponente, und einer manganreichen Matrix welche die Partikel zusammenhält. Eine zur Entstehung beitragende biogene Komponente wird diskutiert. Wüstenlack ist ein Phänomen, welches sich seit mehr als 200 Jahren episodischen wissenschaftlichen Untersuchungen widersetzt hat.

Die in dieser Arbeit verwendete Messinstrumente waren unter anderem fs/ns LA-ICP-MS, fs LA-MC-ICP-MS, Lösungs-ICP-MS, tragbare RFA, stationäre RFA, EMS, NanoSIMS, FIB- und Mikrotom-Schnitte, STXM-NEXAFS, REM, Raman-Spektroskopie, EDX, Röntgenbeugung und TEM. Mehr als 150 Wüstenlackproben wurden mit fs LA-ICP-MS auf ihre chemische Zusammensetzung untersucht, und auf jeder Probe wurden 10-30 Einzelmessungen durchgeführt, um eine gute statistische Genauigkeit zu erhalten, da diese Krusten sehr inhomogen sind. Anhand der Messergebnisse wurden einzelne Proben ausgewählt, welche zusätzlich mit anderen oben erwähnten Messmethoden untersucht wurden, um zusätzliche Informationen, beispielsweise zu Nano- und Mikrostrukturen, Elementverteilungen, in-situ Oxidationsstufenverteilungen und zu Isotopenverhältnissen zu gewinnen. Mineralstaubproben wurden ebenfalls gesammelt und mit Röntgenbeugung und fs LA-ICP-MS aufgrund ihrer Rolle als mögliche Material- und Elementquelle für Wüstenlack untersucht. Zusätzliche STXM-NEXAFS Messungen, Raman-Spektroskopie, umfangreiche PCR, qPCR und NGS Studien, EPR Messungen, lichtmikroskopische Untersuchungen, $\delta^{13}C$ Messungen, sowie fluoreszenzmikroskopische Analysen von DAPI, DRAQ5 und OsO_4 fixierten Dünnschliffen wurden durchgeführt, auf der Suche nach einem Beweis für eine biogene Genese von Wüstenlack.

Es war möglich festzustellen, dass sich Wüstenlacke aus verschiedenen Umgebungen unterscheiden und dass der Begriff daher weiter unterteilt und kategorisiert werden muss. Die Spurenelementzusammensetzung der Mikrostruktur von Wüstenlack wurde ohne Kontamination durch das darunter befindliche Gestein ermittelt. Abbildungen von Nano- und Mikrostrukturen wurden für eine große Menge von Wüstenlackproben, die in unterschiedlichen Umgebungen gesammelt worden waren, bereitgestellt. Es war zusätzlich möglich, Mn-Oxidationsstufen im Nanometerbereich in einzelnen Proben in-situ zu ermitteln und zu lokalisieren. Hiermit konnte gezeigt werden, dass die Matrix in der Umgebung von Hohlräumen oft reduziert wurde, was einen Hinweis auf vorherige Redoxreaktionen darstellt. Auch war es möglich zu zeigen, dass hauptsächlich die feinkörnige Staubfraktion (<50 µm) zur Genese von Wüstenlacken in Wüsten beiträgt, Fahrzeugemissionen die Hauptquelle für Krusten in Stadtgebieten sind und dass Wasser die Elementquelle von Krusten in Spritzwasserzonen ist. In keiner Wüstenlackprobe wurde ein Hinweis auf eine mögliche biogene Genese gefunden, obwohl eine große Vielfalt von Tests durchgeführt wurde. Es wäre jedoch zu erwarten Organismen in den jüngsten Lagen, oder zumindest auf der Wüstenlack Oberflächen, zu finden, welche imstande sind Mn zu oxidieren. Daher erscheint eine abiogene Genese von Wüstenlack am plausibelsten. Zusätzlich zu den Messungen wurden auch technische Entwicklungen gemacht, wie beispielsweise die Entwicklung eines neuen Referenzmaterials für mikroanalytische Messungen von Mn-reichen Gesteinen, eine Kalibration für tragbare RFA-Messungen von dünnen Mn-reichen Lagen, und die Entwicklung einer Messtechnik, welche es erlaubt, Staubprobenmengen (z.B. Mineralstaub) im Femtogrammbereich mit hoher Präzision und Genauigkeit zu messen. Durch das Bereitstellen der technischen Entwicklungen und der großen Vielfalt an Informationen, sowohl über unterschiedliche Wüstenlacktypen als auch Details über einzelne Proben, wurden wichtige Grundsteine für zukünftige Untersuchungen geschaffen, welche mit dem Ziel, das Geheimnis der Entstehung des Wüstenlacks zu lüften, fortfahren können.

Abbreviations and Their Definitions

AMS: accelerator mass spectrometry
AOS: average oxidation states
BSE: backscattered electron
CR-IRMS: Continuous Flow - Isotope Ratio Mass Spectrometer
DAPI: 4',6-diamidino-2-phenylindole
EPMA: electron probe microanalysis
EPR: electron paramagnetic resonance
FIB: focused ion beam
FT-IR spectroscopy: Fourier transformed-infrared spectroscopy
GFS: gas exchange fluorescence system for photosynthesis
GIS: geographic information system
fs/ns LA-ICP-MS: femtosecond/nanosecond laser ablation-inductively coupled plasma-mass spectrometry
ICP-MS: inductively coupled plasma-mass spectrometry
IDL: interactive data language
LacLike: Laccases-like
Mn^{3+}-L: Mn^{3+}-ligand complex
Mn oxyhydroxide: manganese oxides and hydroxides
Mn biooxide: biogenic Mn oxides and hydroxides
MCF: microcolonial fungi
MCO: multicopper oxidases
MRM: microanalytical reference material
NanoSIMS: nanoscale secondary ion mass spectrometry
NGS: next-generation sequencing
OD: optical density
O-layer: octahedral coordinated layer
OSA: order sorting aperture
OSL: optically stimulated luminescence
OTU: operational taxonomic unit
PCR: polymerase chain reaction
PM: particulate matter
PMT: performance photomultiplier
PSL: polystyrene latex spheres
qPCR: quantitative PCR
REE: rare earth element
REM: Raster Elektronenmikroskop
RFA: Röntenfluoreszenzanalyse
RM: reference material
SEM: scanning electron microscopy
STXM-NEXAFS: scanning transmission X-ray microscopy – near edge X-ray absorption fine structure spectroscopy
T-layer: tetrahedral coordinated layer
TEM: transmission electron microscopy
Thin-section: 30-35 µm
Thick-section: about 70 µm
UCC: upper continental crust
Ultra-thin section: 100-200 nm
VCR: varnish cation ratio
VML: varnish microlamination
XRD: X-ray diffraction
XRF: X-ray fluorescence
ZP: zone plate

Table of Contents

1 Introduction and Motivation

1.1 History

Rock varnish is a material of interest for scientists from several research fields. Its examination requires a combination of geological, geomorphological, chemical, mineralogical, and biological fundamental research. The open questions of main interest are its formation mechanisms, and following from this, its application for regional paleoclimate reconstruction, dating of archaeological artifacts (e.g., stone tools, petroglyphs, and geoglyphs), surface stability determinations (e.g., requirements related to the disposal of nuclear and toxic waste), and the general dating of landscapes and surfaces. Rock varnish has been a subject captivating scientists forasmuch as 200 years. The first written record was published in Alexander von Humboldt's "Reisen in die Aequinoktial-Gegenden des neuen Kontinents" (Von Humboldt and Bonpland, 1819). Von Humboldt reports black crusts, which he presumed to be Mn- and Fe-oxide rich and which he observed at the cataracts of the Orinoco River, where water splashed and moistened rocks (Fig. 1). He estimated a coating thickness of about 0.6 mm. According to his assumptions, the elements were introduced by water as chemically dissolved substances, and the host rock was not the element source or even affected by the coating. Von Humboldt mentions that the varnish occurrence is not limited to the Orinoco River, on the contrary, he stated that it is a worldwide phenomenon. The observations reported by him were neither disproved until now, nor are they out of date.

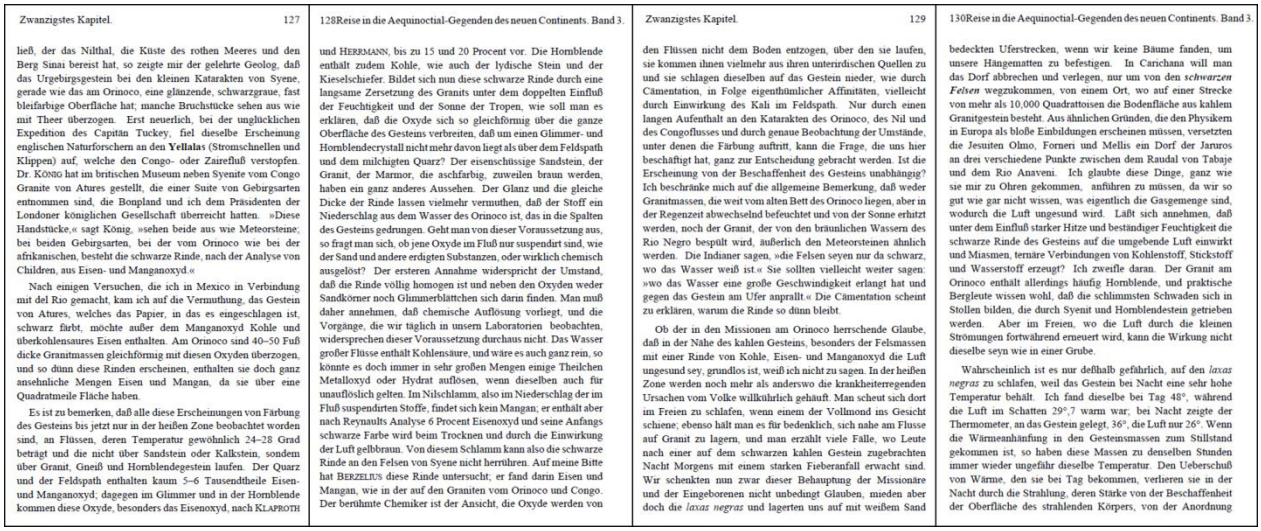

Zwanzigstes Kapitel. 127

ließ, der das Nilthal, die Küste des rothen Meeres und den Berg Sinai bereist hat, so zeigte mir der gelehrte Geolog, daß das Urgebirgsgestein bei den kleinen Katarakten von Syene, gerade wie das am Orinoco, eine glänzende, schwarzgraue, fast bleifarbige Oberfläche hat; manche Bruchstücke sehen aus wie mit Theer überzogen. Erst neuerlich, bei der unglücklichen Expedition des Capitän Tuckey, fiel dieselbe Erscheinung englischen Naturforschern an den **Yellalas** (Stromschnellen und Klippen) auf, welche den Congo- oder Zaireſluß verstopfen. Dr. KÖNIG hat im britischen Museum neben Syenite vom Congo Granite von Atures gestellt, die einer Suite von Gebirgsarten entnommen sind, die Bonpland und ich dem Präsidenten der Londoner königlichen Gesellschaft überreicht hatten. »Diese Handstücke,« sagt König, »sehen beide aus wie Meteorsteine; bei beiden Gebirgsarten, bei der vom Orinoco wie bei der afrikanischen, besteht die schwarze Rinde, nach der Analyse von Children, aus Eisen- und Manganoxyd.«

Nach einigen Versuchen, die ich in Mexico in Verbindung mit del Rio gemacht, kam ich auf die Vermuthung, das Gestein von Atures, welches das Papier, in das es eingeschlagen ist, schwarz färbt, möchte außer dem Manganoxyd Kohle und überkohlensaures Eisen enthalten. Am Orinoco sind 40–50 Fuß dicke Granitmassen gleichförmig mit diesen Oxyden überzogen, und so dünn diese Rinden erscheinen, enthalten sie doch ganz ansehnliche Mengen Eisen und Mangan, da sie über eine Quadratmeile Fläche haben.

Es ist zu bemerken, daß alle diese Erscheinungen von Färbung des Gesteins bis jetzt nur in der heißen Zone beobachtet worden sind, an Flüssen, deren Temperatur gewöhnlich 24–28 Grad beträgt und die nicht über Sandstein oder Kalkstein, sondern über Granit, Gneiß und Hornblendegestein laufen. Der Quarz und der Feldspath enthalten kaum 5–6 Tausendtheile Eisen- und Manganoxyd; dagegen im Glimmer und in der Hornblende kommen diese Oxyde, besonders das Eisenoxyd, nach KLAPROTH

128 Reise in die Aequinoctial-Gegenden des neuen Continents. Band 3.

und HERRMANN, bis zu 15 und 20 Procent vor. Die Hornblende enthält zudem Kohle, wie auch der lydische Stein und der Kieselschiefer. Bildet sich nun diese schwarze Rinde durch eine langsame Zersetzung des Granits unter dem doppelten Einfluß der Feuchtigkeit und der Sonne der Tropen, wie soll man es erklären, daß die Oxyde sich so gleichförmig über die ganze Oberfläche des Gesteins verbreiten, daß um einen Glimmer- und Hornblendecrystall nicht mehr davon liegt als über dem Feldspath und dem milchigten Quarz? Der eisenschüssige Sandstein, der Granit, der Marmor, die aschfarbig, zuweilen braun werden, haben ein ganz anderes Aussehen. Der Glanz und die gleiche Dicke der Rinde lassen vielmehr vermuthen, daß der Stoff ein Niederschlag aus dem Wasser des Orinoco ist, das in die Spalten des Gesteins gedrungen. Geht man von dieser Voraussetzung aus, so fragt man sich, ob jene Oxyde im Fluß nur suspendirt sind, wie der Sand und andere erdigten Substanzen, oder wirklich chemisch ausgelöst? Der ersteren Annahme widerspricht der Umstand, daß die Rinde völlig homogen ist und neben den Oxyden weder Sandkörner noch Glimmerblättchen sich darin finden. Man muß daher annehmen, daß chemische Auflösung vorliegt, und die Vorgänge, die wir täglich in unsern Laboratorien beobachten, widersprechen dieser Voraussetzung durchaus nicht. Das Wasser großer Flüsse enthält Kohlensäure, und wäre es auch ganz rein, so könnte es doch immer in sehr großen Mengen einige Theilchen Metalloxyd oder Hydrat auflösen, wenn dieselben auch für unauflöslich gelten. Im Nilschlamm, also im Niederschlag der im Fluß suspendirten Stoffe, findet sich kein Mangan; er enthält aber nach Reynaults Analyse 6 Procent Eisenoxyd und seine Anfangs schwarze Farbe wird beim Trocknen und durch die Einwirkung der Luft gelbbraun. Von diesem Schlamm kann also die schwarze Rinde an den Felsen von Syene nicht herrühren. Auf meine Bitte hat BERZELIUS diese Rinde untersucht; er fand darin Eisen und Mangan, wie in der auf den Graniten vom Orinoco und Congo. Der berühmte Chemiker ist der Ansicht, die Oxyde werden von

Zwanzigstes Kapitel. 129

den Flüssen nicht dem Boden entzogen, über den sie laufen, sie kommen ihnen vielmehr aus ihren unterirdischen Quellen zu und sie schlagen dieselben auf das Gestein nieder, wie durch Cämentation, in Folge eigenthümlicher Affinitäten, vielleicht durch Einwirkung des Kali im Feldspath. Nur durch einen langen Aufenthalt an den Katarakten des Orinoco, des Nil und des Congoflusses und durch genaue Beobachtung der Umstände, unter denen die Färbung auftritt, kann die Frage, die uns hier beschäftigt hat, ganz zur Entscheidung gebracht werden. Ist die Erscheinung von der Beschaffenheit des Gesteins unabhängig? Ich beschränke mich auf die allgemeine Bemerkung, daß weder Granitmassen, die weit vom alten Bett des Orinoco liegen, aber in der Regenzeit abwechselnd befeuchtet und von der Sonne erhitzt werden, noch der Granit, der von den bräunlichen Wassern des Rio Negro bespült wird, äußerlich den Meteorsteinen ähnlich werden. Die Indianer sagen, »die Felsen seyen nur da schwarz, wo das Wasser weiß ist.« Sie sollten vielleicht weiter sagen: »wo das Wasser eine große Geschwindigkeit erlangt hat und gegen das Gestein am Ufer anprallt.« Die Cämentation scheint zu erklären, warum die Rinde so dünn bleibt.

Ob der in den Missionen am Orinoco herrschende Glaube, daß in der Nähe des kahlen Gesteins, besonders der Felsmassen mit einer Rinde von Kohle, Eisen- und Manganoxyd die Luft ungesund sey, grundlos ist, weiß ich nicht zu sagen. In der heißen Zone werden noch mehr als anderswo die krankheiterregenden Ursachen vom Volke willkührlich gehäuft. Man scheut sich dort im Freien zu schlafen, wenn einem der Vollmond ins Gesicht schiene; ebenso hält man es für bedenklich, sich nahe am Flusse auf Granit zu lagern, und man erzählt viele Fälle, wo Leute nach einer auf dem schwarzen kahlen Gestein zugebrachten Nacht Morgens mit einem starken Fieberanfall erwacht sind. Wir schenkten nun zwar dieser Behauptung der Missionäre und der Eingeborenen nicht unbedingt Glauben, mieden aber doch die *laxas negras* und lagerten uns auf mit weißem Sand

130 Reise in die Aequinoctial-Gegenden des neuen Continents. Band 3.

bedeckten Uferstrecken, wenn wir keine Bäume fanden, um unsere Hängematten zu befestigen. In Carichana will man das Dorf abbrechen und verlegen, nur um von den *schwarzen Felsen* wegzukommen, von einem Ort, wo auf einer Strecke von mehr als 10,000 Quadrattoisen die Bodenfläche aus kahlem Granitgestein besteht. Aus ähnlichen Gründen, die den Physikern in Europa als bloße Einbildungen erscheinen müssen, versetzten die Jesuiten Olmo, Forneri und Mellis ein Dorf der Jaruros an drei verschiedene Punkte zwischen dem Raudal von Tabaje und dem Rio Anavení. Ich glaubte diese Dinge, ganz wie sie mir zu Ohren gekommen, anführen zu müssen, da wir so gut wie gar nicht wissen, was eigentlich die Gasgemenge sind, wodurch die Luft ungesund wird. Läßt sich annehmen, daß unter dem Einfluß starker Hitze und beständiger Feuchtigkeit die schwarze Rinde des Gesteins auf die umgebende Luft einwirkt und Miasmen, ternäre Verbindungen von Kohlenstoff, Stickstoff und Wasserstoff erzeugt? Ich zweifle daran. Der Granit am Orinoco enthält allerdings häufig Hornblende, und praktische Bergleute wissen wohl, daß die schlimmsten Schwaden sich in Stollen bilden, die durch Syenit und Hornblendestein getrieben werden. Aber im Freien, wo die Luft durch die kleinen Strömungen fortwährend erneuert wird, kann die Wirkung nicht dieselbe seyn wie in einer Grube.

Wahrscheinlich ist es nur deßhalb gefährlich, auf den *laxas negras* zu schlafen, weil das Gestein bei Nacht eine sehr hohe Temperatur behält. Ich fand dieselbe bei Tag 48°, während die Luft im Schatten 29°,7 warm war; bei Nacht zeigte der Thermometer, an das Gestein gelegt, 36°, die Luft nur 26°. Wenn die Wärmeanhäufung in den Gesteinsmassen zum Stillstand gekommen ist, so haben diese Massen zu denselben Stunden immer wieder ungefähr dieselbe Temperatur. Den Ueberschuß von Wärme, den sie bei Tag bekommen, verlieren sie in der Nacht durch die Strahlung, deren Stärke von der Beschaffenheit der Oberfläche des strahlenden Körpers, von der Anordnung

Figure 1: Excerpt of Alexander von Humboldt's book "Reise in die Äquinoktialgegenden des neuen Kontinents" (Humboldt, 1859).

Charles Darwin described rock varnish close to San Salvador in Brazil in 1832 (Darwin, 1840). He referred to Alexander von Humboldt's observations of rock varnish at the Orinoco River and set his observations of black crusts in relation to them. His descriptions portray an extremely thin coating, which occurs within the limits of the tidal action. However, samples that

were collected in Brazil in the course of this thesis, from black varnish within the tidal zone, proved to be Mn-free and of biological origin (cyanobacteria). Since no exact locations are given in Darwin's publication, one can only make the assumption that Darwin observed cyanobacteria-covered rocks. Following the description by Darwin, investigations of rock varnish were published from 1876 (Loew, 1876) continuously until today, which provides a tremendous amount of publications, which, unfortunately, are not always in agreement with each other.

Over the years the rock varnish investigations focused on desert varnish, the rock varnish type only found in arid regions. This material is a worldwide phenomenon, easily detected in vegetation-poor areas. Additionally, it was proposed that desert varnish might be a potential paleoclimate archive for arid environments (Broecker and Liu, 2001; Dorn, 1984). Most current-day publications on the subject describe desert varnish. However, varnishes from stream sides (Darwin, 1840; Krinsley et al., 2012; Von Humboldt and Bonpland, 1819), alpine sites (Krinsley et al., 2009; Wang et al., 2011; Zhou et al., 2000), Antarctic environments (Dorn et al., 1992; Glasby et al., 1981; Johnston et al., 1984; Krinsley et al., 1995), urban areas (Grissom et al., 2014; Grüner, 2011; Livingston et al., 2016; Uchida et al., 2016; Vicenzi, 2016), cold environments (Dorn et al., 1992; Douglas, 1987; Whalley et al., 1990), cave locations (Frierdich et al., 2011; Miller et al., 2012; Saiz-Jimenez et al., 2012; Spilde et al., 2002; White et al., 2009), or even extraterrestrial sites (DiGregorio, 2001; Lanza et al., 2012; Lanza et al., 2015; Perry and Kolb, 2004b; Perry and Sephton, 2006) are also under investigation. To encompass all varnishes, the term "rock varnish" was introduced. It is problematic that literature data of rock varnishes, from different regions and environments, are used equivalently by some scientists describing the phenomenon. This is misguiding and might result in false evaluations. In this thesis, varnishes from different regions and environments are described in detail (appendix B.2 and B.4). Structures, chemical compositions, element distributions, and Mn oxidation states were investigated (appendix B.2 and B.4). Furthermore, the dust fraction (Otter et al., in preparation), the Mn- and Fe-rich matrix, and the potential biogenic contribution (Long-Yan et al., in preparation) to the genesis were examined. Urban rock varnishes were examined in detail (appendix B.5) and technical developments were made to facilitate rock varnish research in the future (appendix B.1 and B.3).

1.2 Description of Rock Varnish

"So much has been said about desert varnish that one wonders if there is anything else that can be said about the topic without repetition of old ideas." (Perry and Kolb, 2004a). This could not have been summarized more accurately, however, an introductory synthesis will be given in this thesis. It aims to highlight all factors: past research, the mineralogy, geology, and biology, which needs to be known to understand this highly controversial topic, which has been studied for a surprisingly long time without coming to a final conclusion. Furthermore, difficulties with dating this material will be discussed, as well as its applicability as a paleoclimate proxy, and the

two main methods used in the course of this thesis will be introduced for further understanding of the manuscripts in the appendix.

Rock varnish is an up to 200-250 µm thick (Broecker and Liu, 2001) hard (Mohs hardness about 6.6; Perry and Kolb, 2004a), and resistant (Oberlander, 1994) coating, which grows on rocks, independent of their lithology (Engel and Sharp, 1958; Oberlander, 1994) as a sediment and not as a weathering rind (Engel and Sharp, 1958; Goldsmith et al., 2014; Potter and Rossman, 1977; Potter and Rossman, 1979; Thiagarajan and Lee, 2004). It has been observed on limestones and marble in humid environments, but is best developed on durable silicate rocks (Oberlander, 1994). Arid desert rock varnish pebbles collected from the ground, with direct contact to the soil, usually reveal a Fe-rich, red reversal surface on their underside, and in direct contact to soil a shiny Mn-rich ground-line band (Engel and Sharp, 1958; Potter and Rossman, 1977; Reneau, 1993a). The varnish growth rate must exceed the host rock erosion rate to enable the formation. Estimates of the growth rate of rock varnish vary generally between 1 and 40 µm per 1000 years (Liu and Broecker, 2000; Spilde et al., 2013), but it is thought to be conceivably faster in non-arid environments. Growth rates seem to depend on the humidity of the environment, with slower growth rates for desert climates (Krinsley et al., 2012; Oberlander, 1994). However, the growth rate values published by different authors vary significantly. Rates as high as 639 µm per 1000 years were reported (Spilde et al., 2013), which were calculated from the varnish accumulation subsequent to the accumulation of a layer with assumed anthropogenic Pb enrichment, which grew during a 61 years long smelting period in the early 20th century. Since the genesis of rock varnish is not understood, none of the values published can be disproved or confirmed. However, whether the growth mechanisms of the different reported crusts are similar is still a matter of debate. It is likely that different growth rates and thicknesses represent varnishes from different environments and origins. This is the reason why rock varnish types (I – V) were introduced in this thesis (appendix, B.4) to start a categorization of this subject.

Rock varnish coatings are commonly shiny black, and though they are usually only micrometers in diameter, they are fully opaque. They appear on rock surfaces, frequently distributed as large patches (in the range of centimeters to meters in diameter), on certain outcrops, or on specific geomorphic features. The material is thought to accumulate over thousands of years (Liu and Broecker, 2008a) as a sediment, and thus layer by layer.

The definition of rock varnish implies that the material consists of approximately 60-80% mineral dust (Oberlander, 1994), including a large clay mineral fraction (Thiagarajan and Lee, 2004), and major amounts of Mn oxyhydroxides as matrix material. Potter and Rossman (1977) found in their rock varnish samples a clay mineral fraction of even more than 70% of the total volume. While the clay mineral fraction was found to consist mainly of illite, montmorillonite, or mixed-layer illite-montmorillonite, small amounts of kaolinite, and, in some instances, chlorite (Potter and Rossman, 1979), the Mn oxyhydroxides were reported to usually contain hollandite,

todorokite, birnessite, buserite, poorly crystallized phyllomanganates of unspecified type, and Mn-Fe-spinel (Garvie et al., 2008). A lack of dust would classify the material as heavy metal skin or Mn-dendrite, a lack of manganese as iron skin, and a lack of matrix material as dust film (Dorn, 2009; Potter and Rossman, 1979).

The third component of rock varnish, which is still under heavy discussion, are suggested potential biogenic contributions (Dorn and Oberlander, 1981b; Grote and Krumbein, 1992; Krumbein and Jens, 1981; Kuhlman et al., 2006b). Biogenic Mn oxidation is a fast process compared to abiogenic oxidation. However, the assumption that only biogenic Mn oxidation generates varnish growth would raise the question why some varnishes grow only nanometers per decade, and why remains of casts are scarce.

1.3 Theories of Rock Varnish Genesis

It is commonly accepted that mineral dust is one of the major components and element source providers of varnish. Mineral dust gets leached in low-pH waters such as rain and dew, H^+ ions are adsorbed, and subsequently cations, such as Mn, are released during this process. Manganese oxyhydroxides precipitate by (a)biogenic Mn oxidation, and the released elements are adsorbed mainly by available Mn oxyhydroxides. The abiogenic formation theory claims that the mechanism of Mn oxidation is a pH value increase when rain or dew get in contact with the already present varnish coating, alkali and alkaline earth metal bearing minerals, or clay minerals from the host rock. A large fraction of the remaining leached dust gets removed from the surface by water or wind, and only a minor fraction of the accumulated dust particles, which settled on exposed rock surfaces, are cemented allowing the formation of rock varnish. The genesis of the Mn-rich cement is highly controversial. The source of the high Mn mass fractions (up to 40% MnO) in varnish seems to be leached mineral dust (average mineral dust about 0.1% MnO) (Scheuvens et al., 2013). Nevertheless, the mechanism to oxidize mobile Mn^{2+} to immobile Mn^{4+}, and to selectively scavenge Mn over Fe, allows only a very narrow pH and E_h range.

There are four main theories, which have been suggested for the process of a Mn-rich crust development: I) Abiogenic precipitation with leaching of minerals under well-defined pH (5.7) and E_h (0.8) conditions in rainwater or dew, to allow geochemical fractionation of Mn (Thiagarajan and Lee, 2004). At these pH and E_h conditions Mn is more soluble than Fe. The dissolved Mn content is enhanced relative to the dissolved Fe content. Following increases in the pH values up to 8.5 can oxidize the enriched amounts of Mn to immobile oxyhydroxides. However, this process is slow and the question remains why varnish covers only certain patches and not large areas. The process might be accelerated and partially controlled by autocatalysis. II) Biologically induced growth. Mineralization in this scenario is the result of interactions between biological membranes/cell surfaces and the inorganic environment, changing the direct environmental conditions to induce mineralization (Wang and Müller, 2009; Wang et al., 2011). III) Bio-

logically controlled mineralization during which cellular activities direct the initial nucleation of the inorganic deposition. This is followed by the growth of a mineral product with a biologically directed morphology (Wang and Müller, 2009; Wang et al., 2011). IV) A combination of the processes described above.

1.4 Rock Varnish Components

1.4.1 Mineral Dust

The current hypotheses about the rock varnish formation claim that the source of the enriched elements in varnish is mainly dust, which gets leached in rain water or dew (Fig. 2). Furthermore, the major component of rock varnish is fine-grained mineral dust incorporated in a Mn-rich matrix. Consequently, there are two dust fractions in this model, one which gets leached and subsequently removed by wind or water, and one that gets incorporated into the varnish coating.

1.4.1.1 Phyllosilicates

Mineral dust is not only important as an element contributor, but also as incorporated material, representing about 70% of the varnish fraction in most varnishes. The most important component of the dust fraction are clay minerals, due to their (de)sorption and swelling potential. The definition of clay minerals is either particles smaller than two micrometers, also called the "clay fraction", but it can also be used as a chemically defined term for phyllosilicates, not being restricted to a certain size range. The term clay minerals will be used in the following corresponding to the second definition. In general all phyllosilicates, low and high temperature types, can be considered to be formed from stacked atomic planes parallel to the (001) face (Velde and Meunier, 2008). The minerals are composed of a combination of two types of sheet structures. One structure are tetrahedral sheets (T-sheets), which are composed of SiO_4^{4-} or AlO_4^{5-} tetrahedra linked by sharing 3 of 4 vertices (Velde and Meunier, 2008). The second type are octahedral sheets (O-sheets), in which Al^{3+}, Fe^{3+}, Fe^{2+}, or Mg^{2+}cations exhibit a six-fold coordination when they are bound to O^{2-} or OH^- anions. The octahedra are linked by sharing their six vertices. Clay minerals are composed essentially of Si, O, Al or Mg, or both, and water. Iron substitutes Al and Mg in varying degrees, and appreciable quantities of K, Na, and Ca are frequently present (Velde and Meunier, 2008). Within a structure, T- and O-sheets can be linked to each other. A linkage between the two

Figure 2: Dust accumulation on a rock varnish covered horizontal surface in the Sahara region. Dust accumulates preferentially in microbasins. (Image credit: B. Macholdt)

sheet types, forming a layer, results in deformation of the sheets, since their a- and b-dimensions differ significantly. Thus, they have an offset in space along the c-axis. There are two types of layers: layers with 1:1 (T-O) and 2:1 (T-O-T) ratios. The main clay minerals found in rock varnish are illite ($(K,H_3O)(Al, Mg, Fe)_2(Si, Al)_4O_{10}[(OH)_2, H_2O]$; 2:1 type), montmorillonite ($(Na, Ca)_{0.3}(Al, Mg)_2Si_4O_{10}[(OH)_2*nH_2O]$; 2:1 type), and small amounts of kaolinite ($Al_2Si_2O_5[(OH)_4]$, 1:1 type) (Potter and Rossman, 1979).

If negative charges are present, such as in 2:1 layers, interlayer cations are incorporated to compensate for them. Most of the interlayer cations are exchangeable with those of the solution in contact to the crystallites. Cations incorporated into the interlayer sheets are much more varied than those in tetrahedral and octahedral sheets, since the large-sized interlayer sites are able to house cations with large radii, such as Sr^{2+}, Ba^{2+}, K^+, Rb^+, or Cs^+ (Velde and Meunier, 2008). Cations can even be adsorbed in their hydrated state in the interlayer zone or into hexagonal vacancies, where water molecules form a shell around the cation (Velde and Meunier, 2008).

In addition to incorporation, substitution of cations within a layer is common. It can be either a homovalent substitution of cations of the same valence state (e.g., Fe^{3+} for Al^{3+}), or a heterovalent substitution of cations of different valence states (e.g., Fe^{2+} for Al^{3+}) (Velde and Meunier, 2008). The latter results in an additional negative charge. One very common heterovalent substitution is Si^{4+} by Al^{3+} in the tetrahedral layers. Hence, negative charges and changes of the symmetry of the tetrahedral sheet are common.

The strong cohesion between the Mn oxyhydroxide matrix and the clay minerals in rock varnish might be a result of the similarities of the phyllomanganates and phyllosilicates. “The primary importance of clays to varnish formation may be their active influence on oxide deposition. Besides adsorption of Mn and Fe from solution, the clays may directly influence the Mn-oxide mineralogy. The hexagonal arrangement of the oxygens in either the tetrahedral or the octahedral layers of the clay minerals could form a suitable template for crystallization of the layered structures of birnessite. The average O-O distance of the tetrahedral layer is 3.00 Å in illite--montmorillonite mixed-layered clays, which differs only 3.4% from the 2.90 Å distance of the hexagonally close-packed oxygens in birnessite.” (Potter and Rossman, 1979). Furthermore, clay minerals, especially 2:1 sheet clays, such as illite or bentonite, fix relatively large amounts of Mn, depending on the pH and E_h conditions (Reddy and Perkins, 1974). The amount increases with increasing pH and E_h conditions (Reddy and Perkins, 1974). Manganese does not substitute for Al or Si in this case, since no structural changes occur after absorption (Reddy and Perkins, 1974), and Mn is not absorbed in the interlayer sites of the clay minerals, since this would require a basal spacing of 14 Å or more (Potter and Rossman, 1977). It seems very likely that the oxides are present mainly as external coatings (Potter and Rossman, 1977). “In this way the clay and oxide phases may be mutually dependent: the clay depending on the oxides for resistance to erosion; the oxides depending on the clay for transport and deposition. This would explain why nei-

ther pure clay nor pure ferromanganese oxide coatings are associated with desert varnish." (Potter and Rossman, 1977).

Unfortunately, due to the characteristics of clay minerals, it is likely that the large clay fraction, e.g., of illite or montmorillonite, swells when being wet. Repeated swelling and contracting during wet and dry phases can induce textural changes of the matrix material and structures of rock varnish, even if it is already incorporated into the rock varnish matrix (Garvie et al., 2008). Taking this into account, it is very unlikely that varnishes older than the Quaternary can be found, since continuous swelling and contracting, or long exposure to water such as groundwater, would probably dissolve or recrystallize rock varnish (Garvie et al., 2008).

1.4.1.2 Cation Leaching from Phyllosilicates

Cations incorporated in interlayer sheets of clay minerals can be mobilized under low pH condition, when they get released and exchanged by H^+ ions. Within the mixture of different cations, Mn^{2+} and Fe^{2+} are available. These elements are present in their reduced states due to the low pH conditions e.g., of acidic rain water, dew, or fog. The two elements become immobilized when they are oxidized. The oxidation could occur due to an increase of the pH value, by oxidation by strong oxidants such as Mn oxyhydroxides (autocatalysis), due to the presence of alkali and alkaline earth metal containing minerals, or by biogenic oxidation. The oxidation mechanisms of Mn in rock varnish remain unclear. Manganese, the main matrix element in rock varnish, is discussed in detail in the following chapter (chapter 1.4.2). Most of the dust, along with insoluble (e.g., high field strength elements (HFSEs)) and easily dissolved elements without high adsorption potential (e.g., Rb, Cs), are removed by wind or drained from the rocks by water, leaving behind elements with high adsorption potential and high particle reactivity (e.g., Co, Ni, Pb, Ce) (Thiagarajan and Lee, 2004). Clay minerals and Mn oxyhydroxides, which are great ad- and absorbers, scavenge these elements and become enriched (Thiagarajan and Lee, 2004). Thus, rock varnish has a Rb and Cs depletion and a Co, Ce, Ni, and Pb enrichment. Furthermore, the element enrichment is an indicator that water has to be removed from the system by runoff or wind and not by evaporation. Evaporation could not explain the equilibrium partitioning between water and Mn/Fe oxyhydroxides, as well as the depletion of highly soluble elements such as Rb and Cs (Thiagarajan and Lee, 2004).

An indicator for the involvement of atmospheric particles in the rock varnish formation is the positive Ce-anomaly, which can be observed in almost all rare earth element (REE)-patterns of varnishes (appendix, B.2 and B.4). Prior to its oxidation by Mn oxyhydroxides, Ce must be available in its reduced state, otherwise no positive Ce-anomaly would evolve in varnish. Previous oxidation would precipitate CeO_2 in the water phase and remove it as an insoluble component from the system by wind or water, together with the larger portion of the mineral dust fraction. Furthermore, oxygen isotope ratios ($^{17}O/^{16}O$) in varnish samples are more similar to those found

in mineral dust, rather than to the values found in nearby surface soils (Bao et al., 2001). This indicates that the varnish sources are not necessarily locally derived. Lead-rich horizons (Dorn et al., 2012; Nowinski et al., 2010; Spilde et al., 2013) and unusual element enrichments in varnish, such as Hg, ^{210}Po, ^{210}Pb, ^{137}Cs, and ^{238,239,240}Pu (Fleisher et al., 1999a; Hoar et al., 2011; Hodge et al., 2005; Nowinski et al., 2012; Nowinski et al., 2013; Nowinski et al., 2010), are further evidence for an atmospheric source of varnish, since these elements were released to the atmosphere by nuclear weapon testing, coal-fired power plants, and smelters. The use of varnish as passive environmental monitor of atmospheric pollution was suggested, which might help to detect sources of natural or anthropogenic air pollution (Nowinski et al., 2012; Nowinski et al., 2013; Nowinski et al., 2010).

1.4.2 Manganese Oxyhydroxides

More important than the dust component is the matrix, even though it represents a smaller fraction of the overall rock varnish composition. Manganese oxyhydroxides provide the distinctive physical characteristics to rock varnish, such as the major sorption capabilities, the black color, and the puzzling genesis with unclear accumulation mechanisms. Manganese in rock varnish is of specific interest, since this element has unique qualities. In nature it exists in three different oxidation states: Mn^{2+}, Mn^{3+}, and Mn^{4+}, where Mn^{2+} is usually mobile, while Mn^{4+} is immobile. Iron often occurs in combination with Mn, since the two elements have several characteristics in common. However, Fe exists in nature only in two oxidation states (Fe^{2+}, Fe^{3+}), enabling Mn to develop several additional properties and mineral phases. Iron oxyhydroxides are common minerals in the Earth's crust (such as e.g., in rust, ferrihydrite in creeks, and laterite) and Fe has an abundance of 5.04% FeO_T (Rudnick and Gao, 2003) in the upper continental crust (UCC). Manganese is a geological minor element with an abundance of 0.1% MnO in the UCC (Rudnick and Gao, 2003). It is usually available in reduced or partially oxidized valence states in geological materials (e.g., rhodocrosite ($MnCO_3$), hausmannite (Mn_3O_4), or manganite (γ-MnOOH)).

Figure 3: Varnish covered canyon in the Sahara region. Varnish covers are especially thick on major water discharge pathways (circle 1), and thin or lacking below overhanging rock surfaces (circle 2). (Image credit: B. Macholdt)

The Mn-accumulation in rock varnish might resemble that of Mn-nodules in the ocean (Bauman, 1976; Wang et al., 2011), however, the ion-transport medium and the Mn sources are known for the ocean, while they are under discussion for terrestrial environments. Nonetheless, it

is quite certain that water, such as dew or rain, contributes to the formation of rock varnish (Fig. 3) (Goldsmith et al., 2012; Goldsmith et al., 2014; Northup et al., 2010a; Thiagarajan and Lee, 2004). Interestingly, the most frequently reported growth rate of varnish (1-40 µm/1000 years) is of about the same order of magnitude as that of average deep sea Mn-nodules (a few mm per million years) (Bau et al., 2014). However, while Mn nodules grow undisturbed over a larger time range, terrestrial rock varnish is exposed to weathering and changes of geological settings.

Unlike in terrestrial environments, seawater in coastal fjords and hemipelagic waters was found to contain mainly Mn^{3+} ions as mobile manganese fraction. In oxic and suboxic water environments, soluble Mn^{3+}-ligand (Mn^{3+}-L) complexes are common, which form an intermediate between Mn^{2+} and Mn^{4+} (Oldham et al., 2017). These Mn^{3+}-L complexes are mobile and stable in water (Oldham et al., 2017). They can form via several different reactions, involving surface catalysis (Davies and Morgan, 1989), bacterial mediation (Tebo et al., 1997), or in-situ ligand-promoted oxidation or reduction (Duckworth and Sposito, 2005). The complexes compete with Fe^{3+} for available ligands, however, Mn^{3+}-L complexes bind more strongly to the same ligands than Fe^{3+} (Luther, 2010), and could thus affect the bioavailability of Fe^{3+} (Oldham et al., 2017). Since Mn^{3+}-L complexes do not form colloids, in contrast to Fe^{3+}-L complexes, they have a higher mobility than Fe^{3+}-L complexes and can be transported over longer distances (Oldham et al., 2017). The complexes can donate or accept electrons and can thus be easily oxidized to MnO_x in the oxic zone (Oldham et al., 2017). They are thus possible sources for Mn-rich crusts which form in river splash zones.

Manganese oxyhydroxides can be broken down into octahedra, composed of a Mn ion surrounded by six oxygen atoms. The only exceptions are hausmannite ($Mn^{2+}\,Mn^{3+}{}_2O_4$), which has a spinel-like structure with Mn^{2+} in the tetrahedral and Mn^{3+} in the octahedral sites, and bixbyite ($(Mn, Fe)_2O_3$; Post, 1999). These two minerals are typically found in hydrothermal or metamorphic deposits (Post, 1999). Out of the octahedra described above, more than 30 known Mn oxyhydroxides can be assembled, which can be subdivided into chain- or tunnel structure and layer structure types (Post, 1999). “The tunnel Mn oxides are constructed of single, double, or triple chains of edge-sharing MnO_6 octahedra, and the chains share corners with each other to produce frameworks that have tunnels with square or rectangular cross sections.” (Post, 1999).

Unfortunately, the crystal structures are quite similar for several of the Mn oxyhydroxides. In many cases it is necessary to combine powder X-ray diffraction studies with other techniques, such as transmission electron microscopy (Tebo et al. 2005), IR spectroscopy, and electron microprobe analysis (Post, 1993; Post, 1999), to identify the mineral. Despite the fact that Mn oxyhydroxides have been extensively studied for the past several decades, the details of their mineral structures are still poorly understood (Feng et al., 2007), and there are several phases for which even the basic crystal structures are not known (Mc Kenzie, 1989; Post, 1993; Post, 1999). To allow the investigation of mineral phases, interactions, structures, surface properties, origination

mechanisms, environmental geochemical behaviors, or adsorption properties, it is necessary to synthesize minerals (Feng et al., 2007). However, single-phased Mn oxides are not easy to synthesize due to their non-stoichiometric composition, various species, and close formation conditions (Feng et al., 2007).

The most commonly reported Mn oxyhydroxides in rock varnish are the phyllomanganates (layer-types) birnessite ((Na, Ca, Mn^{2+})Mn_7O_{14}*2.8H_2O) and buserite ((Na, Mn)Mn_3 O_7 *$n$$H_20$), and the tectomanganates (tunnel-types) todorokite ((Ca, Na, K)$_x$(Mn^{4+}, Mn^{3+}, Mg)$_6O_{12}$*3-4.5H_2O) and hollandite (Ba_x(Mn^{4+}, Mn^{3+})$_8O_{16}$) (Burns and Burns, 1977; Post, 1999). While birnessite has an interlayer space of about 7 Å, and therefore incorporates a single layer of water molecules and e.g., Na^+, buserite has an interlayer space of about 10 Å, allowing the incorporation of a double layer of water molecules and cations such as Mg^{2+} (Atkins et al., 2014). Upon drying, buserite collapses to the typical 7 Å birnessite spacing (Post, 1999). Cations such as Ni^{2+}, Mg^{2+}, Ca^{2+}, and Co^{2+} tend to stabilize the buserite structure against collapse (Giovanoli and Burki, 1975; Paterson et al., 1986). Birnessite is available with triclinic and hexagonal symmetry. The hexagonal form shows well-ordered vacancies and mainly Mn^{4+} (Atkins et al., 2014). It is reported that hexagonal birnessite can transform to triclinic birnessite via a topotactic transformation depending on the pH value, with hexagonal birnessite being the low pH modification (Manceau et al., 2002). Todorokite can evolve from birnessite during diagenesis or mild hydrothermal conditions (Atkins et al., 2014). Large amounts of absorbed transition metals hinder the transformation from the phyllomanganate birnessite to the tectomanganate todorokite, which takes place via kinking of layers and subsequent Ostwald ripening (Atkins et al., 2014). While Cu^{2+}, for instance, does not retard the transformation due to its Jahn-Teller distortion, Ni^{2+} does so significantly, until it is finally lost to solution when the transformation takes place (Atkins et al., 2014). The, often secondary, todorokite is able to host Ba^{2+} within its tunnel structure when it is observed in terrestrial surroundings, while it usually hosts Mg^{2+} in seawater. Hence, the high Ni and Ba amounts observed within rock varnish indicate the presence of a mixture of phyllo- and tectomanganates. Todorokite is the main tectomanganate found in nature, and is often reported in manganese nodules (Post, 1999). It is constructed of double chains of edge-sharing MnO_6 octahedra, but they are linked in such a way as to form tunnels with square cross sections, measuring three octahedra on a side (Post, 1999), which is about 10*10 Å (Atkins et al., 2014). Hollandite exhibits a tunnel with two octahedra linked together on each side of the tunnel (Post, 1999), and has thus a smaller cation capacity. Its tunnel sites are partially filled with large uni- or divalent cations, and, in some cases, water molecules (Post, 1999).

All manganese oxyhydroxides are element scavengers, and consequently often used as filter materials (Iannicelli, 1992; Stüben, 2007). They belong to the most widely studied nanosized metal oxides, together with iron oxides, aluminium oxides, and titanium oxides, for the adsorption of heavy metals from aqueous systems (Hua et al., 2012). Due to their great sorption poten-

tial and the preference of the absorption of certain elements in specific Mn oxyhydroxides, a vague discrimination between mineral phases on behalf of element availability is possible. Of several Mn oxyhydroxide minerals tested, birnessite exhibited the largest adsorption capacity for the tested heavy metals Pb^{2+}, Cu^{2+}, Co^{2+}, Cd^{2+}, and Zn^{2+}, while hausmannite revealed the smallest one (Feng et al., 2007). Barium, a very large atom (radius Ba^{2+}~ 2.5 Å) is, on the contrary, mostly restricted to inner-tunnel sites of tectomanganates.

The high absorption capacity of Mn oxyhydroxides is based on their negative charge, which can be observed in all Mn minerals. As discussed for clay minerals, Mn oxyhydroxides are also prone to homo- and heterovalent substitution, interlayer, and inner-tunnel adsorption. The ad- and absorption of Mn oxyhydroxides is especially high, since heterovalent cation substitution is very common (e.g., Co^{3+} for Mn^{4+}), Mn^{4+} is often exchanged by Mn of lower valence states, Mn vacancies are common, and oxygen atoms at the surface are not shared (Manceau et al., 2002). Since Mn oxyhydroxides are often nanocrystalline, large surface areas provide high charges due to non-bound oxygen atoms. Potter and Rossman (1979) reported, on basis of IR spectra, well-ordered birnessite as main Mn oxyhydroxide in rock varnish. Since the same samples are X-ray amorphous, the particle sizes of the minerals are below 0.1 µm (Potter and Rossman, 1979).

As compensation for these negative charges, Mn oxyhydroxides can either react by the uptake of protons (e.g., OH^- as substitution for O^{2-}), or by the absorption of alkali, alkaline earth, and transition metal cations in the interlayer space on well-defined crystallographic sites between two layers, or into a tunnel site of tectomanganates (Manceau et al., 2002). A first sorption on the surface takes place e.g., via vacant sites within a MnO_2 layer (hexagonal birnessite) or by forming surface complexes on edge sites of MnO_2 layers (triclinic birnessite) (Peacock and Sherman, 2007). Sorbed elements, such as Ni in birnessite, can transform from surface complexation to structural incorporation (Peacock and Sherman, 2007). This incorporation is quite important as a potential irreversible sink for elements (Peacock and Sherman, 2007). Manganese oxyhydroxides are furthermore one of the strongest naturally occurring oxidants, oxidation states can thus change, e.g., subsequent to degrading organic matter. Since biogenic reduction of Fe oxyhydroxides is a frequent phenomenon in nature, Mn^{4+} is able to subsequently oxidize Fe via a redox reaction, becoming reduced in an otherwise oxic environment due to this property (Lovley, 1992).

The average oxidation state of typical (arid desert) rock varnish samples lies in the range between +3.76 and +3.93 (Potter and Rossman, 1979). This is quite common for several Mn oxyhydroxides. Feng et al. (2007) report average Mn oxidation states (AOS) for birnessite, todorokite, and cryptomelane being +3.96, +3.82, and +3.90, respectively. Hence, Mn^{4+} oxyhydroxides are usually nonstoichiometric, and thermally induced "electron hopping" between Mn^{3+} and Mn^{4+} is possible. It is generated by optically induced charge-transfer (Sherman, 2005). This might account for the opacity of Mn minerals with high oxidation states ($Mn^{3+/4+}$). They are often black in color, denoting absorption in the visible and near-infrared, while Mn oxyhydroxides with

low oxidation states ($Mn^{2+/3+}$) tend to be lighter colored (Sherman, 2005). This photon absorption is based on the splitting of the d-orbital of Mn^{4+} in the imposed crystal field. The brownish color of some varnishes is a result of the mixture of black Mn oxyhydroxides and orange-red Fe oxyhydroxides (Oberlander, 1994).

However, this optically induced charge-transfer is based on energies significantly smaller than those of the band gaps also present in Mn oxyhydroxides. These account for the photoelectrochemistry of Mn^{4+} oxides (O(2p)→Mn(3d) orbital) (Sherman, 2005). The photoreductive properties of semi-conducting Mn oxyhydroxides allow the oxidation of organic matter and water due to electron loss to the electron hole developed within the Mn oxyhydroxide during the relocation of one electron from the valence to the conduction band (Kwon et al., 2009). Organic ligands are nevertheless more effective hole scavengers than water (Sherman, 2005), which is unfortunate for the identification of organic material within the rock varnish matrix. The reaction

$$MnO_2 + h\nu + RCOOH\ (carboxylic\ acid) + 3H^+ \rightarrow Mn^{2+} + CO_2 + 2H_2O + R^+$$

and furthermore

$$2R^+ + 2H_2O \rightarrow 2RH + H_2O_2$$

is likely to take place (Sherman, 2005). Another result of photoreduction is the dissolution of the Mn oxyhydroxide by reducing Mn^{4+} to Mn^{3+} and further to Mn^{2+}. In most cases the released Mn^{2+} is re-adsorbed to the Mn oxyhydroxide surface instead of being released into the surrounding water.

In conclusion, the rock varnish matrix is of major interest because of three points:

I) Manganese and iron behave very similar, which becomes apparent when one studies their transitions in pH-E_h diagrams (Skinner and Fitzpatrick, 1992). Even though the Fe mass fraction in varnish is high (around 5-10%), it is only enriched by a factor of 2-3 relative to the UCC, while Mn is enriched by a factor of 40-400. The only possibilities to chemically enrich Mn by such a factor, without enriching Fe simultaneously by the same factor, is by moving in certain small pH and E_h ranges, enabling exclusively Mn dissolution and subsequent precipitation (Thiagarajan and Lee, 2004), by the presence of significantly higher Mn mass fractions in the source material, or by biogenic accumulation and oxidation. The questions remain: how do these pH and E_h ranges arise, and why do they only occur on certain patches, outcrops, or areas? Might autocatalysis be important for the patch-like distributed precipitation of Mn oxyhydroxides? Which source could provide significantly higher Mn than Fe mass fractions? Is the oxidation of Mn possibly of biogenic origin, which would eliminate the problem of generating perfect pH and E_h conditions?

II) Some varnishes contain alternating Mn- and Fe-rich layers. How do they develop, and how reliable are they as paleoclimate archives?

III) Manganese oxyhydroxides have high ad- and absorption potentials, higher than those of clay minerals, and are one of the strongest naturally occurring oxidants. Thus, rock varnishes, just as Mn nodules, are great trace element and transition metal sinks. This is not of economic inter-

est, since varnish is too thin to be of importance for mining, but Pb-, Po-, Hg-, and Pu-rich horizons are of interest, since they can be utilized as cross-correlation features to assign time periods to these horizons. The authenticity of petroglyphs engraved in rock varnish can be checked by searching for Pb peaks within the new developed varnish crust (Dorn et al., 2012). This is possible, since Pb^{2+} is the cation with the highest uptake preference, regarding e.g., Pb^{2+}, Cd^{2+}, Zn^{2+}, and Tl^{2+}, which gets absorbed even at very low pH levels. At pH 2 almost 70%, at pH 3 90%, and at pH 6 almost 100% of Pb get absorbed for small Pb amounts in solution (Gadde and Laitinen, 1974). Feng et al. (2007) state that birnessite, cryptomelane and todorokite show the greatest absorption capacity on Pb^{2+} among their tested heavy metals (Pb^{2+}, Cu^{2+}, Co^{2+}, Cd^{2+}, and Zn^{2+}). In a solution containing several cations, Pb gets absorbed first. If a Mn oxyhydroxide absorbed other cations from a Pb-free solution and is charge-neutral by that, it will release those in exchange for a Pb^{2+} uptake when this element is later added to the system (Gadde and Laitinen, 1974). This property of Mn oxyhydroxides allows to interpret the presence or absence of Pb-rich layers as actual indicators for the availability of Pb in the atmosphere. This Pb uptake is true for almost all Mn oxyhydroxides.

1.4.3 Organic Compounds

The oxidation of Mn^{2+} to Mn^{4+} requires certain narrow environmental conditions over a long time period if happening solely by abiogenic chemical precipitation. The oxidation could occur much faster and under a larger range of conditions, if it was biologically induced or controlled. The question why Mn is enriched over Fe would be solved and the occurrence as patches or isolated areas could be explained. It was proven that organisms are capable of oxidizing manganese, but it cannot be fully understood why, since the advantage for the organisms is uncertain up to now (Tebo et al., 2005). However, there are several ideas why bacteria might oxidize $Mn^{2+/3+}$ to Mn^{4+}. It could be a protective mechanism, since by oxidizing $Mn^{2+}_{(aq)}$ to MnO_2 oxyhydroxide minerals, bacteria can encrust themselves to become shielded against UV radiation, predation, viral attacks, or heavy metal toxicity (Tebo et al., 2005). Another theory is that bacteria precipitate Mn oxyhydroxides to obtain an available potential redox substance. Manganese^{4+} oxyhydroxides are capable of oxidizing refractory organic matter and degrading humic substances oxidatively to lower molecular weight compounds that can be used as substrates for microbial growth (Sunda and Kieber, 1994). Manganese^{4+} oxyhydroxides might thus be stored as available electron acceptors, e.g., for future carbon oxidation (Spiro et al., 2009; Tebo et al., 1997).

Several authors list the commonly found cauliflower-like or stromatolitic microstructure of rock varnish as an indicator for a biogenic formation (Krinsley, 1998; Krinsley et al., 2009; Nagy et al., 1991; Perry and Adams, 1978; Raymond et al., 1993). This microstructure, however, was proven to be also producible abiogenically from colloids (McLoughlin et al., 2008). These abiogenic stromatolites, so-called “Taylor stromatolites”, are formed in a turbulent flow regime with

low particle concentrations of high viscosity. A greater particle flux, lower viscosities, and higher impact velocities cause the spreading and merging of the particles and the formation of laminae (McLoughlin et al., 2008). Both features, stromatolite-like structures and laminae, are commonly found within rock varnish. The Taylor stromatolites were produced with spray paint by McLoughlin et al. (2008), which resembles a sediment suspended within a carrier phase (coloring pigment in liquid phase vs. dust particles within a water droplet) distributed by wind.

McLoughlin et al. (2008) state that an abiogenic formation of the stromatolite structures does not negate the fact that biological material, such as spores or amino acid derivatives, which may be passively entombed within such laminated structures, are an important archive of information regarding past environments and biological processes. This is an important statement, which summarizes the main challenge to prove whether rock varnish has a biogenic or abiogenic formation history. The main question is "are the organisms entombed by chance, or responsible for the formation?". In this thesis it was tried to consider this question by searching for live or functional groups entombed within the crusts (by Scanning transmission X-ray absorption microscopy-near edge X-ray absorption fine structure spectroscopy (STXM-NEXAFS)), reveal if the organisms found are actually capable to oxidize Mn (by polymerase chain reaction (PCR) analyses), and check if the same organisms are present on all rock varnish samples investigated.

Organisms oxidize Mn^{2+} by two one-electron transfers, where Mn^{3+} does not occur as a solid intermediate (Tebo et al., 2004). Since these Mn bio-oxides, usually hexagonal birnessite, therefore originally contain only Mn^{4+}, they have large numbers of layer site vacancies (15-50%) to prevent an initial charge of the mineral. Smaller particle sizes, usually nanocrystals, are further common characteristics of Mn bio-oxides. Based on this, Kim et al. (2011) interpreted a full electron paramagnetic resonance (EPR) dataset. These measurements were conducted to categorize Mn-rich geological materials on behalf of resonance peaks of these materials with unpaired electrons. The width, size, and occurrence of these peaks at a certain magnetic field strength depend on the distance of one atom to the next neighboring atom (here Mn) and its oxidation state. The linewidth of the resonance peaks was observed to reveal a fundamental difference between biogenic and abiogenic Mn oxyhydroxides. Kim et al. (2011) explain the observed narrow linewidth of their Mn bio-oxides by large numbers of layer site vacancies present, small particle sizes, and the absence or low abundance (0-5%) of Mn^{3+}. During this study, EPR measurements were performed for several samples, discovering that these rock varnishes consist of a mixture of hexagonal birnessite and other Mn oxyhydroxide phases (appendix B.4).

Manganese oxidizing bacteria and fungal communities are well known (Bromfield and David, 1976; Cahyani et al., 2007; De la Torre and Gomez-Alarcon, 1994; Francis and Tebo, 2001; Spiro et al., 2009; Toner et al., 2005; Villalobos et al., 2005) and were thoroughly examined for their possible contribution to the rock varnish genesis by several authors (Dorn, 1984; Northup et al., 2010b; Parchert et al., 2012; Perry et al., 2003; Staley et al., 1992; Taylor-George et al., 1983).

Publications are available that report the observation of bacteria, algae, lichen, and fungi in and on rock varnishes, several of them capable of Mn oxidation under laboratory conditions (Dorn, 1984; Dorn and Oberlander, 1981b; Krumbein and Jens, 1981; Kuhlman et al., 2006a; Kuhlman et al., 2007; Northup et al., 2010b; Parchert et al., 2012; Raymond et al., 1993; Staley et al., 1992; Taylor-George et al., 1983). Heterotrophic organisms that do not show carbon fixation were found in varnish (Taylor-George et al., 1983). Other authors state that they see clear evidence for photosynthetic activity of endolithic "microbial solution fronts" in all of their varnishes collected from several environments and continents (Krumbein and Jens, 1981). Some authors report only gram-positive bacteria (Perry and Kolb, 2004a), while others report the exclusive occurrence of gram-negative bacteria in their varnishes (Dorn and Oberlander, 1981b). Publications can also be found which report the finding of microcolonial fungi (MCFs) at all sampling sites of rock varnish samples, and claim that MCFs may play a crucial role in the rock varnish formation (Parchert et al., 2012; Taylor-George et al., 1983). In addition, publications are available about biological finds in rock varnish, which are cited quite often as evidence for a biogenic formation of varnish, but which do not indicate if the crusts which were investigated contain elevated amounts of Mn, and therefore fulfill the definition of rock varnish (Esposito et al., 2015; Lebedeva and Shishkov, 2016; Nowinski et al., 2010; Perry and Sephton, 2008; Wang et al., 2011). Two experiments were conducted which report successfully reproduced varnish-like crusts from organisms collected on natural rock varnishes (Dorn and Oberlander, 1981a; Krumbein and Jens, 1981). These two experiments are often cited as proof for the biogenic formation of rock varnish crusts.

However, the mineralogy of the crusts grown by Krumbein and Jens (1981) was not examined, leaving the question open whether varnish was actually formed or not (Perry and Kolb, 2004a). It has been criticized that the generated crusts visually did not resemble real varnish crusts. Krumbein and Jens (1981) investigated the initial natural varnish crusts and found that the number of microorganisms which are able to precipitate Mn and Fe, in relation to the total number of isolates, was not higher in the varnish crusts than in additionally investigated soil environments.

Dorn and Oberlander (1981b) provide no further details about their successful varnish culturing conditions, such as exact time, temperature, and exposition to light. The crusts grown by them contained only minor amounts of Mn and were relatively soft with Mohs hardness of 2.5. The organisms found by Dorn and Oberlander (1981b), which they claimed to be responsible for the Mn oxidation, led to a controversy later on. There was doubt if the observed *Metallogenium* is an actual organism (Gregory et al., 1980; Klaveness, 1977), and it was criticized that previous reports of this organism were solely from aquatic habitats and their sediments (Taylor-George et al., 1983). The organisms reported by Dorn and Oberlander (1981b) were found in no other varnish samples later on. "Unfortunately, it was not possible to further characterize the isolates of

Dorn and Oberlander, or to confirm their results by repeating their laboratory studies, because cultures of their Metallogenium-like and Pedomicrobium-like bacteria have not been maintained (R. Dorn, personal communication)." (Taylor-George et al., 1983).

A third varnish crust growth experiment, taking about two years, was conducted by Palmer, Adams, and Staley. They also used organisms collected from natural rock varnishes. This experiment was unsuccessful, since no varnish-like crusts developed. The experiment was not published (Perry and Kolb, 2004a). To summarize, none of the experiments cited could reproduce the natural conditions under which rock varnish forms (Staley et al., 1992). One reason for this might be that cultivation of microbes from extreme environments is difficult, due to the difficulty of reproducing the proper conditions required for growth in the laboratory (Kuhlman et al., 2008).

To complete this section, one also has to mention the authors who saw no evidence for biogenic contributions during their rock varnish studies, such as Goldsmith et al. (2014), Perry et al. (2006), Potter and Rossman (1977), Smith and Whalley (1988), Smith and Whalley (1989), Thiagarajan and Lee (2004), and Wayne et al. (2006). However, there is only one reported experiment by Elvidge and Moore (1979), which claims successful abiogenic rock varnish growth in a laboratory. Measurements of δ^{56}Fe from natural soil and rock varnish samples indicated that at least the iron in rock varnish precipitated via inorganic processes (Perry and Kolb, 2004a).

Since we can find a large variety of theories in the extensive pool of rock varnish publications, and the theories clearly disagree with each other, we tried to find evidence in our samples, which represent a large collection from several environments, ages, and continents. Staley et al. (1992) stated that "If microorganisms are the causative agents of desert varnish, they would be expected to be found in all varnishes that are actively formed.". Until now, however, there seems to be no one single organism or group of organisms present in a set of different rock varnish samples (Northup et al., 2010b; Perry and Kolb, 2004a).

1.5 Dating Rock Varnish

The history of rock varnish dating spans about 35 years by now. First rock varnish dating attempts were made using varnish thickness as age index (Hayden, 1976; Oberlander, 1994). However, this proved to be unreliable, since varnish is thinner on smoother substrates and thicker over irregular dust- and moisture-trapping substrates. Varnishes that are obviously young are often surprisingly thick, suggesting a rapid rate of accretion until surfaces are smoothed, after which accumulation seems to proceed much more slowly (Oberlander, 1994). Finally, on many rock surfaces varnish accretion is periodically interrupted by surface scaling, aeolian abrasion, or corrosion by organic acids associated with fungi or lichens (Oberlander, 1994).

Attempts have been made to determine the absolute age of rock varnishes using U-series dating (300.000 years for varnish collected in Utah) (Knauss and Ku, 1980). However, Fleisher et al. (1999b) investigated rock varnish for its U and Th mass fractions and found that the two ele-

ments are not separated from each other. Thus, the authors could not use ^{230}Th dating to constrain the ages of layers within the varnish. The absence of a closed system and the large amount of detritus within varnish also indicate that this dating method is not suitable for rock varnish.

Potter (1979) determined that there is too little organic matter in rock varnish to date it by conventional radiocarbon analysis. He also tested palaeomagnetic dating, but found that the magnetic signal was too weak to be of use (Oberlander, 1994). Dorn and Oberlander (1981a) suggested that the relative ages of rock varnish films could be estimated semi-quantitatively by comparison of the proportions of relatively mobile and immobile elements incorporated in varnish films. This suggested the use of the ratio (Ca + K)/Ti as a leaching index, later termed the varnish cation ratio or VCR (Dorn, 1983). "The premise of cation-ratio dating is that with time the leachable cations in varnishes, such as Na, Mg, K, and Ca, are gradually replaced by and/or depleted relative to less mobile cations, such as Ti. The decreasing cation ratio of Na+Mg+K+Ca:Ti, or any component thereof (e.g., Ca:Ti) provides an indication of the length of time that the varnish has been exposed to cation leaching" (Dorn, 1983).

Age determinations by VCR, based on curves calibrated using the chemistry of varnishes found on dated volcanic rocks (the calibration varnishes included tephra layers with high Ti mass fractions), were routinely used by geomorphologists and archaeologists for several years. A tremendous number of papers was published using this method (e.g., Loendorf, 1991; Wells and McFadden, 1987; Whitney et al., 1988). In the course of VCR dating, to validate the results and to resolve problems of late Pleistocene and Holocene age determinations, Dorn et al. (1989) introduced accelerator mass spectrometry (AMS) to the varnish field, in order to obtain radiocarbon dates of organic matter embedded beneath or within basal varnish layers, thus constraining the ages of the rock substrates. The organic matter was supposed to consist of varnish organisms, pollen, and plant debris embedded in the accreting clays and oxides, composing varnish films. Dorn et al. (1989) achieved excellent agreement at a large number of test sites between rock varnish AMS ^{14}C dates and dates measured or inferred by other means. The varnish dates measured by ^{14}C dating were commonly about 10% younger than controls, which was interpreted as the consequence of the expected lag in colonization by varnish-generating organisms (Oberlander, 1994). The procedure has been extended to the dating of petroglyphs, artifacts, moraines, geoglyphs (e.g., the Nazca lines), landforms, alluvial fan segments, and lava flows. In all instances the published AMS ^{14}C dates corresponded strikingly with age estimates by other methods. This seems remarkable, considering the difficulty of stripping varnish from large surfaces (0.5 m²) removing material up to a specified depth (the upper 90% of the upper varnish material) first with a sharp-pointed hand-held tool (Oberlander, 1994).

After several years of research and application, it turned out that VCR dating is not a reliable dating tool. Basal rock varnish was no more leached than recently accreted varnish in many cases, calibration curves were not reproducible, chemical analyses contradicted the fundamental as-

sumptions of the method, results were disturbed by detritus, leaching did not always occur through the dense matrix, three times older varnish was found within petroglyphs compared to the age of the surrounding varnish, and many other disagreements were found (Bierman and Gillespie, 1994; Bierman et al., 1991; Dragovich, 1988b; Oberlander, 1994; Reneau and Raymond, 1991; Watchman, 1992; Watchman, 2000). A huge number of papers published about VCR dating of rock varnishes, from several continents, and reports about the interpretations based on these unreliable dates, remained published and were not re-evaluated. It complicates rock varnish research today, since each paper has to be read with care. "The emphasis for dating rock varnishes now shifted from using cations to carbon leaving a huge pile of literature and dates that must be re-evaluated. This daunting task leaves the researcher in a quandary: either to accept all the previous cation-ratio dating results and disregard the criticisms or to critically review the literature pertaining to their region realizing the likelihood and extent of the problems and uncertainties they face" (Watchman, 2000).

However, after only a few years of ^{14}C dating of varnish, questions concerning the age determinations of rock varnish by AMS were raised by Reneau et al. (1991). Authors questioned the sampling technique (Oberlander, 1994) and the unknown carbon sources (windblown diatoms, charcoal, lichen, fiber, graphite) (Watchman, 2000), while others presumed CO_2 contamination in a system open for cation leaching (Staley et al., 1992). Dragovich (2000) found ages which were younger at the rock/varnish interface than in the overlying varnish, which would be a reversal of expected stratigraphic relations. This observation was previously also made by Watchman (1993). As possible explanations for the inconsistent ages, the presence of organic material, such as bacteria, which could be introduced to lower layers via cracks could be named. Other possible explanations are the presence of deposited older recycled organic material, the dissolution of varnish by acids produced by organisms, the non-simultaneous growth of varnish on a single surface, host rock weathering and exfoliation, and the absence of a closed system (Dragovich, 2000). Based on this data, Dragovich (2000) suggested the potential absence of a link between an organic carbon age and the varnish deposition. Criticism of AMS ^{14}C dating became more frequent (Bednarik, 2002; Dragovich, 1988b; Oberlander, 1994; Watchman, 2000) and finally basis of a large dispute (Beck et al., 1998; Dalton, 1998; Malakoff, 1998; Malakoff, 1999; Whitley, 2009; Whitley, 2012; Whitley, 2013).

From then on almost no ^{14}C and VCR dating was conducted anymore, since the methods both proved to be unreliable. The dispute caused a tremendous decline of the number of papers published on the subject of rock varnish. As part of a settlement following the conflict about AMS dating, "...a disclosure agreement [was made] which has prevented all of the parties involved from discussing the controversy subsequently. One unfortunate outcome of the resulting legally imposed silence, however, is that none of the parties have been able to correct the published scientific record." (Whitley, 2013). For future dating attempts of rock varnish, Watchman (2000)

recommends cosmogenic isotope and luminescence methods as innovative directions. Other options are using the knowledge about the age of the underlying rock, such as the age of in-situ formed volcanic outcrops with original aa- or pahoehoe lava structures (Liu, 2004), archaeological artifacts (Goldsmith et al., 2012; Liu and Broecker, 2007; Zerboni, 2008), petroglyphs (Dietzel et al., 2008), well-dated outcrops (Liu and Broecker, 2008a; Liu and Broecker, 2013; Liu, 2004), or meteorite finds with known terrestrial ages (Lee and Bland, 2003). Since the onset of the varnish formation post-dates the age of the outcrop or rock, the maximum age of the rock varnish crust can be evaluated. Unfortunately, it is not known by how much time the rock varnish growth post-dates the rock age. Since weathering rinds on the host rock below varnish crusts are common, it is likely that rocks can be exposed for long time periods before becoming varnish-covered. An additional minimum age of the varnish can be quantified if carbonate deposits cover rock varnish crusts (Dragovich, 1988a), which is unfortunately very rare.

1.6 Potential Paleoclimate Proxy – A New Correlative Dating Approach

Mineral dust is a mixture of clay minerals and other mineral particles, usually with small grain sizes (nm to µm range) and low densities of the grains. Higher wind speed can mobilize larger sized particles, transport fine particles for longer ranges, and carry them to greater heights. Depending on the vegetation density and distribution of aridity, different dust components and sources can be mobilized, on diverse dust pathways, and with different compositions (e.g., desiccated shelf and lake sediments during cold periods, such as evaporites and calciferous particles).

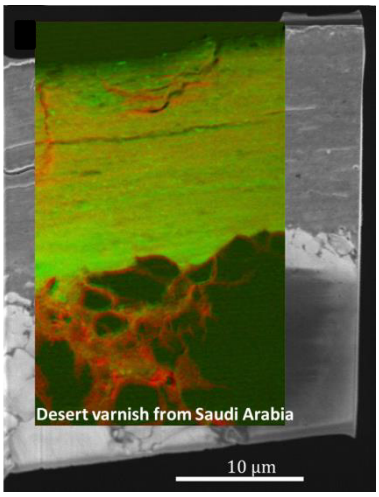

Figure 4: Element distribution map measured by STXM. Green colored areas are Fe-rich, red colored areas Mn-rich.

The dust load of the atmosphere depends on the amount of exposed terrestrial surface and the wind strengths, and thus on the climate. Cold climate exposes more terrestrial surfaces, especially former continental shelf regions, which are subsequently available for erosion by wind and weathering, since the sea level is lower and dense vegetation is rare. Dust has a great impact on the climate, and the climate regulates the dust flux and input. Mineral dust is the major component of varnish, and each layer of varnish is thought to represent dust of a certain time period and accordingly climate.

The growth of the rock varnish matrix seems to happen with time, from the underlying host rock upwards, like a sedimentary sequence. Similar to sedimentary sequences, some varnishes show alternating compositions, depending on the conditions during growth. This layered growth is the basis on which paleoclimate studies are conducted on the material.

Varnish microlamination (VML) dating, which is a correlative dating approach, is discussed and used by several authors (Baied and Somonte, 2013; Dorn, 1988; Liu and Dorn, 1996;

Zerboni, 2008). A full rock varnish master-chronology has been established by Liu and his coworkers for the western drylands of the USA, dating back 300000 years (Liu and Broecker, 2013). The idea that microlaminations, which are laminations of different color and chemical composition within varnish, might be paleoclimate indicators, was proposed by Dorn and Oberlander (1981a). Black, opaque Mn-rich layers, and orange to yellow Mn-poor layers sandwiched in between were described as early as 1978 (Perry and Adams, 1978) (layers are shown in Fig. 4). Dorn (1984) suggested to use Mn:Fe ratios to assign values to the layers. He proposed that Mn-rich layers represent wet climate periods, while Mn-poor layers represent dryer climate episodes. It is presumed, but has not yet been proven, that greater rainfall results in higher MnO_2 contents of varnish (Broecker and Liu, 2001), generating a chemical oscillation in varnish based on changes between arid and semi-arid (or subhumid) climates in Holocene and Pleistocene time (Oberlander, 1994). This change of composition can be due to varying Mn accumulation rates due to different moisture availabilities and/or leaching potentials at constant dust flux, it could be the result of the varying deposition of aeolian mineral dust at constant Mn accumulation rates, or a result of a falloff in Mn fixation by organisms. Thus, it was proposed that rock varnish micro-chemical laminations provide a terrestrial palaeoclimatic record analogous to the oceanic oxygen isotope record (Dorn, 1984; Oberlander, 1994).

Dorn's former PhD student, Tanzhuo Liu, worked on the subject of microlaminations and produced thousands of ultra-thin-sections (5-10 µm) of varnish to investigate them (Liu, 2003). He asserted that the best laminations can be found in microbasins, which are 1-3 mm wide and <1 mm deep, varnish-filled microdepressions on rock surfaces (Liu and Broecker, 2008a). Furthermore, he established the use of the BaO % content as absolute value for climate signals (Liu and Broecker, 2007; Liu and Broecker, 2008a; Liu and Broecker, 2008b; Liu and Broecker, 2013; Liu et al., 2013; Liu, 2003; Liu et al., 2000). Barium occurs in rock varnish together with Mn, but as the MnO_2 content rises, the ratio of BaO to MnO_2 rises simultaneously. As a consequence, the BaO concentration has a higher signal-to-noise ratio than the MnO_2 concentration (Broecker and Liu, 2001). Barium oxide has the advantage that common mineral dust contains only minor amounts of Ba-rich minerals (e.g., in barite, $BaSO_4$), while other elements, which are often correlated with Mn, such as Ca, are incorporated in numerous dust minerals (e.g., calcite, $CaCO_3$, or anorthite, $CaAl_2Si_2O_8$). These Mn:Fe and Ba:Fe ratio sequences from the drylands of western USA have been thoroughly matched to $\delta^{18}O$ (‰) sequences of ice core records (Liu and Broecker, 2008a) and climate records obtained from stable oxygen isotope analyses of marine foraminifera in North Atlantic deep sea sediments (Broecker and Denton, 1989; Liu and Broecker, 2007) to obtain a local paleoclimate proxy.

However, this relatively new correlative dating method has not remained safe from criticism, since growth can be interrupted by surface scaling, the layer sequence is different for almost every microbasin on a single rock, it is not known if varnish growth stops for a certain time and

starts again, having a hiatus which is not identifiable, and varnishes show indicators for continuing adjustment to changing environmental conditions (Dragovich, 1988b; Garvie et al., 2008; Goldsmith et al., 2012; Goldsmith et al., 2014; Reneau, 1993a; Reneau et al., 1992). Varnishes show postdepositional mineralogical, chemical, and structural changes activated by liquid water, and alteration by dissolution of Mn minerals occurs possibly through the reduction by organic matter (Garvie et al., 2008; Krinsley et al., 2013; Krinsley et al., 2012). Aeolian abrasion or corrosion by organic acids associated with fungi or lichens are factors which could additionally remove varnish layers (Oberlander, 1994), as well as deep burial under reducing conditions (Dragovich, 1988a). Many problems which hamper VCR and ^{14}C dating of varnish (chapter 1.5) are also applicable to VML dating. Furthermore, this correlative dating is based on the knowledge of the onset of the varnish growth, and presumes continuous growth from then on. The host rock age is taken, and 60-200 years are subtracted for the delayed start of the varnish accumulation, although the initiation period may vary between environments and rock types (Dorn et al., 1988). The difference is used as the maximum age of the varnish sequence. However, even though one knows the age of the underlying rock, one does not necessarily know the beginning of the varnish formation, since it is not unusual that the varnish crusts grow on deeply weathered rock crusts, which most certainly predate the onset of the varnish growth. Reneau (1993b) stated that on different rocks with known similar Holocene ages, the varnish development on the surfaces can show significant variability over distances as small as 1 km. He explains this with local variations in aeolian sediment flux. He furthermore concludes from his data that varnish loss has occurred in his study site, since Holocene outcrops show thicker and Mn-richer varnish than Pleistocene outcrops (Reneau, 1993a).

The uppermost Mn-poor layer observed in rock varnishes from today's arid deserts is interpreted as proof for the applicability of VML dating for paleoclimate research. However, the Mn-poor uppermost layer was present in all samples collected along a rainfall transect during a study by Goldsmith et al. (2012). No correlation was observed between a GIS rainfall model and the average Mn content in the uppermost layer. The youngest Mn-poor sheet is rather interpreted as leaching horizon, whereas at a depth of 5-10 µm the "active layer" is present in which the varnish formation takes place by pH and E_h shifts (Goldsmith et al., 2014). Goldsmith et al. (2014) propose that surface wetting leads to Mn mobilization, downward leaching, and deposition as insoluble Mn oxyhydroxide at a depth of 5–10 µm. Concluding with a quote from Oberlander (1994): "The basic premises underlying the use of rock varnish for both age determination and palaeoenvironmental research have come into question and will remain in doubt pending future substantive findings concerning varnish-forming processes."

1.7 Measurement Techniques Used

The two methods which proved to provide the most extensive and revealing results during this thesis were femtosecond laser ablation-inductively coupled plasma-mass spectrometry (LA-ICP-MS) and STXM-NEXAFS. Both methods have the advantages of high spatial resolution. While laser ablation ICP-MS is a well-established method in geosciences, STXM-NEXAFS was more recently utilized to gain new knowledge from geological samples. In the following, only these two techniques will be explained in detail, even though several different instrumental (ns LA-ICP-MS, fs LA-multicollector-ICP-MS (fs LA-MC-ICP-MS), solution ICP-MS, portable XRF, stationary XRF, GFS, PCR, NanoSIMS, SEM, Raman spectroscopy, EPR, TEM, EDX, and EPMA), microscopical (polarization microscopy, light microscopy, and fluorescence microscopy), and preparation techniques (thin section preparation, thick section preparation, FIB-slicing, microtome slicing, and abrasion using an electric combination tool) were applied during this thesis, some of which provided valuable additional results.

1.7.1 Femtosecond Laser Ablation-Inductively Coupled Plasma-Mass Spectrometry

Laser ablation ICP-MS is a highly sensitive analytical technique, which is well-established in geosciences, especially for high-resolution in-situ measurements of trace elements. It handles small sample quantities of material and requires no chemical treatment in advance, which reduces the possibilities for contamination and sample loss (Fernández et al., 2007; Hergenröder et al., 2006). While nanosecond laser ablation has been applied for rock varnish investigations before (Nowinski et al., 2010; Wayne et al., 2006; Wayne et al., 2004), 200 nm femtosecond laser ablation is a new technique, which has not yet been applied to varnish research. This method was used in this thesis, since it fulfills the requirements needed for high resolution measurements on thick-sections, such as almost matrix independent measurements. This is important for materials such as rock varnish, which, until recently, lacked a matrix-matched reference material (appendix B.3).

The unknown thicknesses of the varnish crusts produce uncertainties for the interpretation of depth profiles which cannot be retraced. To avoid this problem, measurements were conducted on cross sections prepared as thick sections (70 µm). Using these, it was possible to examine the samples for their crust thickness and ablation trajectory, prior, during, and subsequent to each measurement, by light microscopy.

During laser ablation, material gets ablated by a laser system from a solid material. In this thesis a laser with pulses in the femtosecond range and with a wavelength of 200 nm was used for most measurements. The femtosecond laser is of specific interest, since this device allows an almost matrix independent calibration, and elemental and isotopic fractionation effects are significantly reduced (Jochum et al., 2014; Poitrasson et al., 2003). This is especially important for

materials with unknown matrices and changing compositions, such as rock varnish. The femtosecond laser has the advantages of producing a very hot electron gas, which does not disturb the adjacent lattice in the structures of the samples at the end of the pulse, and the heat-affected zone shrinks significantly (Margetic et al., 2000). Thus, it has a higher spatial resolution and sensitivity, as well as a higher efficiency than the commonly used nanosecond laser (Fernández et al., 2007; Zeng et al., 2005). Furthermore, this resolution, together with a smaller particle-size distribution, provides a better precision and accuracy of fs LA-ICP-MS results compared to ns LA-ICP-MS results (Fernández et al., 2007). During the measurements the liquid state is skipped, turning the sample directly from solid state into plasma, enhancing the measurement potential of volatile elements, such as Zn and Pb (Jochum et al., 2014). The in-situ measurements save time, minimize the sample material needed for one analysis, compared to solution ICP-MS, and allow a match between structures and element distributions, which is especially important for microscale structures, such as those found within rock varnish. Currently, there is a variety of fs lasers with different wavelengths available, coupled to ICP-MS instruments. The advantage of using a wavelength of 200 nm is the production of smaller particle sizes and hence a higher ionization potential (Guillong and Günther, 2002; Günther et al., 1997), a higher absorption potential by minerals in general, and especially an improvement of absorption by transparent minerals (Jeffries et al., 1998). However, UV laser light is a challenge to the design of optical systems, especially when it is combined with high quality visual observation, as it is necessary for LA-ICP-MS measurements (Günther et al., 1997).

The particles ablated in a cell filled with a He atmosphere are discharged from the sample cell by an additional He gas flow. The aerosol, mixed with Ar gas to trigger the plasma torch, is introduced into the inductively coupled plasma for the ionization process (6000-7000 K). A high-voltage spark is applied to the mixed gas flow by an intense electromagnetic field produced by radio frequency (RF) oscillation (power 750-1500 W, frequency 24-40 MHz). Electrons are stripped from Ar atoms, starting a chain-reaction of collision-induced ionization, powered by free electrons accelerated in the magnetic field. Particles ablated from the sample change from solid state to an excited gaseous form, and de-excite into a ground state atom. By collision with electrons set free from Ar atoms, which were multiplied by the chain reaction, the ground state atoms are ionized.

These ions are introduced through (usually Ni) cones into the interface. They pass through a first cone (sampler cone) with an orifice of 0.8-1.2 mm and a second cone (skinner cone) with an opening of only 0.4-0.8 mm. The main challenge is to lead the ions from atmospheric pressure (760 Torr) into the MS analyzer region (10^{-6} Torr). Only about one out of a million ions produced in the plasma reaches the detector, due to the bottleneck of the cones and the following ion optics. Fractionation can occur here or during laser ablation.

The ion optics, a system of electromagnetic lenses, convey a maximum number of positively charged ions from the plasma into the following mass separation devices. It separates the neutral and negatively charged ions from the positive ones, focuses the ion beam, and pulls the ions from the interface. In the double-focusing sector-field ICP-MS, a magnetic field, followed by an electrostatic analyzer (ESA), is positioned behind the ion optics (reverse Nier-Johnson geometry). This geometry allows the decoupling of the electric field of the ESA from any electric field of the RF generator, as well as an increase of abundance sensitivity.

The kinetic energy spread is only a few eV when the ion beam exits the interface and enters the mass analyzer system:

$$E_{kin} = \frac{1}{2}mv^2 = zU$$

where m is the mass, v the velocity, z the particles charge, and U the voltage. The ions are subsequently, in the double-focusing sector field, separated by their mass-to-charge ratios on basis of the Lorentz force law:

$$\vec{F} = z(\vec{E} + \vec{v} \times \vec{B})$$

where E is the electric field strength and B the magnetic field. The magnetic field focuses the ions with diverging angles of motion from the entrance slit and passes them to the ESA, which focuses them onto the exit slit behind which the detector is positioned. In the magnetic sector field, the Lorentz force for a magnetic field equals the centrifugal force in an orbit:

$$F = zv \times B = \frac{mv^2}{r}$$

where r is the radius. Combining this process with an electric field following the magnetic field, a specific ratio can be calculated, and different mass-to-charge ratios can be scanned through by choosing U and B in the electric and magnetic field sectors:

$$r = \frac{1}{B}\sqrt{\frac{2Um}{z}}$$

The cascading multiplier detector creates an electric signal from each arriving ion. The positively charged ions hit the copper-beryllium detector material, which is negatively charged. This material releases electrons, which hit the detector surface again, and the cascade effect is repeated several times. The electrons released by the ion impact are converted into electric pulses. The signal can either be measured in the counting or in the analog mode, depending on the amount of ions detected. While digital counting of the ions provides a higher sensitivity, the analog mode, which measures the voltage produced, reduces the sensitivity but extends the concentration range for which ion signals can be measured.

To obtain quantitative data, reference materials are measured in addition to the unknown samples. “A reference material is a material, sufficiently homogeneous and stable with reference

to specified properties, which has been established to be fit for its intended use in measurement or in examination of nominal properties" (VIM, 2004). Since no suitable homogeneous reference material (RM) for the microanalysis of Mn-rich materials existed up to now, a new RM was developed for rock varnish during this thesis. The extensive description can be found in B.3 in the appendix and in Jochum et al. (2016). The new reference material was investigated in detail for its homogeneity and was thoroughly compared to available Mn-rich RMs and homogeneous glass RMs during this thesis (appendix B.3).

1.7.2 Scanning Transmission X-Ray Microscopy–Near Edge Absorption Fine Structure Spectroscopy

This technique has only recently started to be used in geoscience. It is known to extract new knowledge from geochemical samples with high spatial and temporal resolutions. As requirement to apply STXM-NEXAFS, the samples need to be transparent for light in the energy range of interest, since this method measures transmitted light. To prepare varnish samples thin enough, without the destruction of structures or a contamination by processing, FIB slices were prepared, cutting a piece of rock out of the sample by removing atom by atom from the surface with a Ga^+ ion beam. Subsequent to a first thinning of the samples (30 x 50 µm), they are fixed on a TEM grid by a Pt droplet, and final thinning is conducted to create thicknesses of about 100-200 nm. The TEM grid is mounted on a sample holder, which gets introduced into the STXM instrument. To receive a high resolution (down to about 30 nm) during STXM measurements, a light beam is focused on the surface of the transparent sample and the focused beam is scanned over a certain area of interest. The area and the resolution can be chosen on basis of the question.

Since the measurements are based on X-ray absorption, a tunable X-ray source is necessary. To receive a high energy and high spatial resolution for a wide range of energies, a synchrotron source is used. Soft X-rays are preferred, which results in low radiation damage by light with a high penetration depth. Soft X-rays have a photon energy of about 100-2000 eV, or a wavelength of 0.6-10 nm (Solomon et al., 2012). This is in the range of inner-shell electron binding energies of low-Z elements. The technique is thus especially useful to investigate organic materials, but also L-shell absorption of high-Z elements. Two synchrotron facilities and their microscopes were used for the STXM-NEXAFS

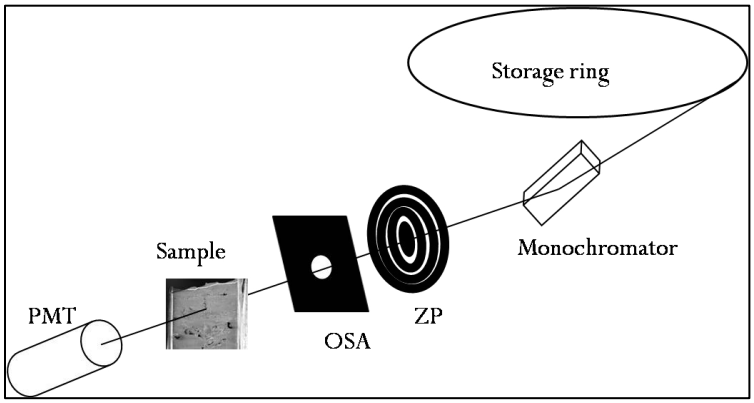

Figure 5: Sketch of a STXM microscope. OSA: order sorting aperture, which filters the positive first diffraction order. ZP: zone plate, which focuses the beam. PMT: high performance photomultiplier, which operates as detector.

measurements in this thesis. One is the X-ray microscope at beamline 5.3.2.2 at the Advanced Light Source, Berkeley, CA, USA, with a bending magnet source. The other instrument is the MAXYMUS microscope at beamline UE46-PGM-2 at the synchrotron BESSY II, Helmholtz-Zentrum Berlin, Germany, which utilizes an undulator. Using a bending magnet, the brightness of the light is about four orders of magnitude lower than using an undulator. Lower brightness results in lower count rates.

To acquire useful information in a reasonable time span, a high photon flux on a small spot is required. Small spots are produced by a zone plate lens, which is introduced into the optical path between the monochromator and the sample. The zone plate is an achromatic lens with a focal length proportional to the photon energy. An additional device is installed between the zone plate and the sample, the order sorting aperture (OSA). It filters the light in order to transmit only the positive first diffraction order (Fig. 5).

The measurement chamber at the ALS is filled with a He atmosphere previous to measuring, while at BESSY II measurements are conducted in vacuum. Comparing He or vacuum to an air atmosphere, one receives a higher amount of photons at the sample surface due to the lower absorption, and smaller interferometer drifts because of the lower index of refraction for the former. The advantage of He over vacuum is the permanent cooling of the motors and other electronics in the measurement chamber (Kilcoyne et al., 2003).

The resulting images are energy-specific. Possible energies at which measurements can be conducted are 250 – 800 eV at the ALS and 120 – 1900 eV at BESSY II. To obtain an element distribution map for a certain element, a scan at a lower or significantly higher energy than the adsorption edge energy must be conducted, which is not influenced by absorption by another element. This energy represents the underground or blank. An additional scan at the energy of greatest adsorption by electrons of the atom of interest in the K, L, or M shell is necessary. These images, subtracted from each other, provide an element map for a certain element. The resulting maps are usually expressed by their optical density (OD) or extinction, given by the Lambert-Beer law:

$$OD = \lg\left(\frac{I_0}{I_t}\right) = \mu(E)\rho d$$

where I_0 is the intensity of the incident light, I_t is the intensity of the transmitted light, μ is the absorption coefficient of the material as function of the energy (E), ρ is the density, and d the sample thickness.

Image sequences at many energy values (so-called stacks) produce 3D matrices where each pixel contains information about the adsorption of all energies measured at this point. The adsorption spectra can be extracted from any pixel or group of pixels of a stack, subsequent to subtracting the background signal, or signal of the incident light, for each energy setting which was measured simultaneously. In addition to element occurrences and distributions, the adsorption

also contains information about binding situations and oxidation states, expressed as the exact energies of the absorption edges.

The detector converts incoming X-rays to visible light via a phosphorus screen. The generated visible photons are counted by a high performance photomultiplier (PMT) with count capabilities in the tens of MHz. For calibration, the characteristic pi resonance peak at 285.2 eV was measured on polystyrene latex spheres (PSLs) prior to each measurement session. The data were evaluated with the Interactive Data Language (IDL) widget "Analysis of X-ray microscopy Images and Spectra" (aXis2000) and IGOR Pro. Subsequently, cluster analyses were conducted utilizing the software Mantis-2.1.01.

Radiation induced damage has to be taken into consideration. Transformation of Mn oxidation states is not unlikely, utilizing a focused soft X-ray beam for STXM measurements, since a very small sample area is subject to a large photon flux (Beetz and Jacobsen, 2003). The radiation damage is interpreted for instance as X-ray induced photoreduction, where the organic carbon present in the sample provides the electrons (Ross et al., 2001). This might explain the observed decrease of the $COOH^-$ resonance peak at 288.5 eV, to form RCO_3, absorbing at 290.2 eV. This suggests the breaking of carboxyl groups and the resulting formation of carbonate within the sample. Braun et al. (2009) proposed a scenario where the $COOH^-$ groups react with oxygen radicals to form an organo-carbonate and water ($2COOH^- + (3O)^{2-} \rightarrow 2CO_3^{2-} + H_2O$). These two reactions might not only be accountable for the presence of CO_3^{2-}, but also for the lack of functional groups, other than carboxylic groups and aromatic π-bonding, found within the varnish samples investigated during this thesis.

2 Results and Discussion

2.1 Sampling Sites Investigated

Varnishes from different regions all over the world and different environments were collected and studied (Fig. 6):

Arid desert regions
- Anza-Borrego Desert, CA, USA*
- Mojave Desert, CA, USA*
- Jubbah, An Nafud, Saudi Arabia*
- Yatib, An Nafud, Saudi Arabia*
- Sde Boker, Negev, Israel*
- Azougui, Sahara, Mauritania

Semi-arid desert regions
- Knersvlakte, South Africa*
- Chihuahuan Desert, TX, USA
- Sonoran Desert, AZ, USA

Urban sandstone buildings
- Smithsonian Institute, Washington D.C., USA
- Freiburger Münster, Freiburg, Germany

River splash zones
- Adirondack Raquette River, NY, USA
- Erie Barge Canal, NY, USA

Fissure precipitate
- Baja California, Puerto Escondido, Mexico**

Cave varnish
- Herbstlabyrinth, Breitscheid, Germany**

In addition, dust samples were collected near varnish samples from the regions asterisked above (*), which were additionally investigated as potential sources of the varnish element enrichments and also as varnish major components.

Some samples, marked above with two asterisks (**), were investigated with several techniques, but are not described in the following results, since they do not fit into the context of subaerial rock varnish.

Rock varnish can be categorized into five types:

Type I): Arid desert varnish

Type II): Semi-arid desert varnish

Type III): Semi-arid desert varnish with special growth forms

Type IV): Urban varnish

Type V): River splash zone varnish

Further descriptions of sampling locations and varnish types can be found in the appendix (B.2 and B.4).

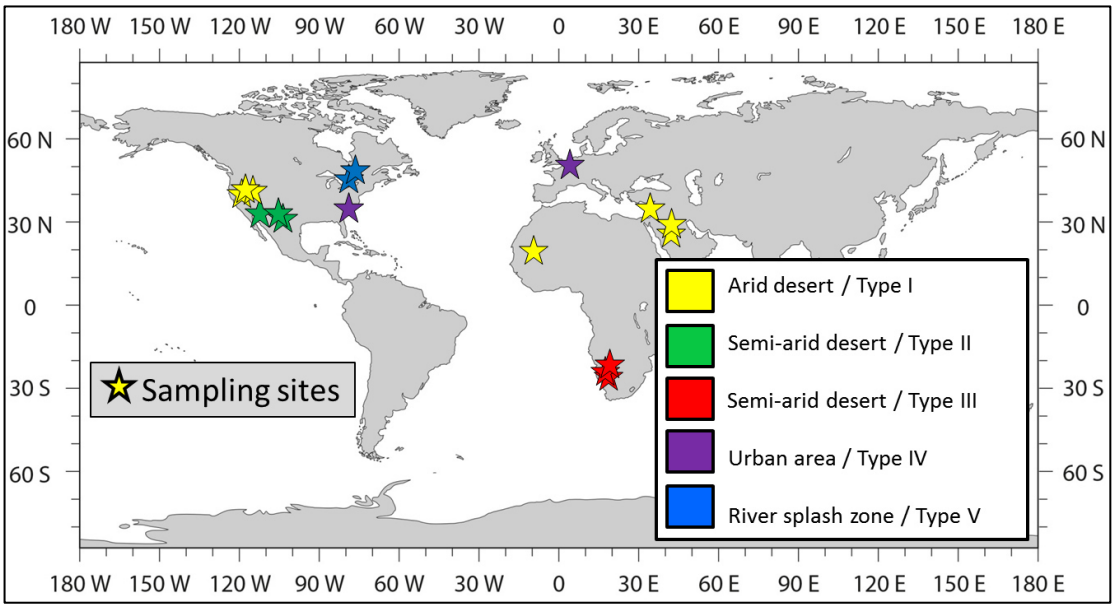

Figure 6: Sampling locations of varnishes used for the categorization of rock varnish types.

2.2 Results of the Rock Varnish Investigations

Each component of varnish was investigated throughout this thesis to obtain an understanding of this complex material. It is important to confirm or disprove the assumption that all varnishes are similar and can be interchangeably used for comparison. Missing data from one kind of rock varnish is often completed with the dataset from another kind of rock varnish. A typical example is that as evidence for life in typical desert varnish, authors publish the finding of cells in (Mn-rich) crusts from non-arid environments, such as from river splash zones (Krinsley et al., 2009; Krinsley et al., 2012). To prevent future misunderstandings, a classification by geochemical and structural features into different varnish types was proposed (appendix, B.4). To this end, the dust component, the Mn-rich matrix, structures and element distributions, as well as biogenic components were investigated throughout this thesis. The following chapters (2.2.1-2.2.4) will be kept rather short, since detailed information is provided in the manuscripts in the appendix. The last chapter about the search for organisms will be more detailed, since this dataset has not been published yet.

2.2.1 Structure Investigations by Imaging

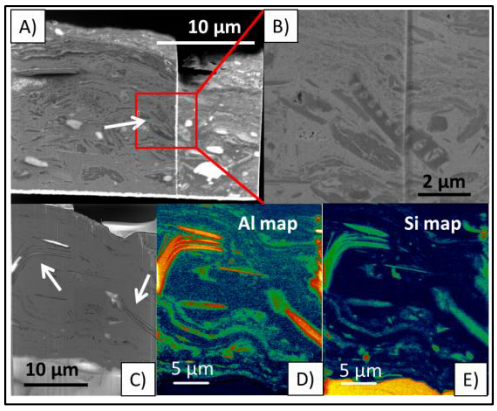

Figure 7: Dust fraction within rock varnish crusts. A and B show a diatom fragment which was integrated into the rock varnish matrix, while C, D, and E show nicely stacked clay minerals. Images A, B, and C were obtained by SEM, while images D and E are STXM element distribution maps of the elements Al and Si, which were measured at the BESSY II. All images were obtained from South African rock varnish samples.

"The cross-sectional texture of rock varnish varies considerably with the scale of analysis and technique used to image a sample. Each jump in resolution results in new insight, with the current state-of-the-art resting at the nanoscale" (Krinsley et al., 2013). The examination of internal structures of rock varnish is of specific interest to advance the understanding of micrometer and nanometer sized features and, by this, the accumulation processes. While macroscopic observations were reported starting about 200 years ago (Von Humboldt and Bonpland, 1819), microscopic features, such as layers, density differences, cauliflower-like growth structures, stromatolitic features, case hardening, particles torn off the underlying rock, cracks, cavities, dust particle sizes and shapes, and dust particle "nests", can only be visualized by modern and state-of-the-art techniques. Furthermore, one can discriminate between microfossils, such as diatoms, which were introduced with the dust fraction (Fig. 7 A and B), and mineral dust such as clay minerals (Fig. 7 C, D, and E).

In this thesis, instruments and techniques, such as polarization microscopy, light microscopy, STXM-NEXAFS, backscattered electron (BSE) microscopy, and SEM imaging, were used to visualize these nano- and microfeatures (appendix, B.2 and B.4).

Rock varnish structures can be grouped into four categories:

- Structures with sedimentary layering, which occur mainly in local microbasins or depressions within the rock surface (Fig. 8 b)
- Stromatolitic structured varnish with upwards growing and outwards branching channels (Raymond et al., 1993)
- Dense varnish showing almost no structure variations such as layers or cavities (Fig. 7 C)
- Cavity-rich varnish showing a porous matrix and large amounts of angular mineral particles. Individual cavities can be found either seemingly randomly distributed within the matrix, or preferentially associated with dust mineral grains, or nests of angular dust minerals (Fig. 11 A)

Varnishes showing these strongly diverging features have been used interchangeably for the description of rock varnish, and thus discussions and arguments about the validity of the different descriptions have been going on for decades. Hence, it is necessary to describe the nano- and micrometer structures of the samples, as well as to study the chemical composition, to allow comparison to equivalent materials. We proposed a categorization of rock varnish into five different types, based on structures, element distributions, and element compositions. The definition of each type is available in the appendix (B.4).

2.2.2 Investigations of the Manganese-Rich Matrix

The matrix, generally in combination with the incorporated dust grains, was investigated in detail. Several measurement techniques were required to cover different scales and demands. While a portable XRF was mainly used to conduct in-situ research on facades (appendix B.5) and outcrops, as well as for a first overview over the manganese presence, an EPMA and a LA-ICP-MS were used for high resolution (2 µm vs. 10-40 µm) measurements of different elements (major elements vs. trace elements).

2.2.2.1 Portable X-Ray Fluorescence

To investigate the chemical composition of the sampled varnishes, MnO mass fractions, or Mn K-α counts per second, were obtained by a portable XRF, to receive rough approximates of the Mn abundance as first indicator whether the crust was varnish or not, and furthermore to evaluate how thick the crust might approximately be. It was used as an in-situ method to determine if black crusts observed on the facade of the Freiburger Münster contain Mn (appendix B.5), and to evaluate the amounts, or surface densities, of the Mn found. Crusts which turned out

to be sufficiently Mn-rich were subsequently investigated by additional high-resolution measurements.

2.2.2.2 Electron Probe Microanalysis

Electron probe microanalyzer investigations were conducted to obtain the major element composition and the composition of the pure Mn-rich matrix between larger dust minerals (spatial resolution 2 µm). The major element abundances determined by EPMA were further used to identify a potential internal standard element for LA-ICP-MS analyses, and to obtain the exact mass fractions of this internal standard element. Moreover, simultaneous to element composition determinations, backscattered electron (BSE) images were produced of the samples (appendix B.2). As first evidence that mineral dust is a major contributor to varnish, fs LA-ICP-MS measurement results were combined with EPMA data. A MnO_2 vs. SiO_2 plot displays clearly, that the Mn-free endmembers of rock varnish fall into the range of average dust compositions (appendix, B.2).

2.2.2.3 Femtosecond Laser Ablation-Inductively Coupled Plasma-Mass Spectrometry

A femtosecond LA-ICP-MS was used to obtain accurate and precise data of trace element contents, with a spatial resolution of 10-40 µm. Measurements were conducted as line scans on thick-section cross-sections through the rock varnish sequence. This allows the examination of the ablated lines before, during, and subsequent to the measurements. It limits the risk of simultaneous ablation of rock varnish and substrate, which was problematic in previous LA-ICP-MS studies of rock varnish (Wayne et al., 2006; Wayne et al., 2004). The enrichment of several elements was observed. Most prominent are high Mn, Ba, Zn, Pb, Co, Cu, Ni, Y, U, and REE mass fractions in most varnishes (appendix, B.2 and B.4). The enrichment differs between different varnish types, even though one type might represent samples from several different continents, and different types might be collected within one country. This indicates that not only the dust source composition differs, but either the integration mechanisms, the leaching mechanisms of dust, ligand presences, the source type (such as mineral dust for Type I varnish, anthropogenic particulate matter (PM) for Type IV varnish, or river water for Type V varnish), the mineralogy of the Mn-rich matrix, or a combination of them. Many other factors are of importance concerning the sorption of trace elements, such as the ionic strength, pH and E_h conditions of the solution, as well as the radii, oxidation states, and coordination forms of the elements available. Moreover, clay minerals incorporated in rock varnish, representing a large fraction of the material, also contribute to the ad- and absorbing processes, due to their high sorption potential. However, this contribution is considerably lower than that of Mn oxyhydroxides. Thus, it is challenging to distinguish which factor contributes to what extent.

2.2.2.4 Scanning Transmission X-Ray Microscopy – Near Edge X-Ray Absorption Fine Structure Spectroscopy

Scanning transmission X-ray microscopy-NEXAFS was used to obtain element distribution maps (appendix B.2 and B.4), especially of low-Z elements, such as carbon, oxygen, and nitrogen, to search for functional groups, and to identify the oxidation states of Mn in-situ. Interestingly, cluster analyses (conducted by the program Mantis) identified areas of different Mn oxidation states within single varnish samples (Fig. 10). This might be an indicator for an initial patchwork made of different Mn oxyhydroxide phases, but it is more likely an indicator for recrystallization, redox reactions, or ionic substitution subsequent to a first crystallization process forming the matrix. Oxidation states found in the rims of cavities were lower than in the matrix distant from cavities. This could indicate that the Mn oxyhydroxides have oxidized material, such as organic matter, via redox reactions. The organic matter could have been previously deposited together with the mineral dust fraction; or it could represent remains of organisms involved in the varnish formation. Manganese oxidation states and functional groups will be discussed in detail in chapter 2.2.5.2.

2.2.3 Sources of Rock Varnish

The major source of rock (or desert) varnish is known to be mineral dust (Otter et al., in preparation). However, detailed studies on the Freiburger Münster (appendix B.5) showed that this is not valid for all rock varnish types. The source for the elements observed within the crusts at the Münster (Type IV varnish) turned out to be most likely anthropogenic released PM or, more specific, emissions from vehicles (appendix B.5). A further type of varnish (Type V) seems to obtain its elements from river water (appendix B.4). Only mineral dust will be discussed in the following, since it satisfies the definition of rock varnish.

2.2.3.1 Mineral Dust

To allow a comparison of the chemical composition of varnish to the dust fraction, which is thought to be a main contributor to the varnish formation, dust, or soil, collected adjacent to several varnishes was investigated. These investigations were made to identify the process behind the leaching-and-precipitation mechanism, and to determine if the process is identical for all rock varnishes. Loose mineral dust grains were analyzed as fine (<50 µm) and coarse (≥50 µm) fraction. The comparison of varnish and dust measurements revealed a correlation between the chemical composition of varnish and the dust, as shown in Otter et al. (in preparation). The correlation is highest for fine grained dust (<50 µm) (Otter et al., in preparation), which is reasonable, since this fraction is easily incorporated due to greater adhesion. It has a higher relative surface area available for leaching processes, and the clay mineral fraction is usually significantly higher in the fine fraction of mineral dust. It was also observed that the enrichment of REEs in varnish, compared to corresponding dust, is high for Type I varnish and low for the Type III varnishes

investigated. The degree of the dust contribution to the varnish genesis seems to depend on the type of varnish, and thus on the formation processes, which we propose differ for the diverse varnish types. The exact mineral composition of the fine fraction of several mineral dust samples was investigated by X-ray diffraction (XRD) (Otter et al., in preparation).

The dust provenance contributing to the varnish formation can change over the centuries or millenia, the time span needed for the varnish accumulation. A changing provenance often coincides with changing Pb isotope signatures. High resolution in-situ Pb isotope measurements by fs LA-MC-ICP-MS were conducted in the search for indicators for provenance changes. Small changes of Pb ratios over the profiles were observed, but they were all in the range of the relatively large measurement errors. Unfortunately, as it turned out later, no layered varnishes were investigated, since the one Type I varnish sample was chosen for the final measurements, which does not reveal these structures (appendix B.4).

2.2.4 Technical Developments

Rock varnish is a material that has been investigated for an exceptionally long time, but the instrumentations available for the investigations have changed. Current-day techniques provide the opportunity to go down to the nanoscale and to study minimal amounts, which was unthinkable 200 years ago when von Humboldt studied rock varnish. However, changing instruments require different measurement techniques and calibration standards. These are available for routine investigations, but usually do not fit the needs for rock varnish research. Due to this lack, new developments were made in order to bridge these gaps.

2.2.4.1 FeMnOx-1 – A New Microanalytical Reference Material for the Analysis of Rock Varnish

Comparative measurement techniques, such as for instance LA-ICP-MS, require reference materials (RMs) to obtain quantitative data. Since major and trace element mass fractions of the rock varnishes investigated during this thesis were determined by LA-ICP-MS, one has to take into account that a suitable microanalytical RM (MRM) is required. Several RMs are available for microanalyses, but all have low Fe and/or Mn mass fractions (e.g., NIST 610 and GSE-1G), while rock RMs with high Mn and Fe mass fractions are, in contrast, not suitable for microanalyses because of sample heterogeneities (e.g., JMn-1, FeMn-1, NOD-P-1, and NOD-A-1). This was investigated in detail during this thesis (appendix, B.3). On behalf of the results, a new MRM, FeMnOx-1, was produced in collaboration with USGS. It was closely studied and compared to already available materials (appendix, B.3). In this thesis, the new material FeMnOx-1 was thoroughly tested for its homogeneity by fs and ns LA-ICP-MS, and the element composition was determined by stationary XRF, solution ICP-MS, and ICP-AES. The investigations of the exact element mass fractions, determined by several methods and at different institutions, are given in Jochum et al. (2016). This allows future researchers to use this MRM as a homogeneous,

well-examined RM to conduct high-resolution microanalytical measurements. Using this new reference material for LA-ICP-MS measurements of rock varnish, smaller spot sizes and shallower ablation depths can be chosen, increasing the resolution for future applications, and matrix-matched analyses can be conducted.

2.2.4.2 Portable X-Ray Fluorescence – In-situ Analyses of the Surface Density of Manganese

As a further project, a calibration was developed to allow the quantification of MnO mass fraction results, or Mn K-α counts per second, of rock varnish crust measurements obtained by a portable XRF. Rock varnish samples were cut into squares and the varnished surface was determined using the software ImageJ. The varnished surface was dissolved by 0.02 M hydroxylamine hydrochloride, and the exact amount of Mn removed from the specific surface was determined by solution ICP-MS. These values, combined with results obtained from a Mn standard from Micromatter^{TM}, were fitted to obtain a calibration curve, which allows the conversion from mass fractions, or counts, to Mn surface densities (µg cm^{-2}). This permits a semi-quantitative evaluation of the results obtained by in-situ portable XRF measurements of thin layers of varnish. The procedure was developed and applied to measurements at the Freiburger Münster, where urban varnish was investigated in cooperation with the Münsterbauverein Freiburg (appendix B.5).

2.2.4.3 Mineral Dust – Requiring only Femtogram Amounts of Material

All mineral dust measurements conducted during this thesis (appendix B.2 and B.4, Otter et al., in preparation, and Long-Yan et al., in preparation) are based on a protocol developed for this purpose during this thesis (appendix, B.1). This method allows to measure small dust amounts, down to femtograms, by fs LA-ICP-MS, obtaining sufficiently accurate and precise data. Dust collected on varnished surfaces can be investigated in-situ, without possible contamination by processing. Rare and chemically distinct minerals, such as zircons ($Zr(SiO_4)$), can be localized by this protocol, and the amount of individual grains can be counted and located for further studies if required (appendix, B.1).

2.2.5 The Search for Life in Rock Varnish

The biogenic formation of rock varnish is highly controversial in the literature. For this reason, we tried to find evidence for a biogenic formation in our rock varnish samples, which represent a large collection from several environments and continents, and of various ages. Different varnish types were investigated with several methods, in search for a potential biogenic formation. Methods such as for instance imaging by BSE, SEM, or light microscopy, fixation and staining, STXM-NEXAFS, EPR spectroscopy, as well as PCR and qPCR were used to fulfill this task.

2.2.5.1 Imaging Micro- and Nanostructures - Scanning Electron Microscopy, Backscattered Electron Imaging, Scanning Transmission X-Ray Microscopy, and Light Microscopy

Investigating varnish samples by SEM, nodules, which are possibly accumulates of nanocrystalline mineral particles, were found on several varnish surfaces (Fig. 8 h, i). Nanocrystalline Mn oxyhydroxides might be indicators for a biogenic origin, but they might also have formed by precipitation of colloids from a supersaturated gel. A stromatolitic inner microstructure can be observed in both, varnishes and colloidal precipitated gels (McLoughlin et al., 2008).

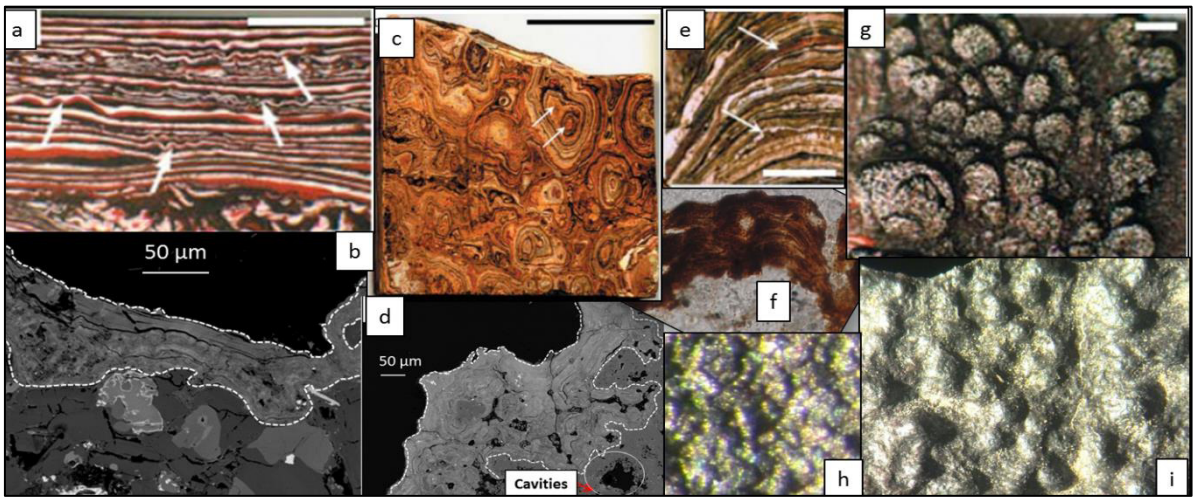

Figure 8: Images a, c, e, and g are taken from McLoughlin et al. (2008) and show Taylor stromatolites, while b, d, f, h, and i are rock varnish images. Figures a and b show laminated structures with wavy layers in between (b is an EPMA backscattered electron image of sample CA13 DV1, the dashed lines mark the varnish boundaries). Figures c and d show cuts at an angle through the upwards and outwards branching nodules (d is an EPMA backscattered electron image of sample IS13 V3, the dashed lines mark the varnish boundaries). Figures e and f show discontinuous laminated structures suddenly disappearing (f is a microscopy image of sample IS13 V3, 100 times enlarged). Figures g, h, and i are nodules on the surface of a varnish (h and i are light microscopy images; i is an image of sample TX FD4, 50 times enlarged, i is an image of sample AR14 2a, 50 times enlarged).

The stromatolitic microstructures found within varnish, and the nodules on the surface of varnish, are very similar to structures observed in synthetic stromatolites, so-called Taylor stromatolites, which formed by the accretion of colloids in a turbulent air flow (McLoughlin et al., 2008).

Figure 8 shows Taylor stromatolites and rock varnish for microstructure comparison. The South African semi-arid desert varnish (Type III) shows additional microcolonial fungi (MCFs) growing on the varnish surface (Fig. 9 A, B). Similar MCFs were observed on varnish coatings before (Dragovich, 1993; Perry and Sephton, 2008; Staley et al., 1982; Stewart-Perry, 1979). However, it is unclear if these fungi are directly involved in the varnish formation (Parchert et al., 2012; Perry and Kolb, 2004a; Taylor-George et al., 1983), or if they rather cause the dissolution of varnish due to their production of organic acids. The dissolution theory is supported by the fact that MCFs are usually found within pits in varnish surfaces (Dorn, 1986; Staley et al., 1982; Taylor-George et al., 1983). From our data, we can only conclude that some biological activity postdates the Mn-deposition. We did not find any evidence for MCFs entombed within the varnish structure, neither by imaging, nor by $\delta^{13}C$ measurements (see chapter 2.2.5.6). One rock varnish sample showed hyphae on the varnished surface (Fig. 9 C), a finding also reported before for

desert varnish (Staley et al., 1982; Taylor-George et al., 1983), urban rock varnish (Vicenzi, 2016), humid environment varnish (Krinsley et al., 2009), and river splash zone varnish (Krinsley et al., 2012) surfaces. We found stacked layers in the 100 nm range in several rock varnishes, but no structures which could definitely account for former bacteria cells with about 1 µm in diameter. The cavities within the stacked layers are at most 0.5 µm in diameter. Furthermore, the nicely stacked layers show no indication for deformation after cavity collapses of former bacterial cells. However, it cannot be excluded that remobilization of Mn from encrusted cell walls, and re-precipitation of the Mn oxyhydroxides as thin layers destroyed all evidence for former biomineralization (Krinsley et al., 1995). Non-stacked varnishes also showed no definite features which could have formerly been cell structures. Ellipsoidal cavities are present which are about 1 µm in diameter. They might be an indicator for Mn oxyhydroxide growth around organisms, but this cannot be proven with the current methods at hand.

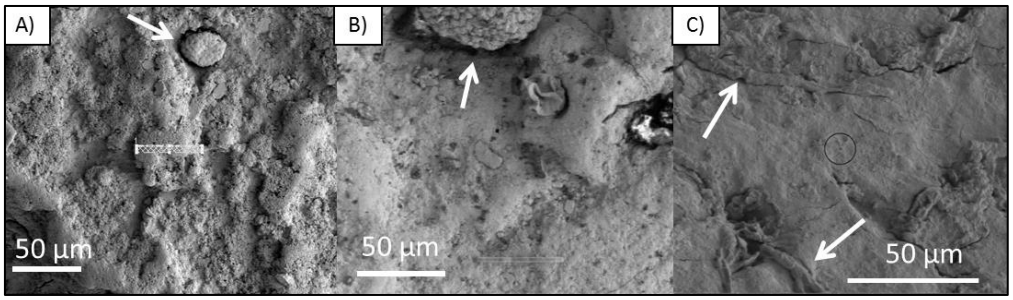

Figure 9: A) Microcolonial fungi on top of a rock varnish surface from a South African varnish sample (SA13 mM-f). B) Close up of microcolonial fungi on a South African sample (SA14 09a). C) Hyphae on the surface of an arid desert varnish sample (IS13V1, Negev Desert, Israel). Arrows point towards fungal colonies and hyphae.

2.2.5.2 Functional Groups and Mn Oxidation States - Scanning Transmission X-Ray Microscopy – Near Edge X-Ray Absorption Fine Structure Spectroscopy

The theory of a biogenic formation was additionally tested by investigating the samples by STXM-NEXAFS. Unfortunately, the amount of organic material within the varnishes is low, some varnishes contain no carbon at all, and nitrogen was found in none of the crusts. The only functional groups found were carboxyl groups (288.5 eV; $(C=O)OH^-$, C 1s-$\pi^*_{C=O}$), aromatic π bonding (285 eV; R(C=C)R, C 1s-$\pi^*_{C=C}$), and carbonate (290.2 eV; CO_3^{2-}) (Fig. 10). A reason for this might be that manganese is a strong electron acceptor and degrades organic matter by photocatalyzed reactions (Sunda et al., 1983). Additionally, bacteria capable to oxidize manganese might degrade organic matter by reducing Mn to make carbon available to them (Spiro et al., 2009; Tebo et al., 1997). Moreover, we cannot exclude that radiation damage occurred during FIB slicing and subsequent imaging by SEM, or that the organic material got "grilled" in the hot desert sun while the varnish was exposed to the environment. The occurrence of carbonate in the spectra might be explained by the reaction:

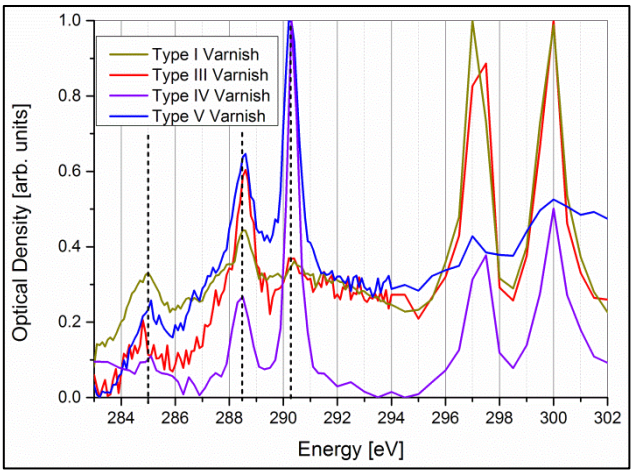

Figure 10: Resonance peaks of carbon at 285 eV and 288.5 eV. Absorption at 290.2 eV indicates the presence of CO_3^{2-} and the two absorption edges at 297.3 and 300 eV mark the presence of potassium. Type V varnish, collected from river splash zones, shows the lack of K in the spectrum. This is due to the fact that this varnish has almost no dust contributing to the varnish matrix. Type IV varnish, urban varnish, shows low K amounts as well.

$$2COOH^- + (3O)^{2-} \rightarrow 3CO_3{}^{2-} + H_2O$$

as proposed by Braun et al. (2009) for sample measurements by EELS and NEXAFS in an O_2 atmosphere. This reaction could also have taken place in the course of the sample preparation and imaging of our samples, and is an indicator for radiation damage. Photoreduction might have happened during the accretion of the varnish, but also during the STXM measurements, where the photon beam provides the necessary energy to cross the band gap. The radiation damage is in this case interpreted as X-ray induced photoreduction, where organic carbon present in the sample provides the electrons (Ross et al., 2001). Grilled material might be a result of the high (up to 57 °C; Furnace Creek, Death Valley) temperatures of arid desert environments (Roof and Callagan, 2003). Direct solar radiation on varnished rocks can even increase the temperature of the crust itself to at least 66 °C (Engel and Sharp, 1958). The small variety of functional groups found might thus be based on the loss of functional groups due to oxidation.

Using STXM-NEXAFS, we were also able to show that Mn is available in its reduced forms (Mn^{2+}/Mn^{3+}) around cavities within a South African and Texan varnish sample (Type II and III), which could be a hint for previously degraded organic matter. When organic matter degrades, the pH value decreases, reducing surrounding materials, such as Mn and Fe. When Mn oxyhydroxide itself oxidizes organic matter, it likewise changes into its reduced state. Other microbacteria present might have also utilized Mn^{4+} to oxidize refractory organic matter and degrade humic substances oxidatively to lower molecular weight compounds, which they were then able to subsequently use as substrates for growth. The reduction process can thus happen with and

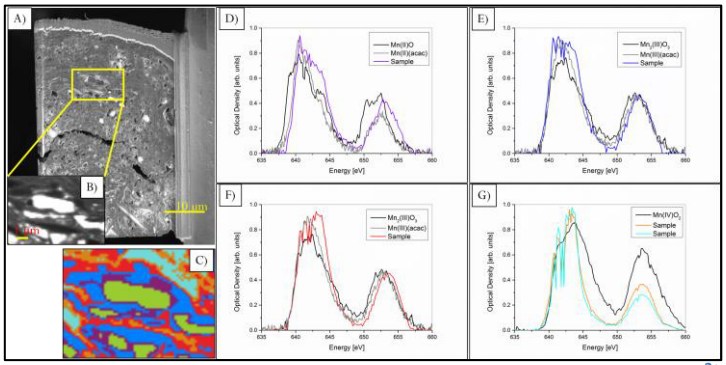

Figure 11: Manganese oxidation states surrounding cavities. A thin Mn^{2+} rim (D; purple in C) is lined with a thick rim of material showing a combination of Mn^{2+} and Mn^{3+} (E and F; blue and red in C). Only in the middle part, at the most protected places, Mn^{4+} (G; orange and light blue in C) is still present, probably representing the primary oxidation state of the matrix material. The colors of the sample plots in D-G correspond to the color code of the cluster analysis in C. C is the cluster analysis of image B, which is the marked excerpt of image A.

without direct involvement of bacteria. It could either be an indicator for former organisms growing on or within varnish, which could act as carbon source, but enclosed organic material could also have been delivered together with the dust fraction. Manganese within the varnish matrix further away from the cavities is available as Mn^{4+}, indicating that the reduction rims only line the cavities (Fig. 11). These observations are in accordance with those made by Krinsley et al. (2013), who found structures they explained with reduction of Mn around cavities and subsequent remobilization of this element, producing, amongst others, the case hardening.

2.2.5.3 Visualization of DNA, Nuclei, and Lipids - DAPI, DRAQ5, and OsO_4 Fixation

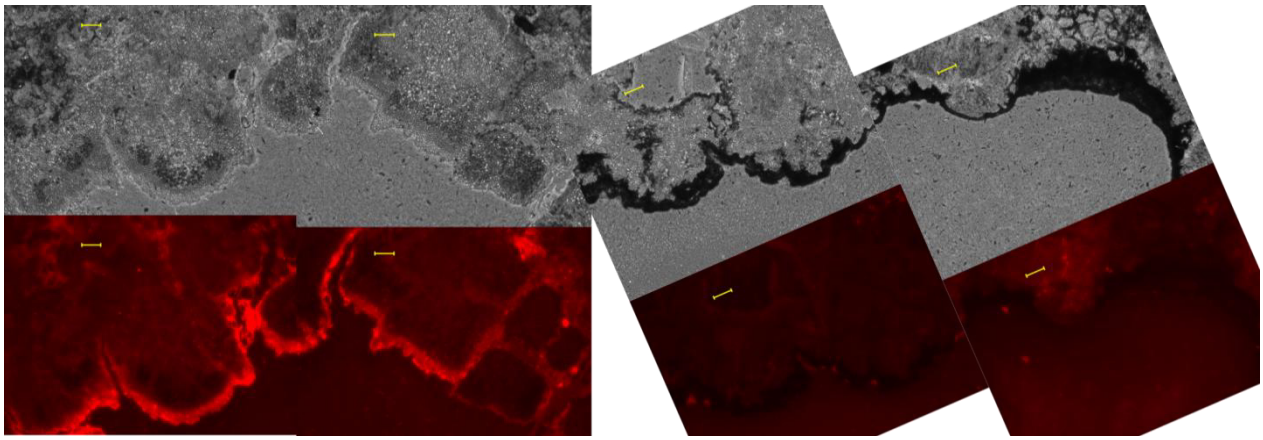

Figure 12: Four images on the left: Lichen cross sections fixed with OsO_4. Bright fluorescence can be observed (OP-6683820 TexasRed: $\lambda_{exitation}$ = 560 nm, $\lambda_{emission}$ = 630 nm). Four images on the right: Rock varnish. No fluorescence can be observed. Lichen and rock varnish were collected adjacent to each other in the Negev Desert, Israel. The scale bar represents 50 µm.

Protocols, such as DAPI and DRAQ5, were used in search for fluorescence of DNA and nuclei. Furthermore, OsO_4 fixed thin sections were investigated by fluorescence microscopy likewise. However, it was impossible to find any evidence for life within the varnish crusts (Fig. 12). Additionally measured lichen samples prepared by OsO_4 fixation clearly indicated the biogenic origin of the material (Fig. 12). Thus, the fixation itself did not influence the measurement outcome.

2.2.5.4 From Lichen to Varnish: Heating and Watering of Desert Inhabitants – Gas Exchange Fluorescence Measurements of Photosynthesis and Light Microscopy

An initial thought at the beginning of this thesis was that rock varnish could be formed by lichen. This thought was based on the finding of lichen in immediate vicinity to rock varnish crusts. An experiment with the aim to activate lichen, collected adjacent to rock varnishes, to precipitate Mn or varnish-like crusts, was unsuccessful. The experiment was conducted by heating and feeding the lichen with artificial rainwater, using a recipe from Johansson et al. (2011). Several cycles of heating, drying, and watering of the lichen produced nothing similar to rock varnish crusts or Mn precipitates. Gas exchange fluorescence measurements (GFS) for photosynthesis were conducted before and after the experiment. It revealed that the lichen were alive at the

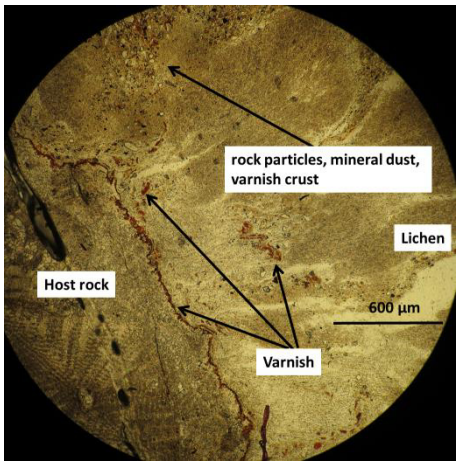

Figure 13: Lichen (right) growing on top of a rock varnish surface, which developed on a silicified limestone (left). The rock varnish crust was removed from the rock surface in the course of the lichen growth.

beginning of the experiment, but did not survive the procedure. Cross-sections through samples of lichen grown on top of rock varnish crusts, imaged by light microscopy, furthermore indicate that lichen rather destroy rock varnish than create it (Fig. 13). This finding is consistent with the observations of other authors (Dorn and Oberlander, 1982; Dragovich, 1987; Dragovich, 1988a; Krumbein and Jens, 1981).

2.2.5.5 Proving the Presence of Hexagonal Birnessite - Electron Paramagnetic Resonance Spectroscopy

Electron paramagnetic resonance spectroscopy was conducted on five rock varnish samples, revealing narrow to medium linewidths of their manganese resonance peaks (images are provided in appendix, B.4). This suggests, after the categorization from Kim et al. (2011), a former biogenic origin of these Mn oxyhydroxides, and a later recrystallization, which sparsely broadened the linewidth. However, the interpretation by Kim et al. (2011) is currently under review. It is criticized that lab bacteria were investigated, and no "real world" bacteria. Furthermore, it is criticized that Fe was not taken into account in these studies, even though its contribution might result in changes of the peak shape. Timothy Raub and Stefan Farsang, from the University of St Andrews, investigated a set of 60 natural Mn oxyhydroxides under these aspects, and disagree with the interpretation by Kim et al. (2011). Unfortunately, their results have not been published yet. Considering the mineralogy of Mn oxyhydroxides, the arguments brought up by Kim et al. (2011) for a biogenic formation is the description of pure hexagonal birnessite. The EPR measurements conducted during this thesis thus indicate that hexagonal birnessite is one of the Mn oxyhydroxide phases present, probably in combination with secondarily formed todorokite, which broadens the linewidth. This is unfortunately no evidence for a biogenic formation, since hexagonal birnessite might have also formed abiogenically, such as in Mn dendrites (McKeown and Post, 2001). On the contrary, other Mn oxyhydroxides, such as hollandite, can in addition be formed biogenically (White et al., 2009).

2.2.5.6 $\delta^{13}C$ Measurements - Nanoscale Secondary Ion Mass Spectrometry and Continuous Flow - Isotope Ratio Mass Spectrometer

Two rock varnish samples were investigated by NanoSIMS to obtain in-situ $\delta^{13}C$ results. The samples used (one from California, Type I varnish, and one from South Africa, Type III varnish) were prepared with a focused ion beam (FIB) to obtain cross sections through the samples without carbon contamination by an epoxy. Unfortunately, the results are inconclusive, since the amount of carbon in the samples is too low to obtain an error small enough for a definite conclusion. Furthermore, due to the lack of a suitable reference material for NanoSIMS measurements

of rock varnish, a SiC standard from Jena was used, providing an additional uncertainty. Our $\delta^{13}C_{VPDB}$ measurements of two rock varnish samples by NanoSIMS revealed values of -27.3 ‰ (± 4.6) for the South African varnish and -22.0 ‰ (± 4.5) for the Californian varnish. These values agree with previously reported $\delta^{13}C$ values of varnish samples, which fall in the range between -23.3 to -31.2 ‰ (no reported errors) (Zerboni, 2008). These results show a signature which could originate from C3 and CAM land plants, bacteria, marine organisms, sediments, and sediment compounds, oxalate, coal, as well as several inorganic carbonate and bicarbonate sources (Coplen et al., 2002). Both signatures measured during this work do not exclude bacteria as carbon source (-31.1 to -24.6 ‰), but the carbon signature of the Californian sample is too high to originate from fungi, which plot in the range from -40.1 to -30.6 ‰ (Kohl et al., 2015). Additional measurements of rock varnish powders, removed from the host rock with an electric combination tool WCT 160 (WorkZone, Hamburg, Germany) under sterile conditions, using autoclaved polishing heads, were made with a Continuous Flow - Isotope Ratio Mass Spectrometer (CR-IRMS). However, these measurements remained inconclusive as well, since the carbon amount within the sample material was too low, although amounts about five times higher were used than typically utilized when carbonates are measured.

2.2.5.7 In the Search for Operational Taxonomic Units and Manganese Oxidizing Organisms – (quantitative) Polymerase Chain Reactions

In addition to imaging, carbon distribution mapping, functional group determinations, lichen growth experiments, EPR investigations, staining experiments, and fluorescence microscopy, a Sanger sequencing study involving PCR and cloning of the PCR fragments into a plasmid were conducted. Several operational taxonomic units (OTUs) were found in five rock varnish samples. The varnishes were removed from the host rock with an electric combination tool WCT 160 (WorkZone, Hamburg, Germany) under sterile conditions, using autoclaved polishing heads. Additionally, one soil sample from underneath the rocks was investigated. The samples were collected from several different environments (Anza-Borrego Desert, CA, USA; Negev Desert, Israel; Knersvlakte, South Africa; Herbstlabyrinth, cave, Germany). All samples were frozen almost the entire time subsequent to their collection. No enrichment of an OTU was consistently found in all varnish samples, which could be an indicator for a similar formation process. To obtain additional information, quantitative PCR (qPCR) analyses (Fig. 14) and Next-Generation Sequencing (NGS) were conducted. For this study, a set of three rock varnishes and corresponding soils from the Anza-Borrego Desert, CA, USA was investigated. The varnish crusts were removed on a sterile working bench with previously autoclaved instruments. The qPCR results showed enrichment in cyanobacterial DNA in rock varnish compared to the soil samples (Fig. 14 A). Manganese ions are found in cyanobacterial photosystem proteins, and might thus explain the enrichment of these taxa on rock varnish. No significant difference was observed for laccases-like multi copper oxidase enzymes from Actinobacteria (LacLike). The superfamily of mul-

ticopper oxidases (MCO) is a widely distributed protein family among pro- and eukaryotes. Together with many other mechanisms, MCO-type enzymes play an integral role in the Mn^{2+} oxidation in diverse species (Tebo et al., 2005). However, within one "soil-varnish set", the total amount of LacLike was not found to be statistically higher in the varnish samples than in the soil samples (Fig. 14 B). Utilizing NGS, some phyla (e.g., Actinobacteria, Proteobacteria, cyanobacteria) were detected to be significantly increased in some varnish samples compared to soil samples. Furthermore, some families being able to bind Mn ions were found to be enriched within the rock varnish samples compared to the soil samples (e.g., Geodermatophilaceae and Rhodobacteraceae). Nevertheless, the differences between rock varnish and soil might be due to exploitive communities, advantageous species that are using the Mn-enriched layer. Due to the lack of findings of larger amounts of organic carbon within the varnish matrix using other techniques, it is probable that the organic compounds found are mainly located on the surface of the coating, supporting the presence of advantageous organisms. Most importantly, no evidence was found for the presence of Mn oxidizing genes, which are necessary in order for the Mn crusts to precipitate, and thus for the rock varnish to form. To conclude, no evidence or prove for a biogenic contribution to the formation of rock varnish was found in any of the varnish samples, even though a large variety of tests were conducted in this study.

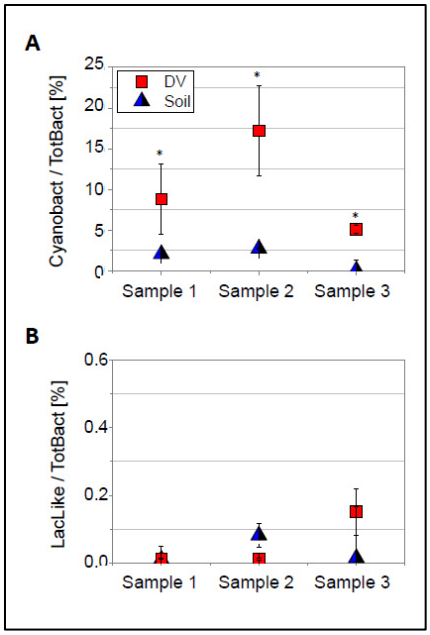

Figure 14: A: enrichment in cyanobacterial DNA in rock varnish and soil samples normalized to the amount of total bacteria. B: amount of laccases found within varnish and corresponding soil normalized to the amount of total bacteria. The image was provided by Naama Long-Yan and will be published soon (Long-Yan et al., in preparation).

3 Conclusions

This thesis is a comparative study of rock varnishes from locations worldwide as well as of the relationship between mineral dust and rock varnish. All samples were investigated using the same methods, hence the results obtained from different varnishes collected from different environments are directly comparable. Structures, element compositions, and element distributions were investigated using different measurement techniques. In addition, developments for future measurements were made and published in the course of this thesis. Their aim is to facilitate and advance measurements in relation to rock varnish in the future.

The analyses of rock varnishes showed that they can be subdivided by "fingerprint" characteristics. Categorization is an important topic since the term "rock varnish" is used too broadly by several authors and thus fails to take into account necessary distinctions. By discussing the investigated samples as different types, one can state that there are crusts which seem to form biogenically (cave varnish), others which seem to form abiogenically (Mn dendrites, fissure and fracture crusts, and we propose also desert varnish (Type I) and urban facade crusts (Type IV)), and that there are Mn-rich crusts the geneses of which are still not yet understood (e.g., river splash zone varnish (Type V), Mn nodules, and Mn-covered pebbles in rivers).

Furthermore, this study revealed that small-sized mineral dust appears to be the main source of desert varnish. The contribution of dust to varnish chemistry is, however, different for different types of rock varnish, a result confirming the findings of our matrix investigations. Vehicle emissions seem to be the major source of Mn-rich crusts on facades in urban, while for Mn-rich crusts which formed in river splash zones, water was found to be the element-providing source. This raises the question whether all crusts currently encompassed by the term rock varnish actually fit the definition, and where the line should be drawn.

The development of natural Mn-rich crusts is very strongly influenced by water. The implication that Mn-rich layers in rock varnishes from desert environments represent wet conditions and Mn-poor layers, in contrast, dry conditions, is reasonable. However, it was found in this thesis that this layer sequence is only present in varnishes accumulated in desert environments (Type I). Unfortunately, the impossibility to date varnish, the lack of information about the onset of the crust growth, possible occasional accumulation stops, growth rates, and past dissolution or exfoliation processes pose a problem for the application of varnish as a paleoclimate archive. One might consider these questions to be important enough to address them before using the layer sequences, or manganese contents, as paleoclimate archives, and before applying this proxy to worldwide locations.

In the course of this thesis, oxidation states were localized in-situ within the microstructures of rock varnishes. They indicate that redox reactions previously had taken place along cavities within the structure. The "fossilized" redox reactions are one indicator for past reworking of the

immensely active minerals combined in this ancient material. Case hardening, which was observed in several varnishes in the course of this study, is another indicator for reworking by manganese remobilization and thus matrix reorganization. Since rock varnish consists of a large amount of clay minerals, which are known to be very (re)active, as well as Mn oxyhydroxides, which are known to be amongst the strongest occurring natural oxidizers and element scavengers, it is very complex, or even impossible, to prove which features are primary and which secondary.

Even though a large amount of publications about biological findings in rock varnish have been published in the past, we were not able to confirm them on the basis of our investigations. No observation was made which could prove a biogenic origin of rock varnish, and the absence of manganese oxidizing genes and similar OTU's within different rock varnishes indicates an abiogenic genesis of the varnishes investigated. However, since clay minerals and Mn oxyhydroxides are amongst the most reactive natural minerals, it cannot be ultimately proved that former organic compounds were not oxidized and destroyed. Furthermore, former biogenic structures could have been erased by reworking of the matrix of the crust. Since desert varnish is an ancient microcrust, a large surface is exposed and available for potential reactions to take place. The great age of the crusts provides enough time to rework the material, maybe even more than once. Contradicting this assumption is the absence of Mn oxidizing organisms in the most recently formed layers and on current rock varnish surfaces. Thus, the data strongly support an abiogenic origin of rock varnish.

4 References

Atkins, A.L., Shaw, S., Peacock, C.L., 2014. Nucleation and growth of todorokite from birnessite: Implications for trace-metal cycling in marine sediments. Geochimica et Cosmochimica Acta, 144: 109-125.

Baied, C.A., Somonte, C., 2013. Mid-Holocene geochronology, palaeoenvironments, and occupational dynamics at Quebrada de Amaicha, Tucuman, Argentina. Quaternary International, 299: 80-89.

Bao, H., Michalski, G.M., Thiemens, M.H., 2001. Sulfate oxygen-17 anomalies in desert varnishes. Geochimica et Cosmochimica Acta, 65(13): 2029-2036.

Bau, M. et al., 2014. Discriminating between different genetic types of marine ferro-manganese crusts and nodules based on rare earth elements and yttrium. Chemical Geology, 381: 1-9.

Bauman, A., 1976. Desert varnish and marine ferromanganese oxide nodules: congeneric phenomena. Nature, 259(5542): 387-388.

Beck, W. et al., 1998. Ambiguities in direct dating of rock surfaces using radiocarbon measurements. Science, 280(5372): 2132-2139.

Bednarik, R.G., 2002. The dating of rock art: a critique. Journal of Archaeological Science, 29(11): 1213-1233.

Beetz, T., Jacobsen, C., 2003. Soft X-ray radiation-damage studies in PMMA using a cryo-STXM. Journal of Synchrotron Radiation, 10(3): 280-283.

Bierman, P.R., Gillespie, A.R., 1994. Evidence sugesting that methods of rock-varnish cation-rato dating are neither comparable nor consistently reliable. Quaternary Research, 41(1): 82-90.

Bierman, P.R., Gillespie, A.R., Kuehner, S., 1991. Precision of rock-varnish chemical analyses and cation-ratio ages. Geology, 19(2): 135-138.

Braun, A., Kubatova, A., Wirick, S., Mun, S., 2009. Radiation damage from EELS and NEXAFS in diesel soot and diesel soot extracts. Journal of Electron Spectroscopy and Related Phenomena, 170(1): 42-48.

Broecker, W.S., Denton, G.H., 1989. The role of ocean-atmosphere reorganizations in glacial cycles. Geochimica et Cosmochimica Acta, 53(10): 2465-2501.

Broecker, W.S., Liu, T., 2001. Rock Varnish: Record of desert Wetness? GSA today, August: 4-10.

Bromfield, S., David, D., 1976. Sorption and oxidation of manganous ions and reduction of manganese oxide by cell suspensions of a manganese oxidizing bacterium. Soil Biology and Biochemistry, 8(1): 37-43.

Burns, R.G., Burns, V.M., 1977. Mineralogy. Elsevier Oceanography Series, 15: 185-248.

Cahyani, V.R., Murase, J., Ishibashi, E., Asakawa, S., Kimura, M., 2007. Bacterial communities in manganese nodules in rice field subsoils: Estimation using PCR-DGGE and sequencing analyses. Soil Science and Plant Nutrition, 53(5): 575-584.

Coplen, T.B. et al., 2002. Compilation of minimum and maximum isotope ratios of selected elements in naturally occurring terrestrial materials and reagents.

Dalton, R., 1998. Dating in doubt as researcher is probed. Nature Publishing Group.

Darwin, C., 1840. Journal of Researches Into the Geology and Natural History of the Varoius Countries Visited by HMS Beagle, Under the Command of Captain Fitzroy from 1832 to 1836 by Charles Darwin. Colburn.

Davies, S.H., Morgan, J.J., 1989. Manganese (II) oxidation kinetics on metal oxide surfaces. Journal of Colloid and Interface Science, 129(1): 63-77.

De la Torre, M., Gomez-Alarcon, G., 1994. Manganese and iron oxidation by fungi isolated from building stone. Microbial Ecology, 27(2): 177-188.

Dietzel, M., Kolmer, H., Poelt, P., Simic, S., 2008. Desert varnish and petroglyphs on sandstone - Geochemical composition and climate changes from Pleistocene to Holocene (Libya). Chemie Der Erde-Geochemistry, 68(1): 31-43.

DiGregorio, B.E., 2001. Rock varnish as a habitat for extant life on Mars. In: Hoover, R.B., Levin, G.V., Paepe, R.R., Rozanov, A.Y. (Eds.), Instruments, Methods, and Missions for Astrobiology Iv. Proceedings of the Society of Photo-Optical Instrumentation Engineers (Spie), pp. 120-130.

Dorn, R., Oberlander, T., 1981a. Rock varnish origin, characteristics, and usage. Zeitschrift fur Geomorphologie, 25(4): 420-436.

Dorn, R., Oberlander, T.M., 1982. Rock varnish. Progress in Physical Geography, 6(3): 317-367.

Dorn, R.I., 1983. Cation-ratio dating: A new rock varnish age-determination technique. Quaternary Research, 20(1): 49-73.

Dorn, R.I., 1984. Cause and implications of rock varnish microchemical laminations. Nature, 310(5980): 767-770.

Dorn, R.I., 1986. Rock varnish as an indicator of aeolian environmental change. Aeolian geomorphology: 291-307.
Dorn, R.I., 1988. A rock varnish interpretation of alluvial-fan development in Death Valley, California. National Geographic Research, 4(1): 56-73.
Dorn, R.I., 2009. Desert rock coatings. In: Parsons, A.J.a.A., A.D (Ed.), Geomorphology of Desert Environments. Springer, Amsterdam, pp. 153-186.
Dorn, R.I., Jull, A.T., Donahue, D., Linick, T., Toolin, L., 1989. Accelerator mass spectrometry radiocarbon dating of rock varnish. Geological Society of America Bulletin, 101(11): 1363-1372.
Dorn, R.I. et al., 1992. Manganese-rich Rock Varnish does occur in Antarctica. Chemical Geology, 99(4): 289-298.
Dorn, R.I. et al., 2012. Assessing Early Spanish Explorer Routes Through Authentication of Rock Inscriptions. Professional Geographer, 64(3): 415-429.
Dorn, R.I., Nobbs, M., Cahill, T.A., 1988. Cation-ratio dating of rock-engravings from the Olary Province of arid South Australia. Antiquity, 62(237): 681-689.
Dorn, R.I., Oberlander, T.M., 1981b. Microbial origin of desert varnish. Science, 213(4513): 1245-1247.
Douglas, G., 1987. Manganese-rich rock coatings from Iceland. Earth surface processes and landforms, 12(3): 301-310.
Dragovich, D., 1987. Weathering of desert varnish by lichens, Readings in Australian Geography. Proceedings of the 21st IAG Conference, Perth, pp. 407-412.
Dragovich, D., 1988a. Desert varnish and environmental change near Broken Hill, western New South Wales. Earth-Science Reviews, 25(5-6): 399-407.
Dragovich, D., 1988b. A preliminary electron probe study of microchemical variations in desert varnish in western New South Wales, Australia. Earth Surface Processes and Landforms, 13(3): 259-270.
Dragovich, D., 1993. Distribution and chemical composition of microcolonial fungi and rock coatings from arid Australia. Physical Geography, 14(4): 323-341.
Dragovich, D., 2000. Rock engraving chronologies and accelerator mass spectrometry radiocarbon age of desert varnish. Journal of Archaeological Science, 27(10): 871-876.
Duckworth, O.W., Sposito, G., 2005. Siderophore− manganese (III) interactions II. Manganite dissolution promoted by desferrioxamine B. Environmental science & technology, 39(16): 6045-6051.
Elvidge, C., Moore, C., 1979. A model for desert varnish formation, Geological Society of America Abstracts with Programs, pp. 1980.
Engel, C.G., Sharp, R.P., 1958. Chemical data on desert varnish. Geological Society of America Bulletin, 69(5): 487-518.
Esposito, A. et al., 2015. Comparison of rock varnish bacterial communities with surrounding non-varnished rock surfaces: taxon-specific analysis and morphological description. Microbial ecology, 70(3): 741-750.
Feng, X.H., Zhai, L.M., Tan, W.F., Liu, F., He, J.Z., 2007. Adsorption and redox reactions of heavy metals on synthesized Mn oxide minerals. Environmental Pollution, 147(2): 366-373.
Fernández, B., Claverie, F., Pécheyran, C., Donard, O.F., 2007. Direct analysis of solid samples by fs-LA-ICP-MS. TrAC Trends in Analytical Chemistry, 26(10): 951-966.
Fleisher, M., Liu, T., Broecker, W.S., Moore, W., 1999a. A clue regarding the origin of rock varnish. Geophysical Research Letters, 26(1): 103-106.
Fleisher, M., Liu, T.Z., Broecker, W.S., Moore, W., 1999b. A clue regarding the origin of rock varnish. Geophysical Research Letters, 26(1): 103-106.
Francis, C.A., Tebo, B.M., 2001. Enzymatic manganese (II) oxidation by a marine α-proteobacterium. Applied and environmental microbiology, 67(9): 4024-4029.
Frierdich, A.J., Hasenmueller, E.A., Catalano, J.G., 2011. Composition and structure of nanocrystalline Fe and Mn oxide cave deposits: Implications for trace element mobility in karst systems. Chemical Geology, 284(1): 82-96.
Gadde, R.R., Laitinen, H.A., 1974. Heavy metal adsorption by hydrous iron and manganese oxides. Analytical Chemistry, 46(13): 2022-2026.
Garvie, L.A.J., Burt, D.M., Buseck, P.R., 2008. Nanometer-scale complexity, growth, and diagenesis in desert varnish. Geology, 36(3): 215-218.
Giovanoli, R., Burki, P., 1975. Comparison of X-Ray Evidence of Marine Mn Nodules and Non-Marine Mn Ore Deposits. Chimia, 29(6): 266-269.

Glasby, G. et al., 1981. Desert varnish in southern Victoria land, Antarctica. New Zealand Journal of Geology and Geophysics, 24(3): 389-397.
Goldsmith, Y., Enzel, Y., Stein, M., 2012. Systematic Mn fluctuations in laminated rock varnish developed on coeval early Holocene flint artifacts along a climatic transect, Negev desert, Israel. Quaternary Research, 78(3): 474-485.
Goldsmith, Y., Stein, M., Enzel, Y., 2014. From dust to varnish: Geochemical constraints on rock varnish formation in the Negev Desert, Israel. Geochimica Et Cosmochimica Acta, 126: 97-111.
Gregory, E., Perry, R., Staley, J., 1980. Characterization, distribution, and significance ofMetallogenium in Lake Washington. Microbial ecology, 6(2): 125-140.
Grissom, C.A. et al., 2014. Manganese in black crusts on Seneca sandstone. Microscopy and Microanalysis, 20(S3): 2044-2045.
Grote, G., Krumbein, W., 1992. Microbial precipitation of manganese by bacteria and fungi from desert rock and rock varnish. Geomicrobiology Journal, 10(1): 49-57.
Grüner, F.W., Otto; Kürten, Luzius; Riemann, Jennifer 2011. Verschwärzung von Sandsteinoberflächen durch Eisen-/Manganoxide, neue Ergebnisse zu Ursache und restauratorischer Behandlung mittels Kompressen. Natursteinsanierung Stuttgart 2011. Neue Natursteinsanierungsergebnisse und messtechnische Erfassungen sowie Sanierungsbeispiele, Conference: 7-21.
Guillong, M., Günther, D., 2002. Effect of particle size distribution on ICP-induced elemental fractionation in laser ablation-inductively coupled plasma-mass spectrometry. Journal of Analytical Atomic Spectrometry, 17(8): 831-837.
Günther, D., Frischknecht, R., Heinrich, C.A., Kahlert, H.-J., 1997. Capabilities of an argon fluoride 193 nm excimer laser for laser ablation inductively coupled plasma mass spectometry microanalysis of geological materials. Journal of Analytical Atomic Spectrometry, 12(9): 939-944.
Hayden, J.D., 1976. Pre-altithermal archaeology in the Sierra Pinacate, Sonora, Mexico. American Antiquity: 274-289.
Hergenröder, R., Samek, O., Hommes, V., 2006. Femtosecond laser ablation elemental mass spectrometry. Mass spectrometry reviews, 25(4): 551-572.
Hoar, K., Nowinski, P., Hodge, V., Cizdziel, J., 2011. Rock varnish: A passive forensic tool for monitoring recent air pollution and source identification. Nuclear Technology, 175(1): 351-359.
Hodge, V.F., Farmer, D.E., Diaz, T., Orndorff, R.L., 2005. Prompt detection of alpha particles from Po-210: another clue to the origin of rock varnish? Journal of Environmental Radioactivity, 78(3): 331-342.
Hua, M. et al., 2012. Heavy metal removal from water/wastewater by nanosized metal oxides: a review. Journal of Hazardous Materials, 211: 317-331.
Humboldt, A.v., 1859. Reise in die Äquinoktialgegenden des neuen Kontinents. Deutsch von Hauff.) Bd, 3.
Iannicelli, J., 1992. Manganese dioxide impregnated filter. Google Patents.
Jeffries, T.E., Jackson, S.E., Longerich, H.P., 1998. Application of a frequency quintupled Nd: YAG source (λ= 213 nm) for laser ablation inductively coupled plasma mass spectrometric analysis of minerals. Journal of Analytical Atomic Spectrometry, 13(9): 935-940.
Jochum, K. et al., 2016. FeMnOx-1: A new microanalytical reference material for the investigation of Mn–Fe rich geological samples. Chemical Geology, 432: 34-40.
Jochum, K.P. et al., 2014. Non-Matrix-Matched Calibration for the Multi-Element Analysis of Geological and Environmental Samples Using 200 nm Femtosecond LA-ICP-MS: A Comparison with Nanosecond Lasers. Geostandards and Geoanalytical Research, 38(3): 265-292.
Johansson, O., Olofsson, J., Giesler, R., Palmqvist, K., 2011. Lichen responses to nitrogen and phosphorus additions can be explained by the different symbiont responses. New Phytologist, 191(3): 795-805.
Johnston, J. et al., 1984. Desert varnish in Antarctica: A nuclear microprobe and backscattered 57Fe Mössbauer spectroscopic study. Chemical geology, 42(1-4): 189-201.
Kilcoyne, A.L.D. et al., 2003. Interferometer-controlled scanning transmission X-ray microscopes at the Advanced Light Source. Journal of Synchrotron Radiation, 10: 125-136.
Kim, S.S. et al., 2011. Searching for biosignatures using electron paramagnetic resonance (EPR) analysis of manganese oxides. Astrobiology, 11(8): 775-786.
Klaveness, D., 1977. Morphology, distribution and significance of the manganese-accumulating microorganism Metallogenium in lakes. Hydrobiologia, 56(1): 25-33.
Knauss, K.G., Ku, T.-L., 1980. Desert varnish: potential for age dating via uranium-series isotopes. The Journal of Geology, 88(1): 95-100.

Kohl, L. et al., 2015. Distinct fungal and bacterial δ13C signatures as potential drivers of increasing δ13C of soil organic matter with depth. Biogeochemistry, 124(1-3): 13-26.
Krinsley, D., 1998. Models of rock varnish formation constrained by high resolution transmission electron microscopy. Sedimentology, 45(4): 711-725.
Krinsley, D., Ditto, J., Langworthy, K., Dorn, R.I., Thompson, T., 2013. Varnish microlaminations: new insights from focused ion beam preparation. Physical Geography, 34(3): 159-173.
Krinsley, D., Dorn, R., Tovey, N., 1995. Nanometer-scale layering in rock varnish: implications for genesis and paleoenvironmental interpretation. The Journal of Geology, 103(1): 106-113.
Krinsley, D., Dorn, R.I., DiGregorio, B., 2009. Astrobiological Implications of Rock Varnish in Tibet. Astrobiology, 9(6): 551-562.
Krinsley, D.H., Dorn, R.I., DiGregorio, B.E., Langworthy, K.A., Ditto, J., 2012. Rock varnish in New York: An accelerated snapshot of accretionary processes. Geomorphology, 138(1): 339-351.
Krumbein, W.E., Jens, K., 1981. Biogenic rock varnishes of the Negev Desert (Israel) an ecological study of iron and manganese transformation by cyanobacteria and fungi. Oecologia, 50(1): 25-38.
Kuhlman, K. et al., 2006a. Diversity of microorganisms within rock varnish in the Whipple Mountains, California. Applied and Environmental Microbiology, 72(2): 1708-1715.
Kuhlman, K., Kuhlman, G.M., La Duc, M.T., McKay, C.P., 2007. Evidence for a cryptoendolithic microbial community in rock varnish at Yungay, Atacama Desert, chile. Abstracts of the General Meeting of the American Society for Microbiology, 107: 453-453.
Kuhlman, K.R. et al., 2006b. Diversity of microorganisms within rock varnish in the Whipple Mountains, California. Applied and Environmental Microbiology, 72(2): 1708-1715.
Kuhlman, K.R., Venkat, P., La Duc, M.T., Kuhlman, G.M., McKay, C.P., 2008. Evidence of a microbial community associated with rock varnish at Yungay, Atacama Desert, Chile. Journal of Geophysical Research-Biogeosciences, 113(G4).
Kwon, K.D., Refson, K., Sposito, G., 2009. On the role of Mn (IV) vacancies in the photoreductive dissolution of hexagonal birnessite. Geochimica et Cosmochimica Acta, 73(14): 4142-4150.
Lanza, N.L. et al., 2012. Examining natural rock varnish and weathering rinds with laser-induced breakdown spectroscopy for application to ChemCam on Mars. Applied Optics, 51(7): B74-B82.
Lanza, N.L. et al., 2015. Understanding the signature of rock coatings in laser-induced breakdown spectroscopy data. Icarus, 249(0): 62-73.
Lebedeva, M., Shishkov, V., 2016. A Comparative Analysis of the Microfabrics of Surface Horizons and Desert Varnish in Extremely Arid Soils of the Mojave (USA) and Trans-Altai Gobi (Mongolia) Deserts. Eurasian Soil Science, 49(2): 163-179.
Lee, M., Bland, P., 2003. Dating climatic change in hot deserts using desert varnish on meteorite finds. Earth and Planetary Science Letters, 206(1): 187-198.
Liu, T., Broecker, W.S., 2007. Holocene rock varnish microstratigraphy and its chronometric application in the drylands of western USA. Geomorphology, 84(1-2): 1-21.
Liu, T., Broecker, W.S., 2008a. Rock varnish evidence for latest Pleistocene millennial-scale wet events in the drylands of western United States. Geology, 36(5): 403-406.
Liu, T., Broecker, W.S., 2008b. Rock varnish microlamination dating of late Quaternary geomorphic features in the drylands of western USA. Geomorphology, 93(3-4): 501-523.
Liu, T., Broecker, W.S., 2013. Millennial-scale varnish microlamination dating of late Pleistocene geomorphic features in the drylands of western USA. Geomorphology, 187: 38-60.
Liu, T., Broecker, W.S., Stein, M., 2013. Rock varnish evidence for a Younger Dryas wet period in the Dead Sea basin. Geophysical Research Letters, 40(10): 2229-2235.
Liu, T.H., Broecker, W.S., 2000. How fast does rock varnish grow? Geology, 28(2): 183-186.
Liu, T.Z., 2003. Blind testing of rock varnish microstratigraphy as a chronometric indicator: results on late Quaternary lava flows in the Mojave Desert, California. Geomorphology, 53(3-4): 209-234.
Liu, T.Z., 2004. Blind testing of rock varnish microstratigraphy as a chronometric indicator: results on late Quaternary lava flows in the Mojave Desert, California (vol 53, pg 209, 2003). Geomorphology, 57(3-4): 445-446.
Liu, T.Z., Broecker, W.S., Bell, J.W., Mandeville, C.W., 2000. Terminal pleistocene wet event recorded in rock varnish from Las Vegas Valley, southern Nevada. Palaeogeography Palaeoclimatology Palaeoecology, 161(3-4): 423-433.
Liu, T.Z., Dorn, R.I., 1996. Understanding the spatial variability of environmental change in drylands with rock varnish microlaminations. Annals of the Association of American Geographers, 86(2): 187-212.

Livingston, R. et al., 2016. Investigation of urban rock varnish on the sandstone of the Smithsonian Castle. Science and Art: A Future for Stone: 399.
Loendorf, L.L., 1991. Cation-ratio varnish dating and petroglyph chronology in southeastern Colorado. Antiquity, 65(247): 246-255.
Loew, O., 1876. US geographic and geological surveys west of the 100th meridian. Annu. Rep. Chief of Engineers, Appendix JJ: 179.
Lovley, D., 1992. Microbial oxidation of organic matter coupled to the reduction of Fe (III) and Mn (IV) oxides. Catena, Supplement(21): 101-114.
Luther, G.W., 2010. The role of one-and two-electron transfer reactions in forming thermodynamically unstable intermediates as barriers in multi-electron redox reactions. Aquatic Geochemistry, 16(3): 395-420.
Malakoff, D., 1998. Rock dates thrown into doubt, researcher under fire. Science, 280(5372): 2041-2042.
Malakoff, D., 1999. Cleared of Misconduct, Geoscientist Sues Critics. Science, 286(5441): 883-885.
Manceau, A., Lanson, B., Drits, V.A., 2002. Structure of heavy metal sorbed birnessite. Part III: Results from powder and polarized extended X-ray absorption fine structure spectroscopy. Geochimica et Cosmochimica Acta, 66(15): 2639-2663.
Margetic, V. et al., 2000. A comparison of nanosecond and femtosecond laser-induced plasma spectroscopy of brass samples. Spectrochimica acta part B: Atomic spectroscopy, 55(11): 1771-1785.
Mc Kenzie, R.M., 1989. Manganese oxides and hydroxides. Minerals in soil environments(mineralsinsoile): 439-465.
McKeown, D.A., Post, J.E., 2001. Characterization of manganese oxide mineralogy in rock varnish and dendrites using X-ray absorption spectroscopy. American Mineralogist, 86(5-6): 701-713.
McLoughlin, N., Wilson, L., Brasier, M., 2008. Growth of synthetic stromatolites and wrinkle structures in the absence of microbes–implications for the early fossil record. Geobiology, 6(2): 95-105.
Miller, A. et al., 2012. Biogenic Mn oxide minerals coating in a subsurface granite environment. Chemical Geology, 322: 181-191.
Nagy, B. et al., 1991. Rock varnish in the Sonoran Desert: microbiologically mediated accumulation of manganiferous sediments. Sedimentology, 38(6): 1153-1171.
Northup, D.E. et al., 2010a. Diversity of rock varnish bacterial communities from Black Canyon, New Mexico. Journal of Geophysical Research: Biogeosciences, 115(G2).
Northup, D.E. et al., 2010b. Diversity of rock varnish bacterial communities from Black Canyon, New Mexico. Journal of Geophysical Research-Biogeosciences, 115.
Nowinski, P., Hodge, V.F., Gerstenberger, S., 2012. Application of field portable X-ray fluorescence to the analysis of desert varnish samples in areas affected by coal-fired power plants. Environmental Chemistry, 9(4): 379-388.
Nowinski, P., Hodge, V.F., Gerstenberger, S., Cizdziel, J.V., 2013. Analysis of mercury in rock varnish samples in areas impacted by coal-fired power plants. Environmental Pollution, 179: 132-137.
Nowinski, P., Hodge, V.F., Lindley, K., Cizdziel, J.V., 2010. Elemental Analysis of Desert Varnish Samples in the Vicinity of Coal-Fired Power Plants and the Nevada Test Site Using Laser Ablation ICP-MS. Chemical and Biomedical Methods Journal, 3: 153-168.
Oberlander, T.M., 1994. Rock varnish in deserts, Geomorphology of desert environments. Springer, pp. 106-119.
Oldham, V.E., Mucci, A., Tebo, B.M., Luther, G.W., 2017. Soluble Mn (III)–L complexes are abundant in oxygenated waters and stabilized by humic ligands. Geochimica et Cosmochimica Acta, 199: 238-246.
Otter, L.M. et al., in preparation. Relationship between Rock Varnish and Adjacent Mineral Dust.
Parchert, K.J., Spilde, M.N., Porras-Alfaro, A., Nyberg, A.M., Northup, D.E., 2012. Fungal Communities Associated with Rock Varnish in Black Canyon, New Mexico: Casual Inhabitants or Essential Partners? Geomicrobiology Journal, 29(8): 752-766.
Paterson, E., Clark, D., Russell, J., Swaffield, R., 1986. Cation exchange in synthetic manganates II. The structure of an alkylammonium-saturated phyllomanganate. Clay Minerals, 21(5): 957-964.
Peacock, C.L., Sherman, D.M., 2007. Crystal-chemistry of Ni in marine ferromanganese crusts and nodules. American Mineralogist, 92(7): 1087-1092.
Perry, R.S., Adams, J.B., 1978. Desert varnish: evidence for cyclic deposition of manganese. Nature, 276(5687): 489-491.
Perry, R.S., Engel, M.H., Botta, O., Staley, J.T., 2003. Amino acid analyses of desert varnish from the Sonoran and Mojave deserts. Geomicrobiology Journal, 20(5): 427-438.

Perry, R.S., Kolb, V.M., 2004a. Biological and organic constituents of desert varnish: review and new hypotheses. In: Hoover, R.B., Rozanov, A.Y. (Eds.), Instruments, Methods, and Missions for Astrobiology Vii. Proceedings of the Society of Photo-Optical Instrumentation Engineers (Spie), pp. 202-217.

Perry, R.S., Kolb, V.M., 2004b. From Darwin to Mars: desert varnish as a model for preservation of complex (bio)chemical systems. In: Hoover, R.B., Rozanov, A.Y. (Eds.), Instruments, Methods, and Missions for Astrobiology Vii. Proceedings of the Society of Photo-Optical Instrumentation Engineers (Spie), pp. 136-144.

Perry, R.S. et al., 2006. Baking black opal in the desert sun: The importance of silica in desert varnish. Geology, 34(7): 537-540.

Perry, R.S., Sephton, M.A., 2006. Desert varnish: an environmental recorder for Mars. Astronomy & Geophysics, 47(4): 34-35.

Perry, R.S., Sephton, M.A., 2008. Solving the mystery of desert varnish with microscopy. Infocus Magazine(11): 62.

Poitrasson, F., Mao, X., Mao, S.S., Freydier, R., Russo, R.E., 2003. Comparison of ultraviolet femtosecond and nanosecond laser ablation inductively coupled plasma mass spectrometry analysis in glass, monazite, and zircon. Analytical Chemistry, 75(22): 6184-6190.

Post, J., 1993. Crystal structures of manganese oxide minerals. Catena supplement, 21: 51-51.

Post, J.E., 1999. Manganese oxide minerals: Crystal structures and economic and environmental significance. Proceedings of the National Academy of Sciences of the United States of America, 96(7): 3447-3454.

Potter, R.M., 1979. The tetravalent manganese oxides: clarification of their structural variations and relationships and characterization of their occurrence in the terrestrial weathering environment as desert varnish and other manganese oxide concentrations, California Institute of Technology Pasadena.

Potter, R.M., Rossman, G.R., 1977. Desert varnish: the importance of clay minerals. Science, 196(4297): 1446-1448.

Potter, R.M., Rossman, G.R., 1979. The Manganese- and iron-Oxide Mineralogy of Desert Varnish. Chemical Geology, 25: 79-94.

Raymond, R., Guthrie, G., Bish, D., Reneau, S., Chipera, S., 1993. Biomineralization of manganese in rock varnish. Catena Supplement, 21: 321-321.

Reddy, M., Perkins, H., 1974. Fixation of zinc by clay minerals. Soil Science Society of America Journal, 38(2): 229-231.

Reneau, S.L., 1993a. Manganese accumulation in rock-varnish on a desert piedmont, Mojave Desert, California, and application to evaluating varnish development. Quaternary Research, 40(3): 309-317.

Reneau, S.L., 1993b. Manganese accumulation in rock varnish on a desert piedmont, Mojave Desert, California, and application to evaluating varnish development. Quaternary Research, 40(3): 309-317.

Reneau, S.L., Oberlander, T.M., Harrington, C.D., Dorn, R.I., 1991. Accelerator mass spectrometry radiocarbon dating of rock varnish: Discussion and reply. Geological Society of America Bulletin, 103(2): 310-314.

Reneau, S.L., Raymond, R., 1991. Cation-ratio dating of rock varnish: Why does it work? Geology, 19(9): 937-940.

Reneau, S.L., Raymond, R., Harrington, C.D., 1992. Elemental relationships in rock varnish stratigraphic layers, Cima Volcanic Field, California - Implications for varnish development and the interpretation of varnish chemistry. American Journal of Science, 292(9): 684-723.

Roof, S., Callagan, C., 2003. The climate of Death Valley, California. Bulletin of the American Meteorological Society, 84(12): 1725.

Ross, D.S., Hales, H.C., Shea-McCarthy, G.C., Lanzirotti, A., 2001. Sensitivity of soil manganese oxides: XANES spectroscopy may cause reduction. Soil Science Society of America Journal, 65(3): 744-752.

Rudnick, R.L., Gao, S., 2003. 3.01 - Composition of the Continental Crust. Treatise On Geochemistry, Elsevier Ltd, 3: 1-64.

Saiz-Jimenez, C., Miller, A.Z., Martin-Sanchez, P.M., Hernandez-Marine, M., 2012. Uncovering the origin of the black stains in Lascaux Cave in France. Environmental microbiology, 14(12): 3220-3231.

Scheuvens, D., Schütz, L., Kandler, K., Ebert, M., Weinbruch, S., 2013. Bulk composition of northern African dust and its source sediments—a compilation. Earth-Science Reviews, 116: 170-194.

Sherman, D.M., 2005. Electronic structures of iron (III) and manganese (IV)(hydr) oxide minerals: Thermodynamics of photochemical reductive dissolution in aquatic environments. Geochimica et Cosmochimica Acta, 69(13): 3249-3255.

Skinner, H., Fitzpatrick, R.W., 1992. Iron and manganese biomineralization. Catena, Supplement(21): 1-6.
Smith, B., Whalley, W., 1988. A note on the characteristics and possible origins of desert varnishes from southeast Morocco. Earth Surface Processes and Landforms, 13(3): 251-258.
Smith, B., Whalley, W., 1989. A note on the characteristics and possible origins of desert varnishes from Southeast Morocco. A reply to comments by RI Dorn. Earth Surface Processes and Landforms, 14(2): 171-172.
Solomon, D. et al., 2012. Micro-and nano-environments of carbon sequestration: Multi-element STXM–NEXAFS spectromicroscopy assessment of microbial carbon and mineral associations. Chemical geology, 329: 53-73.
Spilde, M.N., Boston, P., Northrup, D., 2002. Subterranean manganese deposits in caves: Analogies to rock varnish. Geological Society of American Abstracts with Programs http://gsa.confex.com/gsa/2002AM/finalprogram/abstract 46060. htm.
Spilde, M.N., Melim, L.A., Northup, D.E., Boston, P.J., 2013. Anthropogenic lead as a tracer of rock varnish growth: Implications for rates of formation. Geology, 41(2): 263-266.
Spiro, T.G., Bargar, J.R., Sposito, G., Tebo, B.M., 2009. Bacteriogenic manganese oxides. Accounts of Chemical Research, 43(1): 2-9.
Staley, J.T., Adams, J.B., Palmer, F.E., 1992. Desert varnish: a biological perspective. Soil biochemistry, 7: 173-195.
Staley, J.T., Palmer, F., Adams, J.B., 1982. Microcolonial fungi: common inhabitants on desert rocks? Science, 215(4536): 1093-1095.
Stewart-Perry, R., 1979. Chemistry and structure of desert varnish.
Stüben, D., 2007. Suitability of Mn-Oxihydroxides from Karst Caves as Filter Material for Drinking Water Treatment in Gunung Sewu, Indonesia (6 pp). Journal of Soils and Sediments, 7(1): 53-58.
Sunda, W., Huntsman, S., Harvey, G., 1983. Photoreduction of manganese oxides in seawater and its geochemical and biological implications.
Sunda, W.G., Kieber, D.J., 1994. Oxidation of humic substances by manganese oxides yields low-molecular-weight organic substrates.
Taylor-George, S. et al., 1983. Fungi and bacteria involved in desert varnish formation. Microbial Ecology, 9(3): 227-245.
Tebo, B.M. et al., 2004. Biogenic manganese oxides: Properties and mechanisms of formation. Annual Review of Earth and Planetary Sciences, 32: 287-328.
Tebo, B.M., Ghiorse, W.C., Van Waasbergen, L.G., Siering, P.L., Caspi, R., 1997. Bacterially mediated mineral formation; insights into manganese (II) oxidation from molecular genetic and biochemical studies. Reviews in Mineralogy and Geochemistry, 35(1): 225-266.
Tebo, B.M., Johnson, H.A., McCarthy, J.K., Templeton, A.S., 2005. Geomicrobiology of manganese (II) oxidation. TRENDS in Microbiology, 13(9): 421-428.
Thiagarajan, N., Lee, C.T.A., 2004. Trace-element evidence for the origin of desert varnish by direct aqueous atmospheric deposition. Earth and Planetary Science Letters, 224(1-2): 131-141.
Toner, B., Fakra, S., Villalobos, M., Warwick, T., Sposito, G., 2005. Spatially resolved characterization of biogenic manganese oxide production within a bacterial biofilm. Applied and environmental microbiology, 71(3): 1300-1310.
Uchida, E., Watanabe, R., Osawa, S., 2016. Precipitation of manganese oxides on the surface of construction materials in the Khmer temples, Cambodia. Heritage Science, 4(1): 1.
Velde, B.B., Meunier, A., 2008. The origin of clay minerals in soils and weathered rocks. Springer Science & Business Media.
Vicenzi, E.P., Grissom, C.A., Livingston, R.A., Weldon-Yochim, Z., 2016. Rock varnish on architectural stone: microscopy and analysis of nanoscale manganese oxide deposits on the Smithsonian Castle, Washington, DC. Heritage Science, 4(26).
Villalobos, M., Bargar, J., Sposito, G., 2005. Trace metal retention on biogenic manganese oxide nanoparticles. Elements, 1(4): 223-226.
VIM, I., 2004. International vocabulary of basic and general terms in metrology (VIM). International Organization, 2004: 09-14.
Von Humboldt, A., Bonpland, A., 1819. Voyage aux régions équinoxiales du nouveau continent. II(Book VII Chapter XX): 299-304.
Wang, X., Müller, W.E., 2009. Marine biominerals: perspectives and challenges for polymetallic nodules and crusts. Trends in biotechnology, 27(6): 375-383.

Wang, X. et al., 2011. Evidence for a biogenic, microorganismal origin of rock varnish from the Gangdese Belt of Tibet. Micron, 42(5): 401-411.
Watchman, A., 1992. Cation-leaching sites in rock varnish - comment. Geology, 20(11): 1050-1052.
Watchman, A., 1993. More information about South Australian cation-ratio dates. Rock Art Research, 10(1): 40.
Watchman, A., 2000. A review of the history of dating rock varnishes. Earth-Science Reviews, 49(1): 261-277.
Wayne, D.M., Diaz, T.A., Fairhurst, R.J., Orndorff, R.L., Pete, D.V., 2006. Direct major- and trace-element analyses of rock varnish by high resolution laser ablation inductively-coupled plasma mass spectrometry (LA-ICPMS). Applied Geochemistry, 21(8): 1410-1431.
Wayne, D.M., Diaz, T.A., Orndorff, R.L., 2004. Atmospheric inputs of heavy metals and lead isotopes to rock varnish revealed by high-resolution laser ablation inductivelycoupled plasma mass spectrometry. Abstracts of Papers of the American Chemical Society, 227: U93-U93.
Wells, S., McFadden, L., 1987. Comment and Reply on "Isotopic evidence for climatic influence on alluvial-fan development in Death Valley, California" COMMENT. Geology, 15(12): 1178-1178.
Whalley, W.B., Gellatly, A.F., Gordon, J.E., Hansom, J.D., 1990. Ferromanganese rock varnish in North Norway: a subglacial origin. Earth Surface Processes and Landforms, 15(3): 265-275.
White, W.B., Vito, C., Scheetz, B.E., 2009. The mineralogy and trace element chemistry of black manganese oxide deposits from caves. Journal of Cave and Karst Studies, 71(2): 136-143.
Whitley, D.S., 2009. Cave paintings and the human spirit: the origin of creativity and belief. Prometheus Books.
Whitley, D.S., 2012. In Suspect Terrain: Dating Rock Engravings. A Companion to Rock Art: 605-624.
Whitley, D.S., 2013. Rock art dating and the peopling of the Americas. Journal of Archaeology, 2013.
Whitney, J., Harrington, C., Glancy, P., 1988. Deciphering Quaternary alluvial history in Las Vegas Wash, Nevada by radiocarbon and rock varnish dating, Geological Society of America Abstracts with Programs, pp. 243.
Zeng, X., Mao, X., Greif, R., Russo, R., 2005. Experimental investigation of ablation efficiency and plasma expansion during femtosecond and nanosecond laser ablation of silicon. Applied Physics A, 80(2): 237-241.
Zerboni, A., 2008. Holocene rock varnish on the Messak plateau (Libyan Sahara): Chronology of weathering processes. Geomorphology, 102(3-4): 640-651.
Zhou, B., Liu, T., Zhang, Y., 2000. Rock varnish microlaminations from northern Tianshan, Xinjiang and their paleoclimatic implications. Chinese Science Bulletin, 45(4): 372-376.

Appendix A

List of Publications

Published:

Macholdt, D.S., Jochum, K.P., Stoll, B., Weis, U., and Andreae, M.O. (2014) *A new technique to determine element amounts down to femtograms in dust using femtosecond laser ablation-inductively coupled plasma-mass spectrometry*. Chemical Geology 383, 123-131. DOI: 10.1016/j.chemgeo.2014.06.001

Macholdt, D., Jochum, K.P., Pöhlker, C., Stoll, B., Weis, U., Weber, B., Müller, M., Kappl, M., Buhre, S., Kilcoyne, A.L.D., Weigand, M., Scholz, D., Al-Amri, A.M., and Andreae, M.O. (2015) *Microanalytical methods for in-situ high-resolution analysis of rock varnish at the micrometer to nanometer scale*. Chemical Geology 411, 57-68. DOI: 10.1016/j.chemgeo.2015.06.023

Macholdt, D.S., Jochum, K.P., Wilson, S.A., Otter, L.M., Stoll, B., Weis, U., and Andreae, M.O. (2016) *Suitability of Mn-and Fe-Rich Reference Materials for Microanalytical Research*. Geostandards and Geoanalytical Research, 40, 493-504. DOI: 10.1111/ggr.12119

Jochum, K.P., Wilson, S.A., Becker, H., Garbe-Schönberg, D., Groschopf, N., Kadlag, Y., Macholdt, D.S., Mertz-Kraus, R., Otter, L., and Stoll, B. (2016) *FeMnOx-1: A new microanalytical reference material for the investigation of Mn–Fe rich geological samples.* Chemical Geology 432, 34-40. DOI:10.1016/j.chemgeo.2016.03.026

Macholdt, D.S., Jochum, K.P., Pöhlker, C., Arangio, A., Förster, J.D., Stoll, B., Weis, U., Weber, B., Müller, M., Kappl, M., Shiraiwa, M., Kilcoyne, A.L.D., Weigand, M., Scholz, D., Haug, G., and Andreae, M.O. *Characterization and differentiation of rock varnish types from different environments by microanalytical techniques*. Chemical Geology 495, 91-118. DOI: 10.1016/j.chemgeo.2017.04.009

Submitted:

D.S. Macholdt, S. Herrmann, K.P. Jochum, A.L.D. Kilcoyne, T. Laubscher, J.H.K. Pfisterer, C. Pöhlker, B. Schwager, B. Weber, M. Weigand, K.F. Domke, and M.O. Andreae. *Investigations of black manganese-rich crusts on a cathedral.* Submitted to Atmospheric Environment

Bettina Weber, Jost V. Lavric, Noel van Rooyen, Dorothea S. Macholdt, Margaretha W. van Rooyen, Yvette Naude, and Sabine Fiedler. *Social insects unlikely to cause fairy circles.* Submitted to Nature

Le Thi-Thu Huong, Laura M. Otter, Michael W. Förster, Kurt Krenn, Christoph A. Hauzenberger, Dorothea S. Macholdt, Ulrike Weis, Brigitte Stoll, and Klaus Peter Jochum. *Trace-element chemistry and Raman spectroscopy of danburite from Mexico, Tanzania and Vietnam.* Submitted to Chemie der Erde/Geochemistry

To be submitted:

Otter, L.M., Macholdt, D.S., Jochum, K.P., Stoll, B., Weis, U., Weber, B., Al-Amrid, A.M., Haug, G.H., and Andreae, M.O. *New Insights on the Relationship between Rock Varnish and Adjacent Mineral Dust Compositions.* Prepared for Geochimica et Cosmochimica Acta

Naama Lang-Yona, Stefanie Maier, Dorothea S. Macholdt, Meinrat Andreae, Emilio Rodriguez-Caballero, Isabel Müller-Germann, Petya Yordanova, Ulrich Pöschl, Bettina Weber, and Janine Fröhlich-Nowoisky. *Biological Communities Hinting on Desert Varnish Formation Mechanism.* Prepared for Nature Microbiology

List of Abstracts for International Conferences

2014

D.S. Macholdt, K.P. Jochum, B. Stoll, U. Weis, M.O. Andreae (2014) *A new Technique to Determine Femtogram Amounts of Trace Elements in Dust using 200 nm fs-LA-ICP-MS and 213 nm ns-LA-ICP-MS*. European Workshop on Laser Ablation, London, England

Macholdt D, Jochum KP, Stoll B, Weis U, Weber B, Pöhlker C & Andreae M (2014) *Rock Varnish from Different Locations: An Insight into the Genesis Using in situ Analytical Methods*. Goldschmidt Conference, Sacramento, USA

Jochum K, Macholdt D, Stoll B, Weis U, Jacob D, Mertz-Kraus R & Andreae M (2014) *Non-Matrix-Matched Calibration of Femtosecond LA-ICP-MS Applied to Geochemical and Environmental Analysis*. Goldschmidt Conference, Sacramento, USA

Dorothea Macholdt, Brigitte Stoll, Ulrike Weis, Klaus Peter Jochum, Meinrat O. Andreae (2014) *Analysis of Rock Varnish from Different Locations*. Conference on Earth System Science, Jena, Germany

Meinrat O Andreae , Abdullah Mohammed Al-Amri, Klaus P Jochum, Michael Kappl, A David Kilcoyne, Dorothea Macholdt, Maren Müller, Christopher Pöhlker, Bettina Weber, Markus Weigand (2014) *Searching for Life in Death Valley (and Other Deserts) – Microchemical Investigations on Desert Varnish.* AGU conference, San Francisco, USA

Dorothea Macholdt , Meinrat O Andreae, Klaus P Jochum, Michael Kappl, A.L. David Kilcoyne, Maren Müller, Christopher Pöhlker, Brigitte Stoll, Bettina Weber, Markus Weigand, Ulrike Weis (2014) *Combining fs LA-ICP-MS, FIB and STXM-NEXAFS Methods for in-situ High-Spatial-Resolution Rock Varnish Analyses at the nm to µm Scale*. AGU conference, San Francisco, USA

2015

Dorothea S. Macholdt, Klaus Peter Jochum, Brigitte Stoll, Ulrike Weis, Laura Otter, Meinrat O. Andreae (2015) *The search for suitable reference materials for microanalytical analyses of Mn rich samples*. Geoanalysis Conference, Leoben, Austria

Brigitte Stoll, Klaus Peter Jochum, Ulrike Weis, Dorothea Macholdt, Meinrat O. Andreae (2015) *Advantages and disadvantages of femtosecond 200 nm laser ablation-ICP-mass spectrometry for trace element analysis*. Geoanalysis Conference, Leoben, Austria

Macholdt DS, Jochum KP, Stoll B, Weis U, Otter LM, Pöhlker C, Weber B, Müller M, Kappl M, DiGregorio BE, Al-Amri A, Andreae MO (2015) *Microanalytical Investigations of Rock Varnish from Different Regions*. Goldschmidt Conference, Prague, Czech Republic

Otter LM, Macholdt DS, Jochum KP, Stoll B, Weis U, Weber B, Scholz D, Al-Amri A & Andreae MO (2015) *Desert Varnish and Dust: Nano- and Femtosecond LA-ICP-MS Studies of Major and Trace Elements*. Goldschmidt Conference, Prague, Czech Republic

Jochum K, Macholdt D, Otter L, Pöhlker C, Weber B, Stoll B, Weis U, Al-Amri A, Müller M, Kappl M & Andreae M (2015) *Highly Resolved Mn/Fe Microanalyses in Desert Varnish for Paleoclimate Reconstruction*. Goldschmidt Conference, Prague, Czech Republic

K.P Jochum, B. Stoll, U. Weis, D. Macholdt, L. Otter and M.O. Andreae (2015) *High-resolution measurements using femtosecond and nanosecond LA-ICP-MS and its application in paleoclimate research*. 6th Asia-Pacific Winter Conference on Plasma-Spectrochemistry, Xiamen, China

Dorothea Macholdt, Klaus P Jochum, Laura Otter, Brigitte Stoll, Ulrike Weis, Christopher Pöhlker, Maren Müller, Michael Kappl, Bettina Weber, A.L. David Kilcoyne, Markus Weigand, Abdullah Mohammed Al-Amri and Meinrat O Andreae (2015) *Relationship between Rock Varnish and Adjacent Mineral Dust Compositions Using Microanalytical Techniques*. AGU conference, San Francisco, USA

2016

Livingston, R.A., Grissom, C.A., Vicenzi, E.P., Weldon-Yochim, Z.A., Little, N.C., Douglas, J.G., Fowler, A.J., Santelli, C.M., Macholdt, D.S., Ortiz-Montalvo, D.L. and Watson, S.S. (2016). *Investigation of urban rock varnish on the sandstone of the Smithsonian Castle.* 13th Congress on Stone Deterioration and Conservation, Glasgow, Scotland

Jochum KP, Macholdt D, Zipfel J, Stoll B, Weis U, Haug G & Andreae M (2016) *Fe/Mn and Trace Elements in Layered Varnish on Meteorites for Paleoclimate Investigations*. Goldschmidt Conference, Yokohama, Japan

Macholdt DS, Poehlker C, Foerster J-D, Weber B, Kilcoyne ALD, Weigand M, Mueller M, Lieberwirth I, Jochum KP, Kappl M, Haug G & Andreae MO (2016) *STXM-NEXAFS and fs LA-ICP-MS Investigations of Rock Varnish*. Goldschmidt Conference, Yokohama, Japan

K.P. Jochum, R. Schiebel, D.S. Macholdt, U. Weis, B. Stoll, G.H. Haug and M.O. Andreae (2016) *High-resolution Analyses using Femto- and Nanosecond Laser Ablation-ICP-Mass Spectrometry (and the need for micro-analytical reference materials)*. European Workshop on Laser Ablation, Ljubljana, Slovenia

Ulrike Weis, Klaus P. Jochum, Dorothea S. Macholdt, Brigitte Stoll, Gerald H. Haug and Meinrat O. Andreae (2016) *Mn-Fe-rich Microanalytical Reference Material for LA-ICPMS*. European Workshop on Laser Ablation, Ljubljana, Slovenia

Jochum, K.P., Macholdt, D.S., Weis, U., Stoll, B., Haug, G.H. and Andreae, M.O. (2016) *Femtosecond laser ablation – ICP mass spectrometry: a powerful high-resolution method for in-situ trace element and isotope ratio measurements in climate geochemistry*. International Geological Congress, Cape Town, South Africa

Macholdt, D.S., Pöhlker, C., Förster, J.D., Weber, B., Kilcoyne, A.L.D., Weigand, M., Müller, M., Lieberwirth, I., Jochum, K.P., Kappl, M., Haug, G., and Andreae, M.O. (2016) *STXM-NEXAFS: applying a new technique which helps to unravel the mystery of rock varnish*. International Geological Congress, Cape Town, South Africa

Huong, L.T.T., Otter, L.M., Macholdt, D.S., Foerster, M.W., Stoll, B., Weis, U., Jochum, K.P. (2016) *Discrimination of danburite from different deposits by chemical components: a femtosecond LA-ICP-MS study*. International Geological Congress, Cape Town, South Africa

Macholdt, D.S., Pöhlker, C., Jochum, K.P., Förster, J.D., Weber, B., Kilcoyne, A.L.D., Weigand, M., Müller, M., Kappl, M., Scholz, D., Haug, G., and Andreae, M.O. (2016) *STXM-NEXAFS measurements of rock varnish, investigating element distributions and carbon occurrences in the Mn-rich rock coating*. AGU Conference, San Francisco, USA

2017

Naama Lang-Yona, Stefanie Maier, Dorothea Macholdt, Klaus-Peter Jochum, Emilio Rodriguez-Caballero, Isabel Müller-Germann, Petya Yordanova, Meinrat O. Andreae, Ulrich Pöschl, Bettina Weber, and Janine Fröhlich-Nowoiskya (2017). *Biological Communities On and Within Desert Varnish and Potential Implications for Varnish Formation Mechanisms.* EGU Conference, Vienna, Austria

K.P. Jochum, R. Schiebel, B. Stoll, U. Weis, D.S. Macholdt, G.H. Haug (2017) *Highly resolved determination of Mg/Ca ratios in single foraminifera shells using fs-LA-ICP-MS.* Goldschmidt Conference, Paris, France

D.S. Macholdt, S. Herrmann, K.P. Jochum,A. L. D. Kilcoyne, T. Laubscher, J. Pfisterer, C. Pöhlker, B. Schwager, B. Weber, M. Weigand, K. F. Domke, M.O. Andreae (2017). *Black, anthropogenic, manganese-rich crusts on the Freiburg Minster.* Goldschmidt Conference, Paris, France

Appendix B

B.1: A new technique to determine element amounts down to femtograms in dust using femtosecond laser ablation-inductively coupled plasma-mass spectrometry

Macholdt, D.S., Jochum, K.P., Stoll, B., Weis, U. and Andreae, M.O. (2014) *A new technique to determine element amounts down to femtograms in dust using femtosecond laser ablation-inductively coupled plasma-mass spectrometry*. Chemical Geology 383, 123-131. DOI: 10.1016/j.chemgeo.2014.06.001

B.2: Microanalytical methods for in-situ high-resolution analysis of rock varnish at the micrometer to nanometer scale

Macholdt, D.S., Jochum, K.P., Pöhlker, C., Stoll, B., Weis, U., Weber, B., Müller, M., Kappl, M., Buhre, S., Kilcoyne, A.L.D., Weigand, M., Scholz, D., Al-Amri, A.M., and Andreae, M.O. (2015) *Microanalytical methods for in-situ high-resolution analysis of rock varnish at the micrometer to nanometer scale*. Chemical Geology 411, 57-68. DOI: 10.1016/j.chemgeo.2015.06.023

B.3: Suitability of Mn- and Fe-Rich Reference Materials for Microanalytical Research

Macholdt, D.S., Jochum, K.P., Wilson, S.A., Otter, L.M., Stoll, B., Weis, U., and Andreae, M.O. (2016) *Suitability of Mn- and Fe-Rich Reference Materials for Microanalytical Research*. Geostandards and Geoanalytical Research Vol. 40 – N°4, 493-504.. DOI: 10.1111/ggr.12119

B.4: Characterization and differentiation of rock varnish types from different environments by microanalytical techniques

Macholdt, D.S., Jochum, K.P., Pöhlker, C., Arangio, A., Förster, J.D., Stoll, B., Weis, U., Weber, B., Müller, M., Kappl, M., Shiraiwa, M., Kilcoyne, A.L.D., Weigand, M., Scholz, D., Haug, G.H., Al-Amri, A., and Andreae, M.O. submitted to Chemical Geology. *Characterization and differentiation of rock varnish types from different environments by microanalytical techniques*. Chemical Geology 495, 91-118. DOI: 10.1016/j.chemgeo.2017.04.009

B.5: Investigations of black manganese-rich crusts on a cathedral

D.S. Macholdt, S. Herrmann, K.P. Jochum, A.L.D. Kilcoyne, T. Laubscher, J.H.K. Pfisterer, C. Pöhlker, B. Schwager, B. Weber, M. Weigand, K.F. Domke, and M.O. Andreae. *Investigations of black manganese-rich crusts on a cathedral.* Submitted to Atmospheric Environment

B.1

Macholdt et al., Chem. Geology, 2014

A new technique to determine element amounts down to femtograms in dust using femtosecond laser ablation-inductively coupled plasma-mass spectrometry

Dorothea S. Macholdt[a], Klaus Peter Jochum[a], Brigitte Stoll[a], UlrikeWeis[a], Meinrat O. Andreae[a]

a Max Planck Institute for Chemistry, Biogeochemistry Department, P. O. Box 3060, 55020 Mainz, Germany

Chemical Geology 383, 123-131. DOI: 10.1016/j.chemgeo.2014.06.001

Chemical Geology 383 (2014) 123–131

Contents lists available at ScienceDirect

Chemical Geology

journal homepage: www.elsevier.com/locate/chemgeo

A new technique to determine element amounts down to femtograms in dust using femtosecond laser ablation-inductively coupled plasma-mass spectrometry

Dorothea S. Macholdt *, Klaus Peter Jochum, Brigitte Stoll, Ulrike Weis, Meinrat O. Andreae

Max Planck Institute for Chemistry, Biogeochemistry Department, P. O. Box 3060, 55020 Mainz, Germany

ARTICLE INFO

Article history:
Received 17 March 2014
Received in revised form 30 May 2014
Accepted 1 June 2014
Available online 10 June 2014

Editor: Michael E. Böttcher

Keywords:
Femtosecond LA-ICP-MS
Sahara dust
2D-distribution map
Trace elements
Low sample amount

ABSTRACT

Atmospheric dust has a substantial impact on climate, and climate in turn affects the dust flux and origin. Knowing its composition helps to determine dust sources and climate processes. We have therefore determined 46 major and trace elements in dust samples, using in-situ 200 nm-femtosecond laser ablation-inductively coupled plasma-mass spectrometry (LA-ICP-MS). Very small test portions of 4–7 μg were enough to enable analyses down to detection limits of femtograms and ng g^{-1}, respectively. The data agree within 40 to 15% with the reference values for test portions of 1 to 100 μg, respectively. The femtosecond laser results are compared to those obtained using a 213 nm nanosecond laser, which show the advantages of the femtosecond laser, such as the ability to use non-matrix-matched calibration, reliable measurements of volatile elements, and smaller quantities of material ablation with similar results for the repeatability. The technique is especially useful for measurements of small amounts of dust on filters, and for 2D-distribution maps of selected elements to identify minerals or contamination. To demonstrate the applicability, five dust samples from Niger and Chad, in the Sahara zone, were analyzed. The samples are characterized by enrichment in light REEs and a distinct Eu anomaly, with surface soils as their source.

1. Introduction

For paleoclimatology, tephrochronology, and environmental geology, dust analysis is an important research field. Dust affects the climate indirectly as well as directly. It acts as a nucleus for clouds droplets and ice particles, and can reflect and absorb radiation from the sun and from the Earth (e.g., Andreae and Rosenfeld, 2008). In particular, the arid Sahara and the semiarid Sahel of Africa are the most important dust sources of the global dust budget. They provide 58% of the total global dust emission and 62% of the total global dust load in the atmosphere (Tanaka and Chiba, 2006). This dust has a substantial impact on human health (Giannadaki et al., 2014). It also provides essential nutrients to the ocean and therefore affects marine biological productivity and, through this, the climate (Maher et al., 2010). Its impact reaches far beyond North Africa, due to frequent long-range transports across the Atlantic Ocean, the Mediterranean Sea and the Red Sea (Goudie and Middleton, 2001). To identify the origin of dust, major and trace elements are investigated and compared to dust samples from different regions (Rea, 1994; Scheuvens et al., 2013). Trace elements are of particular interest, since they are, compared to major elements, less affected by weathering processes (Taylor and McLennan, 1985). Especially the rare-earth elements (REEs) are highly immobile during these processes, with the exception of Eu and Ce for some redox environments. For this purpose different analytical techniques have been used, e.g., proton-induced X-ray emission (PIXE: Marino et al., 2008; Lucarelli et al., 2010), thermal ionization mass spectrometry (TIMS: Grousset et al., 1998; Meyer et al., 2001; Abouchami and Zabel, 2003; Skonieczny et al., 2011), inductively coupled plasma-atomic emission spectroscopy (ICP-AES: Schwikowski et al., 1995; Moreno et al., 2006; Castillo et al., 2008), inductively coupled plasma-mass spectrometry (ICP-MS: Ganor et al., 1991; Meyer et al., 2001; Moreno et al., 2006; Castillo et al., 2008), X-ray fluorescence spectroscopy (XRF: Sterling et al., 2000), atomic absorption spectroscopy (AAS: Adedokun et al., 1989; Ganor et al., 1991), instrumental neutron activation analysis (INAA: Ganor et al., 1991), X-ray diffraction (XRD: Rea, 1994; Moreno et al., 2006), scanning electron microscopy with energy-dispersive X-ray analysis (SEM-EDX: Laskin et al., 2006; Moreno et al., 2006) and scanning transmission X-ray microscopy–near edge X-ray absorption fine structure spectroscopy (STXM–NEXAFS: Moffet, 2011). Detailed information on detection limits and sample amounts needed are given by Formenti et al. (2011). PIXE is a method used for minimum sample material, but the measurement accuracy is limited for inhomogeneous samples with heterogeneous matrices (Pavićević and Amthauer, 2000) and elemental distribution maps are not possible. With PIXE, samples of 1–2 μg cm^{-2} (Lucarelli et al., 2010) can be analyzed down to ng cm^{-2}

* Corresponding author. Tel.: +49 6131 305 6705.
E-mail address: d.macholdt@mpic.de (D.S. Macholdt).

http://dx.doi.org/10.1016/j.chemgeo.2014.06.001
0009-2541/

(Marino et al., 2008). Individual dust particles in the size of micrometers can also be analyzed with PIXE, as well as by other single-particle techniques such as SEM-EDX or STXM–NEXAFS. In contrast, TIMS delivers high precision trace element results, but usually requires 20–50 mg of material (Grousset et al., 1998; Abouchami and Zabel, 2003; Skonieczny et al., 2011).

For the analysis of dust, a multi-element analysis method with good sensitivity and reasonable measurement accuracy is required. It should be able to handle small sample quantities, since the sample material is usually limited due to the small amount found on dust filters or in cores. Laser ablation inductively coupled plasma mass spectrometry (LA-ICP-MS) has so far scarcely been used for dust analysis (Abouchami et al., 2013), although it meets most of these requirements, e.g., through in-situ measurements of 46 major and trace elements with high detection power and without sample dissolution. Until now, there has been no report on femtosecond (fs) LA-ICP-MS analysis, which allows a matrix-independent calibration (Poitrasson et al., 2003; Shaheen et al., 2012; Velasquez et al., 2012; Jochum et al., 2014), performed on dust samples. The aim of this paper is to establish this new fs LA-ICP-MS technique for the analysis of small quantities of dust samples, and to compare it to conventional nanosecond (ns) LA-ICP-MS.

2. Analytical

2.1. Samples

Five samples of natural dust, which had been collected in September 2010 in the Sahara zone from dust deposits in Chad and Niger (Abouchami et al., 2013), were used for this work. The "Harmattan Dust" (H) came from near Niamey, Niger (13° 29.492′ N 2° 10.189′ E), and was accumulated during a single wintertime dust event. This reddish, very finely grained (10–100 μm) dust contains a visible amount of organic matter, such as microscopic grass particles. It looks very similar to the "MIT radar site Dust" (R) from the same location, which was accumulated during several wet and dry seasons. The "Faya Largeau Dust" (FL) from Chad (17° 56.113′ N 19° 06.743′ E) has a gray color and different grain sizes. It contains bigger grains (mm range) in a matrix of a finely grained material (<100 μm), very similar to "Mao Dust" (M) from Chad (14° 07.704′ N 15° 18.753′ E). The "Nguimi Police Station Dust" (N) from Niger (14° 15.175′ N 13° 06.878′ E) has a gray color and is finely grained (<100 μm) without bigger grains. Relatively large amounts (~mg) of these samples have been previously analyzed for major and trace element mass fractions in fused samples by EMPA and ns LA-ICP-MS, respectively (Abouchami et al., 2013).

In addition to the dust samples, powdered rock reference materials with particle sizes below 74 μm were analyzed to ensure the measurement accuracy of the analysis: W-1 (diabase) and BCR-2 (basalt) from the U.S. Geological Survey (USGS), a powdered T1-G (diorite glass) from the MPI-DING, and JG-1a (granodiorite) from the Geological Survey of Japan (GSJ) (details of these samples can be found in the GeoReM database http://georem.mpch-mainz.gwdg.de). The silicate reference glasses NIST SRM 612 (Jochum et al., 2011; NIST, 2012) and GSD-1G (Jochum et al., 2007; GeoReM preferred values) were used for calibration purposes.

2.2. Sample preparation

All samples were mounted, without grain size sorting, on a double-sided adhesive tape, which was affixed to an iridium strip. Iridium was chosen since this noble metal is not present in dust, and therefore possible contamination from the strip can generally be easily distinguished from dust sample material. LA-ICP-MS analyses of the strip and tape show that the mass fractions of most elements are close to the detection limits of 0.001–0.01 μg g^{-1}. Significant exceptions are listed in Table 1. In geological materials, most of these elements are much more abundant (>factor of 10–10,000, see Fig. 1), reducing the impact of the background on the measurement. Only Zn has such high values in the tape (up to 3000 μg g^{-1}), that it cannot be reliably measured in the dust samples.

Table 1
Analytical results for the tape and strip combination.

Mg	<300 μg g^{-1}
Al	<400 μg g^{-1}
Si	<5000 μg g^{-1}
Ca	<2000 μg g^{-1}
Cr	<10 μg g^{-1}
Fe	<40 μg g^{-1}
Zn	<3000 μg g^{-1}
Sr	<5 μg g^{-1}
Ba	<5 μg g^{-1}
Others	0.001–0.1 μg g^{-1}
Ir[a]	1–100 μg g^{-1}

[a] Ir is the major component of the strip.

Two different techniques were performed:

(1) Determination of mass fractions of trace elements by covering the whole surface of the tape (about 0.01–0.2 cm^2) with sample amounts of about 100–800 μg. Subsequent measurements can be conducted either of parts of the prepared area to test the homogeneity of the dust samples collected, or of the whole surface area in order to determine element amounts per area.
(2) Element mapping for the identification and localization of μm-sized minerals by scanning the tape and examining selected elements of interest.

2.3. Mass spectrometer and lasers

Measurements were carried out at the Max Planck Institute for Chemistry, Mainz, Germany. A combination of a ThermoFisher Element2 single-collector sector-field ICP-mass spectrometer and an Electro Scientific Industries (ESI) fs laser ablation system, NWR-Femto with a wavelength of 200 nm, producing laser pulses at 150 fs, was used (Jochum et al., 2014). In addition, a New Wave UP213 Nd:YAG laser ablation system with a wavelength of 213 nm, producing laser pulses of 5 ns, was coupled to the Element2 ICP-MS (Jochum et al., 2007). Important parameters of the ICP-MS and the lasers are listed in Tables 2 and 3. Laser ablation was conducted in a He atmosphere. This carrier gas was mixed with an Ar gas flow to transport the aerosol generated by laser ablation. The washout time was 45 s, and the blank count rate was determined prior to each ablation for ca. 21 s. The ion intensities were determined in the low mass resolution mode with flat top peaks. Thirty-eight trace elements and 8 major elements were determined by measuring 36 times all selected elements per line scan; the measuring time for one element cycle (time per pass) was about 1.6 s. One analysis consisted of the average of three line scans.

Measurements of parts of the prepared sample were made at a relatively high scan speed of 30 μm s^{-1}, since scan speeds less than 30 μm s^{-1} have the disadvantage of significant ablation of the adhesive tape and the Ir strip. The measurements of the large surface areas for element mapping, with less distributed sample material, were conducted with an even higher speed of 80 μm s^{-1} to avoid contamination by the tape and strip, since the sample amounts were significantly smaller. 78 line scans were performed at 80 μm s^{-1} for sample BCR-2, 72 for sample H, and 47 for sample FL.

2.4. Evaluation of data

The major element Si was taken as internal standard, since the background from the tape and Ir strip is about two orders of magnitude lower than the average Si content in dust (for comparison Tables 1 and 6). Since the Si content is generally not known, we estimated it by measuring the isotope ion intensities of ^{25}Mg, ^{27}Al, ^{29}Si, ^{31}P, ^{43}Ca, ^{49}Ti,

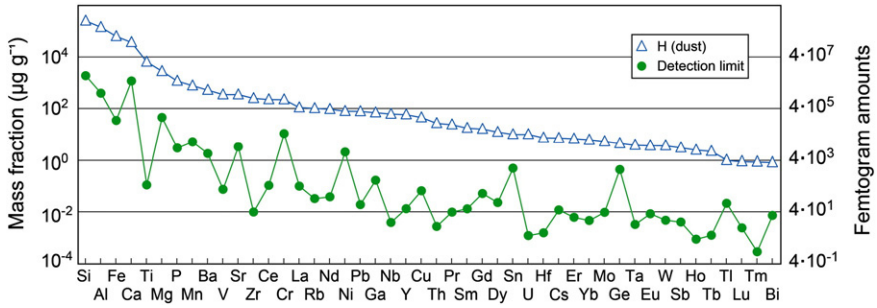

Fig. 1. Analytical data for dust sample H and detection limits of the fs LA-ICP-MS technique. Measurements were performed with a spot size of 65 µm, and a scan speed of 30 µm s^{-1}. Elements are arranged according to decreasing mass fractions in the dust sample. The femtogram amounts are calculated based on a test portion of 4 µg.

^{55}Mn and ^{57}Fe of the major elements by LA-ICP-MS, and assuming a total oxide content of 95% m m^{-1}, a procedure which is similar to that of Liu et al. (2008). The mass fractions of the major elements, including Si, agree within about 5–10% with the reference values, as demonstrated by the analysis of the reference materials W-1, BCR-2 and T1-G. The dust samples analyzed in this work give values for SiO_2 concentrations between 53 and 72% m m^{-1}, which are similar to the range found for other dust analyses (Moreno et al, 2006; Castillo et al., 2008).

The mass fraction of an element of interest, EL (mf_{EL}), was calculated by:

$$mf_{EL} = C_{Si} R_{iSi} (A_{Si}/A_i)(M_{Si}/M_i)(1/RSF) = mf_{uncorrected}(1/RSF) \quad (1)$$

where C_{Si} is the mass fraction of the internal standard Si in µg g^{-1}, and R_{iSi} is the ratio of counts of the isotope of interest, i, of the element EL, to those of the isotope 29 of the internal standard element Si. The values A_{Si} and A_i are the isotope abundances of ^{29}Si and the isotope of interest of element EL, M_{Si} and M_i the relative atomic masses of the internal standard element Si and the element EL, respectively. RSF is the relative sensitivity factor, which is defined by the ratio of the uncorrected mass fraction, $mf_{uncorrected}$, to the "true" value of the reference material. The RSFs for the different elements were determined from the analysis of the certified NIST SRM 612 reference glass assuming no matrix effect during the fs LA-ICP-MS analysis (Jochum et al., 2011; NIST, 2012). Due to the low concentrations of Fe and Ti (about 50 µg g^{-1}) in this reference material, which are much lower than those in the average dust (Moreno et al, 2006; Castillo et al., 2008), we determined the RSFs for these elements from the GSD-1G reference glass, which has a basaltic composition with high Fe (9.3% m m^{-1}) and Ti (0.8% m m^{-1}) amounts (GeoReM database http://georem.mpch-mainz.gwdg.de).

Data reduction was conducted by a programmed routine in Microsoft Excel (Jochum et al., 2007), where outliers and unusual ion intensities were rejected.

Table 2
Operating parameters used for the fs and ns laser ablation systems.

	NWR-Femto	UP213
Laser type	Ti:Sapphire	Nd:YAG
Wavelength [nm]	200	213
Pulse length	150 fs	5 ns
Energy density [J cm^{-2}]	0.8	10
Spot size used [µm]	65	110
Pulse repetition rate used [Hz]	50	10
Scanning time [s]	60	60
Scanning speed [µm s^{-1}]	30	30 and 80, respectively

Table 3
Operating parameters of the Element2 ICP-MS.

rf power [W]	1270
Cool gas flow rate [l min^{-1}]	15
Auxiliary gas flow rate [l min^{-1}]	1
Carrier gas (Ar) flow rate [l min^{-1}]	0.8
Carrier gas (He) flow rate [l min^{-1}]	0.7
Sample time [s]	0.002
Samples per peak	100
Mass window [%]	10
Time per pass [s]	1.6

3. Results

3.1. Repeatability

We determined the repeatability (expressed as RSD) of our analyses by using test portions between 1 and 200 µg. Fig. 2 shows that the RSD values are dependent on the test portion and the inhomogeneity of the sample. As expected, there is a decrease of the RSD values with increasing test portion masses. Both fs and ns data lie on the same curve, but dust analysis using fs LA-ICP-MS has the advantage that it can be performed on smaller sample quantities than using ns LA-ICP-MS. A reasonably good repeatability of 10–25% can be achieved for test portions of 1–10 µg (Fig. 2). The repeatability is even better (RSD = 5–10%) for test portions >10 µg. The reason for the relatively high uncertainty is that the test portions are very small compared to the about 100 mg sample amount proposed for an inhomogeneous rock powder with accessory minerals (Ingamells and Switzer, 1973). The RSD values for

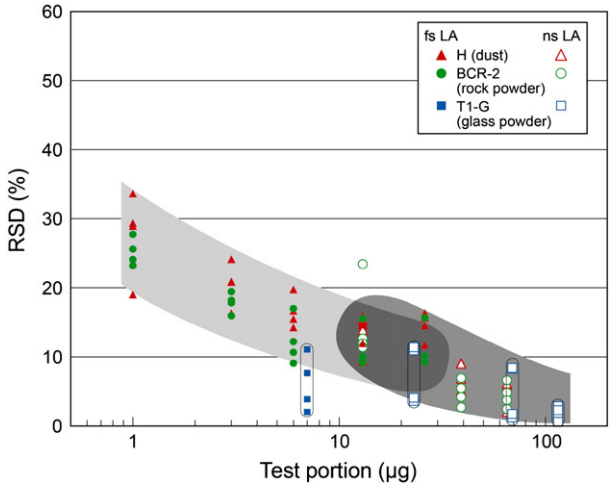

Fig. 2. Dependency of the repeatability (expressed as RSD in %) of fs LA-ICP-MS on the test portion. Data were obtained from the investigation of V, Tb, Yb and U, for which the same symbols were chosen, in dust sample H, the rock reference material BCR-2, and the powdered reference glass T1-G. Both fs and ns data have almost the same trend. Because of smaller amounts ablated at low fluence, dust analysis using fs LA-ICP-MS can be performed on smaller sample quantities than using ns LA-ICP-MS. The powdered reference glass T1-G shows lower RSD values because of the more homogeneous distribution of elements in glass samples.

the powdered homogeneous T1-G reference glass are lower than those for the inhomogeneous dust samples (Fig. 2).

3.2. Detection limit

The detection limit, DL, is defined as the smallest mass fraction that can be distinguished from the background signal at a specified confidence level (Potts, 2012), here defined as three times the standard deviation of the blank values of the measurements. The detection limits are mainly dependent on the isotopic abundance, the elemental sensitivity, the blank of the element of interest, and the operating parameters used (e.g., spot size and scan speed). The DLs range between about 0.1 and 1000 μg g^{-1} for major elements (Fig. 1) and between 0.3 and 10,000 ng g^{-1} for trace elements (Fig. 1 and Table 4). The DLs for the absolute amounts of the trace elements vary between about 1 and 40,000 fg (Table 4).

Converted to absolute amounts, the detection limits would be 1–10 fg for Tb, Ho, Tm, Lu, Hf and U, 10–100 fg for Y, Zr, Nb, Mo, Sb, Cs, Pr, Sm, Eu, Dy, Er, Yb, Ta, W, Tl, Pb, Bi and Th, 100–1000 fg for V, Cu, Ga, Rb, La, Ce, Nd, and Gd and >1000 fg for Cr, Ni, Ge, Sr, Sn and Ba.

3.3. Measurement accuracy

To evaluate the quality of the measurements, the overall analytical uncertainty at the 95% confidence level was determined. This term includes the "true" value within a probability of 95% and is defined by the closeness of the agreement between a measured value and the true value of a quantity (Potts, 2012).

The relative analytical uncertainty, $U_{EL,\ rel}$, is calculated by:

$$U_{EL,\ rel} = k * \left(u^2_{EL/Si,\ sample,\ rel} + u^2_{EL/Si\ NIST\ 612,\ rel} + u^2_{Si,\ rel} + u^2_{RV,\ rel} + u^2_{MX,\ rel} + u^2_{M,\ rel}\right)^{1/2} \quad (2)$$

where $k = 2$ is the coverage factor. The term $u_{EL/Si,\ sample,\ rel}$ is the relative uncertainty of the measured mass fraction ratio of the element EL to the internal standard element Si. This term includes the sample heterogeneity, which is large for small amounts of dust (RSE up to 20% for test portions of 1 μg). The term $u_{EL/Si\ NIST\ 612,\ rel}$ is the relative uncertainty of the measured mass fraction ratio of the element EL to the internal standard element Si in the certified reference material NIST SRM 612. This value is low (RSE ~ 1–5%) since the number of reference measurements is high.

The relative uncertainty of the internal standard element Si, $u_{Si,\ rel}$, is assumed to be around 7%, as explained in Section 2.4. The term $u_{RV,\ rel}$ describes the relative uncertainty of the certified values of NIST SRM 612 for an element, which is between 0.2% and 10% (Jochum et al., 2011). The relative contribution of the matrix to the uncertainty, $u_{MX,\ rel}$, is not detectable for the fs LA-ICP-MS used, and therefore smaller than the measurement error. It is set as 2%, a value derived from Jochum et al. (2014) for the same instrument.

To calculate the overall relative uncertainty at the 95% confidence level for the absolute mass values of an element, the possible errors during the weighing of the sample in ($u_{M,\ rel}$) have to be considered in addition. It is a further summand in Eq. (2), which is 0 for calculations of the overall relative uncertainty for mass fractions. The uncertainty due to weighing is about 10% for sample amounts in the μg range, using a Sartorius model 1712 balance.

Typical overall relative uncertainties of mass fractions and absolute masses at the 95% confidence level are listed in Table 5 for different test portions. Table 6 shows the uncertainties of each element from all measured dust samples, Appendix A (supplementary data) contains the values for the reference samples.

To test the measurement accuracy determined using Eq. (2), we compared our results for the powdered rock reference materials T1-G, W-1, and BCR-2 (Appendix A) with the reference values (Jochum et al., 2005; GeoReM database http://georem.mpch-mainz.gwdg.de). This resulted in relative overall analytical uncertainty values, $U_{EL,\ rel}$, of about 15% for BCR-2, W-1, and T1-G (see Appendix A). The deviation of the LA-ICP-MS values from the reference values is about 25% for test portions between 4 and 21 μg (see Fig. 3). No significant difference can be seen between the femtosecond and the nanosecond laser results. There are some outliers, such as for Mo, which are especially obvious for BCR-2. The Mo values of the BCR-2 sample that diverge from the reference value are caused by a heterogeneous distribution of this element due to contamination during the pulverization process of this rock reference material by the USGS (Jochum and Nohl, 2008; Borisova et al., 2010) (Fig. 4d). The homogeneity of elements in the pulverized glass reference material T1-G is better than that in the rock reference materials, which is shown by RSD values of about 12% for both fs and ns lasers. The deviations of some elements, e.g., Cu, Zr, Hf, and Pb in the rock powders are relatively high, which may be caused by a heterogeneous distribution of accessory minerals (e.g., zircon) or micrometer-size mineral inclusions in the powdered reference glass T1-G (for heterogeneities in reference materials see Borisova et al., 2010).

The average deviation of 25% agrees well with the reproducibility of the LA-ICP-MS measurements of 25%, demonstrating that the term, $u_{EL/Si,\ sample,\ rel}$, which includes the uncertainty due to the sample heterogeneity at extremely low test portions, is the most important term for the overall analytical uncertainty in Eq. (2).

Table 4
Detection limits of fs LA-ICP-MS (spot size = 65 μm; scan speed = 30 μm s^{-1}) for a test portion of 4 μg. Data were evaluated from blank measurements of the tape without sample material.

	[ng g^{-1}]	[pg]		[ng g^{-1}]	[fg]
V	80	0.3	La	100	400
Cr	10,000	40	Ce	100	400
Ni	2000	8	Pr	10	40
Cu	70	0.28	Nd	40	160
Ga	200	0.8	Sm	10	40
Ge	400	1.6	Eu	8	32
Rb	30	0.12	Gd	50	200
Sr	3000	12	Tb	1	4
Y	10	0.04	Dy	20	80
Zr	10	0.04	Ho	0.9	3.2
Nb	4	0.016	Er	6	24
Mo	9	0.036	Tm	0.3	1.2
Sn	500	2	Yb	5	20
Sb	4	0.016	Lu	2	8
Cs	10	0.04	Hf	2	8
Ba	2000	8	Ta	3	12
			W	5	20
			Tl	20	80
			Pb	20	80
			Bi	7	28
			Th	3	12
			U	1	4

Table 5
Relative overall analytical uncertainties (in %) for mass fractions (a) and absolute amounts (b) using different test portions. For abbreviations of the uncertainty terms see Eq. (2).

Test portion [μg]	1	10	50	100
	Uncertainty [%]			
a) Mass fractions				
$u_{EL/Si,\ sample,\ rel}$	20	10	5	3
$u_{Si,\ rel}$	7	7	7	7
$u_{EL/Si\ NIST\ 612,\ rel}$	1	1	1	1
$u_{RV,\ rel}$	2	2	2	2
$u_{MX,rel}$	2	2	2	2
$U_{EL,\ rel}$	40	25	20	15
b) Absolute amounts				
$u_{EL,\ rel}$	40	25	20	15
$u_{M,\ rel}$	10	10	10	10
$U^*_{EL,\ rel}$	45	35	30	25

Table 6
Trace element data of dust samples using fs LA-ICP-MS (spot size = 65 μm; scan speed = 30 μm s^{-1}). Test portion ~ 4 μg. $U_{EL, rel}$ is the relative overall analytical uncertainty at the 95% confidence level.

Element	Isotope used	Sample H				Sample R				Sample FL				Sample M				Sample N			
		Mass fraction [μg g^{-1}]	Mass/area [ng cm^{-2}]	RSD [%]	$U_{EL, rel}$ [%]	Mass fraction [μg g^{-1}]	Mass/area [ng cm^{-2}]	RSD [%]	$U_{EL, rel}$ [%]	Mass fraction [μg g^{-1}]	Mass/area [ng cm^{-2}]	RSD [%]	$U_{EL, rel}$ [%]	Mass fraction [μg g^{-1}]	Mass/area [ng cm^{-2}]	RSD [%]	$U_{EL, rel}$ [%]	Mass fraction [μg g^{-1}]	Mass/area [ng cm^{-2}]	RSD [%]	$U_{EL, rel}$ [%]
Si	^{29}Si	$2.5 * 10^5$	$1.6 * 10^6$			$2.7 * 10^5$	$2.6 * 10^6$			$3.2 * 10^5$	$2.2 * 10^6$			$3.4 * 10^5$	$1.5 * 10^6$			$2.9 * 10^5$	$1.9 * 10^6$		
V	^{51}V	230	1500	9.4	19	210	1100	3.6	17	120	970	13	22	120	770	4.4	17	100	670	6.9	18
Cr	^{53}Cr	140	930	9.1	20	120	660	2.6	18	89	720	15	25	87	580	3.2	18	83	540	1.5	17
Ni	^{62}Ni	50	330	11	20	50	280	1.7	15	33	260	12	20	30	200	16	24	33	220	12	20
Cu	^{65}Cu	29	190	25	33	29	160	4.1	18	15	120	7.1	19	15	99	6.8	19	22	140	7.1	20
Ga	^{71}Ga	45	290	11	21	53	290	7.1	19	33	270	16	25	27	180	3.3	17	30	200	3.5	17
Ge	^{74}Ge	2.8	18	10	28	3.7	20	2.9	26	2.5	20	17	32	2.2	15	3.6	26	2.8	18	6.3	27
Rb	^{85}Rb	66	430	6.9	17	85	470	4.2	16	85	680	0.93	15	81	530	10	19	93	610	12	21
Sr	^{88}Sr	220	1500	29	36	160	870	6.5	17	170	1300	19	26	200	1300	27	35	520	3400	4	15
Y	^{89}Y	37	240	25	34	40	220	15	24	24	190	8.5	19	22	150	16	25	25	160	6.8	18
Zr	^{90}Zr	160	1000	7.8	18	200	1100	8.9	19	120	990	16	24	92	600	6	17	110	700	14	23
Nb	^{93}Nb	39	260	11	22	50	280	6.6	20	28	230	15	26	21	140	14	24	22	140	2	18
Mo	^{95}Mo	3.4	22	7.8	19	2.8	16	10	20	2.2	18	4.9	18	2	13	2.2	17	2.1	14	7.9	19
Sn	^{118}Sn	6.3	41	15	24	5.1	28	3.5	17	3.8	31	10	21	3.1	20	8.6	19	3.8	24	4.6	17
Sb	^{121}Sb	1.9	13	2.5	18	1.2	6.6	6	19	0.64	5.2	15	25	0.6	3.9	4.8	19	0.79	5.2	12	23
Cs	^{133}Cs	4.5	29	4.8	18	6.2	34	8.3	20	3.4	27	13	23	3.5	23	9.2	21	4.3	28	7.1	19
Ba	^{137}Ba	340	2200	18	26	220	1200	13	22	190	1500	14	23	280	1800	15	24	460	3000	12	20
La	^{139}La	70	460	13	21	83	460	3	15	51	410	6.5	17	39	260	6.5	17	46	300	1.5	15
Ce	^{140}Ce	150	940	12	20	180	1000	7.5	17	95	760	8.6	18	79	520	14	22	98	640	10	19
Pr	^{141}Pr	15	99	13	22	19	100	14	23	11	86	1.9	16	9.4	62	15	24	11	74	4.4	16
Nd	^{143}Nd	61	400	24	31	69	380	8	19	39	310	13	22	37	240	10	20	40	260	3.5	16
Sm	^{147}Sm	11	72	17	25	15	80	13	21	7.4	59	5	17	7.2	47	12	21	7.7	50	6.6	17
Eu	^{151}Eu	2.3	15	20	28	2.6	15	2.6	16	1.2	10	7.6	18	1.4	9.2	17	26	1.5	10	7.7	18
Gd	^{157}Gd	10	66	20	28	10	56	6	19	6.1	48	3.3	19	6.3	41	18	28	7.1	46	7.1	17
Tb	^{159}Tb	1.4	9.1	8	18	1.5	8.3	8.2	19	0.91	7.3	7.7	19	0.79	5.2	12	22	0.91	5.9	1.9	16
Dy	^{163}Dy	7.8	51	17	25	7.4	40	3.5	17	4.9	39	3.6	17	4.2	28	9.2	19	5.1	33	3.9	16
Ho	^{165}Ho	1.6	10	12	21	1.6	8.6	11	21	0.89	7.1	3.3	17	0.79	5.2	6.9	18	0.95	6.2	3.3	16
Er	^{167}Er	4.3	28	14	22	3.8	21	6.8	18	2.5	20	13	23	2.2	15	10	20	2.6	17	12	21
Tm	^{169}Tm	0.6	3.6	4.1	16	0.50	2.7	8.9	19	0.35	2.8	8	19	0.3	2	19	27	0.34	2.2	10	19
Yb	^{173}Yb	3.9	25	21	29	3.4	19	16	25	2.3	18	13	22	2.2	14	28	36	2.4	16	10	19
Lu	^{175}Lu	0.58	3.7	11	20	0.50	2.7	19	27	0.34	2.7	7.4	18	0.3	2	10	20	0.32	2.1	7	17
Hf	^{178}Hf	4.6	30	16	24	4.7	26	13	22	3.3	27	14	23	2.6	17	4.2	17	3.2	21	1.8	16
Ta	^{181}Ta	2.4	16	9	21	2.7	15	12	23	1.7	13	20	29	1.2	8.1	5.8	19	1.6	10	7.4	20
W	^{184}W	2.3	15	15	23	2.8	15	20	28	1.3	10	22	31	1.1	7.5	9.2	19	1.6	11	15	23
Tl	^{205}Tl	0.64	4.2	2.9	16	0.58	3.2	14	24	0.67	5.3	10	21	0.7	4.7	15.2	25	0.78	5.1	23	31
Pb	^{208}Pb	50	320	6	18	50	280	20	28	18	140	17	26	18	120	3.7	17	16	110	9.2	19
Bi	^{209}Bi	0.53	3.4	13	26	0.4	2.2	22	33	0.3	2.4	11	25	0.21	1.4	17	30	0.23	1.5	12	25
Th	^{232}Th	17	110	15	23	20	110	6.1	16	15	120	15	23	11	72	17	25	12	81	3.4	15
U	^{238}U	6.3	41	6.9	17	5.3	29	10	19	4.1	33	7.4	18	3.7	24	0.85	15	3.5	23	1.3	15

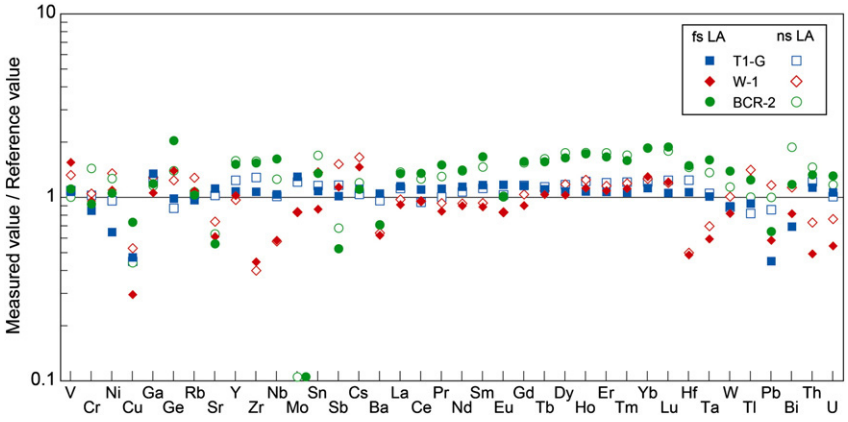

Fig. 3. Comparison of the fs and ns LA-ICP-MS analytical data for the reference materials T1-G, W-1, and BCR-2 with the reference values. Mo in BCR-2 differs significantly due to contamination during the sample preparation by the provider (see Fig. 4d).

4. Discussion

4.1. Mass fractions

To illustrate the geochemical character of the dust samples, the analytical results are presented in Table 6 and Fig. 5. In Fig. 5, the mass fractions of selected trace elements are normalized to those of the primitive mantle and arranged according to their degree of incompatibility, to allow a comparison of results with different orders of magnitude (values from Hofmann, 1988). It is conspicuous that samples H and R from Niamey in Niger are very similar. This is an indicator for similar dust provenances, although sample H is wintertime dust, while R was accumulated during several dry and wet seasons during which the dust source could have been changing. The trace element abundances in the samples from Niamey differ from the dust samples collected in the other regions. As shown by their higher Al and Fe content, these samples are more typical for the clay-rich Central Sahara and Sahel dust sources, whereas the other samples represent more the Lake

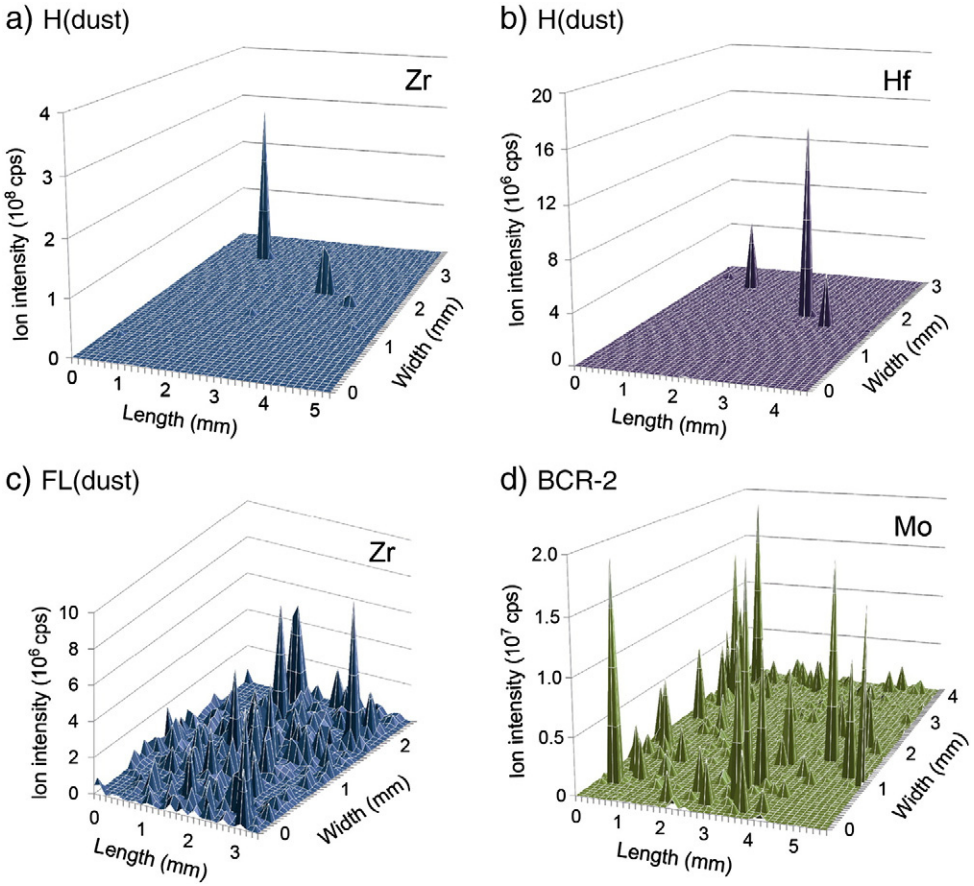

Fig. 4. Ion intensities of Zr, Hf and Mo, determined by fs LA-ICP-MS (spot size = 65 µm, scan speed = 80 µm s^{-1}). a) Distribution of Zr-rich particles in sample H with a high abundance of Hf at the same locations (b). b) Distribution of Hf-rich particles in sample H with a high abundance of Zr at the same locations (a). c) Distribution of Zr-rich particles in sample FL. d) Distribution of the Mo-contamination in BCR-2.

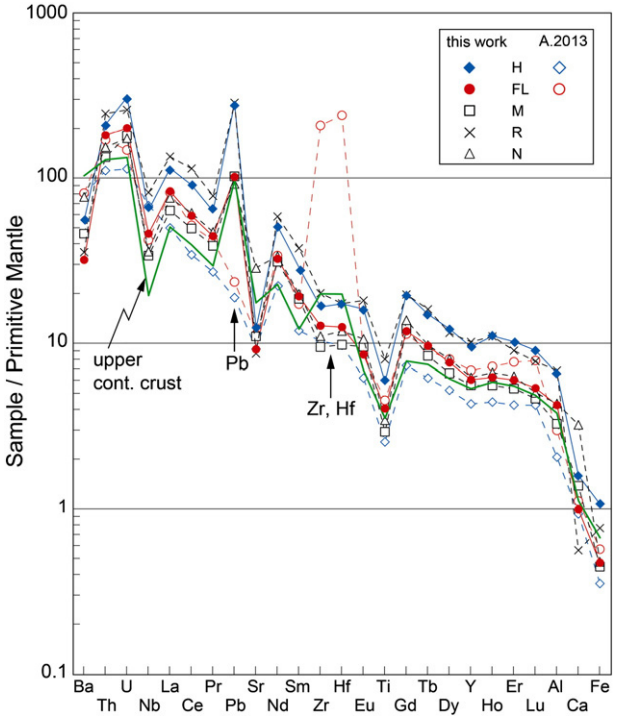

Fig. 5. Element abundances normalized to the values for the primitive mantle (Hofmann, 1988). Also included are values for the upper continental crust (Rudnick and Gao, 2003). Displayed are the mass fractions for the five dust samples analyzed. For comparison, the values of the two previously published dust samples H and FL (Abouchami et al., 2013) are also plotted. Large discrepancies are found for Pb, Zr, and Hf (as explained in the text). The elements are arranged according to their degree of incompatibility.

Chad/Bodélé dust source, with high Si and lower Al and Fe. The normalized trace-element patterns (Fig. 5) also reveal additional, significant compositional differences between the samples R and H, and the samples FL, N and M. The most striking differences are in the abundances of Pb, Nd, Zr and Ti. These differences can only be explained by their differing sampling locations, and thus dust origins, for locations further apart. Comparing the compositions of these dusts to published data from different African dust sources, we find that samples FL, M and N agree with data from the Bodélé region in Chad (data for comparison from Castillo et al., 2008), while samples H and R from Niger have a differing average composition.

The dust samples FL and H have been analyzed previously by another LA-ICP-MS technique, which included a fusing process (Abouchami et al., 2013). The FL values agree well, within about 15%, a value that is similar to the relative overall analytical uncertainty of the mass fractions. However, exceptions are the Zr and Hf values, which are a factor of 10–100 higher in the fused samples (Abouchami et al., 2013), while Pb is about a factor of 10 lower. The high Zr and Hf values can be explained by a high number of high HFSE bearing minerals, such as zircons, in sample FL (displayed in Fig. 4c). We suggest that these grains failed to melt during the fusing process and falsified the results for Zr and Hf. The low Pb values can be explained by a loss of the volatile element Pb during the fusing process at high temperatures of >1300 °C (Stoll et al., 2008). This Pb loss is displayed clearly for both fused samples (Fig. 5). Our analytical data for nearly all elements in sample H disagree with the previously measured data (Abouchami et al., 2013) as shown in Fig. 5. The reason for this is unclear and cannot be explained by the sampling process and the mass spectrometric measurements.

The REE patterns of the different dust samples are very similar (Fig. 6), smooth, enriched in light REEs, and with distinct Eu anomalies, however with different enrichments. The trace element patterns compared to the upper continental crust (Fig. 5) confirm that upper continental crust material is the source of the dust samples probed.

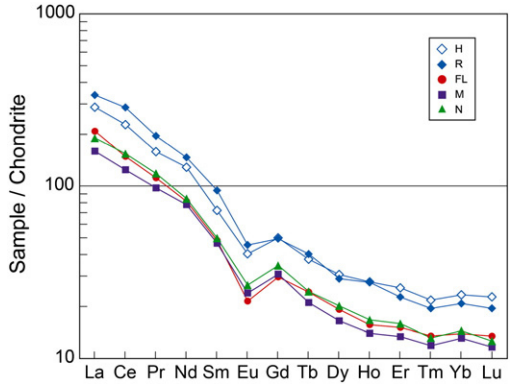

Fig. 6. Chondrite-normalized REE mass fractions of the dust samples. The patterns for the different dust samples are very similar, enriched in light REEs and depleted in Eu. Samples R and H, which were sampled at the same locality, have significantly higher REE contents than the other three dust samples.

4.2. Absolute values

We converted the mass fraction data of Table 6 into ng cm^{-2} units to allow comparisons (e.g., Marino et al., 2008; Lucarelli et al., 2010), by taking the sample mass and ablated area into account. As Table 4 shows, we were able to detect mass area densities of down to 1 ng cm^{-2}. Fig. 1 and Table 4 show the detection limits, which reveal that we are able to determine even lower concentrations, between 0.3 and 10,000 ng g^{-1}.

4.3. Mapping

Since dust filters can have as little as a few tenths to hundreds of micrograms of dust material distributed on a large surface, we tested small sample quantities per area, and investigated whether 2D element distribution mappings of dust on filters are possible. Mapping is a powerful tool to detect and evaluate grains of quite different compositions in the dust samples. Minerals, e.g. zircon, which are characterized by high HFSE contents, can easily be detected by localizing values that are considerably higher than the matrix levels, where those elements occur as trace elements.

For this mapping procedure we used a series of line scans, where the number and the scanning length were chosen to cover the entire area of the sample. Fig. 7 shows the low penetration depth of the laser into the dust minerals, which does not exceed a few micrometers. Furthermore it visualizes the closeness of adjacent line scans and the distribution of the mineral grains on the tape. We were able to map the total dust composition of an amount of about 1000 μg cm^{-2} of dust by scanning the whole sample, giving a detection limit of a few μg g^{-1} or ng cm^{-2} for most trace elements. The count rates of the scans can be used to create 2D element distribution maps. As mentioned above, high HFSE bearing minerals are of particular interest and can be easily detected. In sample H, three large Zr- and Hf-rich minerals, which could be zircons, were located by high ion intensities (cps) of Zr (600 times the average count rate) and Hf (340 times the average count rate) (Fig. 4a and b). The higher abundance of Zr-rich minerals in sample FL could be visualized as well (Fig. 4c), facilitating the interpretation of the differing Zr and Hf values measured previously (Abouchami et al., 2013) in comparison to our values. It should be kept in mind that the size of the peaks in Fig. 4a–d is dependent not only on the mass fraction of the element, but also on the amount of sample ablated. Mapping is therefore suitable for identifying minerals, but not for quantitative analysis.

5. Conclusions

We developed a new, highly sensitive in-situ technique for the simultaneous determination of 46 major and trace elements in dust

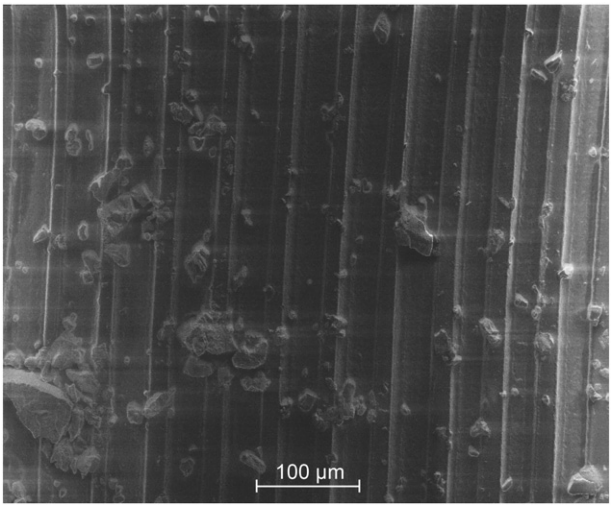

Fig. 7. Line scans on sample BCR-2, visualized with a scanning electron microscope after vapor coating with carbon. A scanning speed of 80 µm s^{-1} was used. This picture shows the low penetration depth of the laser into the dust minerals, which does not exceed a few µm.

samples, without any chemical treatment of the samples. The sample preparation is simple and fast (about 10 min per sample). Mass spectrometric measurements, using a new 200-nm-femtosecond laser, are also fast and take only a few minutes per sample. One of the major advantages of this technique is its high sensitivity. The mass fractions and total amounts of the trace elements can be determined down to detection limits of ng g^{-1} and femtograms, respectively. The overall analytical uncertainty, using this technique, is about 15–25% for dust quantities of 100- to 200 µg, with a precision (RSD) of about 15%. It is also possible to perform 2D mappings with the femtosecond LA-ICP-MS. It is particularly easy to detect high HFSE bearing minerals and other minerals that have elements as major components, which are usually only found as traces in the matrix. The newly developed technique can be applied for in-situ measurements of small amounts of dust on dust collecting filters or samples from surfaces using adhesive tape.

Five dust samples from different collection sites in the Sahara region were investigated in order to verify the technique. For the few samples examined in this study from locations in Niger and Chad, we were able to distinguish between samples from the clay-rich Central Sahara and Sahel dust sources and samples from the Lake Chad/Bodélé dust source. Dust samples H and R, collected at the same location in Niger, show many similarities regarding the trace element and REE patterns, while dust samples FL, N and M (where N and M are sampled at locations not far from each other) have quite similar REE and trace element patterns. All measured dust samples exhibit similar REE patterns with depleted HREE (Gd_N/Yb_N = 2.6–2.9) and negative Eu anomalies, which are typical features of the upper continental crust, a source that is also confirmed by the trace element patterns. This fast in-situ analysis of dust can therefore help to extend the amount of data from sampled dust and dust sources, and enable provenance analysis for samples from large and important dust-producing areas, such as the Sahara region. The femtosecond LA-ICP-MS technique described in this manuscript provides a convenient approach for quick data collection, which can help to trace collected dust to its origin.

Supplementary data to this article can be found online at http://dx.doi.org/10.1016/j.chemgeo.2014.06.001.

Acknowledgments

This work was financially supported by the Max Planck Society and the Max Planck Graduate Center with the Johannes Gutenberg University Mainz (MPGC).

References

Abouchami, W., Zabel, M., 2003. Climate forcing of the Pb isotope record of terrigenous input into the Equatorial Atlantic. Earth Planet. Sci. Lett. 213, 221–234.
Abouchami, W., Näthe, K., Kumar, A., Galer, S.J.G., Jochum, K.P., Williams, E., Horbe, A.M.C., Rosa, J.W.C., Balsam, W., Adams, D., Mezger, K., Andreae, M.O., 2013. Geochemical and isotopic characterization of the Bodélé Depression dust source and implications for transatlantic dust transport to the Amazon Basin. Earth Planet. Sci. Lett. 380, 112–123.
Adedokun, J.A., Emofurieta, W.O., Adedeji, O.A., 1989. Physical, Mineralogical and Chemical Properties of Harmattan Dust at Ile-Ife, Nigeria. Theor. Appl. Climatol. 40, 161–169.
Andreae, M.O., Rosenfeld, D., 2008. Aerosol–cloud–precipitation interactions. Part 1. The nature and sources of cloud-active aerosols. Earth Sci. Rev. 89, 13–41.
Borisova, A.Y., Freydier, R., Polvé, M., Jochum, K.P., Candaudap, F., 2010. Multi-Elemental Analysis of ATHO-G Rhyolitic Glass (MPI-DING Reference Material) by Femtosecond and Nanosecond LA-ICP-MS: Evidence for Significant Heterogeneity of B, V, Zn, Mo, Sn, Sb, Cs, W, Pt and Pb at the Millimetre Scale. Geostand. Geoanal. Res. 34 (3), 245–255.
Castillo, S., Moreno, T., Querol, X., Alastuey, A., Cuevas, E., Herrmann, L., Mounkaila, M., Gibbons, W., 2008. Trace element variation in size-fractionated African desert dusts. J. Arid Environ. 72, 1034–1045.
Formenti, P., Schütz, L., Balkanski, Y., Desboeufs, K., Ebert, M., Kandler, K., Petzold, A., Scheuvens, D., Weinbruch, S., Zhang, D., 2011. Recent progress in understanding physical and chemical properties of African and Asian mineral dust. Atmos. Chem. Phys. 11, 8231–8256.
Ganor, E., Foner, H.A., Brenner, S., Neeman, E., Lavi, N., 1991. The Chemical Composition Of Aerosols Settling In Israel Following Dust Storms. Atmos. Environ. 25A (12), 2665–2670.
Giannadaki, D., Pozzer, A., Lelieveld, J., 2014. Modeled global effects of airborne desert dust on air quality and premature mortality. Atmos. Chem. Phys. 14, 957–968.
Goudie, A.S., Middleton, N.J., 2001. Saharan dust storms: nature and consequences. Earth Sci. Rev. 56, 179–204.
Grousset, F.E., Parra, M., Bory, A., Martinez, P., Bertrand, P., Shimmield, G., Ellam, R.M., 1998. Saharan Wind Regimes Traced By The Sr–Nd Isotopic Composition Of Subtropical Atlantic Sediments: Last Glacial Maximum vs Today. Quat. Sci. Rev. 17, 395–409.
Hofmann, A.W., 1988. Chemical differentiation of the Earth: the relationship between mantle, continental crust, and oceanic crust. Earth Planet. Sci. Lett. 90, 297–314.
Ingamells, C.O., Switzer, P., 1973. A Proposed Sampling Constant For Use In Geochemical Analysis. Talanta 20, 547–568.
Jochum, K.P., Nohl, U., 2008. Reference materials in geochemistry and environmental research and the GeoReM database. Chem. Geol. 253, 50–53.
Jochum, K.P., Nohl, U., Herwig, K., Lammel, E., Stoll, B., Hofmann, A.W., 2005. GeoReM: A New Geochemical Database for Reference Materials and Isotopic Standards. Geostand. Geoanal. Res. 29 (3), 333–338.
Jochum, K.P., Stoll, B., Herwig, K., Willbold, M., 2007. Validation of LA-ICP-MS trace element analysis of geological glasses using a new solid-state 193 nm Nd:YAG laser and matrix-matched calibration. J. Anal. At. Spectrom. 22, 112–121.
Jochum, K.P., Weis, U., Stoll, B., Kuzmin, D., Yang, Q., Raczek, I., Jacob, D.E., Stracke, A., Birbaum, K., Frick, D.A., Günther, D., Enzweiler, J., 2011. Determination of Reference Values for NIST SRM 610–617 Glasses Following ISO Guidelines. Geostand. Geoanal. Res. 35 (4), 397–429.
Jochum, K.P., Stoll, B., Weis, U., Jacob, D.E., Mertz-Kraus, R., Andreae, M.O., 2014. Non-matrix-matched calibration for the multi-element analysis of geological and environmental samples using 200 nm femtosecond LA-ICP-MS: A comparison with nanosecond lasers. Geostand. Geoanal. Res.. http://dx.doi.org/10.1111/j.1751-908X.2014.12028.x (Published online).
Laskin, A., Cowin, J.P., Iedema, M.J., 2006. Analysis of individual environmental particles using modern methods of electron microscopy and X-ray microanalysis. J. Electron Spectrosc. Relat. Phenom. 150, 260–274.
Liu, Y., Hu, Z., Gao, S., Günther, D., Xu, J., Gao, C., Chen, H., 2008. In situ analysis of major and trace elements of anhydrous minerals by LA-ICP-MS without applying an internal standard. Chem. Geol. 257, 34–43.
Lucarelli, F., Nava, S., Calzolai, G., Chiari, M., Udisti, R., Marino, F., 2010. Is PIXE still a useful technique for the analysis of atmospheric aerosols? The LABEC experience. X-Ray Spectrom. 40, 162–167.
Maher, B.A., Prospero, J.M., Mackie, D., Gaiero, D., Hesse, P.P., Balkanski, Y., 2010. Global connections between aeolian dust, climate and ocean biogeochemistry at the present day and at the last glacial maximum. Earth Sci. Rev. 99, 61–97.
Marino, F., Calzolai, G., Caporali, S., Castellano, E., Chiari, M., Lucarelli, F., Maggi, V., Nava, S., Sala, M., Udisti, R., 2008. PIXE and PIGE techniques for the analysis of Antarctic ice dust and continental sediments. Nucl. Inst. Methods Phys. Res. B 266, 2396–2400.
Meyer, I., Davies, G.R., Stuut, J.-B.W., 2001. Grain size control on Sr-Nd isotope provenance studies and impact on paleoclimate reconstructions: An example from deep-sea sediments offshore NW Africa. Geochem. Geophys. Geosyst. 12 (3), 1–14. http://dx.doi.org/10.1029/2010GC003355.
Moffet, R.C., 2011. Scanning Transmission X-ray Microscopy: Applications in Atmospheric Aerosol Research. Lawrence Berkeley National Laboratory, (http://escholarship.org/uc/item/0gh7r6z4).
Moreno, T., Querol, X., Castillo, S., Alastuey, A., Cuevas, E., Herrmann, L., Mounkaila, M., Elvira, J., Gibbons, W., 2006. Geochemical variations in Aeolian mineral particles from the Sahara–Sahel Dust Corridor. Chemosphere 65, 261–270.
NIST, 2012. Certificate of Analysis — Standard Reference Material 612. NIST, Gaithersburg, MD.
Pavićević, M.K., Amthauer, G., 2000. Physikalisch-chemische Untersuchungsmethoden in den Geowissenschaften. Band 1 Mikroskopische, analytische und massenspektrometrische MethodenSchweizerbart'sche Verlagsbuchhandlung 3-510-65196-0.

Poitrasson, F., Mao, X., Mao, S.S., Freydier, R., Russo, R.E., 2003. Comparison of Ultraviolet Femtosecond and Nanosecond Laser Ablation Inductively Coupled Plasma Mass Spectrometry Analysis in Glass, Monazite, and Zircon. Anal. Chem. 75 (22), 6184–6190.

Potts, P.J., 2012. A proposal for the Publication of Geochemical Data in the Scientific Literature. Geostand. Geoanal. Res. 36, 225–230.

Rea, D.K., 1994. The Paleoclimatic Record Provided By Eolian Deposition In The Deep Sea: The Geologic History Of Wind. Rev. Geophys. 32, 159–195.

Scheuvens, D., Schütz, L., Kandler, K., Ebert, M., Weinbruch, S., 2013. Bulk composition of northern African dust and its source sediments — A compilation. Earth Sci. Rev. 116, 170–194.

Schwikowski, M., Seibert, P., Baltensperger, U., Gäggeler, H.W., 1995. A study of an outstanding Saharan dust event at the high-alpine site Jungfraujoch, Switzerland. Atmos. Environ. 29 (15), 1829–1842.

Shaheen, M.E., Gagnon, J.E., Fryer, B.J., 2012. Femtosecond (fs) laser coupled with modern ICP-MS instruments provide new and improved potential for in situ elemental and isotopic analyses in the geosciences. Chem. Geol. 330–331, 260–273.

Skonieczny, C., Bory, A., Bout-Roumazeilles, V., Abouchami, W., Galer, S.J.G., Crosta, X., Stuut, J.-B., Meyer, I., Chiapello, I., Podvin, T., Chatenet, B., Diallo, A., Ndiaye, T., 2011. The 7–13 March 2006 major Saharan outbreak: Multiproxy characterization of mineral dust deposited on the West African margin. J. Geophys. Res. 116, 1–10. http://dx.doi.org/10.1029/2011JD016173.

Sterling, D.A., Lewis, R.D., Luke, D.A., Shadel, B.N., 2000. A Portable X-Ray Fluorescence Instrument for Analyzing Dust Wipe Samples for Lead: Evaluation with Field Samples. Environ. Res. Sect. A 83, 174–179. http://dx.doi.org/10.1006/enrs.2000.4058.

Stoll, B., Jochum, K.P., Herwig, K., Amini, M., Flanz, M., Kreuzburg, B., Kuzmin, D., Willbold, M., Enzweiler, J., 2008. An Automated Iridium-Strip Heater for LA-ICP-MS Bulk Analysis of Geological Samples. Geostand. Geoanal. Res. 32 (1), 5–26.

Tanaka, T.Y., Chiba, M., 2006. A numerical study of the contributions of dust source regions to the global dust budget. Glob. Planet. Chang. 52, 88–104.

Taylor, S.R., McLennan, S.M., 1985. The Continental Crust: its composition and evolution. An examination of the geochemical record preserved in sedimentary rocksBlackwell Scientific Publications, (312 pp.).

Velasquez, G., Borisova, A.Y., Salvi, S., Béziat, D., 2012. In Situ Determination of Au and Cu in Natural Pyrite by Near-Infrared Femtosecond Laser Ablation-Inductively Coupled Plasma-Quadrupole Mass Spectrometry: No Evidence for Matrix Effects. Geostand. Geoanal. Res. 36 (3), 315–324.

		T1-G			W-1			BCR-2			JG-1a		
Element	Isotope used	mass fraction	RSD	$U_{EL, rel}$	mass fraction	RSD	$U_{EL, rel}$	mass fraction	RSD	$U_{EL, rel}$	mass fraction	RSD	$U_{EL, rel}$
		[µg g^{-1}]	[%]	[%]	[µg g^{-1}]	[%]	[%]	[µg g^{-1}]	[%]	[%]	[µg g^{-1}]	[%]	[%]
Si	^{29}Si	274000		4	245500		4	253000		4	245500		4
V	^{51}V	195	2	8	358	26	31	428	31	37	35	13	17
Cr	^{53}Cr	17	1	10	102	8	14	15	22	27	31	3	12
Ni	^{62}Ni	7	4	8	74	11	14	18	25	29	8	19	23
Cu	^{65}Cu	8	3	11	30	5	13	14	26	32	1	8	14
Ga	^{71}Ga	25	2	9	17	14	18	25	3	10	21	13	18
Ge	^{74}Ge	2	1	22	2	8	24	3	10	24	2	13	26
Rb	^{85}Rb	74	4	7	21	13	16	45	11	14	227	9	11
Sr	^{88}Sr	304	7	9	102	17	20	176	18	22	90	7	10
Y	^{89}Y	25	6	11	24	9	13	52	7	12	9	32	38
Zr	^{90}Zr	148	7	11	38	5	9	262	13	17	6	8	12
Nb	^{93}Nb	9	6	13	5	21	27	19	28	35	18	15	21
Mo	^{95}Mo	5	19	24	1	13	17	20	38	44	0	15	20
Sn	^{118}Sn	2	6	11	2	7	11	2.5	9	14	6	31	37
Sb	^{121}Sb	0	14	20	1	9	15	0	49	58	0	57	66
Cs	^{133}Cs	3	1	10	1	16	20	1	23	29	19	22	27
Ba	^{137}Ba	390	3	7	90	16	20	445	9	13	266	8	12
La	^{139}La	78	4	7	9	6	9	31	7	10	5	12	15
Ce	^{140}Ce	134	5	8	20	7	10	66	10	13	14	39	45
Pr	^{141}Pr	13	5	9	2	2	7	9	14	18	2	28	34
Nd	^{143}Nd	45	8	10	12	13	16	37	5	10	5	18	23
Sm	^{147}Sm	7	8	11	3	4	8	10	17	21	2	26	31
Eu	^{151}Eu	1	4	7	1	9	12	2	6	11	0	6	10
Gd	^{157}Gd	6	9	12	3	6	10	10	10	17	1	1	12
Tb	^{159}Tb	1	8	11	1	9	12	2	5	11	0	12	16
Dy	^{163}Dy	5	14	17	4	9	12	10	3	9	2	31	37

Ho	^{165}Ho	1	8	11	1	4	8	2	9	13	0	18	22
Er	^{167}Er	3	14	17	2	2	7	6	7	12	1	19	23
Tm	^{169}Tm	0	11	14	0	13	16	1	5	10	0	15	19
Yb	^{173}Yb	3	11	14	2	9	12	6	3	9	1	20	25
Lu	^{175}Lu	0	12	15	0	9	13	1	3	9	0	17	21
Hf	^{178}Hf	4	7	12	1	11	14	7	6	11	0	2	9
Ta	^{181}Ta	0	11	17	0	12	18	1	14	20	2	12	18
W	^{184}W	1	4	8	0	8	11	1	21	26	16	6	11
Tl	^{205}Tl	0	17	22	0	19	23	0	19	25	2	7	13
Pb	^{208}Pb	5	5	10	4	10	14	7	16	21	19	8	13
Bi	^{209}Bi	0	18	26	0	35	44	0	2	18	1	7	19
Th	^{232}Th	34	1	5	1	7	10	7	10	13	5	9	12
U	^{238}U	2	4	6	0	13	16	2	14	17	2	14	17

B.2

Macholdt et al., Chem. Geology, 2015

Microanalytical methods for in-situ high-resolution analysis of rock varnish at the micrometer to nanometer scale

Dorothea S. Macholdt[a,b], Klaus Peter Jochum[a], Christopher Pöhlker[a], Brigitte Stoll[a], Ulrike Weis[a], Bettina Weber [b], Maren Müller[c], Michael Kappl[c], Stefan Buhre[d], A. L. David Kilcoyne[e], Markus Weigand[f], Denis Scholz[d], Abdullah M. Al-Amri[g], Meinrat O. Andreae[a,g]

a Biogeochemistry Department, Max Planck Institute for Chemistry, Mainz, Germany
b Multiphase Chemistry Department, Max Planck Institute for Chemistry, Mainz, Germany
c Physics of Interfaces Department, Max Planck Institute for Polymer Research, Mainz, Germany
d Institute of Geosciences, Johannes Gutenberg University, Mainz, Germany
e Lawrence Berkeley National Laboratory, Berkeley, CA, United States
f Modern Magnetic Systems Department, Max Planck Institute for Intelligent Systems, Stuttgart, Germany
g Geology and Geophysics Department, King Saud University, Riyadh, Saudi Arabia

Chemical Geology 411, 57-68. DOI: 10.1016/j.chemgeo.2015.06.023

Chemical Geology 411 (2015) 57–68

Contents lists available at ScienceDirect

Chemical Geology

journal homepage: www.elsevier.com/locate/chemgeo

Microanalytical methods for in-situ high-resolution analysis of rock varnish at the micrometer to nanometer scale

D.S. Macholdt [a,*], K.P. Jochum [a], C. Pöhlker [a], B. Stoll [a], U. Weis [a], B. Weber [b], M. Müller [c], M. Kappl [c], S. Buhre [d], A.L.D. Kilcoyne [e], M. Weigand [f], D. Scholz [d], A.M. Al-Amri [g], M.O. Andreae [a,g]

[a] Biogeochemistry Department, Max Planck Institute for Chemistry, Mainz, Germany
[b] Multiphase Chemistry Department, Max Planck Institute for Chemistry, Mainz, Germany
[c] Physics of Interfaces Department, Max Planck Institute for Polymer Research, Mainz, Germany
[d] Institute of Geosciences, Johannes Gutenberg University, Mainz, Germany
[e] Lawrence Berkeley National Laboratory, Berkeley, CA, United States
[f] Modern Magnetic Systems Department, Max Planck Institute for Intelligent Systems, Stuttgart, Germany
[g] Geology and Geophysics Department, King Saud University, Riyadh, Saudi Arabia

ARTICLE INFO

Article history:
Received 9 December 2014
Received in revised form 22 May 2015
Accepted 23 June 2015
Available online 30 June 2015

Keywords:
Rock varnish
Desert varnish
Femtosecond LA-ICP-MS
EPMA
STXM-NEXAFS
FIB slicing

ABSTRACT

A wide range of analytical techniques were used to investigate rock varnish from different locations (Negev, Israel; Knersvlakte, South Africa; Death Valley and Mojave Desert, California): a 200 nm-femtosecond laser ablation-inductively coupled plasma-mass spectrometer (LA-ICP-MS), an electron probe microanalyzer (EPMA), focused ion beam (FIB) slicing, and scanning transmission X-ray microscopy–near edge X-ray absorption fine structure spectroscopy (STXM–NEXAFS). This combination enables comprehensive high-spatial-resolution analysis of rock varnish. Femtosecond LA-ICP-MS and EPMA were used for quantitative determination of element concentrations. In-situ measurements were conducted on thick and thin sections with a resolution of 10–40 μm and 2 μm, respectively. The results demonstrate that some elements, such as Mn, Co, Pb, Ni, and Cu, are highly enriched in varnish relative to the upper continental crust (up to a factor of 100). The varnish composition is not influenced by the composition of the underlying rock, which is witnessed by plots of MnO_2 vs. SiO_2 contents. Furthermore, the Mn-free end members fall in the range of average dust compositions.

The varnishes from the various locations show distinct differences in some elemental ratios, in particular Mn/Fe (0.3–25.1), Mn/Ba (4–170), Ni/Co (0.03–1.8) and Pb/Ni (0.4–23). The rare earth element (REE) patterns vary with $La_N/Yb_N = 3.5–12$ and different degrees of Ce anomalies ($Ce/Ce^* = 1.5–5.3$).

To study the internal structure of the varnish, 100–200 nm thick FIB slices were prepared and mappings of Fe, Mn, N, CO_3^{2-}, Ca, C, and Si at the nm scale performed. Banded internal structures of Mn, Fe and organic C were observed in the Israeli and Californian samples, however, no Fe-rich layers are present in the South African rock varnish samples. Furthermore, cavities were found that are partly filled by C, Fe, and Mn rich material. Internal structures are different for varnish from different locations, which might reflect different types of genesis. The results of the combined microanalytical techniques give important detailed insights towards unraveling the genesis of rock varnish.

1. Introduction

The genesis of rock varnish has been a matter of debate since 1812, when Alexander von Humboldt first observed it at the cataracts of the Orinoco River (Von Humboldt and Bonpland, 1819, Dorn et al., 2012a). Meanwhile, similar rock varnishes have been observed in a wide variety of terrestrial environments and there have been quite a number of studies discussing the origin of these coatings. Both biological and inorganic processes, as well as a combination of both, have been suggested.

Rock varnish is a black, sometimes red or brown, shiny layer on rock surfaces, present on slowly weathering rocks, independent of their lithology (Engel and Sharp, 1958). The main components of varnish are poorly crystallized Mn oxides (usually hollandite–todorokite, birnessite and buserite, poorly crystallized phyllomanganates of unspecified types, and Mn–Fe spinel), poorly crystallized Fe oxides (e.g., hematite, Fe_2O_3), and clay minerals (Potter and Rossman, 1979; Garvie et al., 2008). The clay mineral fraction in varnish, reaching up to 70% of the varnish volume (Thiagarajan and Lee, 2004) is most likely introduced by the atmospheric deposition of dust (Thiagarajan and Lee, 2004), whereas the origin and precipitation of Mn are not yet fully understood.

Manganese has an abundance of 0.1% (as Mn oxide, MnO) in the upper continental crust, while it is enriched up to 40% (as MnO_2) in

* Corresponding author at: P.O. Box 3060, 55020 Mainz, Germany.
E-mail address: d.macholdt@mpic.de (D.S. Macholdt).

http://dx.doi.org/10.1016/j.chemgeo.2015.06.023
0009-2541/

rock varnish (Rudnick and Gao, 2003). Therefore, it has to be preferentially reduced and dissolved from dust, and re-precipitated by oxidation for the formation of varnish. One suggestion is a chemical reduction and precipitation under the pH (5.7) and Eh (~0.8) conditions of rainwater (Thiagarajan and Lee, 2004). The second hypothesis is biological reduction by Mn reducing bacteria (Perry and Kolb, 2004). SiO_2 is also found in large amounts in varnish, as a component of the clay mineral fraction and as silica glaze, and has been suggested to be involved in varnish formation (Perry et al., 2006; Wang et al., 2011). Varnish grows in almost every type of terrestrial weathering environment (Krinsley et al., 2009; Krinsley et al., 2012), but distinctive varnishes are found in arid to semi-arid desert climates. Desert varnish is of specific interest, since it has been suggested as a possible paleoclimate archive (Perry and Adams, 1978; Liu and Dorn, 1996). Since there are almost no climate archives present in deserts, especially beyond the range of ^{14}C dating, rock varnish might be an important tool in bridging this gap (Broecker and Liu, 2001). An understanding of its genesis is therefore required.

Estimates of the growth rate of rock varnish vary between 1 and 640 μm per 1000 a (Liu and Broecker, 2000; Spilde et al., 2013), with its maximum thickness rarely exceeding about 250 μm (Northup et al., 2010). The growth rates seem to depend on the humidity of the environment, with slower growth rates for desert climates (Krinsley et al., 2012).

Many studies on varnish and its composition have been published (Reneau et al., 1992; Thiagarajan and Lee, 2004; Dorn, 2008; Goldsmith et al., 2014) with differing techniques. Detailed information on used techniques are provided by. Krinsley et al. (2013). However, only a few studies examined the major element distribution in combination with trace element measurements at the μm to nm scale.

Since varnish is a micrometer-scale, thin crust, the aim of this paper is to combine different microanalytical techniques to investigate samples from different locations, USA, Israel and South Africa, at μm to nm scales. Each technique provides additional and complementary information for understanding the structures within rock varnish:

- a femtosecond laser ablation-inductively coupled plasma-mass spectrometer (fs LA-ICP-MS) with a spatial resolution of 10–40 μm provides precise and accurate determination of major, and in particular, trace element concentrations,
- an electron probe microanalyzer (EPMA) yields major element measurements at a scale of a few micrometers,
- scanning transmission X-ray microscopy–near edge X-ray adsorption fine structure spectroscopy (STXM–NEXAFS), using focused ion beam (FIB) milled ultra-thin sections, contributes element distribution mappings at the nanometer scale.

2. Analytical methods

2.1. Samples

Rock samples covered with varnish were collected at different sampling sites in the Mojave Desert (California, USA, Fig. 1a), the Negev Desert (Israel, Fig. 1b), and the Knersvlakte (South Africa, Fig. 1c) during several field campaigns from 2010 to 2014. The Mojave and Negev deserts have arid climates, while the Knersvlakte is a semi-arid desert. Varnish samples were chosen in the field, giving preference to darker coatings which would therefore presumably have a thicker varnish crust. All rocks from California and South Africa were taken from the ground, and therefore consist of pebbles and small rocks (a few to tens of centimeters) which had direct contact to the underlying soil. The Israeli samples were collected as fragments or chips from larger boulders (Table 1) and were subdivided into those with a macroscopical botryoidal surface structure, and those with a smooth and flat surface. The South African samples, mostly pebbles of a few cm, had a black, shiny varnish crust with metallic luster on their tops and a slightly duller tinge on the bottom sides. The top and bottom sides of the rocks were often not fully enclosed by the varnish, which appears to have grown from the rock–soil–atmosphere contact upwards and downwards at the rock surface. Neighboring varnish samples partially had lichen growing on top. Most Californian samples were varnish-covered on their atmosphere facing side. The soil-facing side was usually covered by an orange-red coating. No preferred growth direction or starting point of varnish growth was observed.

Table 1 lists the specimens used for analysis together with information about the sampling location, the underlying rock type, and the varnish thickness

2.2. Sample preparation

Thick sections (about 70 μm thick) were prepared for EPMA and fs LA-ICP-MS measurements. For the EPMA measurements, the thick sections were polished, in contrast to the samples for the fs

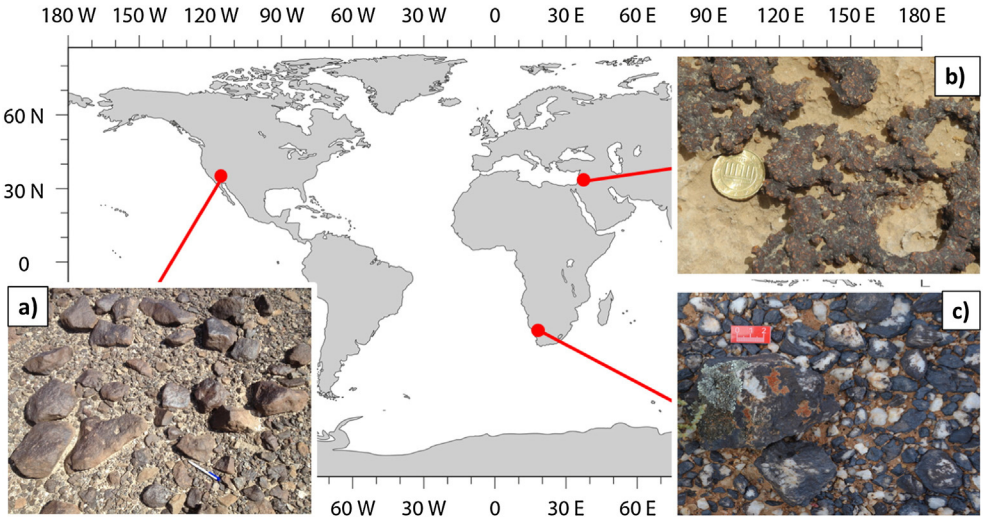

Fig. 1. Sampling locations of rock varnish, a) Mojave Desert, California, USA, b) Negev Desert, Israel, c) Knersvlakte, South Africa.

Table 1
Varnish samples with information about their sampling location, underlying rock type, and maximum varnish thickness.

Sample name	Country	Location	Rock type	GPS coordinates	Max. varnish thickness	Sampling	Lamination
IS13 V1[a]	Israel	Negev Desert, Sde Boker	Quartz-rimmed limestone	30°52′25.13″N, 34°47′3.8″E	130 μm	Chip of a horizontal top of a boulder about 25 cm above the ground	Yes
IS13 V2a[a]	Israel	Negev Desert, Sde Boker	Quartz-rimmed limestone	30°52′25.13″N, 34°47′3.8″E	160 μm	Chip of a boulder about 50 cm above the ground	Yes
IS13 V3[a]	Israel	Negev Desert, Sde Boker	Quartz-rimmed limestone	30°52′25.13″N, 34°47′3.8″E	250 μm	Chip of a boulder about 30 cm above the ground	Yes
IS13 V4[a]	Israel	Negev Desert, Sde Boker	Quartz-rimmed limestone	30°52′25.13″N, 34°47′3.8″E	110 μm	From the ground	Yes
CA13 SWS1[b]	California, USA	Mojave Desert, Stoddard Wells South	Dacite with sperulites	34°44′28.62″N, 117°4′10.14″W	60 μm	From the ground	Yes
CA13 SWW1[b]	California, USA	Mojave Desert, Stoddard Wells West	Dacite with sperulites	34°45′13.8″N, 117°03′58.8″W	55 μm	From the ground	Yes
CA13 SWW3[b]	California, USA	Mojave Desert, Stoddard Wells West	Dacite with sperulites	34°45′13.8″N, 117°03′58.8″W	50 μm	From the ground	Yes
CA13 SWW4[b]	California, USA	Mojave Desert, Stoddard Wells West	Impure quartzite	34°46′19.74″N, 117°03′28.86″W	140 μm	From the ground	Yes
CA13 DV1[b]	California, USA	Death Valley	Foid bearing andesite	36°21′16.798″N, 116°38′39″W	110 μm	From the ground	Yes
CA13 SCH45[b]	California, USA	Mojave Desert, S of Death Valley Junction	Foid bearing andesite	36°11′51.3″N, 116°22′27.6″W	50 μm	From the ground	yes
CA13 SS2[b]	California, USA	Mojave Desert, Salt Spring	Impure quartzite	35°36′55″N, 116°38′39″W	70 μm	From the ground	Yes
CA WS-18[c]	California, USA	Death Valley	Weathered magmatite		150 μm		Yes
CA14 JC-8[b]	California, USA	Death Valley, Johnson Canyon	Spotted slate	36°05′49.87″N, 116°51′30.32″W	80 μm	From the ground	Yes
CA14 DV11[b]	California, USA	Death Valley, near Scotty's Castle	Basanite	36°51′31″N, 117°15′59″W	60 μm	From the ground	Yes
SA10 #4[a]	South Africa	Knersvlakte	Quartzite	31°16′45.2″S, 18°35′42.6″E	180 μm	From the ground	No
SA10 #8[a]	South Africa	Knersvlakte	Quartzite	31°16′45.2″S, 18°35′42.6″E	180 μm	From the ground	No
SA10 #9[a]	South Africa	Knersvlakte	Quartzite	31°16′45.2″S, 18°35′42.6″E	80 μm	From the ground	No
SA10 #12[a]	South Africa	Knersvlakte	Quartzite	31°16′45.2″S, 18°35′42.6″E	300 μm	From the ground	No
SA13 mM-d[a]	South Africa	Knersvlakte	Quartzite	31°16′55.41″S, 18°35′17.8″E	120 μm	From the ground	No
SA13 mM-f[a]	South Africa	Knersvlakte	Quartzite	31°16′55.41″S, 18°35′17.8″E	250 μm	From the ground	No

[a] Samples were provided and collected by Bettina Weber.
[b] Samples were provided and collected by Meinrat O. Andreae.
[c] Sample was provided by Tanzhuo Liu.

LA-ICP-MS determination of major and trace elements, where polishing was avoided to exclude trace-element contamination from the polishing material. The roughness of the unpolished surfaces can be neglected for fs LA-ICP-MS measurements because the pre-ablation step produced almost flat surfaces. Thin sections (25–30 μm) were prepared to determine the lithology of the underlying rocks. The varnish coatings were cut perpendicular to their layers (Fig. 2a), whereby cross-sections through the sedimentation sequence were exposed, similar to the procedure described by Reneau et al. (1992). All thin and thick sections were prepared in an enclosing resin prior to thinning.

FIB slices, similar to those produced of rock varnish by Krinsley et al. (2013), were milled to sizes of about 50 × 30 μm and thicknesses of about 100–200 nm to perform X-ray micro-spectroscopy in transmission mode. For this purpose, micro-basins, which contain thicker varnish, were selected by microscopy (Fig. 2b), located by scanning electron microscopy (SEM) (Fig. 2c), and milled by a Ga^+ ion beam (Fig. 2d).

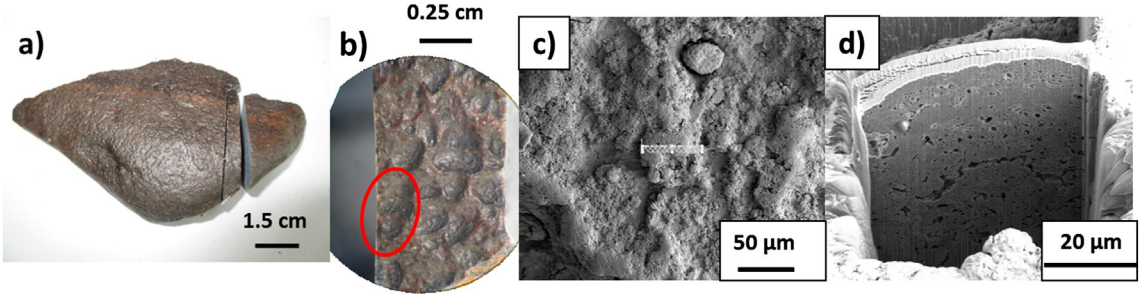

Fig. 2. Sample preparation, a) CA14 JC-8 sample, cut perpendicular to the varnish coating, b) Example of a micro-basin chosen on CA14 JC-8 for FIB preparation, c) FIB sampling location and area marked for Pt deposition and ion beam sputtering on sample SA13 mM-f, d) SA13 mM-f after FIB preparation, before liftout and thinning.

2.3. Imaging

A Leica DM RX polarizing microscope was used for the investigation of the varnish structure in thick sections and to observe ablated line scans subsequent to the analysis (Fig. 3). The underlying rocks and the approximate thicknesses of the varnish layers were determined by thin sections with a polarizing microscope. Pictures were taken of each thin and thick section, interesting sites were chosen and line scans were then performed on the thick sections with the fs LA-ICP-MS on these selected sites. Fig. 3 demonstrates the measurement procedure on a detailed image of two line scans, 40 μm and 10 μm wide, which were produced by fs LA-ICP-MS. Objectives from 1.6 to 100 were used for internal structure examinations (1–10 μm range) of varnish. Back-scattered electron images were recorded by EPMA, to visualize the samples by variations in back-scattering intensity resulting from differing atomic numbers, Z, displaying internal structures. Furthermore, prepared FIB slices were imaged by SEM, to allow the comparison of structures and element distribution by STXM–NEXAFS.

2.4. Femtosecond laser ablation-inductively coupled plasma-mass spectrometry

Measurements were carried out at the Max Planck Institute for Chemistry (Mainz, Germany). A combination of a ThermoFisher Element 2 single-collector sector-field ICP-mass spectrometer and an ESI fs laser ablation system NWRFemto with a wavelength of 200 nm, producing laser pulses at 150 fs, was used. The fs LA-ICP-MS is especially suitable for the analysis of small sample amounts (Macholdt et al., 2014) and has the advantage of an almost matrix-independent calibration (Jochum et al., 2014). Important parameters of the ICP-MS and the lasers are listed in Tables 2 and 3. Laser ablation was conducted in a New Wave Large Format Cell in a He atmosphere. This carrier gas was mixed with an Ar gas flow to transport the aerosols generated by ablation. The washout time was about 30 s and the blank count rate was determined prior to each ablation for about 15 s.

A new ThermoFisher medium mass resolution mode (2000) with flat top peaks was chosen for all measurements, since in this way many oxides and molecules from Ar, O, and the major compounds of varnish produced in the plasma can be separated from the ions, giving an improvement of the signal to blank ratio for many elements.

After pre-ablation, each sample was scanned along a profile from the underlying rock through the varnish into the embedding resin. The varnish region was defined by high (≥2%) MnO_2 abundances. Measurements with exceptionally low count rates for all elements, an indicator for holes and cracks, were excluded. To obtain a representative bulk analysis for the varnish, the concentration for each measurement was averaged over the profile from the underlying rock contact to the resin. Bulk analyses were performed for the major elements (Na, Mg, Al, Si, P, K, Ca, Ti, Mn, Fe) and 24 trace elements (isotopes used are listed in Appendix A) with a scan speed of 1 μm s^{-1}, a spot size of 40 μm and a time per pass of about 0.8 s, using a combination of magnetic and electrical scan modes. Adjacent to these measurements, higher resolved profile measurements of the "neighboring" elements with similar atomic masses, V, Cr, Mn, Fe, Co, Ni, and Cu, could be performed using solely the fast electrical scan mode. In this case, a scan speed of 5 μm s^{-1} and a spot size of 10 μm were chosen. Since no suitable micro-analytical varnish reference material exists, the homogeneous GSE-1G glass (GeoReM database http://georem.mpch-mainz.gwdg.de) with high trace element contents (ca. 500 μg g^{-1}) and a basaltic matrix with 12.7% FeO and 590 μg g^{-1} Mn was used for calibration. It is applicable due to the nearly matrix-independent calibration for fs LA-ICP-MS.

The element concentrations were determined by measuring the ion intensities of the elements of interest using Al as the internal standard (analogous to Goldsmith et al. (2014)). This element was measured by EPMA on three to nine varnish samples from each location, analyzing 11–16 spots per sample. For further correction, a total oxide content of about 95% was assumed, which was obtained from the EPMA results of the samples. However, the concentrations of the higher-resolved profile measurements by fast electrical scans are less precise, since no internal standard with constant amounts throughout the profiles was available and no total oxide content could be assumed.

The concentration of an element of interest, EL, (mf_{EL}) was calculated by a procedure described in Jochum et al. (2007). The precision (RSD) of the fs LA-ICP-MS data, determined by three independent analyses of the homogeneous GSE-1G glass, was about 3%. However, due to the large sample heterogeneity, it was much higher for the bulk varnish analyses, determined by 12–30 independent analyses on each sample at different locations, and varied between 25 and 80%. The measurement accuracy, defined as the overall analytical uncertainty at the 95% confidence level, is listed for each element in Appendix A. It was about 35% for most elements. The detection limits, DLs (defined as three times the standard deviation of the blank values), are listed in Table 4. The DLs ranged between <0.01–1100 μg g^{-1} and 1–26 μg g^{-1} using spot

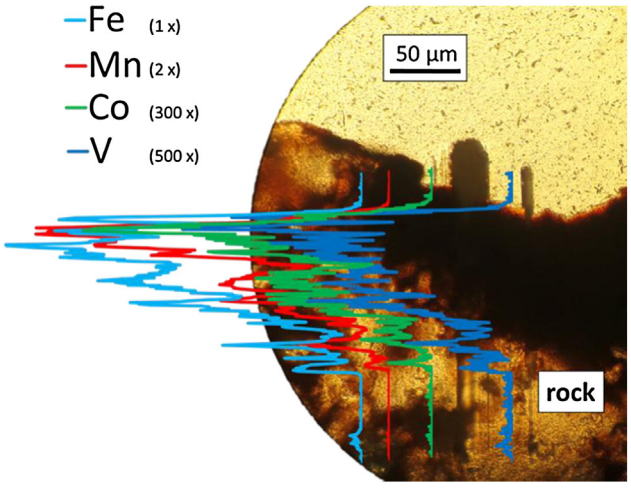

Fig. 3. Thick (~70 μm) section of sample IS13 V2a imaged by microscopy with tracks from two LA-ICP-MS line scans (40 μm and 10 μm wide lines). The image shows the results of the measurements along the narrower scan line. The graphs are not to scale to allow comparison. The factors with which the element abundances were multiplied are 2 for Mn, 300 for Co, and 500 for V.

Table 2
Operating parameters used for the fs laser ablation system.

	NWRFemto
Laser type	Ti:sapphire
Wavelength [nm]	200
Pulse length [fs]	150
Energy density [J cm^{-2}]	0.8
Spot size [μm]	10 (fast scan), 40 (slow scan)
Pulse repetition rate [Hz]	50
Scan time [s]	250, 350
Scan speed [μm s^{-1}]	1 (slow scan), 5 (fast scan)

Table 3
Operating parameters of the Element2 ICP-MS.

rf power [W]	1270
Cooling gas flow rate [l min^{-1}]	15
Auxiliary gas flow rate [l min^{-1}]	1
Carrier gas (Ar) flow rate [l min^{-1}]	0.8
Carrier gas (He) flow rate [l min^{-1}]	0.7
Sample time [s]	0.002
Samples per peak	25
Mass window [%]	40
Time per pass [s]	0.2 (fast scan), 1.4 (slow scan)
Mass resolution	2000

Table 4
Detection limits of the fs LA-ICP-MS analysis. Data were evaluated from blank measurements without sample material (DL = three times the variability of the blank). A: spot size = 40 μm; scan speed = 1 μm s^{-1} (slow line scan); B: spot size = 10 μm; scan speed = 5 μm s^{-1} (fast line scan).

A				B	
[μg g^{-1}]		[ng g^{-1}]		[μg g^{-1}]	
Na	150	La	7	V	1
Mg	25	Ce	80	Cr	5
Al	160	Pr	16	Mn	5
Si	1100	Nd	80	Fe	30
P	70	Sm	<0.01	Co	1
K	50	Eu	<0.01	Ni	20
Ca	320	Gd	55	Cu	5
Ti	7	Tb	13		
Mn	20	Dy	<0.01		
Fe	90	Ho	<0.01		
Co	1	Er	<0.01		
Ni	40	Tm	<0.01		
Rb	0.8	Yb	<0.01		
Sr	0.7	Lu	<0.01		
Y	0.3	Pb	60		
Cs	0.8	Th	5		
Ba	0.4	U	5		

sizes of 40 μm and 10 μm and scan speeds of 1 μm s^{-1} and 5 μm s^{-1}, respectively (Table 4).

2.5. Electron probe microanalysis

Quantitative measurements of major element concentrations were conducted at the Institute of Geosciences at the Johannes Gutenberg University (Mainz, Germany) using a JEOL JXA-8200 electron microprobe. The samples were diamond-polished, cleaned with petrol ether in an ultrasonic bath and kept dry in a vacuum furnace before being coated with ~20 nm of thermally evaporated carbon. The microprobe was operated at an accelerating voltage of 15 kV, a beam current of 12 nA and a beam diameter of 2 μm. Five wavelength dispersive X-ray spectrometers (WDS) were used to measure Kα lines of Mn, Na, Al, Cr, Fe, Mg, Ti, K, Ca, and Si with peak counting times of 20 s. Natural and synthetic phases ($NaAlSi_3O_8$, Al_2O_3, Cr_2O_3, Fe_2O_3, MgO, $MnTiO_3$, $KAlSi_3O_8$ and $CaSiO_3$) were utilized as reference materials and for instrument stability monitoring. For data correction the Phi-rho-z method based on the CITZAF correction (Armstrong, 1991) was applied.

2.6. Scanning transmission X-ray microscopy–near edge X-ray adsorption fine structure spectroscopy and focused ion beam sputtering

Focused ion beam (FIB) sputtering (milling) was performed at the Max Planck Institute for Polymer Research (Mainz, Germany) using a Nova600Nanolab FIB dual-beam instrument of FEI. Simultaneous SEM microscopy was used to carefully determine and monitor the site of milling. Selected micro-basins were used for the preparation of the 50 × 30 μm FIB slices. The samples were sputtered with Pt using Baltec MED020 sputtering equipment to avoid charging effects during electron- and ion radiation, and to acquire a stable image. Subsequent to sputtering the whole sample with a 50 nm thick Pt coating, preparation sites were coated with an additional Pt layer, about 2 μm thick, using beam-induced Pt deposition from a metallo-organic precursor gas (1 nA at 30 kV). Milling was performed by Ga^+-ion sputtering with a resolution of about 10 nm. In a first milling step (20 nA, 30 kV), two trenches on both sides of the Pt deposition were created, followed by a second milling step at lower beam currents (7 nA and 5 nA at 30 kV) to receive flat surfaces of the pre-thinned, about 1 μm thick, lamella. After liftout, the samples were transferred to a TEM grid and were attached onto it with a small Pt spot. Stepwise thinning and polishing at further reduced ion beam currents (1 nA and 0.5 nA at 30 kV) produced lamellae with thicknesses of about 100–200 nm. These thin slices and the transfer onto a TEM grid are necessary for measurements by the STXM.

The STXM–NEXAFS analysis was conducted using two X-ray microscopes: (i) the X-ray microscope at beamline 5.3.2.2 (Kilcoyne et al., 2003) at the Advanced Light Source, Berkeley, CA, USA and (ii) the MAXYMUS microscope at beamline UE46-PGM-2 (Follath et al., 2010) at the synchrotron BESSY II, Helmholtz-Zentrum Berlin, Germany. Both STXM instruments are equipped with a high energy resolving grating (resolving power at the carbon K-edge: ALS $E/\Delta E \leq 5000$; BESSY II: $E/\Delta E \leq 8000$), a Fresnel zone plate, providing a spatial resolution of about 30 nm, and phosphor-coated Lucite photomultiplier tubes for the detection of transmitted photons. In this study, STXM elemental maps of certain elements of interest (i.e., Fe, Mn, Ca, and C) are presented, which have been recorded as images at discrete energies. Data were evaluated with the Interactive Data Language (IDL) widget "Analysis of X-ray microscopy Images and Spectra" (aXis2000) and the overlay images (Fig. 10) produced by Adobe Photoshop CS6.

3. Results and discussion

3.1. Imaging

Microscopic investigations revealed that the maximum thicknesses of the coatings, deposited on different underlying rock types varied between 50 and 300 μm (see Table 1). They also show that the varnish covers topographical highs of the sample surfaces, but is thicker in the micro-basins (Liu and Broecker, 2013). The varnish material fills cracks and fissures, intruding into the underlying rocks.

Internal structures of the varnish coatings were studied for comparison and characterization. Since these structures are μm to nm in size, they were visualized by the highly resolving techniques of SEM, using backscattered electron (BSE) images on FIB slices, and EPMA, on thin sections. In the microscopic view, cross sections of the South African varnishes revealed stromatolitic structures (Fig. 4a), rock varnish features observed before (Perry and Adams, 1978). Mineral grains up to 70 μm in size and cavities were identified within the South African varnish coating SA13 mM-f (Fig. 4b). Furthermore, up to 10 μm large mineral detritus, enveloped in depressions between protrusions of the stromatolitic features, were observed, similar to those described by Perry and Adams (1978) and Dorn et al. (2013) in detail. The underlying rocks of the South African samples are quartzite pebbles. The rocks underneath the varnish coatings collected in Israel are limestones with significant amounts of diatom fossils and varying amounts of quartz minerals. At the surface, in direct contact with the varnish, the calcite had been dissolved, leaving a SiO_2 rich, insoluble matrix. The Israeli varnish has an orange to black and brown color and shows cauliflower shaped internal structures (Fig. 4a). Mineral grains, which are only a few micrometers in size, are incorporated in the varnish coatings IS13 V3 and V1. Close to the contact with the coating, cavities are present within the varnish and the underlying rock (Fig. 4c, d). These cavities and mineral grains can also be observed in the Californian varnish coating CA14 JC-8 (Fig. 4f). The Californian coatings are dark brown and have smooth surfaces. Sample CA13 DV1 displays a wavy internal varnish structure in contact with the underlying rock, which is covered by flat deposits (Fig. 4e). The interpretation provided by Reneau et al. (1992), who suggested a higher trapping efficiency and higher accretion rates for rougher, lower surfaces, which decrease to the top, producing smoother surfaces over time, seems suitable to these observations. The Californian samples exhibit multiple underlying rock types, magmatites, metamorphites, and sediments (see Table 1). All varnish coatings contain cavities and cracks, but while the cavities are <0.5 μm for the Israeli and Californian samples, they can be up to 1 μm large in the South African samples. However, it cannot be excluded that the cracks are partially preparation artifacts.

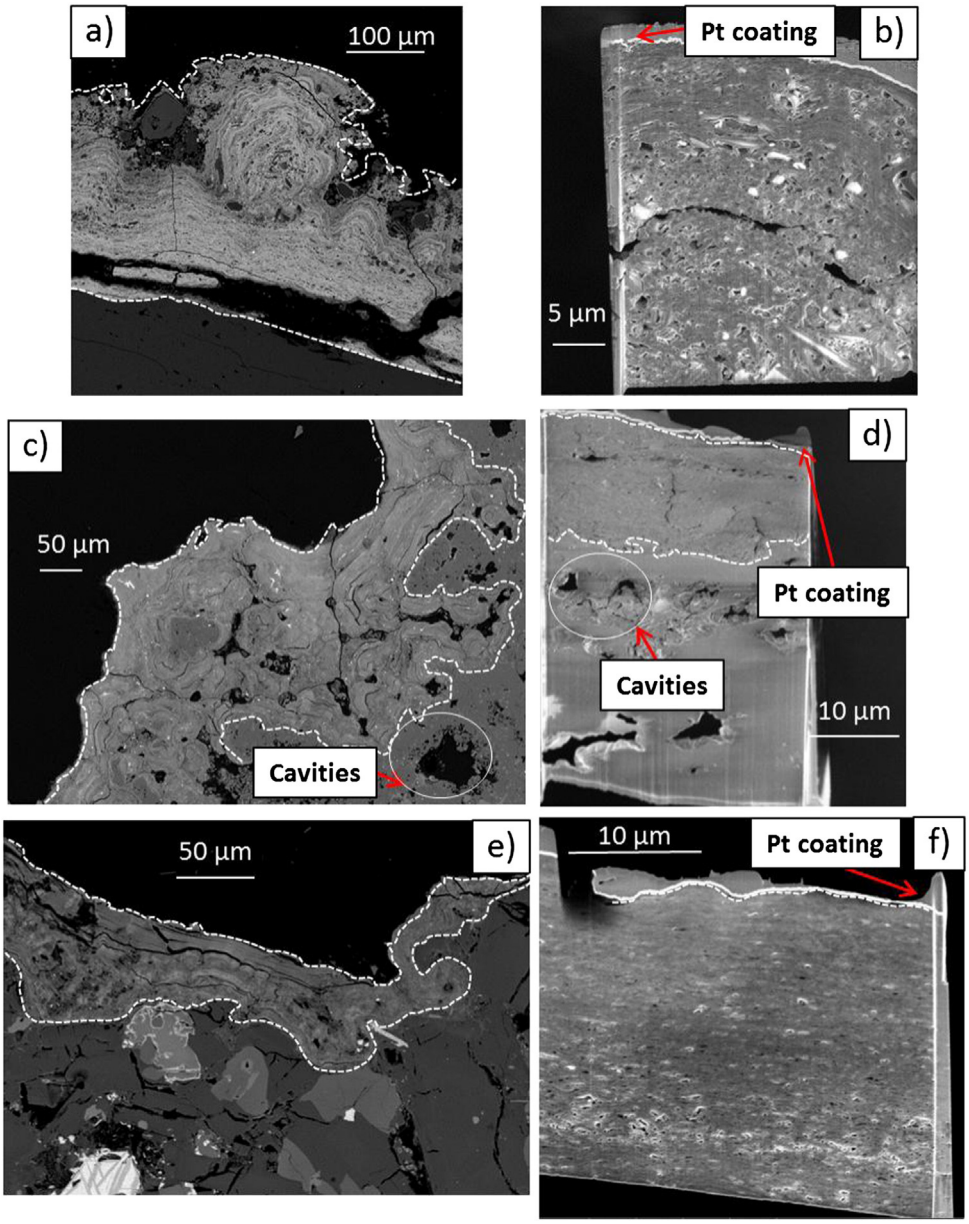

Fig. 4. a), c), e): Backscattered electron (BSE) images of varnish thick sections, revealing structures with differing average atomic numbers, Z, a) SA13 mM-f, c) IS13 V3, e) CA13 DV1. All BSE images were taken by an EPMA with an accelerating voltage of 15 kV and a beam current of 12 nA. Images b), d), f) are SEM images of FIB slices, revealing topographic structures, such as cracks, holes, and mineral inclusions, with b) SA13 mM-f, d) IS13 V1, and f) CA14 JC-8. All SEM images were produced by an FIB instrument with an accelerating voltage between 2 and 5 kV. All FIB slices had been coated on their top side by Pt, which is imaged as a light line on top of the samples and the gray matrix above. Rock-to-varnish and varnish-to-Pt boundaries are marked by white, dashed lines.

3.2. Major and trace element determination by fs LA-ICP-MS

3.2.1. Bulk analysis of major and trace elements

Appendix A shows the average analytical results for each sample. Some characteristic element enrichments are plotted in Fig. 5, where the values are normalized to those of the upper continental crust (Rudnick and Gao, 2003) and arranged approximately according to decreasing enrichments in the varnish samples. In addition to the high Mn concentrations, Pb, Co, Ce, Ni, and Ba are also enriched in all varnish samples. High Ba values have also been observed by Garvie et al. (2008). Barium is known to be capable of incorporation into manganese oxihydroxide structures, e.g., in hollandite (Post, 1999). The high enrichment of Ni, Co, and Pb is presumably due to the high adsorption potential of the Mn oxihydroxides (Thiagarajan and Lee, 2004). The source of these elements might be dust that was leached by rain or dew (Thiagarajan and Lee, 2004). An atmospheric contribution to the varnish genesis was previously verified for Pb, Hg (Nowinski et al., 2010; Nowinski et al., 2013), and ^{210}Po (Hodge et al., 2005) enrichments in the outer varnish layers, elements that were emitted by nuclear testing sites, coal-fired power plants and smelters. The enrichments in Ce, also observed in the REE patterns as positive Ce anomalies (Fig. 6), may be caused by the change from a REE-leaching reducing environment (Ce^{3+}) to an oxidizing environment (Ce^{4+}) where Ce(IV) can precipitate or be adsorbed to δ-MnO_2 or Fe oxihydroxides (Ohta and Kawabe, 2001). It strengthens the hypothesis of an aqueous atmospheric deposition as a source of these elements, previously suggested for varnish samples from the Mojave Desert and Death Valley (Thiagarajan and Lee, 2004), it might be an indicator for direct oxidation of Ce by birnessite (Post, 1999) or for the role of Mn-oxides as repositories of trace elements presumably derived from atmospheric aerosols (Garvie

et al., 2008). A positive correlation between Mn and Ce was observed for all Californian and Israeli varnish samples. However, no correlation was present for any South African varnish sample.

The element abundances agree well with literature values of rock varnish (Fig. 5, gray shaded area) published for California (Thiagarajan and Lee, 2004), Utah (Wayne et al., 2006), Nevada (Wayne et al., 2006) and Israel (Goldsmith et al., 2014). However, not all element values were provided by the manuscripts, hindering a direct comparison. The enrichments of most elements are similar, with some exceptions, such as Ti, Al, and Mg, for which few literature values are provided in these manuscripts. The differences between the Israeli and the Californian samples of this work are mostly restricted to the elements Ni and Pb, while the South African samples differ from the other locations with regard to several elements, such as Mn, Co, Ce, and Ba (Fig. 5). The Californian samples were subdivided into two groups, California A (CA WS-18, CA13 SS2, CA13 SCH45, CA13 DV1) and California B (CA13 SWS1, CA13 SWW1, CA13 SWW3, CA13 SWW4), depending on their major and trace element composition (see Appendix A). Interestingly, no chemical difference can be seen between the Israeli samples that showed different macroscopical surface structures (smooth and botryoidal). The REE results (Fig. 6) were normalized to a chondritic composition, and display positive Ce and negative Eu anomalies in all samples. The REE patterns of the samples from Israel and California are very similar, enriched in light REE (La_N/Yb_N = 11–12) and with significant positive Ce anomalies (Ce/Ce^* = 2.1–5.3). The South African samples have significantly lower light REE contents (La_N/Yb_N = ~3.5) and less positive Ce anomalies (Ce/Ce^* = ~1.5) than the other samples. The negative Eu anomaly is of about the same order for all samples (Eu/Eu^* = 0.6–0.7). The ratios of Mn/Fe (3.1–25.1 South Africa, 0.4–0.6 Israel, 0.3–1.2 California A and 0.9–2 California B), Mn/Ba (112–170 South Africa, 5–9.9 Israel, 12–28 California A and 4–11 California B), Ni/Co (0.03–2.1 South Africa, 1.1–1.8 Israel, 0.4–0.7 California A and 0.2–0.4 California B) and Pb/Ni (1.1–1.3 South Africa, 0.4–0.8 Israel, 4–13 California A, and 4–23 California B) exhibit strong variations between different locations. Fig. 7 demonstrates that these ratios are suitable for distinguishing between the locations of the varnish samples analyzed in this work. Possible reasons for these differences might be differing genesis, but also diverging dust source compositions, ages, climates,

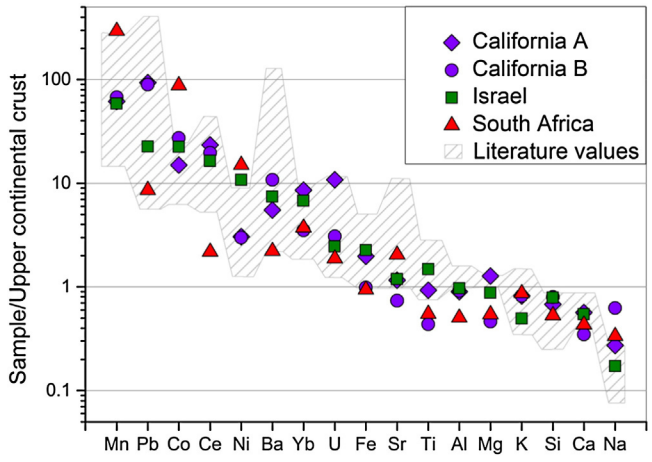

Fig. 5. Element abundances normalized to the values for the upper continental crust (Rudnick and Gao, 2003). Displayed are the enrichment factors of selected elements in the varnish. Elements are arranged approximately according to decreasing enrichment in the varnish samples. The differences between the Israeli samples and the Californian samples are most striking for the elements Ni and Pb, while the South African samples deviate for several elements, such as Mn, Co, Ce, and Ba. Within the Californian samples one can distinguish between the mean results of the samples CA WS-18, CA13 SS2, CA13 SCH45 and, CA13 DV1 (California A) and those of the samples CA13 SWS1, CA13 SWW1, CA13 SWW3 and CA13 SWW4 (California B). The gray shaded area represents the range of literature rock varnish values (Thiagarajan and Lee, 2004; Wayne et al., 2006; Goldsmith et al., 2014).

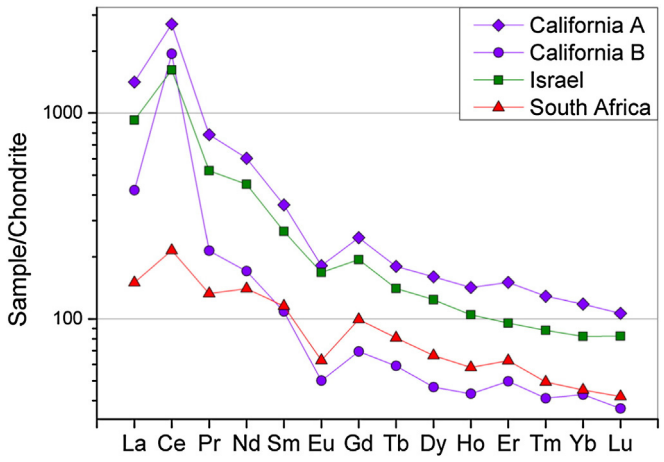

Fig. 6. Chondrite-normalized REE concentrations in the varnish samples. The patterns show a distinct positive Ce anomaly and a negative Eu anomaly. The samples from Israel and California are very similar, enriched in light REE (La_N/Yb_N = 11–12) and with a significant positive Ce anomaly (Ce/Ce^* = 2.1–5.3). The South African samples have lower light REE enrichments with La_N/Yb_N = ~3.5 and less positive Ce anomalies (Ce/Ce^* = ~1.5) than the other samples. The negative Eu anomaly is similar for all samples (Eu/Eu^* = 0.6–0.7).

rain or dew amounts or pH conditions during their growth, or even a combination of them (Engel and Sharp, 1958; Broecker and Liu, 2001).

Literature rock varnish element ratios from California, Nevada and Utah (Thiagarajan and Lee, 2004; Wayne et al., 2006) fall into the range of the Californian and Israeli rock varnish ratios from our studies. Interestingly, literature element ratios falling into the range of this studies Israeli rock varnish samples are without exception samples collected in the Cima volcanic field in the Mojave Desert (Thiagarajan and Lee, 2004). Literature values from the Death Valley (Thiagarajan and Lee, 2004), Nevada (Wayne et al., 2006) and Utah (Wayne et al., 2006) plot in the fields of this studies Californian rock varnish element ratios.

3.2.2. Profiles

Profile patterns of Mn and Fe within varnish have been used by some authors as paleoclimate reconstruction tools (Liu and Dorn, 1996), where Mn rich (25–45% MnO) layers are interpreted as wet periods, Mn poor layers (5–15% MnO) as dry periods, and layers containing moderate amounts of Mn (15–25% MnO) as periods of climatic transition between extremely dry and extremely wet conditions

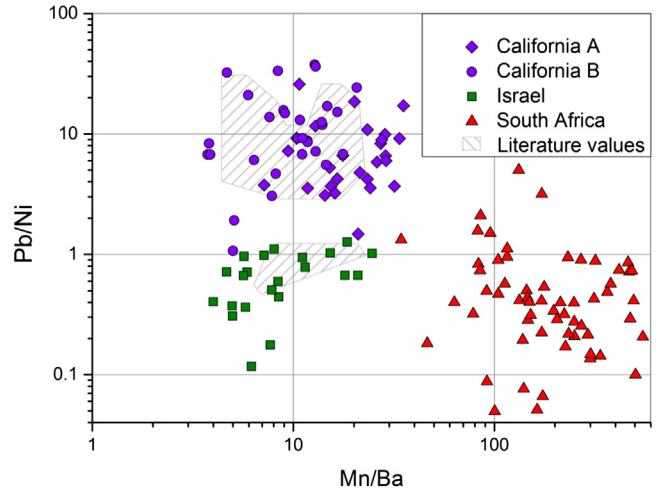

Fig. 7. Pb/Ni vs. Mn/Ba values for the three sampling locations. The data for the different sampling locations plot well separated from each other and can therefore be easily distinguished. The gray shaded area represents the range of literature rock varnish values (Thiagarajan and Lee, 2004, Wayne et al., 2006).

(Dorn, 1984; Liu and Broecker, 2013). However, these layers are extremely thin and only longer wet or dry periods can be detected by fs LA-ICP-MS with its spatial resolution of 10 μm.

Therefore, 7 to 15 high resolution MnO_2 and Fe_2O_3 profile measurements were conducted on each varnish thick section (Fig. 3). The profile patterns vary within each sample, a variation that might be influenced by the deposition process, but also by sample inhomogeneities, such as thickness differences, cavities, and mineral grain inclusions (see Fig. 4). Although there is a large scatter in the profile measurements, it is insignificant compared to the differences between the three sampling locations. This is shown in Fig. 8, where for each location one profile is plotted, representing a "typical" profile of the location (Fig. 8a, b, d). Most of the measured values of rock and resin are left out for clarity. Fig. 8 c shows the values for the MnO_2/Fe_2O_3 ratios, which differ significantly for the different locations. Typically ratios are <1 for Californian and Israeli samples for most parts of the profiles, and 10–200 for the South African samples, with variations within the profiles.

The typical Californian profile (Fig. 8b) shows a high Fe abundance (about 20%) close to the underlying rock, with MnO_2 concentrations of about 2%. About 20 μm closer to the rim, or varnish surface, the MnO_2 and Fe_2O_3 amounts rise, forming small plateaus with about 4% MnO_2 and 45% Fe_2O_3 (no. 1 in Fig. 8b). About 5 μm further outward the Fe_2O_3 concentration rises to 50% and the MnO_2 concentration increases significantly to 25% (no. 2 in Fig. 8b). At the outer rim of the varnish, MnO_2 and Fe_2O_3 have approximately the same abundance, with high Fe_2O_3 and MnO_2 concentrations of up to 50% (no. 3 in Fig. 8b).

The Israeli samples (Fig. 8c) show variations of the MnO_2 values with significant peaks for Mn and Fe. They reveal a higher total value of Fe_2O_3 throughout the profiles than the Californian samples. Manganese and Fe show common highs for some peaks, but for others, especially in the youngest and oldest varnish layers, Fe is enriched without a simultaneous Mn enrichment at the same location. The South African profiles (Fig. 8a) show significantly higher abundances of MnO_2 compared to Fe_2O_3. The MnO_2/Fe_2O_3 ratios are about 40 (Fig. 8d), and for some samples even up to 180 (not displayed). These profiles show no recurring peaks at the same distances from the rim that could be used as paleoclimate indicators. The profile patterns here might mostly depend on mineral inclusions and cavities, both of which are highly abundant in the South African samples (Fig. 4a, b). These South African rock varnish samples show therefore no internal Mn–Fe-rich VMLs (varnish microlaminations).

3.3. Major element analysis by electron probe microanalysis

The spatial resolution of the electron probe microanalysis is higher (~2 μm) than that of the fs LA-ICP-MS (10–40 μm). Since solid and homogeneous areas with few mineral grains or cavities were analyzed by EPMA, the results represent the composition of areas containing more cementing material, which is enriched in MnO_2. The data, therefore, show significantly higher MnO_2 values than those obtained by fs LA-ICP-MS (Fig. 9, Table 5). However, the values of both analytical methods from the same varnish sample lie on the same trend line in a MnO_2 vs. SiO_2 plot. These plots suggest linear mixing series between Mn/Fe oxide-rich components and Mn-free silicate end members for each sample. The correlation lines converge towards a similar SiO_2 content for the Mn-free end members, in the range of average dust compositions (50–75%, Moreno et al., 2006; Castillo et al., 2008). The individual end member values may be characteristic for the composition of the dust involved (Fig. 9). This value is lower for the Israeli samples (about 50% SiO_2) than for the South African and Californian varnish samples (about 60–65% SiO_2). A reason for this difference might be a SiO_2-poor dust composition of the Israeli varnish source. Recent Israeli dust has SiO_2 amounts of about 38% (Goldsmith et al., 2014), while recent air-borne material from the Coxcomb Mountains has much higher SiO_2 values of approximately 51% (Engel and Sharp, 1958). There is no

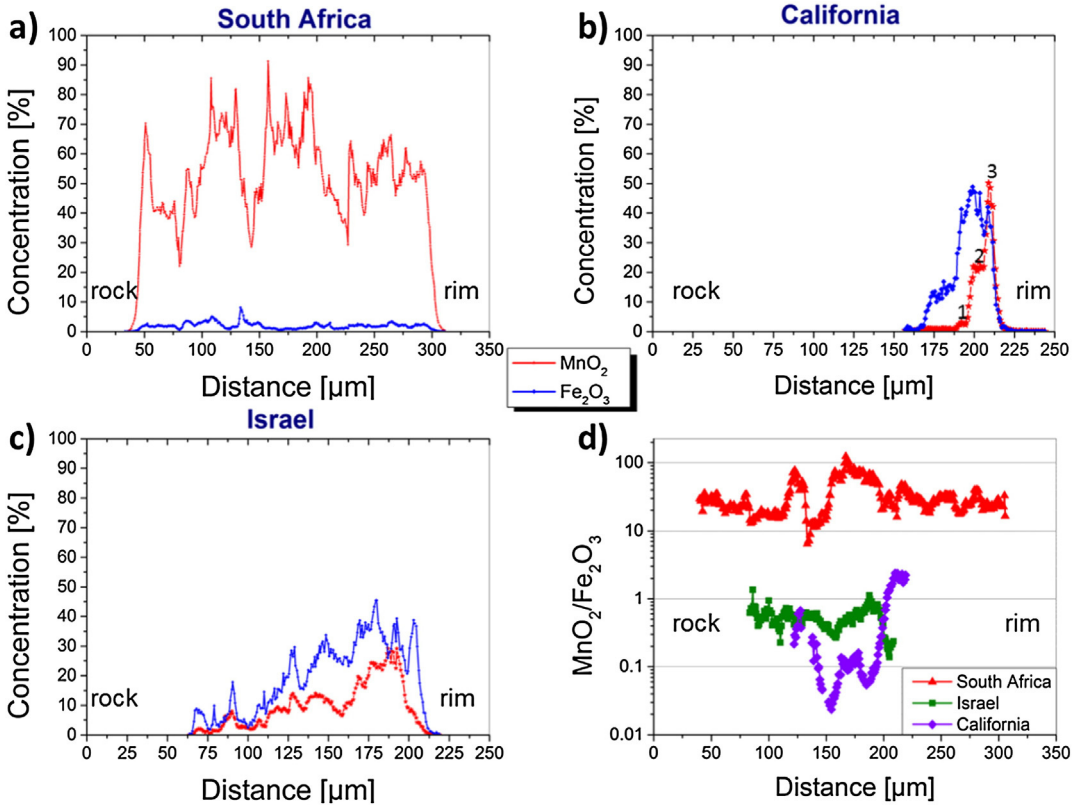

Fig. 8. Typical profiles of a) South African, b) Californian, and c) Israeli varnish samples are plotted with their MnO_2 and Fe_2O_3 concentrations. d) displays the MnO_2/Fe_2O_3 ratios of profiles a), b), and c). All measurements were performed by fs LA-ICP-MS with a scan speed of 5 μm s^{-1} and a spot size of 10 μm.

indication for a relationship between the SiO_2 content of the end member and the SiO_2 value of the underlying rock (Fig. 9), in contrast to the conclusions stated by Engel and Sharp (1958). This is especially obvious for the samples IS13 V1 and SA13 mM-f, where the quartzite in contact with the coating has a composition of almost 100% SiO_2.

3.4. Element distribution maps

For each location, one or two samples were prepared as ultra-thin FIB slices to analyze the distribution of certain elements and molecules (i.e., Mn, Fe, Ca, and CO_3^{2-}) in the varnish at the nm scale by STXM–NEXAFS. Since the NEXAFS spectra at the X-ray absorption edge are specific to functional groups and bonding states, C-, N-, and O-NEXAFS spectra were measured in addition. These elements and their bonding types can be indicators of a biological origin. A systematic investigation of the NEXAFS spectroscopy will be the focus of a future study. An organic carbon signal was detected in all samples, but no significant N was found in any mapped area. This might be an indicator for the absence of living matter, but N might also have been leached by water in strongly decomposed biological matter, or it might even be present in concentrations below the detection limit of STXM (1–3 mol% in humic substances in soil). $CaCO_3$ was excluded as a possible C-phase by selective measurements of CO_3^{2-} for each sample.

Fig. 10a displays the enrichment of Fe and Mn in a cross section through the varnish layer of the Israeli sample IS13 V1. Manganese and Fe show distinctive layers throughout the coating (at scales of about 100–500 nm), running parallel to the rock surface. This feature can be interpreted as an indicator for the sedimentary origin of the coating and the thin layers are similar to those observed by Liu and Broecker (2013), which were used for paleoclimate reconstruction. Some larger Ca-containing mineral grains (~500 nm) are mapped in sample IS13 V1 (Fig. 10a), whereas cavities are rare in this sample. The dense structure of the Israeli sample is pervaded by cracks and fissures compared to varnish from other locations (Fig. 10b, c). Carbon in the Israeli sample IS13 V1 is mostly present as a lining of cavities underneath the varnish crust in the underlying rock, and along the cracks and fissures within the varnish (Fig. 10d). This feature is distinct from the samples collected in California (Fig. 10e) and South Africa (Fig. 10f), where carbon occurs in layers or chaotic patterns.

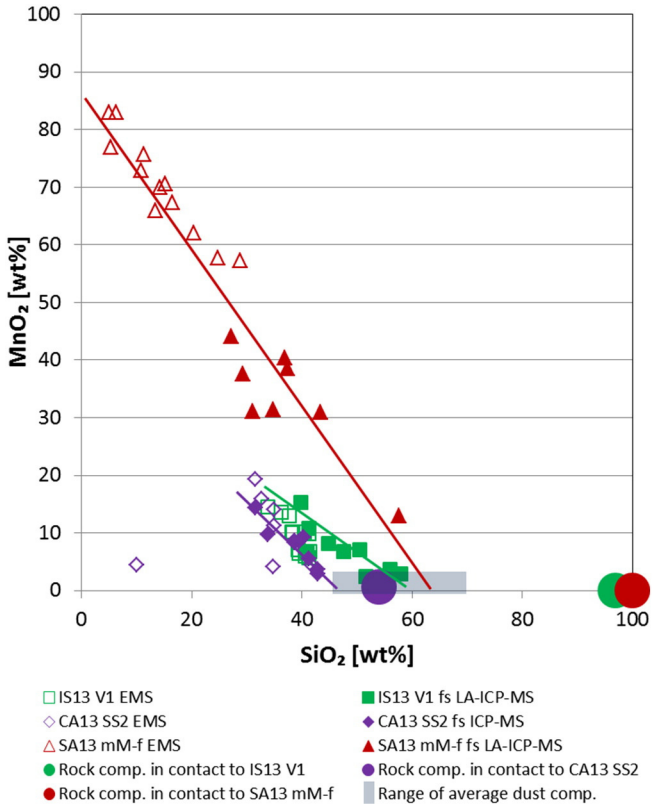

Fig. 9. EPMA and fs LA-ICP-MS MnO_2 vs. SiO_2 plots with trend lines for one sample from each sampling location. No indication of a relationship between the SiO_2 concentration of the manganese free end member and that of the rock in contact to the varnish is evident. All plots converge towards SiO_2 values in the range of average dust compositions (Moreno et al., 2006; Castillo et al., 2008).

The cavities in the underlying rock of sample IS13 V1 also show linings of Mn and Fe, and similar cavities were also observed in the Californian FIB slice, with similar element abundances (Fig. 10 g). These cavities are of specific interest, since they occur in a quartz rich limestone (IS13 V1), as well as in a basaltic rock (CA14 DV11). Their genesis might be similar to the submicron deposited Mn–Fe skins described by Garvie et al. (2008), subsequent to mineral decay in the less stable underlying rocks (Dorn et al., 2013), and is referred to as case hardening (Dorn, 2008).

The Californian samples display homogeneously distributed cavities inside the varnish (Fig. 10c) similar to those observed by Krinsley et al. (2013). In sample CA14 JC-8, Fe-containing minerals were mapped in some of these cavities which were a few hundred nanometers in size and are displayed as green areas (Fig. 10c). In the varnish FIB samples CA14 JC-8 and CA14 DV11, Mn and Fe show distinct layers parallel to the rock surface (Fig. 10c and g), similar to the layering previously observed in a FIB slices of a Death Valley sample (Krinsley et al., 2013) and furthermore used as paleoclimate reconstruction tools (Perry and Adams, 1978). A carbon-rich band, ~1 μm thick, is evident in the ultra-thin section of sample CA14 JC-8 (Fig. 10c, e). In the lower part of this sample, C is present as thin (~100 nm) rippled layers or chaotic structures (Fig. 10e). These bands are layers with higher abundances of organics, which could be residues of organisms that grew on the former varnish surfaces, as proposed by Wang et al. (2011), or organic-rich dust that was deposited with the sedimentation process, and that was incorporated during the varnish genesis.

The South African sample SA13 mM-f contains numerous large (up to 5 μm long) mineral grains, many of them containing Fe (Fig. 10b, h). Large cavities of several μm are irregularly distributed throughout the sample. Structures defined by elevated Fe and Mn contents are present, but seem to be mainly an effect of density variations rather than compositional differences. Calcium is enriched in the upper part of the FIB slice as layers, following a cauliflower-like structure (Fig. 10 h) similar to those observed in rock varnish FIB slices before (Krinsley et al., 2013). Carbon is present throughout the sample, but is especially enriched in the lining of cavities (Fig. 10f). A possible interpretation is that the cavities were formerly filled by organic material that decayed leaving cavities with organic C signatures at their rims.

3.5. Structures at the nm to μm scale

The combination of different analytical techniques at different scales demonstrates considerable variability within the coatings. The techniques used were the fs LA-ICP-MS with 10–40 μm spatial resolution, the EPMA with 2 μm resolution, and the STXM–NEXAFS with a resolution of about 30 nm. Layerings in the Israeli and Californian rock varnish samples can be observed at each scale, with the thinnest detected Mn layers in the 100–500 nm range. These layers have similar extensions to those observed by Liu and Broecker (2013), who interpreted them as indicators for climate fluctuations and as a paleoclimate reconstruction tool for the Quaternary period. A layer of 100–500 nm thickness could represent an age interval of about 100–500 years, assuming a growth rate of 1 μm per 1000 a. These intervals are in the range of typical climate fluctuations during the Holocene.

The Israeli and Californian samples seem very similar regarding their elemental composition at the 10–40 μm scale, but differ for selected elemental abundances, such as Ni and Pb (Fig. 7). The Californian samples can furthermore be subdivided into California A and B, based on their

Table 5
Concentrations of major elements in the varnishes, obtained by EPMA measurements.

	Na_2O	SiO_2	K_2O	TiO_2	Fe_2O_3	Al_2O_3	MgO	CaO	Cr_2O_3	MnO_2
SA10 #4 [wt %]	0.97	17.40	2.32	0.20	4.69	8.29	1.06	0.60	0.04	54.09
RSD [%]	28	46	15	52	52	39	24	13	59	23
SA10 #8 [wt %]	1.47	9.52	3.51	0.07	2.58	4.27	0.88	0.38	0.05	71.51
RSD [%]	9	40	11	71	45	41	32	19	76	11
SA13 mM-d [wt %]	0.83	10.29	2.44	0.11	3.52	5.95	1.99	1.58	0.04	60.07
RSD [%]	23	59	14	77	56	57	15	16	47	21
SA13 mM-f [wt %]	0.96	14.35	3.73	0.05	2.24	3.39	0.82	0.43	0.03	68.50
RSD [%]	29	52	13	68	50	49	38	34	87	15.12
Average South Africa [wt %]	0.91	12.29	3.05	0.10	3.01	5.73	1.26	1.11	0.03	63.56
RSD [%]	33	30	21	46	29	32	42	51	36	12
CA13 SWW1 [wt %]	0.37	33.32	1.92	0.44	10.80	19.56	2.16	0.84	0.04	18.04
RSD [%]	50	4	12	24	14	3	9	13	36	13
CA13 SWW3 [wt %]	0.29	30.22	1.81	0.44	12.25	19.58	2.21	1.17	0.04	19.46
RSD [%]	28	5	10	22	19	4	8	17	77	16
CA13 SS2 [wt %]	0.30	31.52	1.95	0.50	20.82	17.34	2.84	1.22	0.02	10.46
RSD [%]	21	32	48	43	93	27	29	27	87	60
CA13 DV1 [wt %]	0.44	28.78	1.70	0.58	15.69	19.15	2.19	1.18	0.04	16.90
RSD [%]	35	14	12	29	36	8	16	31	63	46
Average California [wt %]	0.31	27.89	1.65	0.51	14.18	18.19	2.12	1.15	0.04	19.27
RSD [%]	25	19	19	12	27	10	23	13	21	34
IS13 V1 [wt %]	0.25	39.01	1.67	0.74	12.68	20.13	2.53	1.30	0.04	9.67
RSD [%]	18	6	8	25	11	9	7	16	50	32
IS13 V2a [wt %]	0.26	35.97	1.61	0.72	14.02	19.69	2.38	1.58	0.05	9.00
RSD [%]	40	8	10	35	9	4	10	14	55	28
IS13 V3 [wt %]	0.22	32.80	1.34	0.63	10.13	17.40	2.99	1.88	0.04	17.11
RSD [%]	25	9	15	54	18	9	7	21	57	36
Average Israel [wt %]	0.24	35.93	1.54	0.70	12.28	19.08	2.63	1.59	0.04	11.92
RSD [%]	10	9	11	8	16	8	12	18	9	38

elemental abundances. Interestingly, these two groups were collected from two differing sampling areas within California, which are located 120–250 km apart from each other (see Table 1). An explanation might therefore be a slightly different composition of the varnish dust source. Nevertheless, all Californian samples have significantly higher Pb concentrations than the samples from Israel and South Africa (about 10 times more). The explanation therefore might be a larger Pb input by human activity in this area, for example from the previous use of leaded gasoline or from power plants (Nowinski et al., 2010; Dorn et al., 2012b).

By combining EPMA with its 2 μm spatial resolution, and fs LA-ICP-MS, each analyzed varnish coating can be extrapolated back to a manganese free end member, which differs for the various sampling locations. Furthermore, future fs LA-ICP-MS measurements provide the possibility to add compositional variations to areas of a given climate. Adding STXM–NEXAFS at the nm scale, layers in the nm range can also be observed, and C abundances and speciation can be detected and characterized.

4. Conclusions

Rock varnishes show chemical and structural features at the μm to nm scale. The most striking ones are layerings, mineral grain inclusions, and cavities within the varnish. Internal layerings in the 100–500 nm range within the coatings are defined by differing Mn, Fe, and C abundances. Cavities lined by Mn, Fe, and C rich material were found in the underlying rocks of the Californian and Israeli samples, close to and in contact with the varnish coating. The South African samples differ from those from the other analyzed locations at all scales, based on elemental ratios and internal structures without Mn and Fe layering, larger mineral grains, and bigger cavities than the other samples.

The SiO_2 contents of the Mn free end members are independent of the composition of the underlying rock. The SiO_2 concentrations in these Mn free end members are similar to those in dust from different locations, with 50–75% SiO_2 (Moreno et al., 2006; Castillo et al., 2008). The Israeli end member is at the lower end of the range (about 50%) and the Californian and South African end members are in the middle of the range of dust values (about 60%).

The analyzed coatings from different regions can be distinguished by their elemental ratios. The Californian samples can be further separated into two sub-regions that are about 120–250 km apart. Bulk analyses of the coatings show that of the major elements, only Mn and Fe are enriched in comparison to the upper continental crust (Rudnick and Gao, 2003), whereas many trace elements, such as Pb, Co, Ni, Ba, the REEs, U, Th, and Y, are significantly enriched. These enrichments occur in all samples, but differ in their magnitude. Ratio plots of Pb/Ni vs. Mn/Ba show similarities within one sampling location and significant differences between the various regions. The MnO_2/Fe_2O_3 ratios show significant differences (a factor of 10 to 100) between the South African varnish samples and those collected in Israel and California. However, a significant positive Ce anomaly was detected in all samples, which might be an indicator for a direct atmospheric deposition of the REEs, and therefore an atmospheric contribution to the origin of all varnish coatings analyzed. A positive correlation between Ce and Mn was observed for the Israeli and Californian varnish samples, though no correlation was found concerning the South African rock varnish samples.

Carbon was found in every analyzed FIB sample, but in the Israeli sample it was found solely along cracks and fissures. In this sample the carbon could have been introduced subsequent to the varnish genesis, unlike in the other samples, where C was detected as layers or cavity linings. The C signatures, analyzed by STXM–NEXAFS, are dominated by carboxylate functionalities and are therefore indicators of a biological contribution to the varnish composition. Whether these organic contributions triggered the varnish growth, or if the availability of a solid and stable inorganic crust allowed organisms to accrete, or if the organic material was incorporated from particles with an atmospheric origin cannot be determined up to now.

Profile plots of the varnish measurements perpendicular to its growth direction display nicely the transition metal variations within the varnish. Such profiles display internal features, such as layerings within the varnish, and may be used for paleoclimate reconstruction (Dorn, 1984; Liu and Broecker, 2013). The profiles vary within one location and even within one rock, and differ significantly between different sampling countries.

The differences in structure and chemical composition found in our samples suggest at least two different groups of the analyzed varnish,

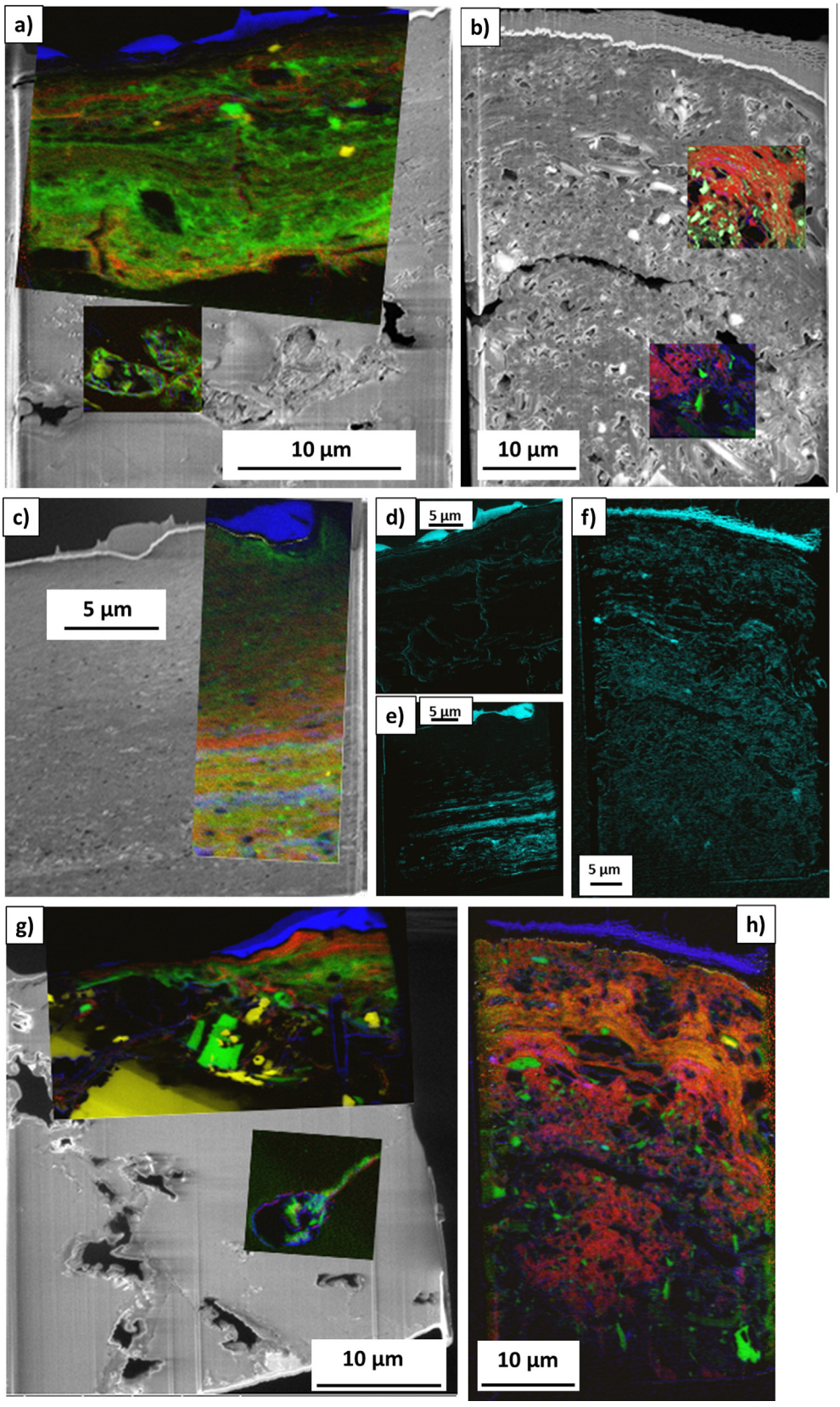

Fig. 10. FIB slices with element maps to display the elemental distribution. Color keys for the multi-element maps: red: Mn; green: Fe; blue: C; yellow: Ca. a) FIB slice of IS13 V1 with mapped varnish area and cavity fillings. b) FIB slice of SA13 mM-f with selected mapped areas. h) Map of the whole FIB-prepared varnish SA13 mM-f. c) FIB slice of CA14 JC-8 with selected mapped area. g) FIB-prepared varnish sample CA14 DV11 with mapped cavity filling and thin varnish. d), e), f) C-maps of the samples, C mapped in blue. d) sample IS13 V1, e) sample CA14 JC-8, f) sample SA13 mM-f. The Pt coating on top of the samples (displayed in the FIB slices as a light colored cover with a gray topping) shows C enrichments that are not related to the varnish but to the metallo-organic Pt precursor.

one represented by the South African samples, the other by the Californian and Israeli samples. One may even distinguish three categories, where the Israeli samples represent a third, carbon-poor category. Further investigations are necessary to see whether the differences observed here can be generalized to other regions, and how they can be used to resolve the enigma of the formation of rock varnishes.

Supplementary data to this article can be found online at http://dx.doi.org/10.1016/j.chemgeo.2015.06.023.

Acknowledgments

This work was supported by the Max Planck Graduate Center with the Johannes Gutenberg University Mainz (MPGC), the Max Planck Society, and King Saud University. The ALS is supported by the Director, Office of Science, Office of Basic Energy Sciences, of the US Department of Energy under Contract DE-AC02-05CH11231. We thank the Helmholtz-Zentrum Berlin for the allocation of the synchrotron radiation beamtime at BESSY II. Sampling of desert varnish in Israel was conducted during a granted ExpeER project. We furthermore thank Maik Biegler who prepared the varnish thin and thick sections, Jan-David Förster who helped with the thin section preparation and the STXM measurements, Tanzhuo Liu who provided the sample CA WS-18, and Michael Bechtel (BESSY) who always helps a lot with the STXM sessions.

References

Armstrong, J.T., 1991. Quantitative elemental analysis of individual microparticles with electron beam instruments. In: Heinrich, K.F.J., Newbury, D.E. (Eds.), Electron Probe Quantitation. Plenum Press, pp. 261–315.
Broecker, W.S., Liu, T., 2001. Rock varnish: record of desert wetness? GSA Today 4–10 (August: 4–10).
Castillo, S., Moreno, T., Querol, X., Alastuey, A., Cuevas, E., Herrmann, L., Mounkaila, M., Gibbons, W., 2008. Trace element variation in size-fractionated African desert dusts. J. Arid Environ. 72 (6), 1034–1045.
Dorn, R.I., 1984. Cause and implications of rock varnish microchemical laminations. Nature 310 (5980), 767–770.
Dorn, R.I., 2008. Rock Varnish in Geochemical Sediments and Landscapes. In: Nash, D.J., McLaren, S.J. (Eds.), Blackwell Publishing Ltd., Oxford, UK, pp. 246–297 (Chapter 8).
Dorn, R.I., Krinsley, D.H., Ditto, J., 2012a. Revisiting Alexander von Humboldt's initiation of rock coating research. J. Geol. 120 (1), 1–14.
Dorn, R.I., Moore, G., Pagan, E.O., Bostwick, T.W., King, M., Ostapuk, P., 2012b. Assessing early Spanish explorer routes through authentication of rock inscriptions. Prof. Geogr. 64 (3), 415–429.
Dorn, R.I., Krinsley, D.H., Langworthy, K.A., Ditto, J., Thompson, T.J., 2013. The influence of mineral detritus on rock varnish formation. Aeolian Res. 10, 61–76.
Engel, C.G., Sharp, R.P., 1958. Chemical data on desert varnish. Geol. Soc. Am. Bull. 69 (5), 487.
Follath, R., Schmidt, J.S., Weigand, M., Fauth, K., 2010. The X-ray microscopy beamline UE46-PGM2 at BESSY. In: Garrett, R., Gentle, I., Nugent, K., Wilkins, S. (Eds.), Sri 2009: The 10th International Conference on Synchrotron Radiation Instrumentation. AIP Conference Proceedings, pp. 323–326.
Garvie, L.A.J., Burt, D.M., Buseck, P.R., 2008. Nanometer-scale complexity, growth, and diagenesis in desert varnish. Geology 36 (3), 215–218.
Goldsmith, Y., Stein, M., Enzel, Y., 2014. From dust to varnish: geochemical constraints on rock varnish formation in the Negev Desert, Israel. Geochim. Cosmochim. Acta 126, 97–111.
Hodge, V.F., Farmer, D.E., Diaz, T., Orndorff, R.L., 2005. Prompt detection of alpha particles from Po-210: another clue to the origin of rock varnish? J. Environ. Radioact. 78 (3), 331–342.
Jochum, K.P., Stoll, B., Herwig, K., Willbold, M., 2007. Validation of LA-ICP-MS trace element analysis of geological glasses using a new solid-state 193 nm Nd:YAG laser and matrix-matched calibration. J. Anal. At. Spectrom. 22 (2), 112–121.
Jochum, K.P., Stoll, B., Weis, U., Jacob, D.E., Mertz-Kraus, R., Andreae, M.O., 2014. Non-matrix-matched calibration for the multi-element analysis of geological and environmental samples using 200 nm femtosecond LA-ICP-MS: a comparison with nanosecond lasers. Geostand. Geoanal. Res. 38 (3), 265–292.
Kilcoyne, A.L.D., Tyliszczak, T., Steele, W.F., Fakra, S., Hitchcock, P., Franck, K., Anderson, E., Harteneck, B., Rightor, E.G., Mitchell, G.E., Hitchcock, A.P., Yang, L., Warwick, T., Ade, H., 2003. Interferometer-controlled scanning transmission X-ray microscopes at the Advanced Light Source. J. Synchrotron Radiat. 10, 125–136.
Krinsley, D., Dorn, R.I., DiGregorio, B., 2009. Astrobiological implications of rock varnish in Tibet. Astrobiology 9 (6), 551–562.
Krinsley, D.H., Dorn, R.I., DiGregorio, B.E., Langworthy, K.A., Ditto, J., 2012. Rock varnish in New York: an accelerated snapshot of accretionary processes. Geomorphology 138 (1), 339–351.
Krinsley, D., Ditto, J., Langworthy, K., Dorn, R.I., Thompson, T., 2013. Varnish microlaminations: new insights from focused ion beam preparation. Phys. Geogr. 34 (3), 159–173.
Liu, T.H., Broecker, W.S., 2000. How fast does rock varnish grow? Geology 28 (2), 183–186.
Liu, T., Broecker, W.S., 2013. Millennial-scale varnish microlamination dating of late Pleistocene geomorphic features in the drylands of western USA. Geomorphology 187, 38–60.
Liu, T.Z., Dorn, R.I., 1996. Understanding the spatial variability of environmental change in drylands with rock varnish microlaminations. Ann. Assoc. Am. Geogr. 86 (2), 187–212.
Macholdt, D.S., Jochum, K.P., Stoll, B., Weis, U., Andreae, M.O., 2014. A new technique to determine element amounts down to femtograms in dust using femtosecond laser ablation-inductively coupled plasma-mass spectrometry. Chem. Geol. 383, 123–131.
Moreno, T., Querol, X., Castillo, S., Alastuey, A., Cuevas, E., Herrmann, L., Mounkaila, M., Elvira, J., Gibbons, W., 2006. Geochemical variations in aeolian mineral particles from the Sahara-Sahel Dust Corridor. Chemosphere 65 (2), 261–270.
Northup, D.E., Snider, J.R., Spilde, M.N., Porter, M.L., van de Kamp, J.L., Boston, P.J., Nyberg, A.M., Bargar, J.R., 2010. Diversity of rock varnish bacterial communities from Black Canyon, New Mexico. J. Geophys. Res. Biogeosci. 115.
Nowinski, P., Hodge, V.F., Lindley, K., Cizdziel, J.V., 2010. Elemental analysis of desert varnish samples in the vicinity of coal-fired power plants and the Nevada test site using laser ablation ICP-MS. Chem. Biomed. Methods J. 3, 153–168.
Nowinski, P., Hodge, V.F., Gerstenberger, S., Cizdziel, J.V., 2013. Analysis of mercury in rock varnish samples in areas impacted by coal-fired power plants. Environ. Pollut. 179, 132–137.
Ohta, A., Kawabe, I., 2001. REE(III) adsorption onto Mn dioxide (delta-MnO_2) and Fe oxyhydroxide: Ce(III) oxidation by delta-MnO_2. Geochim. Cosmochim. Acta 65 (5), 695–703.
Perry, R.S., Adams, J.B., 1978. Desert varnish: evidence for cyclic deposition of manganese. Nature 276 (5687), 489–491.
Perry, R.S., Kolb, V.M., 2004. Biological and organic constituents of desert varnish: review and new hypotheses. In: Hoover, R.B., Rozanov, A.Y. (Eds.), Instruments, Methods, and Missions for Astrobiology VII 5163, pp. 202–217.
Perry, R.S., Lynne, B.Y., Sephton, M.A., Kolb, V.M., Perry, C.C., Staley, J.T., 2006. Baking black opal in the desert sun: the importance of silica in desert varnish. Geology 34 (7), 537–540.
Post, J.E., 1999. Manganese oxide minerals: crystal structures and economic and environmental significance. Proc. Natl. Acad. Sci. U. S. A. 96 (7), 3447–3454.
Potter, R.M., Rossman, G.R., 1979. The manganese- and iron-oxide mineralogy of desert varnish. Chem. Geol. 25, 79–94.
Reneau, S.L., Raymond, R., Harrington, C.D., 1992. Elemental relationships in rock varnish stratigraphic layers, Cima volcanic field, California — implications for varnish development and the interpretation of varnish chemistry. Am. J. Sci. 292 (9), 684–723.
Rudnick, R.L., Gao, S., 2003. 3.01 — Composition of the Continental Crust 3. Treatise On Geochemistry, Elsevier Ltd., pp. 1–64.
Spilde, M.N., Melim, L.A., Northup, D.E., Boston, P.J., 2013. Anthropogenic lead as a tracer of rock varnish growth: implications for rates of formation. Geology 41 (2), 263–266.
Thiagarajan, N., Lee, C.T.A., 2004. Trace-element evidence for the origin of desert varnish by direct aqueous atmospheric deposition. Earth Planet. Sci. Lett. 224 (1–2), 131–141.
Von Humboldt, A., Bonpland, A., 1819. Voyage aux régions équinoxiales du nouveau continent. pp. 299–304 (II(Book VII Chapter XX)).
Wang, X., Zeng, L., Wiens, M., Schlossmacher, U., Jochum, K.P., Schroeder, H.C., Mueller, W.E.G., 2011. Evidence for a biogenic, microorganismal origin of rock varnish from the Gangdese Belt of Tibet. Micron 42 (5), 401–411.
Wayne, D.M., Diaz, T.A., Fairhurst, R.J., Orndorff, R.L., Pete, D.V., 2006. Direct major- and trace-element analyses of rock varnish by high resolution laser ablation inductively-coupled plasma mass spectrometry (LA-ICPMS). Appl. Geochem. 21 (8), 1410–1431.

Appendix A

Table A: Results of fs LA-ICP-MS measurements of all samples. Measurements were conducted with 40 µm spot sizes, 1 µm s^{-1} scan speed, and all results are averaged values of each sample.

		CA WS18			CA DV1			CA SCH45		
Element	Isotope used	mass fraction	RSD	$U_{El,rel}$	mass fraction	RSD	$U_{El,rel}$	mass fraction	RSD	$U_{El,rel}$
		[µg g^{-1}]	[%]	[%]	[µg g^{-1}]	[%]	[%]	[µg g^{-1}]	[%]	[%]
Na	^{23}Na	1914	42	34	7784	31	24	7694	70	55
Mg	^{25}Mg	13267	24	22	24267	54	35	42658	49	39
Al	^{27}Al	116581	11	17	87366	24	20	63702	43	35
Si	^{29}Si	124600	9	17	168434	11	17	189302	24	23
P	^{31}P	23808	15	42	10857	54	50	4138	83	74
K	^{39}K	15839	13	18	12392	30	23	9583	61	48
Ca	^{43}Ca	19492	25	24	25277	80	49	42269	74	58
Ti	^{47}Ti	5911	59	45	6618	68	43	6623	71	56
Mn	^{55}Mn	116592	11	17	78293	35	25	57149	62	49
Fe	^{57}Fe	100441	12	18	114588	30	23	113292	63	50
Co	^{59}Co	553	13	18	447	33	24	385	54	44
Ni	^{60}Ni	252	20	21	191	38	28	264	41	34
Rb	^{85}Rb	96	20	21	78	26	21	64	61	48
Sr	^{88}Sr	1350	29	26	374	23	20	516	54	44
Y	^{89}Y	273	17	20	271	33	24	199	53	43
Cs	^{133}Cs	9	14	19	11	29	23	7	66	52
Ba	^{138}Ba	8527	17	19	2745	35	25	3879	65	51
La	^{139}La	535	14	18	479	33	24	448	62	49
Ce	^{140}Ce	2756	15	19	2451	35	25	1922	71	56
Pr	^{141}Pr	123	16	19	108	34	25	96	64	50
Nd	^{143}Nd	469	16	18	427	35	25	363	62	49
Sm	^{147}Sm	90	14	18	85	33	24	68	58	46
Eu	^{151}Eu	17	17	19	15	32	24	12	53	43
Gd	^{157}Gd	76	14	18	79	34	24	58	59	47
Tb	^{159}Tb	11	17	19	11	34	25	8	54	43
Dy	^{161}Dy	63	18	19	66	33	24	50	57	45
Ho	^{165}Ho	12	16	19	13	32	24	9	59	47
Er	^{167}Er	42	17	23	42	31	23	27	57	45
Tm	^{169}Tm	5	17	19	5	32	24	4	57	45
Yb	^{173}Yb	29	18	19	30	32	24	23	60	47
Lu	^{175}Lu	4	18	19	5	30	23	3	57	45
Pb	^{208}Pb	946	15	18	1383	44	30	3286	91	71
Th	^{232}Th	153	10	17	177	31	24	135	135	103
U	^{238}U	52	10	17	36	28	22	25	69	54

Table A continued

		CA SS2			CA SWW1			CA SWW3		
Element	Isotope used	mass fraction	RSD	$U_{El,rel}$	mass fraction	RSD	$U_{El,rel}$	mass fraction	RSD	$U_{El,rel}$
		[µg g^{-1}]	[%]	[%]	[µg g^{-1}]	[%]	[%]	[µg g^{-1}]	[%]	[%]
Na	^{23}Na	8389	36	28	12951	27	26	24006	67	69
Mg	^{25}Mg	22602	35	27	6292	43	36	6239	28	32
Al	^{27}Al	94016	11	16	83621	23	23	76446	21	26
Si	^{29}Si	190993	10	16	258067	22	22	242669	22	27
P	^{31}P	6414	31	45	3253	31	46	5694	34	50
K	^{39}K	28357	45	33	18278	16	19	14387	44	46
Ca	^{43}Ca	10114	29	25	17265	44	36	13057	27	31
Ti	^{47}Ti	7303	107	73	1786	44	38	2556	21	27
Mn	^{55}Mn	52693	44	33	53466	59	47	83191	50	52
Fe	^{57}Fe	109461	22	20	50091	37	32	41807	30	34
Co	^{59}Co	293	39	30	686	52	42	877	41	44
Ni	^{60}Ni	160	28	24	118	51	41	168	62	64
Rb	^{85}Rb	155	31	25	90	24	23	72	35	38
Sr	^{88}Sr	363	24	21	217	58	46	365	56	58
Y	^{89}Y	182	52	38	243	50	41	88	79	80
Cs	^{133}Cs	17	86	59	4	40	34	4	41	44
Ba	^{138}Ba	4434	27	23	5909	90	69	8076	52	54
La	^{139}La	348	57	41	291	48	39	227	68	69
Ce	^{140}Ce	1667	42	31	1303	45	37	1550	45	47
Pr	^{141}Pr	80	55	39	65	40	34	45	76	77
Nd	^{143}Nd	302	55	39	254	42	35	169	72	74
Sm	^{147}Sm	58	55	39	67	39	33	32	74	75
Eu	^{151}Eu	11	42	31	7	55	44	7	64	66
Gd	^{157}Gd	50	55	39	63	41	34	27	81	83
Tb	^{159}Tb	7	53	38	10	39	33	4	77	79
Dy	^{161}Dy	46	51	37	57	42	35	22	77	79
Ho	^{165}Ho	9	52	37	11	46	38	4	84	85
Er	^{167}Er	30	52	39	29	53	44	12	77	78
Tm	^{169}Tm	4	55	39	3	46	38	2	78	79
Yb	^{173}Yb	26	66	46	18	61	48	11	62	64
Lu	^{175}Lu	4	71	49	2	38	32	2	52	54
Pb	^{208}Pb	2099	46	34	1439	87	67	3223	30	34
Th	^{232}Th	95	38	29	82	43	36	43	42	45
U	^{238}U	39	49	36	20	32	29	13	59	61

Table A continued

		CA SWW4			CA SWS1			IS V1		
Element	Isotope used	mass fraction	RSD	$U_{El,rel}$	mass fraction	RSD	$U_{El,rel}$	mass fraction	RSD	$U_{El,rel}$
		[µg g^{-1}]	[%]	[%]	[µg g^{-1}]	[%]	[%]	[µg g^{-1}]	[%]	[%]
Na	^{23}Na	8765	26	29	25576	56	52	5206	47	33
Mg	^{25}Mg	10343	44	42	5258	36	35	14754	12	13
Al	^{27}Al	65715	47	44	78972	17	21	88706	12	13
Si	^{29}Si	224318	29	30	266817	17	21	233399	14	14
P	^{31}P	23770	72	76	2565	52	60	4243	31	41
K	^{39}K	11350	39	38	35647	52	49	12595	7	11
Ca	^{43}Ca	35586	27	29	12299	42	40	15955	26	20
Ti	^{47}Ti	2760	77	71	4193	109	99	4784	25	21
Mn	^{55}Mn	75570	42	40	36215	31	31	50628	57	40
Fe	^{57}Fe	52455	71	65	40153	140	126	81468	17	15
Co	^{59}Co	621	45	43	214	43	41	382	31	23
Ni	^{60}Ni	225	57	53	118	47	45	449	26	20
Rb	^{85}Rb	68	46	44	92	36	36	80	7	11
Sr	^{88}Sr	257	28	29	224	19	22	367	63	43
Y	^{89}Y	125	88	80	51	56	52	127	33	25
Cs	^{133}Cs	5	52	50	4	19	22	5	13	14
Ba	^{138}Ba	6877	30	31	8970	23	25	5173	90	61
La	^{139}La	301	85	77	131	37	36	178	35	25
Ce	^{140}Ce	2061	45	43	565	39	38	912	27	21
Pr	^{141}Pr	56	88	80	33	38	37	43	31	23
Nd	^{143}Nd	213	85	78	133	47	44	177	34	25
Sm	^{147}Sm	40	78	71	24	55	51	37	27	21
Eu	^{151}Eu	8	82	75	5	117	106	8	30	23
Gd	^{157}Gd	35	78	71	18	54	51	34	31	23
Tb	^{159}Tb	4	77	71	2	66	61	5	33	24
Dy	^{161}Dy	26	81	74	13	58	53	28	32	23
Ho	^{165}Ho	5	81	74	2	44	42	5	32	23
Er	^{167}Er	19	81	74	7	36	37	15	31	23
Tm	^{169}Tm	2	67	62	1	34	33	2	30	22
Yb	^{173}Yb	12	71	65	6	36	35	13	25	20
Lu	^{175}Lu	2	82	75	1	49	46	2	27	21
Pb	^{208}Pb	1680	122	110	301	59	55	339	31	23
Th	^{232}Th	39	86	79	21	36	36	19	31	23
U	^{238}U	19	106	97	8	27	28	5	18	17

Table A continued

		IS V2a			IS V4			SA #4		
Element	Isotope used	mass fraction	RSD	$U_{El,rel}$	mass fraction	RSD	$U_{El,rel}$	mass fraction	RSD	$U_{El,rel}$
		[µg g^{-1}]	[%]	[%]	[µg g^{-1}]	[%]	[%]	[µg g^{-1}]	[%]	[%]
Na	^{23}Na	7025	59	54	3609	46	35	7266	26	26
Mg	^{25}Mg	11557	28	27	11375	52	38	10421	20	24
Al	^{27}Al	74413	29	28	63468	49	36	46179	28	26
Si	^{29}Si	250056	15	17	250049	20	18	122129	37	29
P	^{31}P	5435	41	52	4409	35	48	3887	29	58
K	^{39}K	10277	29	27	10168	62	45	20842	18	24
Ca	^{43}Ca	15762	16	18	12780	28	23	15935	24	25
Ti	^{47}Ti	6265	41	39	8492	64	47	3688	83	49
Mn	^{55}Mn	41958	11	14	48220	31	24	285341	23	25
Fe	^{57}Fe	85519	29	28	98859	39	30	42345	33	28
Co	^{59}Co	352	17	19	432	27	22	1627	30	27
Ni	^{60}Ni	392	13	16	683	38	29	504	18	24
Rb	^{85}Rb	57	25	25	53	58	42	90	23	25
Sr	^{88}Sr	426	34	32	524	36	27	921	22	24
Y	^{89}Y	145	39	37	151	37	29	83	11	23
Cs	^{133}Cs	4	29	28	4	56	41	6	32	28
Ba	^{138}Ba	4612	55	50	8923	48	36	1888	37	29
La	^{139}La	227	46	42	296	40	30	49	30	27
Ce	^{140}Ce	977	27	26	1102	20	17	171	35	28
Pr	^{141}Pr	52	42	39	63	36	28	16	21	24
Nd	^{143}Nd	209	42	39	254	38	28	79	18	24
Sm	^{147}Sm	42	36	33	48	35	27	18	19	24
Eu	^{151}Eu	10	37	34	11	29	24	3	19	24
Gd	^{157}Gd	39	38	35	46	29	23	21	16	23
Tb	^{159}Tb	5	38	36	6	36	27	3	19	24
Dy	^{161}Dy	32	34	32	35	31	24	18	17	23
Ho	^{165}Ho	6	33	31	7	36	27	3	18	23
Er	^{167}Er	16	33	32	17	37	28	12	16	23
Tm	^{169}Tm	2	31	30	2	42	31	1	28	26
Yb	^{173}Yb	13	38	35	14	31	24	9	20	24
Lu	^{175}Lu	2	31	29	2	38	29	1	41	30
Pb	^{208}Pb	354	26	25	473	56	43	198	55	36
Th	^{232}Th	20	31	30	27	32	25	23	35	28
U	^{238}U	9	44	41	7	47	37	4	45	32

Table A continued

		SA #8			SA #9			SA #12		
Element	Isotope used	mass fraction	RSD	$U_{El,rel}$	mass fraction	RSD	$U_{El,rel}$	mass fraction	RSD	$U_{El,rel}$
		[µg g^{-1}]	[%]	[%]	[µg g^{-1}]	[%]	[%]	[µg g^{-1}]	[%]	[%]
Na	^{23}Na	10074	37	32	8735	37	40	6082	19	25
Mg	^{25}Mg	9027	50	37	7755	49	49	6051	36	29
Al	^{27}Al	39380	41	33	37134	41	43	22543	19	24
Si	^{29}Si	153391	31	29	239841	17	27	84145	58	37
P	^{31}P	3522	30	46	3129	25	50	2466	33	57
K	^{39}K	23039	32	29	15243	35	38	24205	17	24
Ca	^{43}Ca	12223	38	32	13609	24	31	6710	85	49
Ti	^{47}Ti	2176	53	39	2167	62	60	1581	179	95
Mn	^{55}Mn	262416	36	31	158371	32	36	402063	11	23
Fe	^{57}Fe	33390	41	33	30792	49	49	18862	26	26
Co	^{59}Co	1340	39	32	1042	38	40	3527	29	27
Ni	^{60}Ni	315	34	30	277	53	52	123	52	35
Rb	^{85}Rb	90	42	33	79	57	55	49	15	23
Sr	^{88}Sr	738	36	31	527	32	36	372	54	35
Y	^{89}Y	108	60	42	79	12	25	70	86	50
Cs	^{133}Cs	5	38	32	5	48	48	3	14	24
Ba	^{138}Ba	1351	39	32	969	24	30	1245	54	35
La	^{139}La	47	57	41	44	19	28	20	36	29
Ce	^{140}Ce	136	31	29	120	36	38	119	17	24
Pr	^{141}Pr	16	35	30	13	22	29	9	28	26
Nd	^{143}Nd	80	26	27	67	26	32	52	28	26
Sm	^{147}Sm	22	21	25	18	16	26	16	24	25
Eu	^{151}Eu	5	31	29	4	23	30	3	27	26
Gd	^{157}Gd	28	29	28	23	16	26	16	28	28
Tb	^{159}Tb	4	31	29	3	25	31	3	27	26
Dy	^{161}Dy	24	35	30	19	20	28	16	29	26
Ho	^{165}Ho	5	36	30	4	12	24	3	27	26
Er	^{167}Er	16	60	43	13	12	24	8	24	25
Tm	^{169}Tm	2	57	41	1	28	33	1	25	25
Yb	^{173}Yb	10	52	38	8	28	33	6	25	25
Lu	^{175}Lu	2	61	42	1	25	31	1	19	24
Pb	^{208}Pb	142	60	42	218	73	68	146	158	85
Th	^{232}Th	14	39	32	15	46	47	10	52	35
U	^{238}U	6	24	27	4	31	36	5	43	32

Table A continued

		SA mM-d			SA mM-f		
Element	Isotope used	mass fraction	RSD	$U_{El,rel}$	mass fraction	RSD	$U_{El,rel}$
		[µg g^{-1}]	[%]	[%]	[µg g^{-1}]	[%]	[%]
Na	^{23}Na	10874	65	58	8467	54	44
Mg	^{25}Mg	7898	44	42	9868	34	32
Al	^{27}Al	36202	59	53	61274	29	30
Si	^{29}Si	235476	22	28	159831	26	29
P	^{31}P	2894	27	50	4609	17	46
K	^{39}K	14465	35	36	22006	18	25
Ca	^{43}Ca	11649	34	35	8057	44	38
Ti	^{47}Ti	1961	65	58	3564	46	40
Mn	^{55}Mn	161339	75	65	197990	29	30
Fe	^{57}Fe	36387	59	53	68228	25	28
Co	^{59}Co	840	67	59	1319	24	28
Ni	^{60}Ni	786	64	57	2021	61	48
Rb	^{85}Rb	66	51	47	104	39	35
Sr	^{88}Sr	709	40	39	911	44	38
Y	^{89}Y	46	35	36	71	46	39
Cs	^{133}Cs	5	68	59	7	30	31
Ba	^{138}Ba	1084	36	37	1954	13	23
La	^{139}La	47	59	53	50	44	38
Ce	^{140}Ce	145	40	39	225	52	43
Pr	^{141}Pr	12	17	26	17	46	39
Nd	^{143}Nd	53	26	30	79	50	41
Sm	^{147}Sm	13	32	34	21	46	39
Eu	^{151}Eu	3	39	39	4	43	37
Gd	^{157}Gd	14	35	36	22	46	39
Tb	^{159}Tb	2	44	42	3	45	38
Dy	^{161}Dy	14	34	35	18	39	35
Ho	^{165}Ho	2	39	38	3	42	37
Er	^{167}Er	7	51	48	12	43	38
Tm	^{169}Tm	1	30	32	1	33	32
Yb	^{173}Yb	7	73	63	8	38	34
Lu	^{175}Lu	1	48	45	1	34	32
Pb	^{208}Pb	234	56	50	259	30	31
Th	^{232}Th	17	41	40	24	40	36
U	^{238}U	5	33	35	8	33	32

B.3

Macholdt et al., GGR, 2016

Suitability of Mn- and Fe-Rich Reference Materials for Microanalytical Research

Dorothea S. Macholdt[a], Klaus Peter Jochum[a], Stephen A. Wilson[b], Laura M. Otter[a], Brigitte Stoll[a], Ulrike Weis[a] and Meinrat O. Andreae[a,c]

a Biogeochemistry and Climate Geochemistry Departments, Max Planck Institute for Chemistry, Mainz, Germany
b U.S. Geological Survey, Denver, CO, USA
c Department of Geosciences, King Saud University, Riyadh, Saudi Arabia

Geostandards and Geoanalytical Research Vol. 40 – N°4, 493-504. DOI: 10.1111/ggr.12119

Vol. 40 — N° 4 12 16 p. 493–504

GEOSTANDARDS and GEOANALYTICAL RESEARCH

Suitability of Mn- and Fe-Rich Reference Materials for Microanalytical Research

Dorothea S. **Macholdt** (1)*, Klaus Peter **Jochum** (1), Stephen A. **Wilson** (2), Laura M. **Otter** (1), Brigitte **Stoll** (1), Ulrike **Weis** (1) and Meinrat O. **Andreae** (1, 3)

(1) Biogeochemistry and Climate Geochemistry Departments, Max Planck Institute for Chemistry, Mainz, Germany
(2) U.S. Geological Survey, Denver, CO, USA
(3) Department of Geosciences, King Saud University, Riyadh, Saudi Arabia
* Corresponding author. e-mail: d.macholdt@mpic.de

Manganese- and iron-rich materials are of major geoscientific and economic interest, many of which contain microscopic features that provide valuable information. To obtain accurate results, a homogeneous microanalytical reference material for calibration is needed. Several researchers have used the Mn- and Fe-rich RMs, JMn-1, NOD-A-1, NOD-P-1 and FeMn-1, for this purpose; therefore, they were tested in this study to determine their suitability for microanalysis. Their homogeneity was investigated by laser ablation-inductively coupled plasma-mass spectrometry (LA-ICP-MS) with two different types of lasers (nano- and femtosecond), with spot and line scan analyses and with different operating parameters, such as spot size, pulse repetition rate and fluence. As the established manganese nodule RMs revealed inhomogeneities for picogram to microgram test portions, we also investigated the new synthetic Fe- and Mn-rich RM, FeMnOx-1. FeMnOx-1 was found to be homogeneous for large (ø 40 µm: 2% RSD repeatability) and small (ø 8–10 µm: 10% RSD repeatability) spot sizes. This homogeneity is in the range of the homogeneous NIST SRM 610 and GSE-1G reference glasses. Furthermore, FeMnOx-1 revealed a large-scale homogeneity within uncertainties of a few per cent, using test portions in the ng range, when measuring four individual mounts of this material.

Keywords: laser ablation-inductively coupled plasma-mass spectrometry, microanalysis, reference materials, rock varnish, manganese rich, homogeneity, measurement accuracy.

Les matériaux riches en manganèse et en fer sont économiquement et scientifiquement d'un intérêt majeur. Certaines caractéristiques microscopiques, pour beaucoup de ces matériaux, fournissent des informations précieuses. L'exactitude des résultats micro-analytiques passe par l'étalonnage des mesures au moyen d'un matériau de référence suffisamment homogène. À cette fin plusieurs chercheurs ont utilisé les matériaux de référence riches en Mn et en Fe JMn-1, NOD-A-1, NOD-P-1 et FeMn-1. Ces matériaux ont été testés, dans le cadre de cette étude, afin de déterminer leur aptitude à l'étalonnage de ces microanalyses. Leur homogénéité a été étudiée par ablation laser et spectrométrie de masse à plasma induit couplé (LA-ICP-MS); avec deux types de laser différents (nano- et femto-seconde), et par analyse point par point et par balayage linéaire. Différents paramètres de fonctionnement ont été testés (la taille du spot, le taux de répétition des impulsions et la fluence). Comme les matériaux de référence à base de nodules de Mn avaient révélé des inhomogénéités pour des portions d'essais variant du picogramme au microgramme, nous avons également étudié le nouveau matériau de référence synthétique riche en Mn et en Fe, FeMnOx-1. FeMnOx-1 s'est révélé être homogène pour de larges (diamètre de 40 µm: 2% RSD répétabilité) et petites (diamètre de 8–10 µm: 10% RSD répétabilité) tailles de spot. Cette homogénéité est dans la gamme de celles des verres de références homogènes NIST SRM 610 et GSE-1G. En outre, FeMnOx-1 a révélé une homogénéité à grande échelle avec des incertitudes de quelques pour cent, en utilisant des portions d'essais de l'ordre du ng, lors de mesures sur quatre échantillons distincts de ce matériau.

Mots-clés : ablation laser et spectrométrie de masse à plasma induit couplé, microanalyse, matériaux de référence,

GEOSTANDARDS and GEOANALYTICAL RESEARCH

Received 30 Nov 15 – Accepted 10 Apr 16

roches vernissées riche en manganèse, homogénéité, exactitude de mesure.

A large number of natural geological samples require microanalytical techniques for high-resolution analyses of micrometre-sized structures. An example of this is rock varnish, a naturally occurring sediment that may bear palaeoclimate information covering several tens of thousands of years in layered sequences with thicknesses of only up to 250 μm in total (Dorn 2009). Rock varnish is a Mn- and Fe-rich material that requires an equally Mn- and Fe-enriched reference material for most microanalytical techniques. Especially for small ablation rates and small spot sizes, high Mn and Fe mass fractions are preferable to allow shallow ablation depths with low sample consumption and therefore high spatial resolution. However, Mn- and Fe-rich microanalytical reference materials (RMs) are needed not only for rock varnish research. For other scientific investigations, such as ferromanganese crust, manganese nodule and manganese dendrite research, or even for economic applications, Mn-rich microanalytical RMs are important for calibration. An abundant literature on Mn- and Fe-rich materials has been published, but no suitable and matrix-matched microanalytical RM exists so far to calibrate the analytical data from microanalytical techniques (Garbe-Schönberg and McMurtry 1994, Hoffmann *et al.* 1997).

To overcome this limitation, several investigations have been performed previously, using nodule powders of the RMs NOD-A-1 and NOD-P-1 that were processed into pressed pellets for the purpose of these studies. The RMs were then used as microanalytical RMs for LA-ICP-MS investigations of Mn-rich materials (Garbe-Schönberg and McMurtry 1994, Axelsson *et al.* 2002, Hlawatsch *et al.* 2002), assuming a sufficient homogeneity. Furthermore, the homogeneous NIST SRM 61X and USGS GSE-1G glasses were used for calibration of Mn-rich materials (Hlawatsch *et al.* 2002, Huelin *et al.* 2006, Wayne *et al.* 2006, Xu *et al.* 2007, Nowinski *et al.* 2010, Macholdt *et al.* 2015), although these samples have low Mn and/or Fe contents.

Experiments on the suitability of laser ablation (LA) spot analyses on pressed manganese nodule powders (VS 5373-90, VS 5374-90, VS 5375-90) have been conducted previously by Hoffmann *et al.* (1997). The authors gave an overview over the number of measurements that they had performed on the specific nodules to be usable as RMs. However, the chosen crater diameter of 500 μm is not suitable for highly spatially resolved analyses of structures in the nanometre- to low-micrometre range. Furthermore, Hirata *et al.* (2013) investigated the manganese nodule JMn-1 as pressed powder pellet with a newly tested dilution and correction method. They concluded that accurate results could be obtained for fifteen elements tested. However, they too used a relatively large spot size of 100 μm, which is also not suitable for high-resolution measurements.

The aim of this study was to investigate the four manganese nodule RMs FeMn-1, NOD-P-1, JMn-1 and NOD-A-1 for their suitability as microanalytical RMs for high-resolution measurements of Mn- and Fe-rich materials by LA-ICP-MS. This was achieved by varying operating parameters such as fluence, pulse repetition rate and spot diameter (8–40 μm) to determine measurement precision, sensitivity and homogeneity. In addition, the newly produced FeMnOx-1 powder reference material, designed by the USGS in collaboration with the Max Planck Institute for Chemistry, was investigated to characterise its homogeneity for different test portions and to confirm its suitability as future calibration material. The results are compared to the homogeneous GSE-1G and NIST SRM 610 glasses, using a 213-nm nanosecond and 200-nm femtosecond laser. An alternative would have been a pressed nodule powder pellet with smaller grain diameters (about 1 μm), as produced by Garbe-Schönberg and Müller (2014). However, these materials have low trace element mass fractions, which lead to higher uncertainties. Especially when applying small ablation rates and small spot sizes, high Mn and Fe mass fractions are preferable to allow shallow ablation depths and therefore high spatial resolution.

Analytical procedures

Samples

Four different Mn- and Fe-rich natural nodule RMs were investigated: the IAG sample FeMn-1 (Webb *et al.* 2008), the USGS samples NOD-A-1 and NOD-P-1 (Flanagan and Gottfried 1980), as well as the GSJ sample JMn-1 (Terashima *et al.* 1995). The powder RMs were pressed (4 t, 15 min, evacuated press, resin and additive free) to produce pellets suitable for LA-ICP-MS measurements. Element content, colour and hardness of these pressed pellets are similar to natural samples such as manganese

nodules (Garbe-Schönberg and McMurtry 1994) or rock varnish. The samples were not dried prior to pressing, as LA-ICP-MS measurements are performed under atmospheric pressure, where evaporating H_2O cannot interfere with any vacuum (Hirata *et al.* 2013). In addition, the synthetic RM FeMnOx-1 (Jochum *et al.* 2016) was investigated. This material was designed to become a microanalytical RM for the calibration of microanalytical techniques. The FeMnOx-1 material was prepared using a USGS-developed co-precipitation procedure that has proved to be an efficient method to develop customised microanalytical reference materials with a specific set of major and trace element mass fractions. Major and minor elements that required mass fractions of ≥ 1000 mg kg^{-1} in the final product were prepared from nitrate and chloride salts. Notable exceptions were Na, K and Si, for which the solutions were produced from hydroxide or phosphate salts. The Zr solution was prepared from a sulfate salt. Pellets were produced by the USGS.

In addition to the pressed powder pellets, glass RMs with high trace element contents were analysed: the synthetic NIST SRM 610 silicate glass (Jochum *et al.* 2011) and the GSE-1G basaltic glass (USGS; GeoReM database 2015, preferred values). Both glasses were used for calibration purposes, even though they suffer from low Mn (NIST SRM 610, GSE-1G) and Fe (NIST SRM 610) mass fractions.

Mass spectrometer and lasers

Analyses were performed at the Max Planck Institute for Chemistry, Mainz, Germany, using a combination of a ThermoFisher Element2 single-collector sector-field ICP-MS and two different types of lasers: an Electro Scientific Industries (ESI) femtosecond laser ablation system, NWR-Femto200 operating at a wavelength of 200 nm (Jochum *et al.* 2014, Macholdt *et al.* 2015) and a New Wave UP213 Nd:YAG nanosecond laser ablation system with a wavelength of 213 nm. Important parameters of the ICP-MS and lasers are listed in Tables 1 and 2. Operating parameters such as spot size, line scan speed and energy density were adjusted to determine the precision and measurement accuracy. Pre-ablation was conducted prior to each line scan measurement with a scan speed of 80 µm s^{-1}. Concerning the spot measurements, the first few values of each measurement were rejected to avoid incorrect results due to surface contamination.

Table 1.
Operating parameters used for the fs and ns laser ablation systems

	NWRFemto200	UP213
Laser type	Ti:Sapphire	Nd:YAG
Wavelength	200 nm	213 nm
Pulse length	150 fs	5 ns
Energy density	0.14–0.34 J cm^{-2}	0.1–9.3 J cm^{-2}
Spot size used	10, 20, 40 µm	8, 15, 40 µm
Pulse repetition rate	10, 50, 100 Hz	5, 10, 20 Hz
Scanning time spots	30 s	45 s
Scanning time lines [s]	45 (1 µm s^{-1}), 30 (5 µm s^{-1})	45 (1 µm s^{-1}), 30 (5 µm s^{-1})
Scanning speed lines	1, 5 µm s^{-1}	1, 5 µm s^{-1}

Table 2.
Operating parameters of the Element2 ICP-MS

rf power	1260 W (ns laser), 1040 W (fs laser)
Cool gas flow rate	15 l min^{-1}
Auxiliary gas flow rate	1 l min^{-1}
Carrier gas (Ar) flow rate	0.8 l min^{-1}
Carrier gas (He) flow rate	0.7 l min^{-1}
Sample time	0.002 s
Samples per peak	25
Mass window	40%
Time per pass	1.6 s
Mass resolution mode	2000
Washout time	30 s
Blank count rate	15 s

Laser ablation was conducted in a large format cell under a He atmosphere. The carrier gas was mixed with an Ar gas flow prior to entering the plasma torch. The ion intensities were determined at a medium mass resolution of 2000 with flat top peaks to separate molecules from ions of interest, for example of $^{40}Ar^{14}N^{1}H^{+}$ from ^{55}Mn, which is especially important for the Mn-poor reference glasses. Twenty-nine trace elements and ten major elements were measured, and one analysis consisted of three separate spot or line analyses.

Data evaluation

The major element Al was used as the internal standard element, as it is known to be hardly affected by fractionation and mass load effects, and is generally used as an internal standard for rock varnish research due to its nearly uniform distribution in this material (Wayne *et al.* 2006, Goldsmith *et al.* 2014). The mass fraction of an element of interest, EL, (mf_{EL}) was calculated from its ion count rate by:

$$mf_{EL} = C_{Al} R_{iAl} (A_{Al}/A_i)(M_{Al}/M_i)(1/RSF) = mf_{uncorr}(1/RSF) \quad (1)$$

where C_{Al} is the mass fraction of the internal standard Al in mg kg^{-1}, and R_{iAl} is the ratio of the count rates of the isotope

of interest, i, of the element EL, to those of the internal standard isotope ^{27}Al. The values A_{Al} and A_i are the isotope abundances of the internal standard element, which is 1 for ^{27}Al, and the isotope of interest of element EL, M_{Al} and M_i the relative atomic masses of the internal standard element Al and the element EL, respectively. The relative sensitivity factor (RSF) is defined by the ratio of the uncorrected mass fraction, mf_{uncorr}, to the reference value of the RM. The RSFs of the different elements were determined from the analyses of the certified NIST SRM 610 reference glass (Jochum *et al.* 2011). As the low amount of Fe and K in the NIST SRM 610 glass (458 mg kg^{-1} and 62.3 mg kg^{-1}, respectively) provides low precision of the RSF values of these elements, especially for the fs laser measurements with its lower sensitivity, the RSFs of Fe and K were determined from the non-certified, but well-characterised GSE-1G reference glass, which has a basaltic composition with high Fe and K_2O amounts (9.8 g/100 g, and 2.6 g/100 g, respectively; GeoReM database 2015). The mean RSF values obtained from the NIST SRM 610 and GSE-1G analyses were used to calculate the corresponding element mass fractions for the samples. Data reduction was conducted by a routine programmed in Microsoft Excel, where outlier values were rejected. Outliers were defined for each analysis as values deviating more than 100% from the median. To provide a reasonable comparison, only data of elements with mass fractions of ≥ 100 mg kg^{-1} are presented. Therefore, twenty-two elements of the manganese nodules and thirty-two elements of the new FeMnOx-1 were measured and are presented in this manuscript. As no published literature values are yet available for the FeMnOx-1, the abundance of the internal standard element Al was calculated by averaging the values of three independent XRF measurements and one ICP-MS/OES measurement, resulting in an Al_2O_3 mass fraction of 3.69 g/100 g with an RSD of 4% (Jochum *et al.* 2016).

The measured element compositions obtained from line and spot analyses of the pressed nodule powders are provided in Table S1, the preliminary mass fractions determined by LA-ICP-MS of the new FeMnOx-1 in Table S2. Final results for calibration are provided in Table S5. These data were obtained from analyses of seven laboratories with five different analytical techniques (Jochum *et al.* 2016).

Results and discussion

Detection limit

The detection limit, DL, is defined as the smallest mass fraction that can be distinguished from the background signal at a specified confidence level (Potts 2012). It is calculated as three times the standard deviation of the blank values of the measurements and is mainly dependent on the isotopic

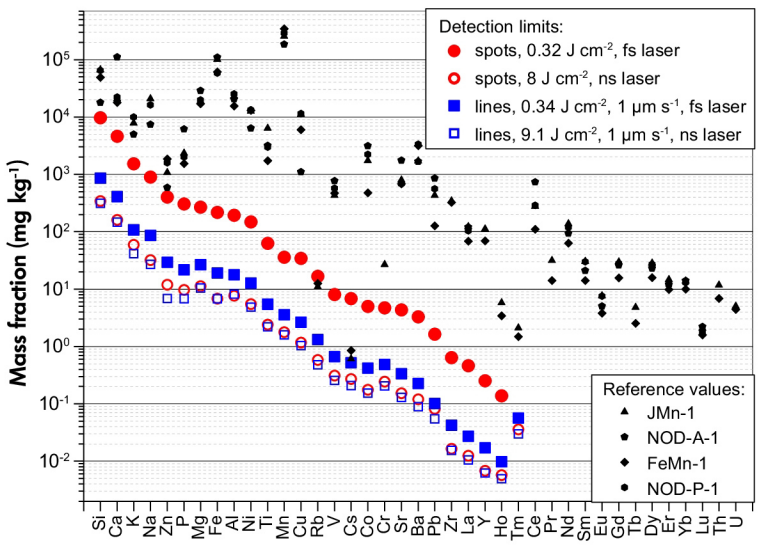

Figure 1. Detection limits obtained with four different laser settings and reference mass fractions of four natural Mn nodule powders for comparison. Elements are arranged according to decreasing detection limits, to allow a better overview. All measurements were performed with 40 µm spot diameter and 10 and 50 Hz pulse repetition rate for ns and fs laser measurements, respectively. The DLs for most elements plot significantly below the mass fractions present in the pressed nodule powder pellets. The detection limits from Tm onwards lie off the scale of the diagram. [Colour figure can be viewed at wileyonlinelibrary.com].

abundance of an element, the elemental sensitivity, the molecular interferences of the gas blank of the element of interest, and the operating parameters (e.g., spot size, mass resolution and scan speed). The DLs shown in Figure 1 were calculated for spot and line measurements with 40 µm spot size, 10 and 50 Hz, respectively, and for ns and fs laser ablation using a mass resolution of 2000. The DLs ranged between about 0.2 and 10000 mg kg^{-1} for major elements and between about < 0.01 and 20 mg kg^{-1} for trace elements (Table S3). Nearly all element mass fractions in the samples are much higher (factor of about 10–10000) than the respective DLs (Figure 1). Exceptions are Rb, Cs and Zn, where the abundances in the nodules are similar to the DLs (Figure 1). Of these three elements, only Zn has mass fractions of more than 100 mg kg^{-1} in the samples. For smaller spot sizes and lower energy densities, the DLs increase, as the ion intensities decrease due to lower ablation depths.

Measurement precision

An important aspect for microanalytical RMs is the measurement precision, expressed as % RSD, which is dependent on the homogeneity at the micrometre scale, spot size, fluence and the pulse repetition rate.

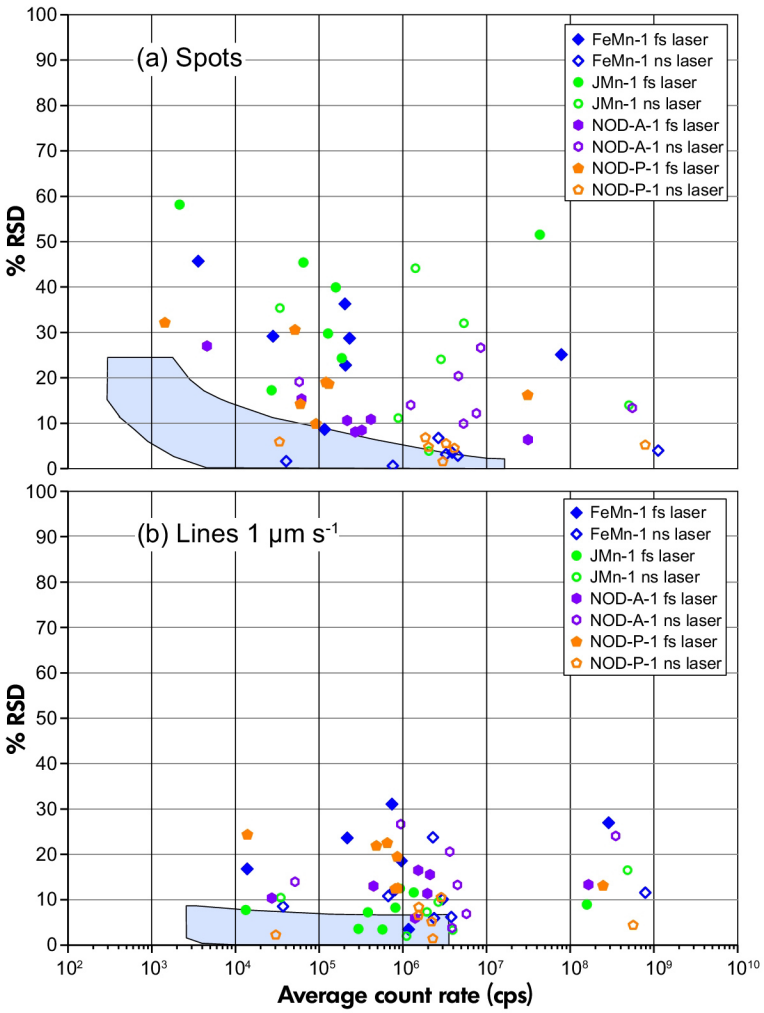

Figure 2. Small-scale homogeneity expressed as repeatability or RSD values, which was calculated from three independent measurements, about 15 µm apart from each other. The shaded field marks the GSE-1G and NIST SRM 610 values. Plotted are the values for the elements Mg, Mn, Fe, Sr, Ba, Ce and U to cover a large range and important elements. Figure 2a shows the spot measurements (fs laser: Ø 40 µm, 50 Hz and 0.32 J cm^{-2}; ns laser: Ø 40 µm, 10 Hz and 8 J cm^{-2}), Figure 2b the line measurements (fs laser: Ø 40 µm, 50 Hz, 1 µm s^{-1} and 0.34 J cm^{-2}; ns laser: Ø 40 µm, 10 Hz, 1 µm s^{-1} and 9.1 J cm^{-2}). The Mn nodule powders have RSD values significantly above those of the homogeneous reference glasses NIST SRM 610 and GSE-1G. An overview over the RSD values for each element can be found in Table S4. [Colour figure can be viewed at wileyonlinelibrary.com].

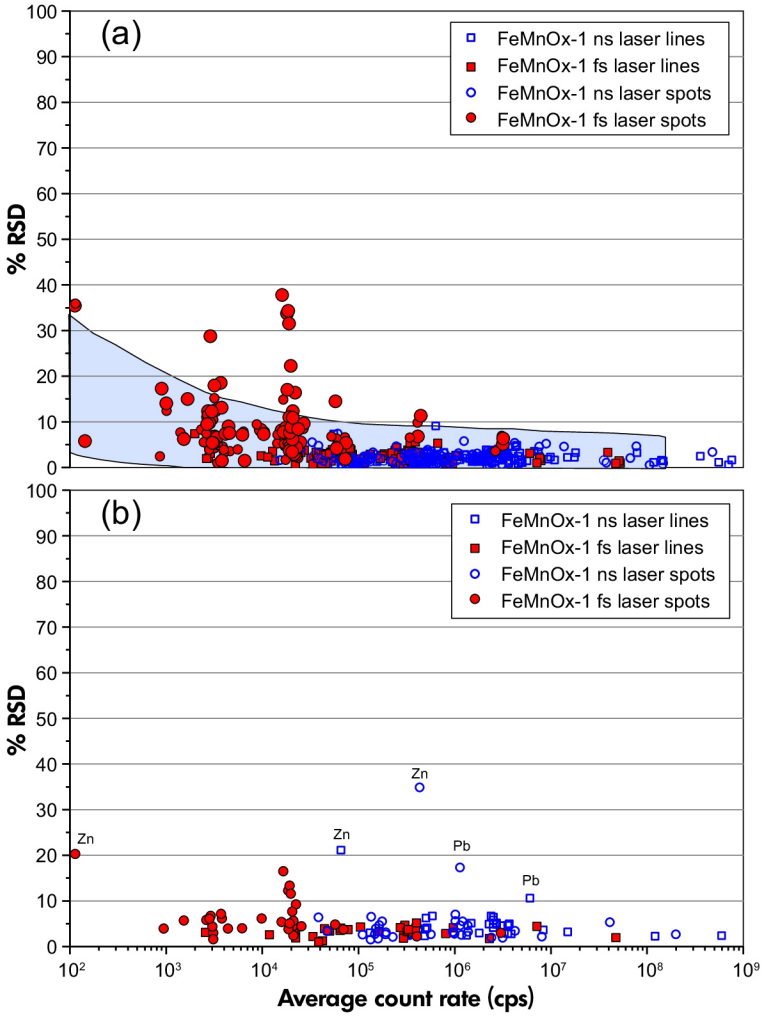

Figure 3. Large-scale homogeneity (a) expressed as RSD of three individual measurements. The measurements were performed on four individual pressed powder pellets. The shaded field marks the repeatability field of GSE-1G and NIST SRM 610 RSD. The measurements were performed with Ø 40 µm, 10 Hz, 12 J cm^{-2} and 1 µm s^{-1} scan speed for lines conducting ns LA, and Ø 40 µm, 50 Hz, 0.16 J cm^{-2} and 1 µm s^{-1} scan speed for lines conducting fs LA. Plot (b) refers to the mean repeatability of four different pressed powder pellets. Large discrepancies can be observed for ns LA data of Zn and Pb, caused by fractionation occurring during nanosecond laser measurements. Femtosecond laser data showed no discrepancies for these elements. The measurement parameters are the same as in (a). [Colour figure can be viewed at wileyonlinelibrary.com].

Homogeneity: To determine the homogeneity of the RMs, the repeatability or RSDs calculated from three independent measurements are plotted as a function of the average count rates in Figures 2 and 3. This allows comparison of elements with different abundances and of lasers with different ablation volumes. Small-scale homogeneity was tested by investigating the homogeneity within a single pellet of the material about 40 µm apart from each other (test portion about 170 ng for ns LA and 20 ng for fs LA), while the large-scale homogeneity was determined by the variation or RSDs between four independent pellets on four different mounts (test portion about 500 ng for ns LA and 60 ng for fs LA).

Small scale: Using 40 µm spot size, the measurement repeatability (RSD) for fs and ns LA measurements of the pressed nodule powders are significantly higher than the RSD values of the glasses (average pellet RSDs of all elements measured: 11–14% for ns and fs line analyses, and 12–25% for ns and fs spot analyses, respectively). Exemplary RSDs for certain elements are shown in Figure 2. In comparison, the repeatability of the pressed FeMnOx-1 powder is in the range of the reference glasses (average FeMnOx-1 RSDs of all elements measured on a single pellet: 2.3% for ns and fs line analyses, and 2.1–10% for ns and fs spot analyses, respectively; Figure 3a), indicating a small-

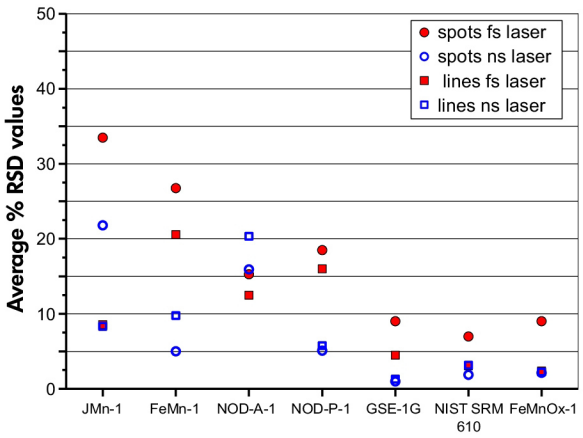

Figure 4. Average homogeneity, expressed as RSD values, of all samples tested. Line measurements (10 and 50 Hz pulse repetition rate or ns and fs laser measurements, respectively) show a deviation from literature values of about 10% with slightly lower (about 1%) deviations for ns laser measurements. The RSD values of GSE-1G, NIST SRM 610 and FeMnOx-1 are significantly lower than those of the pressed nodule powders. Due to higher count rates, ns laser data showed significantly lower RSD values than fs laser-produced data for most of the samples. [Colour figure can be viewed at wileyonlinelibrary.com].

scale homogeneity similar to that of the homogeneous reference glasses. Manganese nodule RMs, in contrast, are inhomogeneous for small test portions of < 1 μg.

Large scale: Due to the significant inhomogeneity of the pressed nodule powders, observed when conducting measurements with 40 μm spot sizes (Figure 2), the large-scale homogeneity of these materials was not tested. However, this was studied for the new FeMnOx-1 sample (Figure 3a), which is homogeneous with respect to the small scale. The mean RSD value of all investigated element mass fractions is about 3% for fs line measurements and, excluding Zn and Pb due to occurring fractionation in ns LA (Figure 3b), about 4% performing ns LA spot and line analyses (Figure 3b). An overview of the homogeneity for the different RMs tested is given in Figure 4. All values shown in Figure 2 are provided in Table S4.

Fluence: The magnitude of fluence affects the ablation volume and therefore the depth resolution of measurements. The range of fluence that was used for laser ablation with the two lasers in this study, using 40 μm spot diameter, is plotted in Figure 5.

Figure 5 shows that the repeatability of line scan measurements is less dependent on the fluence, due to a sufficiently large test portion for the majority of tested fluences (> 20 ng). The spot analyses of the manganese nodule RMs show significantly higher RSD values than the glasses, but this might also be an effect of the inhomogeneity of the samples for the test portions used. A significant difference in the repeatability (about 5% RSD for the homogeneous glasses) can be observed between ns and fs laser ablation for spot analyses, while almost no difference between the lasers was observed for line scans, even though the test portions are much higher (8.5 times) for the former. The reason for the sharp increase of the RSD values of fs laser spot analyses is the fast count rate drop of spot measurements when the fluence is reduced, due to the limited ablation depth of this laser system.

Spot size: To receive a high spatial resolution of micrometre-sized features, the spot size should be chosen as small as possible. As line scans were found to produce data with good measurement precision, the line width dictates the spatial resolution in lateral directions and the scan speed the overlapping area and therefore the spatial resolution into depth. Three spot sizes were tested for each laser, 10, 20 and 40 μm for fs LA and 8, 15 and 40 μm for ns LA (Table 1).

As expected, the repeatability, expressed as RSD, gets worse with decreasing spot sizes (Figure 6), with no significant difference between fs and ns measurements. The homogeneous glasses GSE-1G and NIST SRM 610 as well as the new FeMnOx-1 powder pellet produce equally good results for spot sizes of 40 μm (2% RSD) down to about 8 μm (10% RSD for ns LA of FeMnOx-1). However, it has to be taken into account that more material is ablated from the powder pellets than from the glasses, using similar operating parameters. The best repeatability or lowest RSDs of 1–2% are obtained with 40 μm spot size conducting ns laser ablation line measurements (Figure 6a) and ns laser spot measurements (Figure 6b) of the microanalytical RM glasses and the FeMnOx-1.

Pulse repetition rate: The pulse repetition rate (PRR) was not found to have a significant effect on the precision. Higher PRRs produce higher count rates. As the repeatability (RSD) is dependent on the ion count rate (Figures 2, 3), the RSDs decrease with increasing PRRs but the influence is not strong enough to significantly influence the measurement precision.

Measurement accuracy

The measurement accuracy is the closeness of agreement between a measured quantity value and a true quantity value of a measurand (VIM3-ISO 2012). Accurate data are characterised by a low overall analytical uncertainty, *U*. There

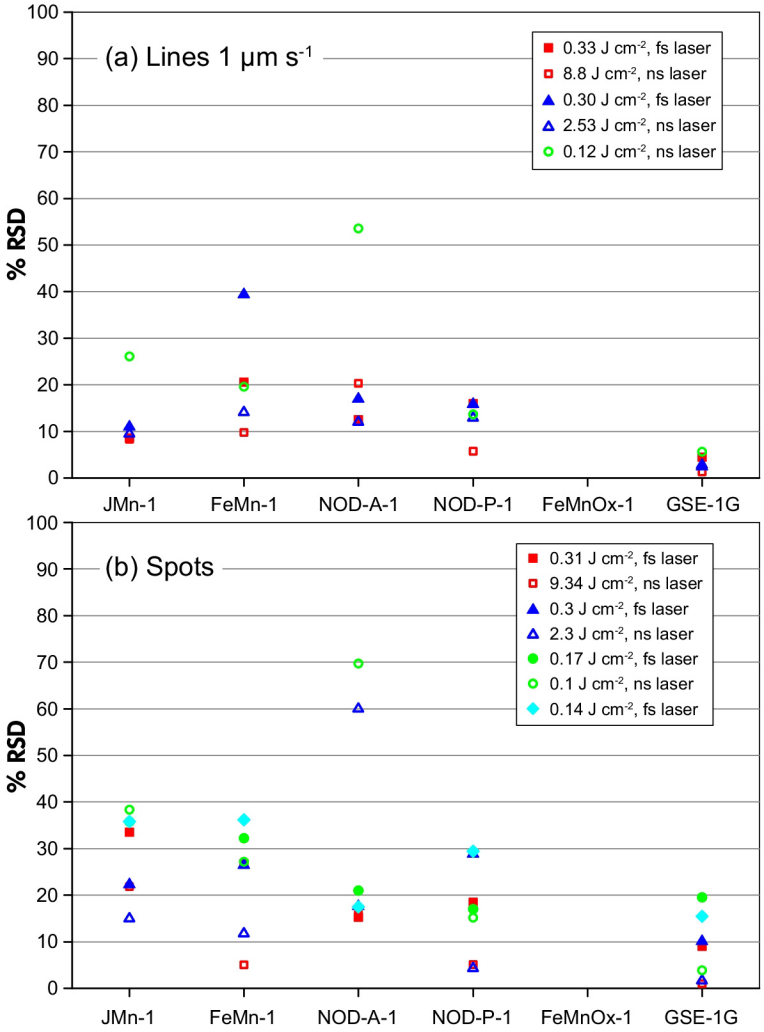

Figure 5. Repeatability expressed as RSDs of measurements with low and high fluence and with two different lasers (Ø 40 µm): (a) shows that line measurements conducted with 1 µm s^{-1} scan speed are almost energy independent, from 0.12 to 8.8 J cm^{-2}, using ns laser ablation, and 0.3 to 0.33 J cm^{-2}, using fs laser ablation. No significant difference can be observed between ns and fs laser repeatability nor RSDs. (b) shows that the spot measurement repeatability has a significant dependency on energy density and thereby test portion. High energy densities provide RSDs of 5–30%. Smaller energy densities than 0.23 J cm^{-2} provide RSDs of up to 70%. Only the homogeneous RM glasses GSE-1G and NIST SRM 610 show RSDs of 1–20% for spots measurements of all energy densities, with the exception of the 0.14 J cm^{-2} fs laser ablation energy density, where the average RSD value rises to 30% for NIST SRM 610. [Colour figure can be viewed at wileyonlinelibrary.com].

are several factors affecting *U*, such as the uncertainty of the reference values of the calibration material (u_{RMused}), the relative sensitivity factor, RSF, uncertainty (u_{RSF}), the measurement of the sample ($u_{measurement}$), the uncertainty of the internal standard element, Al, of the calibration material ($u_{AlNIST\ 610}$) and the uncertainty of the internal standard element value, Al, of the sample ($u_{Alsample}$). The measurements were conducted with 40 µm spot size and maximum energy densities (Table 1), as both, spots and line scans. In addition to this overall uncertainty, the uncertainty of the reference value, $u_{ref.\ value}$, of the sample of interest has a major influence on the measurement accuracy.

$$U = k^* \sqrt{(u_{RMused}{}^2 + u_{RSF}{}^2 + u_{measurement}{}^2 + u_{AlNIST610}{}^2 + u_{Alsample}{}^2 + u_{ref.value}{}^2)} \quad (2)$$

where k is the coverage factor. In Figure 7, deviations from reference values are plotted individually for each element in the four pressed nodule powders and the new FeMnOx-1.

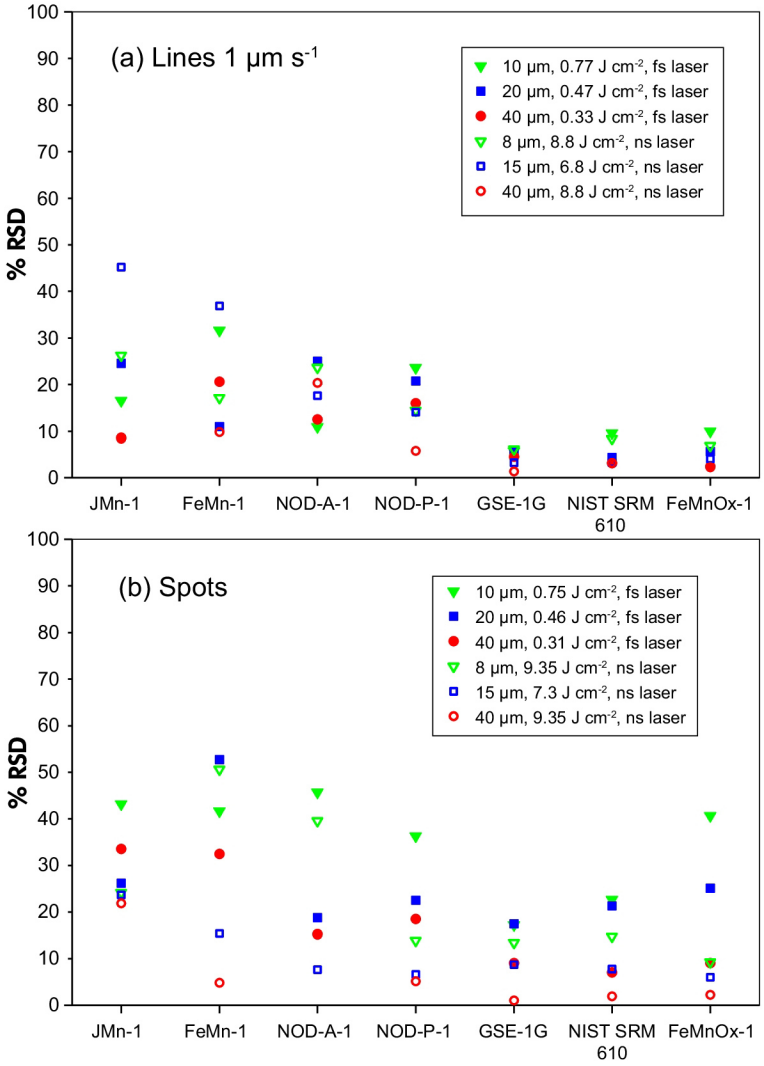

Figure 6. Repeatability expressed as RSDs of measurements with small and large (Ø 8–40 µm) spot sizes and with two different lasers. (a) shows that line measurements conducted with 1 µm s^{-1} scan speed show a decreasing repeatability or increasing RSDs for the nodule pellets from about 10% to 40% RSD, when the spot size is reduced from 40 to 8 µm, but no significant difference between fs and ns results could be observed. The homogeneous glasses and FeMnOx-1 produce equally good results of < 10% RSDs for spot sizes down to 8–10 µm, respectively. Spot measurements, shown in (b), show that the homogeneous glasses and FeMnOx-1 produce low RSD values (10% RSD for FeMnOx-1) for spots of only 8 µm diameter by ns LA. Regarding the pressed powder pellets, the repeatability decreases with decreasing spot diameters: ø 40 µm: up to 20% RSD, Ø 15 µm: up to 25% RSD, and Ø 8 µm: up to 50% RSD by ns LA spot measurements. Femtosecond spot measurements produce higher RSDs due to significantly lower test portions for all RMs. [Colour figure can be viewed at wileyonlinelibrary.com].

The mass fractions obtained by line scans fall within an average deviation of about 15% from the literature value (Figure 7a). Line scan analyses of sample FeMn-1 yield an average deviation from literature values of only 7%, probably due to the well-established reference values provided (Webb *et al.* 2008).

Spot measurements are less accurate, especially for 200 nm fs laser ablation with its low fluence and shallow ablation depths and, therefore, its low count rates and test portions (Figure 7b), which is why ns lasers are still applied preferentially.

Conclusions

Four Mn-rich nodule RMs, JMn-1, FeMn-1, NOD-A-1 and NOD-P-1, measured as epoxy-free pressed pellets,

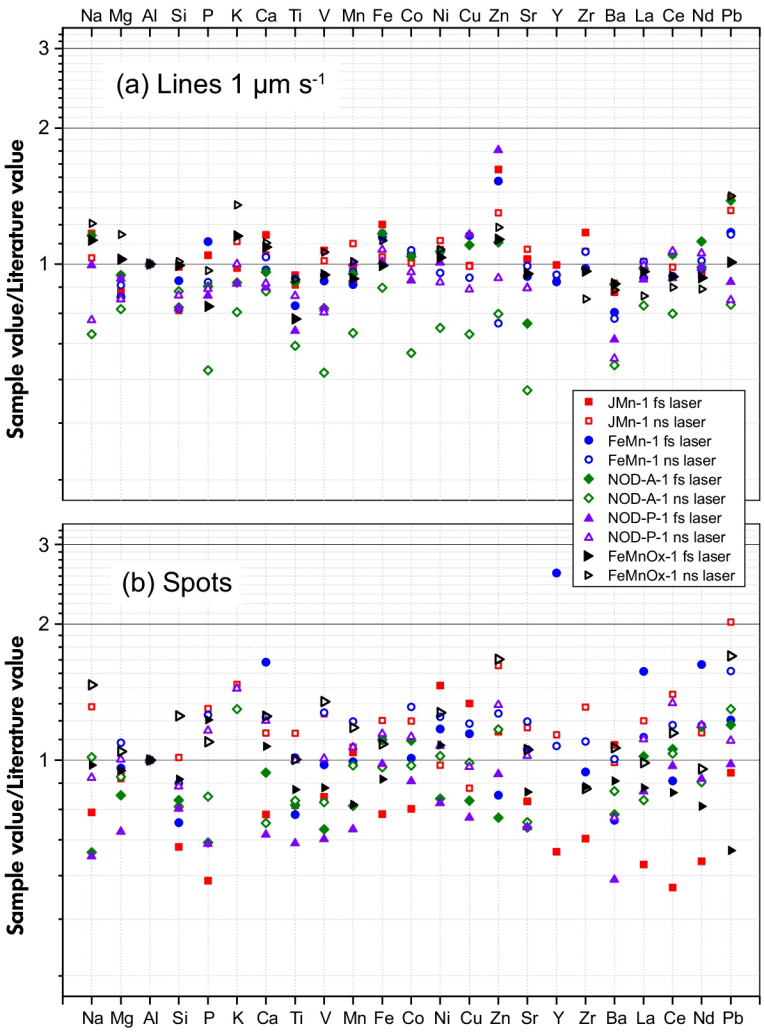

Figure 7. Measurement accuracy expressed as deviation from literature values for the twenty-three measured elements of the pressed powder RMs. (a) shows that laser ablation measurements performing line scans (fs laser: Ø 40 µm, 50 Hz, 1 µm s^{-1} and 0.34 J cm^{-2} (0.16 J cm^{-2} for FeMnOx-1); ns laser: Ø 40 µm, 10 Hz, 1 µm s^{-1} and 9.1 J cm^{-2} (12 J cm^{-2} for FeMnOx-1) lie within 20–30% from the literature value. The largest deviations can be observed for the elements Zn, Cs, Ba and Pb, for both fs and ns laser ablation. (b) shows that spot measurements (fs laser: Ø 40 µm, 50 Hz and 0.32 J cm^{-2} (0.16 J cm^{-2} for FeMnOx-1); ns laser: Ø 40 µm, 10 Hz and 8 J cm^{-2} (12 J cm^{-2} for FeMnOx-1) of the nodules display larger deviations, especially for fs laser ablation with its low count rates and test portions. [Colour figure can be viewed at wileyonlinelibrary.com].

were tested for their suitability as microanalytical reference materials for the analysis of varnish and other Mn-rich samples. Line ablations with a spot size of 40 µm and a scan speed of 1 µm s^{-1} proved to give a measurement precision of about 10% RSD and an average deviation from literature values of about 15% for 160 and 20 ng test portions, for ns and fs LA, respectively. The high Mn and Fe mass fractions in the nodule materials are suitable to calibrate Mn- and Fe-rich materials, such as rock varnish. The disadvantage of the Mn-rich nodule RMs is the heterogeneity of small test portions, consisting of a few hundred picograms to nanograms consumed by fs, and nanograms to micrograms consumed by ns LA-ICP-MS, respectively. Inhomogeneities on the micrometre scale due to large grain sizes produce low precision and limited accurate data for small test portions.

Additionally, the materials suffer from low trace element mass fractions. Small spot sizes (8–10 µm) and low energy densities (about 0.1 J cm^{-2}), however, are necessary for highly spatially resolved measurements. There is no significant difference in the degree of inhomogeneity of the four nodule powders tested.

We found that the new FeMnOx-1 is a suitable microanalytical RM for the calibration of microanalytical measurements, as it has high Mn and Fe mass fractions and high (> 100 mg kg^{-1}) trace element contents of the elements of interest. The high Mn, Fe, and trace element mass fractions qualify it as possible calibration material for a matrix-matched calibration of, for example, rock varnish. This work shows that the preferred values of this material are accurate enough to receive a measurement accuracy in the range of other well-known Mn-rich reference materials and that it is sufficiently homogeneous for high precision analyses with spot sizes down to 8 µm. FeMnOx-1 is therefore applicable as a future calibration material for Mn-rich materials using microanalytical techniques.

Acknowledgements

This work was supported by the Max Planck Graduate Centre with the Johannes Gutenberg University Mainz (MPGC) and the Max Planck Society.

References

Axelsson M.D., Rodushkin I., Baxter D.C., Ingri J. and Öhlander B. (2002)
High spatial resolution analysis of ferromanganese concretions by LA-ICP-MS. **Geochemical Transactions, 3**, 40–47.

Dorn R.I. (2009)
Desert rock coatings. **In: Parsons A.J. and Abrahams A.D. (eds), Geomorphology of desert environments (2nd edition). Springer (Amsterdam)**, 153–186.

Flanagan F.J. and Gottfried D. (1980)
USGS rock standards, III: Manganese-nodule reference samples USGS-NOD-A-1 and USGS-NOD-P-1. **U.S. Geological Survey Professional Paper, 1155**, 39pp.

Garbe-Schönberg C.-D. and McMurtry G.M. (1994)
In-situ micro-analysis of platinum and rare earths in ferromanganese crusts by laser ablation-ICP-MS (LA-ICP-MS). **Fresenius' Journal of Analytical Chemistry, 350**, 264–271.

Garbe-Schönberg D. and Müller S. (2014)
Nano-particulate pressed powder tablets for LA-ICP-MS. **Journal of Analytical Atomic Spectrometry, 29**, 990–1000.

GeoReM database (2015)
http://GeoReM.mpch-mainz.gwdg.de Application version 18 (January 2015)

Goldsmith Y., Stein M. and Enzel Y. (2014)
From dust to varnish: Geochemical constraints on rock varnish formation in the Negev Desert, Israel. **Geochimica et Cosmochimica Acta, 126**, 97–111.

Hirata J., Takahashi K. and Tanaka M. (2013)
Determination method of multi elements in ferromanganese samples by LA-ICP-MS. **Analytical Sciences, 29**, 151–155.

Hlawatsch S., Garbe-Schönberg C.D., Lechtenberg F., Manceau A., Tamura N., Kulik D.A. and Kersten M. (2002)
Trace metal fluxes to ferromanganese nodules from the western Baltic Sea as a record for long-term environmental changes. **Chemical Geology, 182**, 697–709.

Hoffmann E., Lüdke C. and Scholze H. (1997)
Is laser-ablation-ICP-MS an alternative to solution analysis of solid samples? **Fresenius' Journal of Analytical Chemistry, 359**, 394–398.

Huelin S.R., Longerich H.P., Wilton D.H.C. and Fryer B.J. (2006)
The determination of trace elements in Fe-Mn oxide coatings on pebbles using LA-ICP-MS. **Journal of Geochemical Exploration, 91**, 110–124.

Jochum K.P., Weis U., Stoll B., Kuzmin D., Yang Q., Raczek I., Jacob D.E., Stracke A., Birbaum K., Frick D.A., Günther D. and Enzweiler J. (2011)
Determination of reference values for NIST SRM 610–617 glasses following ISO guidelines. **Geostandards and Geoanalytical Research, 35**, 397–429.

Jochum K.P., Stoll B., Weis U., Jacob D.E., Mertz-Kraus R. and Andreae M.O. (2014)
Non-matrix-matched calibration for the multi-element analysis of geological and environmental samples using 200 nm femtosecond LA-ICP-MS: A comparison with nanosecond lasers. **Geostandards and Geoanalytical Research, 38**, 265–292.

Jochum K.P., Wilson S.A., Becker H., Garbe-Schönberg D., Groschopf N., Kadlag Y., Macholdt D.S., Mertz-Kraus R., Otter L.M., Stoll B., Stracke A., Weis U., Haug G.H. and Andreae M.O. (2016)
FeMnOx-1: A new microanalytical reference material for the investigation of Mn-Fe rich geological samples. **Chemical Geology, 432**, 34–40.

Macholdt D.S., Jochum K.P., Pöhlker C., Stoll B., Weis U., Weber B., Müller M., Kappl M., Buhre S., Kilcoyne A.L.D., Weigand M., Scholz D., Al-Amri A.M. and Andreae M.O. (2015)
Microanalytical methods for *in-situ* high-resolution analysis of rock varnish at the micrometre to nanometre scale. **Chemical Geology, 411**, 57–68.

Nowinski P., Hodge V.F., Lindley K. and Cizdziel J.V. (2010)
Elemental analysis of desert varnish samples in the vicinity of coal-fired power plants and the Nevada test site using laser ablation ICP-MS. **The Open Chemical and Biomedical Methods Journal, 3**, 153–168.

references

Potts P.J. (2012)
A proposal for the publication of geochemical data in the scientific literature. **Geostandards and Geoanalytical Research, 36**, 225–230.

Terashima S., Usui A. and Imai N. (1995)
Two new GSJ geochemical reference samples: Syenite JSy-1 and Manganese Nodule JMn-1. **Geostandards Newsletter, 19**, 221–229.

VIM3-ISO (2012)
International vocabulary of metrology–Basic and general concepts and associated terms (3rd Edition). **Joint Committee for Guides in Metrology, 200:2012**, 91pp.

Wayne D.M., Diaz T.A., Fairhurst R.J., Orndorff R.L. and Pete D.V. (2006)
Direct major- and trace-element analyses of rock varnish by high resolution laser ablation inductively coupled plasma-mass spectrometry (LA-ICP-MS). **Applied Geochemistry, 21**, 1410–1431.

Webb P.C., Thompson M., Potts P.J., Watson J.S. and Kriete C. (2008)
Geo*PT*23 – An international proficiency test for analytical geochemistry laboratories – Report on round 23. **International Association of Geoanalysts Report 2008**, 7pp.

Xu H.-Z., Hu S.-H., Hu Z.-C., Jiang J.-F. and Wang X.-H. (2007)
Element distribution in cobalt-rich crust profile by laser ablation-inductively coupled plasma-mass spectrometry. **Chinese Journal of Analytical Chemistry, 35**, 1099–1104.

Supporting information

The following supporting information may be found in the online version of this article:

Table S1. Results for natural nodule powders.

Table S2. FeMnOx-1 preliminary mass fractions.

Table S3. Detection limits.

Table S4. Count rates and RSD values in Figure 2.

Table S5. Preferred values of FeMnOx-1.

This material is available as part of the online article from: http://onlinelibrary.wiley.com/doi/10.1111/ggr.12119 (This link will take you to the article abstract).

Table S1: Results of the natural nodule powders

***s* = standard deviation**

		FeMn-1								
		Spots				Lines 1 µm s^{-1}				
		40 µm, 10 (ns laser) - 50 (fs laser) Hz								
		fs laser, 0.31 J cm^{-2}		ns laser, 9.35 J cm^{-2}		fs laser, 0.33 J cm^{-2}		ns laser, 8.8 J cm^{-2}		Lit. values
	Isotope measured	[µg g^{-1}]	*s*	[µg g^{-1}]	*s*	[µg g^{-1}]	*s*	[µg g^{-1}]	*s*	[µg g^{-1}]
Na	^{23}Na	22197	*7539*	28025	*1398*	26573	*6489*	20202	*1884*	
Mg	^{25}Mg	16291	*3717*	18549	*587*	14343	*4452*	15252	*905*	16987
Si	^{29}Si	35645	*897*	43575	*2008*	45059	*3560*	39088	*930*	49081
P	^{31}P	5646	*7589*	1932	*145*	1722	*322*	1399	*126*	1536
K	^{39}K			12587	*1018*	8266	*2307*	7725	*598*	
Ca	^{43}Ca	29409	*22050*	22236	*339*	17331	*2766*	18519	*2320*	17871
Ti	^{47}Ti	1311	*402*	1753	*19*	1399	*255*	1607	*66*	1731
V	^{51}V	457	*104*	596	*18*	430	*73*	442	*56*	469
Cr	^{53}Cr	95	*126*	16	*6*	544	*837*	26	*27*	
Mn	^{55}Mn	340539	*85534*	418428	*16618*	309431	*83418*	330659	*38154*	343750
Fe	^{57}Fe	67117	*19296*	68658	*1964*	69643	*2405*	71076	*4378*	60756
Co	^{59}Co	480	*156*	623	*25*	500	*65*	509	*20*	475
Ni	^{60}Ni	15354	*2952*	16318	*847*	13943	*3957*	12515	*1047*	13100
Cu	^{63}Cu	6809	*1394*	7175	*501*	6878	*2294*	5553	*580*	5957
Zn	^{67}Zn	1542	*396*	2339	*391*	2814	*1027*	1363	*147*	1845
Rb	^{85}Rb	12	*4*	17	*1*	14	*2*	12	*0*	13
Sr	^{88}Sr	721	*262*	831	*29*	641	*119*	676	*68*	683
Y	^{89}Y	179	*200*	74	*2*	63	*10*	65	*8*	69
Zr	^{90}Zr	306	*88*	357	*9*	318	*56*	346	*36*	325
Cs	^{133}Cs	0.82	*0.27*	1.2	*0.1*	0.90	*0.09*	0.82	*0.06*	0.85
Ba	^{137}Ba	2322	*201*	3175	*214*	2469	*299*	2391	*568*	3158
La	^{139}La	107	*86*	77	*2*	64	*10*	69	*7*	68
Ce	^{140}Ce	99	*29*	131	*1*	103	*24*	116	*12*	110
Pr	^{141}Pr	23	*18*	17	*1*	13	*2*	15	*2*	14
Nd	^{143}Nd	102	*91*	75	*3*	61	*8*	64	*7*	63
Sm	^{147}Sm	22	*17*	17	*1*	14	*2*	14	*2*	14
Eu	^{151}Eu	5.3	*3.8*	4.4	*0.1*	3.6	*0.5*	3.8	*0.5*	3.8
Gd	^{157}Gd	25	*17*	19	*1*	16	*2*	16	*3*	16
Tb	^{159}Tb	4.1	*2.8*	2.9	*0.1*	2.4	*0.4*	2.6	*0.4*	2.5
Dy	^{161}Dy	33	*28*	18	*1*	15	*2*	16	*2*	16
Ho	^{165}Ho	6.4	*6.1*	3.9	*0.1*	3.3	*0.4*	3.6	*0.5*	3.4
Er	^{167}Er	19	*13*	12	*0*	9.6	*1.6*	11	*1*	9.8
Tm	^{169}Tm			1.9	*0.1*	1.6	*0.2*	1.7	*0.2*	1.5
Yb	^{173}Yb	19.8	*18.9*	11.9	*0.2*	9.8	*1.8*	11.2	*1.4*	10
Lu	^{175}Lu	3.3	*2.4*	1.9	*0.0*	1.5	*0.2*	1.6	*0.2*	1.6
Pb	^{208}Pb	155	*33*	199	*16*	149	*24*	147	*24*	127
Th	^{232}Th	7.2	*2.5*	7.6	*0.5*	7.3	*1.9*	7.2	*0.9*	6.9
U	^{238}U	5.6	*2.5*	5.4	*0.1*	3.6	*0.6*	4.4	*0.4*	4.4

Table S1 continued

		JMn-1								
		Spots				Lines 1 µm s^{-1}				
		40 µm, 10 (ns laser) - 50 (fs laser) Hz								
		fs laser, 0.31 J cm^{-2}		ns laser, 9.35 J cm^{-2}		fs laser, 0.33 J cm^{-2}		ns laser, 8.8 J cm^{-2}		Lit. values
	Isotope measured	[µg g^{-1}]	*s*	[µg g^{-1}]	*s*	[µg g^{-1}]	*s*	[µg g^{-1}]	*s*	[µg g^{-1}]
Na	^{23}Na	15895	*4931*	27259	*3951*	24259	*2271*	21417	*2044*	20751
Mg	^{25}Mg	17597	*7024*	17101	*658*	16307	*555*	17710	*1284*	18784
Si	^{29}Si	42371	*7294*	66890	*4943*	65004	*1713*	52062	*3460*	65950
P	^{31}P	1263	*233*	3035	*628*	2442	*333*	2085	*111*	2335
K	^{39}K			11537	*487*	7688	*522*	8797	*649*	7837.1
Ca	^{43}Ca	15755	*5121*	23874	*5086*	24111	*1226*	21784	*1872*	20791
Ti	^{47}Ti	5057	*3010*	7287	*2103*	6012	*822*	5721	*497*	6360
V	^{51}V	355	*68*	541	*129*	458	*47*	435	*46*	428
Cr	^{53}Cr	42	*29*	11	*1.5*	8	*1.7*	5	*0.81*	26.6
Mn	^{55}Mn	266796	*137397*	274121	*38299*	250677	*22294*	284621	*46971*	256282.1
Fe	^{57}Fe	76529	*18592*	123353	*39501*	123194	*14248*	104497	*3416*	100713
Co	^{59}Co	1351	*619*	2112	*454*	1792	*175*	1740	*150*	1732
Ni	^{60}Ni	18477	*11105*	12316	*995*	13586	*1294*	14252	*3596*	12632
Cu	^{63}Cu	14849	*9926*	9649	*1308*	11050	*847*	11013	*1718*	11132
Zn	^{67}Zn	1234	*763*	1729	*63*	1728	*171*	1387	*187*	1068
Rb	^{85}Rb	8	*3.6*	15	*2.3*	12	*0.14*	12	*0.80*	11
Sr	^{88}Sr	642	*191*	935	*225*	812	*67*	854	*81*	792
Y	^{89}Y	70	*17*	126	*46*	110	*11*	105	*4.8*	111
Zr	^{90}Zr	231	*35*	451	*146*	404	*31*	367	*11*	344
Cs	^{133}Cs	0.86	*0.46*	0.5	*0.01*	0.33	*0.11*	0.41	*0.01*	0.604
Ba	^{137}Ba	1851	*840*	1694	*188*	1485	*53*	1554	*193*	1714
La	^{139}La	72	*21*	149	*61*	123	*7.5*	124	*1.3*	122
Ce	^{140}Ce	145	*25*	388	*171*	292	*21*	273	*5.3*	277
Pr	^{141}Pr	19	*6.0*	39	*15*	31	*1.8*	31	*0.31*	31
Nd	^{143}Nd	82	*13*	157	*68*	133	*7.6*	129	*1.1*	137
Sm	^{147}Sm	17	*1.9*	37	*15*	32	*2.0*	31	*0.79*	30
Eu	^{151}Eu	4.6	*2.5*	9.3	*4.1*	7.4	*0.64*	7.3	*0.16*	7.58
Gd	^{157}Gd	16	*2.8*	38	*15*	31	*3.2*	31	*0.81*	30
Tb	^{159}Tb	3.0	*0.58*	5.6	*2.3*	4.8	*0.36*	4.8	*0.20*	4.8
Dy	^{161}Dy	19	*2.1*	33	*14*	29	*2.8*	29	*0.35*	28
Ho	^{165}Ho	4.0	*1.9*	6.5	*2.7*	5.5	*0.62*	5.7	*0.16*	5.8
Er	^{167}Er	11	*4.2*	19	*7.9*	15.7	*1.3*	16	*0.31*	14.6
Tm	^{169}Tm			2.9	*1.1*	2.3	*0.21*	2.4	*0.06*	2.1
Yb	^{173}Yb	9.9	*2.0*	17.4	*6.6*	14.3	*2.0*	14.6	*0.21*	13.8
Lu	^{175}Lu	1.7	*0.37*	2.6	*1.0*	2.1	*0.20*	2.2	*0.07*	2.1
Pb	^{208}Pb	403	*64*	869	*264*	603	*106*	565	*17*	430
Th	^{232}Th	6.9	*1.7*	17.7	*8.5*	13.8	*2.3*	13.6	*0.51*	11.7
U	^{238}U	4.1	*2.4*	7.0	*2.5*	5.3	*0.41*	5.7	*0.60*	5.0

Table S1 continued

		Nod A-1								
		Spots				Lines 1 µm s^{-1}				
		40 µm, 10 (ns laser) - 50 (fs laser) Hz								
		fs laser, 0.31 J cm^{-2}		ns laser, 9.35 J cm^{-2}		fs laser, 0.33 J cm^{-2}		ns laser, 8.8 J cm^{-2}		Lit. values
	Isotope measured	[µg g^{-1}]	*s*	[µg g^{-1}]	*s*	[µg g^{-1}]	*s*	[µg g^{-1}]	*s*	[µg g^{-1}]
Na	^{23}Na	4641	*407*	7527	*1275*	8588	*1035*	5189	*724*	7419
Mg	^{25}Mg	24001	*1934*	26343	*2615*	27111	*1616*	22830	*871*	28703
Si	^{29}Si	14522	*1581*	14050	*1943*	14278	*2346*	15515	*2259*	17808
P	^{31}P	4013	*624*	5074	*1090*	5453	*335*	3553	*105*	6110
K	^{39}K			6459	*584*	4536	*271*	3901	*134*	4981.2
Ca	^{43}Ca	103322	*34443*	79876	*43652*	105676	*39210*	95879	*44266*	110064
Ti	^{47}Ti	2526	*410*	2585	*407*	2901	*82*	2094	*426*	3177
V	^{51}V	541	*51*	622	*81*	615	*85*	443	*57*	770
Cr	^{53}Cr	35	*11*	22	*3.7*	25	*7.2*	58	*55*	
Mn	^{55}Mn	146692	*9378*	180136	*24141*	176120	*23503*	130307	*31327*	185105.5
Fe	^{57}Fe	120964	*13103*	105169	*12844*	127461	*19765*	96741	*6637*	109106
Co	^{59}Co	3437	*98*	3028	*587*	3237	*527*	1978	*690*	3110
Ni	^{60}Ni	5225	*559*	6501	*701*	6788	*771*	4597	*1439*	6360
Cu	^{63}Cu	895	*266*	1085	*11*	1212	*162*	770	*227*	1100
Zn	^{67}Zn	440	*131*	690	*45*	660	*55*	457	*109*	590
Rb	^{85}Rb	7	*1.7*	11	*2.5*	11	*2.6*	12	*3.3*	
Sr	^{88}Sr	1242	*105*	1276	*340*	1294	*147*	920	*122*	1750
Y	^{89}Y	105	*25*	88	*8.5*	121	*24*	98	*35*	
Zr	^{90}Zr	288	*48*	270	*44*	326	*46*	230	*31*	
Cs	^{133}Cs	0.56	*0.13*	0.7	*0.16*	0.63	*0.23*	0.79	*0.28*	
Ba	^{137}Ba	1266	*194*	1426	*200*	1506	*196*	997	*266*	1670
La	^{139}La	122	*24*	98	*8.2*	117	*9.1*	97	*26*	120
Ce	^{140}Ce	772	*82*	755	*154*	767	*126*	567	*116*	730
Pr	^{141}Pr	29	*3.2*	21	*1.7*	25	*2.1*	22	*8.7*	
Nd	^{143}Nd	111	*23*	84	*2.7*	106	*11*	93	*40*	94
Sm	^{147}Sm	24	*3.7*	18	*1.0*	24	*1.7*	22	*10*	21
Eu	^{151}Eu	6.0	*0.6*	4.6	*0.16*	5.7	*1.0*	5.4	*2.5*	5
Gd	^{157}Gd	24	*4.2*	21	*1.9*	25	*3.7*	23	*10*	26
Tb	^{159}Tb	4.2	*0.7*	3.1	*0.16*	3.8	*0.24*	3.5	*1.4*	
Dy	^{161}Dy	27	*10*	19	*0.54*	24	*2.1*	21	*7.8*	23
Ho	^{165}Ho	5.1	*0.9*	4.0	*0.26*	5.1	*0.39*	4.4	*1.6*	
Er	^{167}Er	19	*1.2*	12	*1.2*	14.9	*1.0*	13	*4.2*	12.0
Tm	^{169}Tm			1.9	*0.05*	2.2	*0.09*	1.9	*0.46*	
Yb	^{173}Yb	13.3	*3.2*	11.8	*1.4*	14.4	*1.0*	11.8	*2.6*	14
Lu	^{175}Lu	2.2	*0.31*	1.9	*0.17*	2.3	*0.01*	1.8	*0.33*	2.2
Pb	^{208}Pb	1013	*195*	1097	*169*	1170	*118*	688	*214*	846
Th	^{232}Th	23.6	*4.0*	20.4	*2.1*	23.0	*4.3*	18.5	*2.9*	
U	^{238}U	7.1	*1.9*	7.4	*1.4*	7.3	*0.75*	5.4	*0.76*	

Table S1 continued

		Nod P-1								
		Spots				Lines 1 μm s^{-1}				
		40 μm, 10 (ns laser) - 50 (fs laser) Hz								
		fs laser, 0.31 J cm^{-2}		ns laser, 9.35 J cm^{-2}		fs laser, 0.33 J cm^{-2}		ns laser, 8.8 J cm^{-2}		Lit. values
	Isotope measured	[μg g^{-1}]	*s*	[μg g^{-1}]	*s*	[μg g^{-1}]	*s*	[μg g^{-1}]	*s*	[μg g^{-1}]
Na	^{23}Na	9985	*1375*	14925	*854*	16231	*1636*	12266	*404*	16321.8
Mg	^{25}Mg	13818	*2626*	19970	*1101*	18483	*2314*	16634	*850*	19899
Si	^{29}Si	50739	*1304*	56790	*1481*	51888	*5364*	55423	*3594*	64969
P	^{31}P	1309	*230*	2332	*17*	1710	*317*	1771	*144*	2008
K	^{39}K			14351	*570*	9015	*1060*	9957	*126*	9962.4
Ca	^{43}Ca	15151	*1110*	27086	*5449*	19648	*2857*	20085	*1115*	22156
Ti	^{47}Ti	1962	*255*	2992	*195*	2134	*429*	2549	*185*	2998
V	^{51}V	381	*52*	574	*20*	454	*81*	446	*5.9*	570
Cr	^{53}Cr	24	*4.3*	16	*1.6*	16	*8.8*	29	*15*	
Mn	^{55}Mn	204664	*33130*	310672	*16116*	292640	*38180*	269261	*11725*	291212
Fe	^{57}Fe	56903	*10615*	66401	*2959*	58769	*11425*	62409	*6553*	58050
Co	^{59}Co	2009	*386*	2523	*86*	2060	*407*	2151	*59*	2240
Ni	^{60}Ni	10763	*2366*	14422	*609*	13494	*737*	12206	*978*	13400
Cu	^{63}Cu	8577	*1646*	11110	*685*	13377	*1631*	10101	*854*	11500
Zn	^{67}Zn	1489	*359*	2119	*190*	2860	*402*	1489	*114*	1600
Rb	^{85}Rb	18	*2.4*	33	*1.7*	24	*2.1*	27	*0.19*	
Sr	^{88}Sr	483	*47*	695	*11*	603	*75*	601	*8*	680
Y	^{89}Y	65	*15*	96	*3.3*	77	*19*	83	*5.3*	
Zr	^{90}Zr	216	*40*	294	*21*	248	*44*	272	*44*	
Cs	^{133}Cs	0.79	*0.18*	2.6	*0.14*	1.74	*0.19*	1.95	*0.07*	
Ba	^{137}Ba	1820	*259*	2494	*170*	2280	*513*	2067	*134*	3350
La	^{139}La	89	*29*	116	*2.3*	96	*23*	103	*8.8*	104
Ce	^{140}Ce	281	*86*	388	*18*	270	*59*	309	*26*	290
Pr	^{141}Pr	27	*7.0*	34	*0.46*	27	*5.8*	30	*1.4*	
Nd	^{143}Nd	109	*34*	143	*2.5*	118	*24*	127	*6.9*	120
Sm	^{147}Sm	27	*5.3*	34	*0.94*	29	*5.3*	31	*2.1*	30
Eu	^{151}Eu	6.1	*1.5*	8.5	*0.38*	7.0	*1.6*	7.6	*0.39*	7.5
Gd	^{157}Gd	26	*2.5*	33	*0.32*	28	*5.4*	29	*2.0*	28
Tb	^{159}Tb	3.3	*0.25*	4.8	*0.16*	4.2	*0.86*	4.4	*0.22*	
Dy	^{161}Dy	22	*4.1*	28	*1.0*	24	*4.5*	26	*1.5*	27
Ho	^{165}Ho	3.9	*0.93*	5.2	*0.08*	4.4	*0.82*	4.8	*0.31*	
Er	^{167}Er	13	*1.4*	15	*0.34*	12.2	*2.7*	13	*1.0*	12.0
Tm	^{169}Tm			2.3	*0.05*	1.9	*0.39*	2.0	*0.09*	
Yb	^{173}Yb	11.6	*1.8*	13.8	*0.28*	12.4	*2.0*	12.6	*0.69*	13
Lu	^{175}Lu	1.9	*0.33*	2.0	*0.05*	1.7	*0.42*	1.9	*0.16*	1.8
Pb	^{208}Pb	548	*135*	619	*24*	511	*97*	466	*21*	560
Th	^{232}Th	14.8	*5.8*	17.8	*1.6*	14.3	*3.1*	15.1	*1.3*	
U	^{238}U	3.4	0.7	4.9	*0.29*	4.1	*1.0*	4.0	*0.09*	

Table S2: FeMnOx-1 preliminary mass fractions

Abbreviations: RSD = relative standard deviation [%] obtained from three line scans; *U* = uncertainty [%]

		FeMnOx-1					
		line scan 1 µm s^{-1}, 40 µm spot size					
		fs LA-ICP-MS 0.34 J cm^{-2} fluence			ns LA-ICP-MS 9.3 J cm^{-2} fluence		
	Isotope measured	[g/100 g]	RSD [%]	*U* [%]	[g/100 g]	RSD [%]	*U* [%]
SiO_2	^{29}Si	20.7	2.8	7.5	21.2	1.7	4.2
Al_2O_3	^{27}Al	3.69		3.3	3.69		3.3
Fe_2O_3(t)	^{57}Fe	8.82	2.8	7.8	10.0	1.9	7.4
MnO	^{55}Mn	24.7	2.4	6.3	26.9	1.9	6.6
MgO	^{25}Mg	0.55	2.3	11	0.63	1.3	12
CaO	^{43}Ca	4.39	3.0	5.3	4.49	4.4	4.5
Na_2O	^{23}Na	1.08	3.2	5.7	1.18	4.1	5.2
K2O	^{39}K	4.49	2.3	7.1	5.25	2.9	6.9
TiO_2	^{47}Ti	0.29	2.6	6.5	0.35	2.6	13
P_2O_5	^{31}P	0.053	8.4	15	0.064	9.4	34
Cr_2O_3	^{53}Cr	0.160	2.4	6.3	0.213	1.0	9.0
NiO	^{60}Ni	0.319	2.5	5.2	0.330	1.8	12
		[mg kg^{-1}]			[mg kg^{-1}]		
Ba	^{137}Ba	4880	4.6	6.0	4721	3.7	9.3
Ce	^{140}Ce	591	4.8	5.3	559	4.7	7.4
Co	^{59}Co	2.8	3.6	7.0	2.8	7.5	7.1
Cr	^{53}Cr	1122	2.4	6.3	1442	1.0	9.0
Cs	^{133}Cs	40	3.8	11	60	5.4	11
Cu	^{63}Cu	11	3.6	9.0	7.6	81	16
Dy	^{161}Dy	553	6.3	4.6	498	3.3	7.2
Er	^{167}Er	571	6.7	5.2	503	3.4	8.5
Eu	^{151}Eu	506	5.1	3.9	492	3.4	10
Gd	^{157}Gd	527	4.9	4.6	484	3.3	10
Ho	^{165}Ho	531	6.7	5.3	469	3.5	8.4
La	^{139}La	641	4.2	4.0	566	4.4	7.7
Lu	^{175}Lu	584	5.2	5.4	485	4.0	8.4
Nd	^{143}Nd	574	4.1	3.8	542	3.8	8.7
Ni	^{60}Ni	2480	2.5	5.2	2584	1.8	12
Pb	^{208}Pb	1640	11	8.1	2297	3.7	9.3
Pr	^{141}Pr	636	4.7	3.9	585	4.1	8.3
Rb	^{85}Rb	3.65	2.5	5.1	4.94	11	6.7
Sm	^{147}Sm	537	3.9	4.6	499	3.9	7.6
Sr	^{88}Sr	2170	3.7	3.6	2157	3.1	7.5
Tb	^{159}Tb	531	5.8	5.2	462	3.5	9.2
Th	^{232}Th	516	4.9	4.5	430	5.2	6.3

Tm	^{169}Tm	567	6.4	5.1	488	3.1	7.9
U	^{238}U	538	5.0	8.0	531	3.7	7.8
V	^{51}V	198	4.1	7.2	222	2.2	5.1
Y	^{89}Y	1	3.8	10	0.9	5.3	11
Yb	^{173}Yb	568	3.8	4.8	488	3.7	8.3
Zn	^{67}Zn	1710	21	12	1818	4.3	11
Zr	^{90}Zr	1268	3.0	4.8	1101	2.8	6.2

Table S3: Detection limits

Isotope measured		Detection Limits			
		Spots		Lines 1 µm s^{-1}	
		40 µm, 10 (ns laser) - 50 (fs laser) Hz			
		fs laser, 0.31 J cm^{-2}	ns laser, 9.35 J cm^{-2}	fs laser, 0.33 J cm^{-2}	ns laser, 8.8 J cm^{-2}
		[µg g^{-1}]	[µg g^{-1}]	[µg g^{-1}]	[µg g^{-1}]
Na	^{23}Na	904	32	87	27
Mg	^{25}Mg	269	11	27	10
Al	^{27}Al	194	8	18	8
Si	^{29}Si	9782	344	862	312
P	^{31}P	305	10	22	7
K	^{39}K	1546	59	108	42
Ca	^{43}Ca	4629	161	410	147
Ti	^{47}Ti	63	2.4	5.4	2.2
V	^{51}V	8.1	0.31	0.7	0.26
Cr	^{53}Cr	4.7	0.24	0.49	0.21
Mn	^{55}Mn	36	1.8	3.6	1.6
Fe	^{57}Fe	218	6.9	19	6.8
Co	^{59}Co	5.0	0.18	0.42	0.15
Ni	^{60}Ni	149	5.5	13	4.8
Cu	^{63}Cu	34	1.2	2.6	1.0
Zn	^{67}Zn	406	12	29	6.9
		[ng g^{-1}]	[ng g^{-1}]	[ng g^{-1}]	[ng g^{-1}]
Rb	^{85}Rb	16770	583	1314	483
Sr	^{88}Sr	4371	154	336	129
Y	^{89}Y	253	7	17	6
Zr	^{90}Zr	644	17	43	15
Cs	^{133}Cs	6887	271	521	207
Ba	^{137}Ba	3286	121	225	89
La	^{139}La	464	12	27	11
Ce	^{140}Ce	<0.01	<0.01	<0.01	<0.01
Pr	^{141}Pr	<0.01	<0.01	<0.01	<0.01
Nd	^{143}Nd	<0.01	<0.01	<0.01	<0.01
Sm	^{147}Sm	<0.01	<0.01	<0.01	<0.01
Eu	^{151}Eu	<0.01	<0.01	<0.01	<0.01
Gd	^{157}Gd	<0.01	<0.01	<0.01	<0.01
Tb	^{159}Tb	<0.01	<0.01	<0.01	<0.01
Dy	^{161}Dy	<0.01	<0.01	<0.01	<0.01
Ho	^{165}Ho	139	6	10	5
Er	^{167}Er	<0.01	<0.01	<0.01	<0.01
Tm	^{169}Tm		36	56	30
Yb	^{173}Yb	<0.01	<0.01	<0.01	<0.01
Lu	^{175}Lu	<0.01	<0.01	<0.01	<0.01
Pb	^{208}Pb	1644	82	101	55
Th	^{232}Th	<0.01	<0.01	<0.01	<0.01
U	^{238}U	<0.01	<0.01	<0.01	<0.01

Table S4: Count rates and RSD values in Figure 2

Abbreviations: RSD = relative standard deviation [%] obtained from three line or spot scans, respectively

		Mg	Mn	Fe	Sr	Ba	Ce	U
		Spot measurements						
fs LA								
NIST SRM 610	cps	927	17733	398	26048	4247	23289	54592
	RSD	8	6	22	4	14	6	4
GSE-1G	cps	50370	25383	84599	26151	4792	26817	60203
	RSD	0.8	4	2	3	1.4	3	7
JMn-1	cps	158523	43200900	186145	128165	64702	26949	2149
	RSD	40	51	24	30	45	17	58
FeMn-1	cps	207155	78249900	230530	202547	115790	28013	3576
	RSD	23	25	29	36	9	29	46
NOD-A-1	cps	269159	31323900	416076	324939	61711	217405	4567
	RSD	8	6	11	8	15	11	27
NOD-P-1	cps	120997	31090800	130869	91752	59954	51644	1435
	RSD	19	16	19	10	14	31	32
ns LA								
NIST SRM 610	cps	32650	511396	13271	1030810	151337	1079860	1446540
	RSD	2	3	4	0.4	1.0	0.7	2
GSE-1G	cps	1379710	665187	2689410	923876	168031	1139740	1676730
	RSD	0.4	1.2	0.6	0.9	1.0	0.9	2
JMn-1	cps	2044870	505365000	5367600	2853220	884173	1410280	33989
	RSD	4	14	32	24	11	44	35
FeMn-1	cps	3299340	1127070000	4554300	3879420	2651720	758792	40489
	RSD	3	4	3	4	7	0.6	2
NOD-A-1	cps	5330850	554139000	7559280	8509830	1243090	4599390	57817
	RSD	10	13	12	27	14	20	19
NOD-P-1	cps	3302370	787275000	4144380	3019740	1863940	2040630	33813
	RSD	6	5	4	2	7	5	6

Table S4 continued

		Mg	Mn	Fe	Sr	Ba	Ce	U
		Line measurements, 1 µm s^{-1}						
fs LA								
NIST SRM 610	cps	8498	156248	3422	280710	48547	325018	635413
	RSD	3	1.0	3	2	0.9	4	2
GSE-1G	cps	534053	285488	966951	363928	68335	443177	837056
	RSD	2	5	6	2	3	4	5
JMn-1	cps	573371	157686000	1351580	814216	293558	381782	13253
	RSD	3	9	12	8	4	7	8
FeMn-1	cps	741502	287360000	1174690	964683	803229	216770	13870
	RSD	31	27	3	19	12	24	17
NOD-A-1	cps	1407220	166246000	2122810	1965970	447159	1529860	27291
	RSD	6	13	16	11	13	16	10
NOD-P-1	cps	872748	248134000	858984	814483	650828	484035	13970
	RSD	13	13	19	12	22	22	24
ns LA								
NIST SRM 610	cps	31632	496973	13352	1063470	174908	1220000	1873800
	RSD	2	2	5	3	4	3	2
GSE-1G	cps	1369760	664870	2713390	883816	164508	1152400	1823630
	RSD	0.6	1.2	0.9	1.8	1.0	1.3	0.1
JMn-1	cps	1933330	482238000	3933930	2659680	934788	1106090	34773
	RSD	7	17	3	9	12	2	10
FeMn-1	cps	2359210	790648000	3790780	2992380	2284860	670411	37084
	RSD	6	12	6	10	24	11	9
NOD-A-1	cps	3896590	349296000	5735760	4521660	945567	3641220	51507
	RSD	4	24	7	13	27	21	14
NOD-P-1	cps	2222850	564571000	2887540	2288780	1538570	1556360	30306
	RSD	5	4	11	1.4	6	8	2

Table S5: Preferred values of FeMnOx-1 (further information and values of each measurement are provided in Jochum *et al.*, submitted)

	[g/100 g]	*s*
SiO_2	20.9	0.6
Al_2O_3	3.69	0.08
Fe_2O_3(t)	8.88	0.47
MnO	26.6	1.3
MgO	0.54	0.1
CaO	4.03	0.21
Na_2O	0.96	0.13
K_2O	3.89	0.56
TiO_2	0.38	0.04
P_2O_5	0.066	0.009
LOI	25.6	
	[mg kg^{-1}]	
Ba	5392	497
Ce	630	39
Cr	1172	134
Cs	46	11
Dy	568	34
Er	548	40
Eu	537	25
Gd	535	27
Hf	632	29
Ho	543	33
La	666	43
Lu	576	41
Nd	616	40
Ni	2399	142
Pb	1624	280
Pr	660	33
Rb	4.5	0.5
Sm	565	34
Sr	2278	140
Tb	538	33
Th	534	40
Tm	569	37
U	547	17
V	209	20
Yb	565	37
Zn	1508	153
Zr	1314	95

B.4

Macholdt et al., Chem. Geology, 2017

Characterization and differentiation of rock varnish types from different environments by microanalytical techniques

Dorothea S. Macholdt[a,b], Klaus Peter Jochum[b], Christopher Pöhlker[a], Andrea Arangio[c], Jan-David Förster[a], Brigitte Stoll[b], Ulrike Weis[b], Bettina Weber[c], Maren Müller[d], Michael Kappl[d], Manabu Shiraiwa[c], A. L. David Kilcoyne[e], Markus Weigand[f], Denis Scholz[g], Gerald H. Haug[b], Abdullah M. Al-Amri[h], and Meinrat O. Andreae[a,h]

a Biogeochemistry Department, Max Planck Institute for Chemistry, Mainz, Germany.
b Climate Geochemistry Department, Max Planck Institute for Chemistry, Mainz, Germany.
c Multiphase Chemistry Department, Max Planck Institute for Chemistry, Mainz, Germany.
d Physics of Interfaces Department, Max Planck Institute for Polymer Research, Mainz, Germany.
e Lawrence Berkeley National Laboratory, Berkeley, CA, United States.
f Modern Magnetic Systems Department, Max Planck Institute for Intelligent Systems, Stuttgart, Germany.
g Geology Department, Johannes Gutenberg University, Mainz, Germany.
h Geology and Geophysics Department, King Saud University, Riyadh, Saudi Arabia.

Chemical Geology 495, 91-118. DOI: 10.1016/j.chemgeo.2017.04.009

Chemical Geology 459 (2017) 91–118

Contents lists available at ScienceDirect

Chemical Geology

journal homepage: www.elsevier.com/locate/chemgeo

Characterization and differentiation of rock varnish types from different environments by microanalytical techniques

D.S. Macholdt[a,b,*], K.P. Jochum[b], C. Pöhlker[a], A. Arangio[c], J.-D. Förster[a], B. Stoll[b], U. Weis[b], B. Weber[c], M. Müller[d], M. Kappl[d], M. Shiraiwa[c,e], A.L.D. Kilcoyne[f], M. Weigand[g], D. Scholz[h], G.H. Haug[b], A. Al-Amri[i], M.O. Andreae[a,i]

[a] Biogeochemistry Department, Max Planck Institute for Chemistry, Mainz, Germany
[b] Climate Geochemistry Department, Max Planck Institute for Chemistry, Mainz, Germany
[c] Multiphase Chemistry Department, Max Planck Institute for Chemistry, Mainz, Germany
[d] Physics of Interfaces Department, Max Planck Institute for Polymer Research, Mainz, Germany
[e] Department of Chemistry, University of California, Irvine, CA, United States
[f] Lawrence Berkeley National Laboratory, Berkeley, CA, United States
[g] Modern Magnetic Systems Department, Max Planck Institute for Intelligent Systems, Stuttgart, Germany.
[h] Geology Department, Johannes Gutenberg University, Mainz, Germany
[i] Geology and Geophysics Department, King Saud University, Riyadh, Saudi Arabia

ARTICLE INFO

Keywords:
Rock varnish
Varnish types
Desert varnish
fs LA-ICP-MS
EPR
SEM
STXM-NEXAFS
Categorization

ABSTRACT

We investigated rock varnishes collected from several locations and environments worldwide by a broad range of microanalytical techniques. These techniques were selected to address the challenges posed by the chemical and structural complexity within the micrometer- to nanometer-sized structures in these geological materials. Femtosecond laser ablation-inductively coupled plasma-mass spectrometry (fs LA-ICP-MS), scanning transmission X-ray microscopy-near edge X-ray adsorption fine structure spectroscopy (STXM-NEXAFS) in combination with scanning electron microscopy (SEM) of focused ion beam (FIB) ultra-thin (100–200 nm) sections, conventional and polarization microscopy, as well as electron paramagnetic resonance (EPR) measurements were used to obtain information about these rock varnishes.

Rock varnishes from different environments, which cannot readily be distinguished based on their macroscopic appearance, differ significantly in their constituent elemental mass fractions, e.g., of Mn, Fe, Ni, Co, Ba, and Pb, and their rare earth element (REE) patterns. Structural characteristics such as the particle sizes of embedded dust grains, internal structures such as layers of Mn-, Fe-, and Ca -rich material, and structures such as cavities varied between varnishes from different environments and regions in the world. The EPR spectra were consistent with aged biogenic Mn oxides in all samples, but showed subtle differences between samples of different origin.

Our observations allow us to separate rock varnishes into different types, with differences that might be indicators of distinct geneses. Five different types of rock varnish could be distinguished, Type I–V, of which only Type I might be used as potential paleoclimate archive. Each varnish type has specific characteristics in terms of their elemental composition, element distribution, and structures. The combination of element ratios (Mn/Ba, Al/Ni, Mn/REY, Mn/Ce, Mn/Pb, La_N/Yb_N, and Ce/Ce*), total REE contents, and structures can be used to separate the different types of rock varnish from each other.

1. Introduction

Rock varnishes are black layers of unknown geneses, occurring on rock surfaces of slowly weathering rocks, independent of the lithology of the underlying rock (Engel and Sharp, 1958). They consist of poorly crystallized Mn and Fe oxides, as well as clay minerals (Potter and Rossman, 1979). The clay mineral fraction, which is thought to be derived from dust, represents up to 70% of the varnish volume (Thiagarajan and Lee, 2004) and is cemented together by a nanocrystalline matrix of Mn- and Fe-oxides and hydroxides. The origin and precipitation of the Mn-rich matrix material is not fully understood, but airborne dust, from which Mn and other constituents of the varnish are

* Corresponding author at: P.O. Box 3060, 55020 Mainz, Germany.
E-mail address: d.macholdt@mpic.de (D.S. Macholdt).

http://dx.doi.org/10.1016/j.chemgeo.2017.04.009
Received 10 January 2017; Received in revised form 10 April 2017; Accepted 11 April 2017
Available online 13 April 2017
0009-2541/

leached and reprecipitated before the dust particles are removed again by wind erosion, is considered the most likely element source (Hodge et al., 2005; Nowinski et al., 2013; Thiagarajan and Lee, 2004). While the upper continental crust has a mass fraction of about 0.1% MnO (Rudnick and Gao, 2003), varnish is strongly enriched (40–200 times) in this element. Rock varnish deposited in the form of a layered sediment is potentially applicable as paleoclimate archive (Dorn, 1984).

The first description of rock varnish was written in 1812 by the so-called father of rock varnish, Alexander von Humboldt (Dorn, 2008; Von Humboldt and Bonpland, 1819), who observed it in the splash zone at the cataracts of the Orinoco River. He was aware that similar rock varnishes can be found in a wide variety of terrestrial environments. Currently, biological and abiotic processes, as well as a combination of both, have been suggested for the genesis of rock varnish, but definite proof has eluded the research community so far (Dorn, 2009).

There are three main theories how varnish forms (Dorn, 2008): I) Abiogenic leaching from Mn-bearing minerals under well-defined pH (5.7) and Eh (0.8) conditions in rainwater or dew to geochemically fractionate Mn (Thiagarajan and Lee, 2004). At these pH and Eh conditions, Mn is more soluble than Fe and consequently the dissolved Mn content is enhanced relative to the dissolved Fe content. Following increases in pH up to ~8.5 can oxidize and enrich Mn without a simultaneous enrichment of Fe. However, this process is very slow and the question remains why varnish covers only certain patches and not large areas. II) Biologically induced or controlled varnish growth. Here, the Mn oxyhydroxide mineralization is either the result of interactions between biological membrane/cell surfaces and the inorganic environment, or cellular activities provide the initial nucleation of the Mn oxyhydroxides, followed by growth of the mineral product (Northup et al., 2010; Perry et al., 2004; Perry and Kolb, 2004; Perry et al., 2005). Biogenic Mn oxidation is a fast process compared to abiogenic oxidation, which raises the question why some varnishes grow only nanometers per decade. III) A combination of the processes described above.

The general structure of Mn oxides and hydroxides, called Mn oxyhydroxides for simplification, are octahedrally coordinated Mn ions, which have the ability to be stacked in several different ways and build sheet, chain, and tunnel structures. Which oxyhydroxide mineral forms depends on several factors, such as pH, Eh, temperature, biological mediation, and cation availability (Tebo et al., 2004). Biologically mediated Mn oxyhydroxides are called Mn bio-oxides in the following chapters. Manganese minerals, which are often quite small or even nanocrystalline, are known for their large surface areas and negative charges due to non-shared oxygen atoms at the surfaces. Vacancies, reduced valence states of Mn, or isomorphic substitution of lower valence state elements for Mn add additional negative charge, which can be balanced by cation absorption. These structural properties make manganese oxyhydroxides well-known but poorly understood ad- and absorbants.

Estimates of the growth rate of rock varnish vary between 1 and 40 μm per 1000 a (Liu and Broecker, 2000; Spilde et al., 2013) but growth might be much faster in non-arid environments. The growth rate seems to depend on the humidity of the environment, with slower growth rates for desert climates (Krinsley et al., 2012). The maximum thickness of rock varnish is about 250 μm (Northup et al., 2010), but the values are controversial. Commonly found thicknesses are in the range of 50 μm (Raymond et al., 1993). Rock varnish is thought to be suitable as correlative dating tool for desert environments, usable beyond ^{14}C dating (Broecker and Liu, 2001). Unfortunately, no direct dating of rock varnish has yet been successful (Watchman, 2000), but an upper age limit can be given if the exposure age of the host rock or varnished surface is known (Lee and Bland, 2003).

Many studies on varnish and its chemical composition have been published (Dorn, 2008; Goldsmith et al., 2014; Reneau et al., 1992; Thiagarajan and Lee, 2004), and most publications describe arid desert varnish. However, some authors also discuss samples from more humid areas (Krinsley et al., 2012), urban areas (Vicenzi et al., 2016), cold environments (Dorn et al., 1992), cave samples (Spilde et al., 2002), or even extraterrestrial sites (DiGregorio, 2001; Lanza et al., 2012; Perry and Sephton, 2006). All of these samples fall under the term “rock varnish”. However, it is problematic that data from all types of varnishes, independent of region and environment, are used indiscriminately to explain a phenomenon that might originate from different formation processes. This might result in incorrect conclusions and therefore prevent us from gaining an insight into a mystery that has puzzled scientists since over 200 years. In this study we therefore compare typical arid desert varnish, which can be useful for future regional paleoclimate reconstruction (Dorn, 1984), to varnishes from several regions and environments worldwide.

We approached the categorization into different varnish types by using several microanalytical techniques. Femtosecond LA-ICP-MS was used to provide major-, minor-, and trace element information to gain a geochemical “varnish fingerprint”, STXM-NEXAFS was chosen to visualize nanostructures and element distributions on FIB milled ultra-thin sections (100–200 nm), electron paramagnetic resonance (EPR) spectroscopy was applied to investigate the Mn oxyhydroxide matrix, and SEM of FIB slices was utilized to visualize cavities and layered and disordered nanostructures.

In EPR spectroscopy, species with unpaired electrons immersed in a magnetic field can absorb energy from microwave radiation. ^{55}Manganese and ^{57}Fe in rock varnish are magnetically active and are the main contributors to the EPR signals, which are characterized by an unstructured and broad peak and linewidth. Kim et al. (2011) proposed that manganese bio-oxides produce EPR spectral signatures different from those formed by abiogenic and synthetic processes. In their study, they observed a considerably narrower linewidth (< 560 G) for biogenic samples than for abiogenic Mn oxide minerals, which have a 2–6 times broader (> 1200 G) linewidth. These narrow linewidths of Mn bio-oxide minerals are unique for pure Mn oxides, since they are usually only observed for highly diluted samples, e.g., 0.5% m m^{-1} Mn ions supported on alumina (Kijlstra et al., 1997). Kim et al. (2011) explained the narrow linewidths with high amounts of layer site vacancies (15–50%), small particle sizes, and the absence or lack (0–5%) of Mn^{3+} in Mn bio-oxides. Furthermore, they investigated rock varnish to see into which category, biogenic or abiogenic it falls, and observed an intermediate linewidth between 600 and 1200 G for their samples. This was explained by an originally biogenic origin, followed by an abiogenic transformation from birnessite to todorokite during aging processes, a common transformation process based on observations from Mn nodules by Tebo et al. (2005). Biogenic layered Mn oxides may partially transform to tunnel structure minerals and/or acquire cations with aging, filling up vacancies (Tebo et al., 2004). Kim et al. (2011) chose for their investigations a rock varnish sample from Four Buttes, Mojave Desert, CA, USA. In our paper, we interpret our EPR dataset on basis of their observations and interpretation.

2. Samples

Several different environments were studied (Fig. 1):

1. Arid desert environments in California (Kohl et al., 2015), Mauritania, and Saudi Arabia. These samples are compared to previously investigated arid desert varnishes from California and Israel (Macholdt et al., 2015). In California, the additional samples studied were collected in the Anza Borrego desert (part of the Colorado desert) and in Johnson Canyon in the Mojave Desert, the driest desert in North America. In Saudi Arabia, they were collected near Jubbah and on Jebel Yatib, both in the An Nafud desert. In Mauritania, samples were taken in a canyon northwest of Azougui, in the Sahara region. The previously studied samples had been collected from different locations in the Mojave Desert and Sde Boker in the Negev Desert in Israel. All of these samples will be

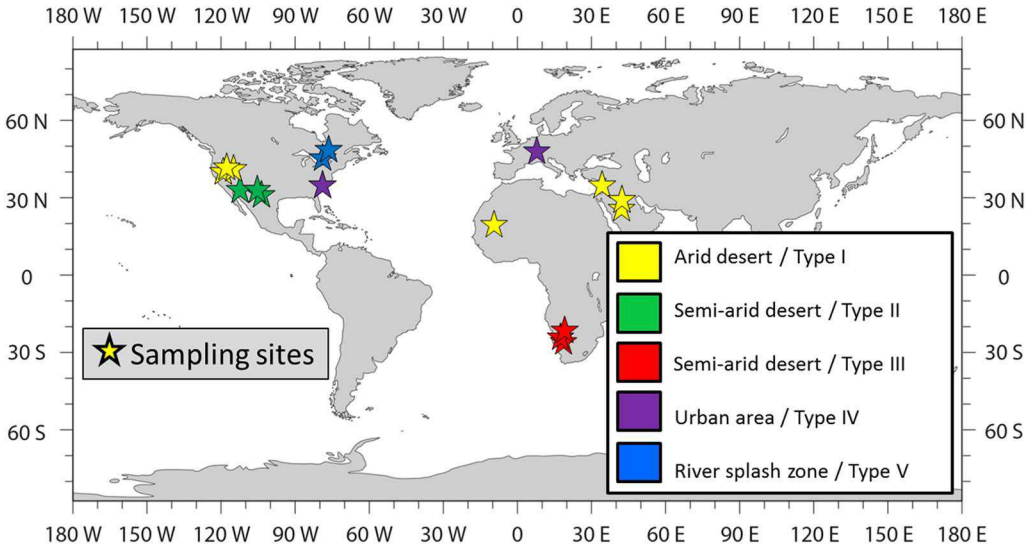

Fig. 1. Sampling locations of rock varnish. Yellow stars: Type I varnish; green stars: Type II varnish; red stars: Type III varnish; purple stars: Type IV varnish; blue stars: Type V varnish. (For interpretation of the references to color in this figure legend, the reader is referred to the web version of this article.)

assigned to the term Type I varnish in the following.

2. Semi-arid desert environments in the Chihuahuan Desert, Texas, and the Sonoran Desert, Arizona. This type of varnish, in the following called Type II, differs from Type III varnish by its typical rock varnish appearance, i.e., full coverage of the rock surfaces. It covers larger surfaces on the top and sides of rock outcrops, without visible growth directions. It differs from typical arid desert varnishes (Type I) by its mostly thicker crusts and the growth features without detectable layering.
3. Semi-arid desert or coastal desert environments in the Knersvlakte, South Africa. Previously collected and investigated samples from South Africa (Macholdt et al., 2015) will be referred to as SA-1 in the following text, the new samples as SA-2. This type of varnish, called Type III in the following, differs from the Type II semi-arid desert varnish (described above) by its growth direction and appearance. The South African samples grew on host rock pebbles with diameters of a few centimeters. The pebbles occur in round patches of about 1–10 m diameter that are conspicuously colored dark black to brown. The pebbles in the middle of the patches show a black varnish crust with metallic luster on their top and a slightly duller tinge on the subsoil part and sides, the pebbles closer to the rim were dull brown. The top and bottom sides of the rocks were often not fully enclosed by the varnish, which appears to have grown from the rock-soil-atmosphere contact upwards and downwards on the rock surface, and therefore also within the subsoil.
4. Urban environments with varnishes on sandstone buildings, e.g., varnish from the Smithsonian Castle, Washington, D.C., USA (Vicenzi et al., 2016) and the Freiburger Münster, Freiburg, Germany. This varnish seems to grow preferentially on sandstone buildings. At the Freiburger Münster, Mn-rich varnish was found up to a height of about 7 m, whereas all black patches above this height were significantly less Mn-rich and are probably soot or fungi covered areas. This varnish will be called Type IV in the following.
5. River splash zones, e.g., from the Erie Barge Canal, close to Middleport, and the Adirondack Raquette River, close to South Colton. Both sampling sites are located in New York State, USA (Krinsley et al., 2012), an area with about 1028 mm of annual precipitation. The rock varnish sample from Erie Barge canal is $\leq$ 100 years old. These varnishes will be called Type V varnish in the following.

All rock varnish samples from California and South Africa were taken from the ground, and have therefore pebbles and small rocks (a few to tens of centimeters) as host rocks, which had direct contact with the underlying soil. The Israeli, Texan, Arizonian, Mauritanian, and Saudi Arabian samples were collected as fragments or chips from larger boulders or outcrops (meters in diameter). Type IV varnish from the Freiburger Münster was collected as a mm-size chip from the minster's wall, at a height of about 0.5 m from the ground. The Smithsonian Castle varnish was taken from the castle wall at a height of about 2 m. Type V varnishes were taken from boulders within the river splash zone.

We performed fs LA-ICP-MS measurements on 9–16 different spots on each sample. For the FIB and SEM investigations, three samples from California (2 × Death Valley, 1 × Johnson Canyon; Type I varnish), four samples from South Africa (2 × SA-1, 2 × SA-2; Type III varnish), one sample from Israel (Type I varnish), two samples from Saudi Arabia (1 × Jubbah, 1 × Yatib; Type I varnish), one sample from NY state (Erie Barge Canal; Type V varnish), two urban varnish samples (1 × Smithsonian Castle, 1 × Freiburger Münster; Type IV varnish), and one sample from Texas (Type II varnish) were chosen. Table 1 lists the specimens used for the analyses together with information about the sampling locations, and Fig. F in the Appendix shows exemplary outcrop conditions and sample images.

Soil dust samples were collected underneath or adjacent to Type I varnished rocks in the Anza Borrego Desert and the Mojave Desert (CA, USA) and in Jubbah and Jebel Yatib (An Nafud desert, Saudi Arabia) using a stainless steel spoon. Furthermore, dust grains accumulated on top of varnished rocks were collected in Sde Boker (Negev, Israel). For comparison with Type III varnish, we collected dust underneath varnished rocks in the Knersvlakte, South Africa.

2.1. Sample preparation

Thick sections (about 70 µm thick) were prepared for fs LA-ICP-MS measurements. To exclude trace element contamination from the polishing material, we avoided polishing of the samples. The roughness of the unpolished surfaces can be neglected for fs LA-ICP-MS measurements, since a pre-ablation step prior to each measurement produced almost flat surfaces and potential biases from remaining roughness were corrected by using Al as internal standard element. The varnish coatings were cut perpendicular to the rock surfaces, whereby cross-sections through the sedimentation sequence of the varnishes were exposed, similar to the procedure described by Reneau et al. (1992). All thick section samples were enclosed by resin (EpoxiCure™ 2 Resin and Hardener from Buehler) prior to thinning.

Table 1
Varnish samples with information about their sampling location, underlying rock type, and environment.

Varnish type	Sample name	Country	Location	Rock type	GPS coordinates	# of samples	Environment
Type I	IS	Israel	Negev Desert, Sde Boker	Quartz-rimmed limestone	30°52′25.13″N 34°47′3.8″E	4	Arid desert
Type I	CA-JC	California, USA	Johnson Canyon	Magmatic and metamorphic	36°05′49.87″N 116°51′30.32″W	4	Arid desert
Type I	CA-MD	California, USA	Mojave Desert	Magmatic and metamorphic	34°44′28.62″N, 117°4′10.14″W 34°45′13.8″N, 117°03′58.8″W 34°46′19.74″N, 117°03′28.86″W 36°11′51.3″N, 116°22′27.6″W 35°36′55″N, 116°38′39″W	7	Arid desert
Type I	CA-AB	California, USA	Anza Borrego	Magmatic and metamorphic	33°17′4″N 116°8′2″W	3	Arid desert
Type I	CA-DV	California, USA	Death Valley	Magmatic and metamorphic	36°51′31″N 117°15′59″W 36°21′16.798″N, 116°38′39″W 36°05′49.87″N, 116°51′30.32″W	5	Arid desert
Type I	MT	Mauritania	Azougui, Sahara	Sandstone	20°37′46.40″N 13° 8′15.44″W	1	Arid desert
Type I	AR-J	Saudi Arabia	Jubbah, An Nafud	Sandstone	28°01′54.51″N 40°55′5.67″E	6	Arid desert
Type I	AR-Y	Saudi Arabia	Jebel Yatib, An Nafud	Sandstone	27°29′22.40″N 41°58′35.19″E	6	Arid desert
Type III	SA-1	South Africa	Knersvlakte	Quartzite	31°16′45.2″S 18°35′42.6″E	8	Semi-arid desert
Type III	SA-2	South Africa	Knersvlakte	Quartzite	31°16′55.4″S 18°35′17.8″E	4	Semi-arid desert
Type II	TX FD 1	Texas, USA	Fort Davis, Chihuahuan Desert	Magmatic	30°36′6.48″N 103°54′46.8″W	1	Semi-arid desert
Type II	TX FD 2–4	Texas, USA	Fort Davis, Chihuahuan Desert	Magmatic	30°46′36″N 103°44′46″W	3	Semi-arid desert
Type II	TX FD 5–6	Texas, USA	Fort Davis, Chihuahuan Desert	Magmatic	30°39′36.72″N 103°47′31.56″W	2	Semi-arid desert
Type II	TX FD 7	Texas, USA	Fort Davis, Chihuahuan Desert	Magmatic	30°35′58.95″N 103°53′38.76″W	1	Semi-arid desert
Type II	AZ AL	Arizona, USA	Arizona, Sonoran Desert	Magmatic	32°4′19.92″N 112°43′42.96″W	1	Semi-arid desert
Type IV	SC	USA	Washington D.C., Smithsonian Castle, facade	Sandstone	38°53′19.63″N 77° 1′33.68″W	2	Urban varnish
Type IV	FM	Germany	Freiburger Münster, Freiburg, facade	Sandstone	47°59′43.52″N 7°51′11.85″E	1	Urban varnish
Type V	R River	NY State, USA	Adirondack Raquette River, South Colton	Gneiss	44°30′31.24″N 74°53′5.16″W	1	River splash zone
Type V	E Canal	NY State, USA	Erie Barge Canal, Middleport	Sandstone	43°12′42.09″N 78°28′43.23″W	1	River splash zone

For measurements of desert dust composition, we sieved the samples with a 50 μm sieve. Grains < 50 μm were directly mounted on double-adhesive tape and mineral grains > 50 μm were ground to grain sizes < 100 μm prior to mounting. These mounts were measured as line-ablations by fs LA-ICP-MS.

For analysis by scanning transmission X-ray micro-spectroscopy (STXM), we selected suitable sample areas by a combination of microscopy and scanning electron microscopy (SEM). Ultra-thin FIB slices, comparable to those produced from rock varnish by Krinsley et al. (2013), were milled to sizes of about 50 × 30 μm and thicknesses of about 100–200 nm. Furthermore, SEM images of the ultra-thin sections were used for structure investigations.

The EPR spectroscopy measurements were carried out on varnish powders of five samples (CA-JC, CA-AB, AR-Y, SA-2, IS). The powders were produced by taking off the upper layer of varnish from the host rock using a dremel™ mechanical abrasion instrument. We collected ca. 1 g of material from each sample and used 11 mg for the actual analyses. The material was prepared on filters, which were used for both room temperature (RT) and 90 K experiments.

3. Analytical methods

3.1. Imaging and underlying rock identification

A Leica DM RX polarizing microscope was used for investigations of varnish structures in thick sections (about 70 μm) and to check ablated line scans by LA-ICP-MS subsequent to the analysis. The host rock types were determined based on thin section observations via polarization microscopy. During the FIB slice preparation, slices were visualized by SEM. These SEM images give insights into the nanometer structures, growth features, and grain- and cavity-distributions within the varnishes.

3.2. Femtosecond laser ablation-inductively coupled plasma-mass spectrometry

We carried out the fs-LA-ICP-MS measurements using the ThermoFisher Element 2 single-collector sector-field ICP-mass spectrometer combined with an ESI 200 nm fs laser ablation system NWRFemto at the Max Planck Institute for Chemistry (Mainz, Germany). Important parameters of the ICP-MS and the laser are listed in Tables 2 and 3. Laser ablation was conducted in a New Wave Large Format Cell in a He atmosphere. This carrier gas was mixed with an Ar gas flow to transport the aerosols generated by ablation to the ICP-MS.

All measurements were conducted in medium mass resolution mode (2000) with flat top peaks, since in this way many oxides and molecules produced from Ar and O in the plasma can be separated from the atomic ions, e.g., $^{40}Ar^{14}N^{1}H^{+}$ can be separated from ^{55}Mn, giving an improvement of the signal to blank ratio for many elements.

After pre-ablation, each sample was scanned along a profile from the underlying rock through the varnish into the embedding resin. To define the varnish region, we chose a threshold value of ≥ 2% MnO_2, since lower values are usually mixtures of varnish and host rock. At the varnish-rock interface, the Mn signal drops abruptly to values below 2% MnO_2. To obtain a representative bulk analysis for the varnishes, the concentrations of each element were averaged over the full varnish profile between the host rock contact and the resin. Bulk analyses were performed for the major elements (Na, Mg, Al, Si, P, K, Ca, Ti, Mn, and Fe) and 30 trace elements (isotopes used and all measurement results are listed in Table 1 of the Appendix). The element concentrations were determined by measuring the ion intensities of the elements of interest using Al as the internal standard element, analogous to Goldsmith et al. (2014). Since no suitable microanalytical varnish reference material existed until recently (Jochum et al., 2016; Macholdt et al., 2016), the homogeneous GSE-1G glass (GeoReM database http://georem.mpch-mainz.gwdg.de) was used for calibration. This was possible, since fs LA-ICP-MS allows nearly matrix-independent calibration (Jochum et al., 2014). To normalize the data, the oxides of the major elements (Na_2O, MgO, Al_2O_3, SiO_2, P_2O_5, K_2O, CaO, TiO_2, MnO_2, and Fe_2O_3) were assumed to add up to 98% m m^{-1}. By this method, the procedure is reproducible and easily recalculated if future measurements can provide the exact amount of water and organics within the rock varnish.

Furthermore, dust collected under or adjacent to the varnish samples was measured by fs LA-ICP-MS. The method, detection limits, measurement parameters, and tape blanks are described in detail in Macholdt et al. (2014). The dust grains and the powder reference material T1-G (GeoReM database http://georem.mpch-mainz.gwdg.de) were mounted on double-adhesive tape, which was attached to a pure Ir-strip prior to measuring.

Table 2
Operating parameters used for the fs laser ablation system.

	NWRFemto
Laser type	Ti:Sapphire
Wavelength [nm]	200
Pulse length [fs]	150
Energy density [J cm^{-2}]	0.3
Spot size [μm]	40
Pulse repetition rate [Hz]	50
Scan time [s]	350
Scan speed [μm s^{-1}]	1
Warmup and blank measurement [s]	15
Washout [s]	30

Table 3
Operating parameters of the Element2 ICP-MS.

rf power [W]	1270
Cooling gas flow rate [l min^{-1}]	15
Auxiliary gas flow rate [l min^{-1}]	1
Carrier gas (Ar) flow rate [l min^{-1}]	0.8
Carrier gas (He) flow rate [l min^{-1}]	0.7
Sample time [s]	0.002
Samples per peak	25
Mass window [%]	40
Time per pass [s]	1.4
Mass resolution	2000
Measuring type	Both; E-scan and counting mode

3.3. Electron paramagnetic resonance analysis

The EPR measurements were carried out with a CW-EPR (Continuous Wave) model EMX-plus (Bruker) at the Max Planck Institute for Chemistry (Mainz, Germany). The powdered rock varnish material was prepared on a Teflon membrane filter (Merck Millipore, reference number JVWP04700), which was folded and inserted into a glass tube prior to introducing it in the EPR instrument. For the experiments at 90 K, the system was cooled by a liquid nitrogen vapor stream. The temperature was carefully monitored by the EPR software and an additional thermometer for verification. The frequency used was 9.837440 GHz for room temperature experiments (RT, about 293 K) and 9.418697 GHz for 90 K measurements, the magnetic field was scanned from 0 to 6000 G. For each sample and temperature, the EPR spectra were recorded at eleven different microwave radiation powers, sweeping between 0.22 and 224 mW to study the saturation behavior of the signal. Further instrumental parameters were: modulation amplitude, 3.0 G; modulation frequency, 100 kHz; conversion time, 30 ms; time constant, 0.01 ms; sweep time, 300 s; number of scans, 1.

3.4. Scanning transmission X-ray microscopy-near edge X-ray adsorption fine structure spectroscopy and focused ion beam sputtering

Focused ion beam (FIB) sputtering (milling) was performed at the Max Planck Institute for Polymer Research (Mainz, Germany) using a Nova600Nanolab FIB dual-beam instrument of FEI. Simultaneously, SEM microscopy was applied to carefully determine and monitor the site of milling. Micro-basins were located by microscopy and used for the preparation of the 50 × 30 μm FIB slices. The entire samples were sputtered with 50 nm of Pt using a Baltec MED020 sputtering equipment. The selected preparation sites were coated with an additional, approximately 2 μm thick Pt layer using beam-induced Pt deposition from a metallo-organic precursor gas (1 nA at 30 kV). Milling was performed by Ga^+-ion sputtering with a resolution of about 10 nm. In a first milling step (20 nA, 30 kV), two trenches on both sides of the Pt deposition were created, followed by a second milling step at lower beam currents (7 nA and 5 nA at 30 kV) to obtain flat surfaces of the pre-thinned, about 1 μm thick, lamella. The thinned samples were lifted out and transferred to a TEM grid onto which they were attached with Pt. Stepwise thinning and polishing (1 nA and 0.5 nA at 30 kV) produced FIB slices with thicknesses of about 100–200 nm. These ultra-thin sections and the transfer onto a TEM grid are necessary for transmission measurements by STXM-NEXAFS.

The STXM-NEXAFS analyses were conducted using soft X-ray synchrotron light and two X-ray microscopes: I) the instrument at beamline 5.3.2.2 (Kilcoyne et al., 2003) at the Advanced Light Source (Berkeley, CA, USA, and II) the MAXYMUS microscope at beamline UE46-PGM-2 (Follath et al., 2010) at the synchrotron BESSY II, Helmholtz-Zentrum Berlin, Germany (Table 4). Both STXM instruments are equipped with a high energy resolving grating (resolving power at the carbon K-edge: ALS $E/\Delta E \leq 5000$; BESSY II: $E/\Delta E \leq 8000$), a Fresnel zone plate, providing a spatial resolution of about 30 nm, and phosphor-coated Lucite photomultiplier tubes for the detection of transmitted photons. At the ALS, the measurement chamber was filled with a He atmosphere prior to measuring, whereas at BESSY the measurements were conducted in a vacuum. In this study, STXM-NEXAFS elemental maps of Fe, Mn, and Ca are presented, which were recorded as images produced at discrete energies. For calibration, the characteristic pi resonance peak at 285.2 eV was measured before each measurement session. The data were evaluated with the Interactive Data Language (IDL) widget "Analysis of X-ray microscopy Images and Spectra" (aXis2000) and IGOR Pro.

4. Results

4.1. Scanning electron microscopy images and structures

Significantly denser packing and smaller dust grains can be observed in layered varnishes (Fig. 2 A, B) compared to unstructured ones (Fig. 2 C–H). These fine-grained layers were only found in Type I varnishes. However, at the contact from matrix and dust to the underlying rock, the layered varnish structure becomes disordered and cavities are present. The rock at the rock-varnish interface appears to have broken up prior or contemporaneous to growing or depositing. Either these rock fragments were broken off and dragged upwards until they were incorporated into the structure (Fig. 2 B, arrow), or the underlying rock was dissolved after evolving a varnish cover, and the developing crack system was filled up by unstructured varnish material (Fig. 2 A, arrow). However, not all Type I varnishes show layers. Some Type I varnishes show stromatolite-like features. Furthermore, the Saudi Arabian varnish from Jubbah, collected only 110 km away from the arid desert varnish location at Jebel Yatib, shows a disordered structure with large (up to 1 μm), sometimes angular, mineral fragments (Fig. 2 E, arrow). This structure is very similar to those observed in Type II, III, and IV varnishes, which show no plane layers parallel to the underlying rock, but exhibit large angular cavities and mineral grains. These cavities seem to be the result of loose packing and fast growth around the grains (Fig. 2 C–F, I), since angular mineral grains are found to be wedged in several samples, providing large openings. Sheets of matrix material often bend around mineral dust clusters and thereby incorporate them into their botryoidal structure (Fig. 2 C, E). The ellipsoidal cavities (about 1 μm in diameter) might be an indicator for Mn oxyhydroxide growth around organisms, but this cannot be proven with the current methods at hand.

The structures of the two Type IV varnishes seem to differ significantly from each other, even though they were both sampled from sandstone buildings. The sample from the Smithsonian Castles western facade (SC) shows a disordered structure with large particles and cavities (Fig. 2 F), while the Freiburger Münster (FM) sample shows parallel layers with almost no cavities, incorporating large (~1 μm) round features that are overgrown by layers, resulting in a partially botryoidal structure (Fig. 1 H). The Type V varnish structure resembles the Type III varnish structure, but no mineral grains can be observed in the SEM images of the former (Fig. 2 G).

Fig. 3 shows close-up reflected light microscopy images (B-(A-D)) and transmission light polarization microscopy images (B-(E, F)), which were taken to explain the differences between the SEM appearance of AR-Y (Fig. 2 B) and AR-J (Fig. 2 E). Larger mineral grains and a significant topography can be observed in the Saudi Arabian sample from Jubbah, which are absent in the varnish sample collected at Jebel Yatib. The large quartz grains, the high porosity, and the sparsity of the calcite matrix of the sandstone of sample AR-J result in a high topography where varnish only fills up the interspaces (Fig. 3 C). Material might be washed into these areas and larger dust grains can become caught without the potential to be blown away after leaching. This varnish does not cover the whole surface, and quartz minerals stick out (Fig. 3 B). This is dissimilar to the sample AR-Y, which is fully covered by varnish (Fig. 3 C). Both sandstone host rocks have a $CaCO_3$-rich cement. However, according to polarization microscopy (Fig. 3 E, F), the sandstone AR-Y has much smaller quartz grains than AR-J, and therefore no similarly steep topography can arise. Furthermore, the sandstone AR-J has a larger percentage of pore volume, and the matrix material is rare. The large minerals, the pore space, and the sparsity of the matrix material result in a brittle cohesion of sample AR-J, due to the high quartz grain/cement ratio, and also in superelevation of the surface topography. The lack of layers is not due to a vertical sample exposure, since similar layering was found covering a non-horizontal sample collected at Jebel Yatib (Figs. A and B in the Appendix).

4.2. Major and trace element determination by fs LA-ICP-MS

Femtosecond LA-ICP-MS is a reliable tool to measure major and trace element concentrations. In this work, 39 element mass fractions were measured for each rock varnish. From each sampling site, one to nine varnish samples were investigated, depending on the sample material available, and on each sample nine to fifteen microbasins were analyzed to obtain average element compositions. To allow a better overview, Fig. 4 shows the range in which the typical arid desert varnish samples plot as gray shaded field. Only Type I varnish plots within this range for the elements analyzed. However, Type II varnishes only diverge for the transition metals, Cu, Co, and Cr. The other varnish

Table 4
Synchrotron facilities used and their beamlines.

Synchrotron light source	Location	Beamline	Source	Energy range [eV]
Advanced light source (ALS)	Berkeley, California	5.3.2.2	Bending Magnet	250–780
Bessy II	Berlin, Germany	MAXYMUS, beamline UE46-PGM-2	Undulator	150–1900

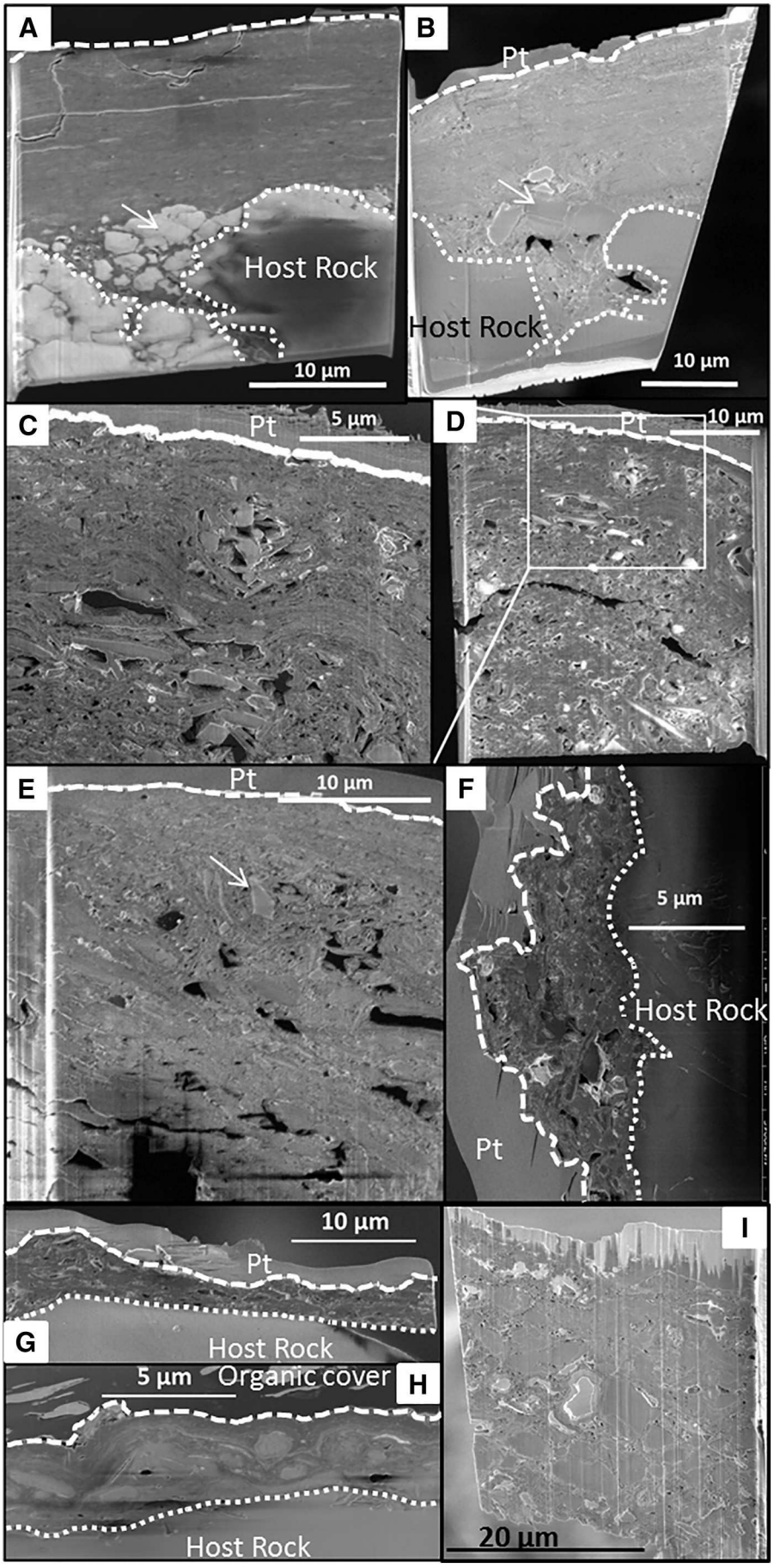

(caption on next page)

Fig. 2. SEM images of five ultra-thin (100–200 nm) transections. All SEM images were produced by an FIB instrument with an accelerating voltage between 2 and 5 kV. A) Type I varnish, Saudi Arabia (AR14 Y1), B) Type I varnish, California (CA WS18), C) close-up of D), D) Type III varnish, South Africa (SA13 mM-f), E) Type I varnish, Saudi Arabia (AR14 J1), F) Type IV varnish, Washington D.C. (SC, castle west facade). G) Type V varnish, NY State (E Canal), H) Type IV varnish, Germany (FM), and I) Type II varnish, Texas (TX). All FIB slices had been coated on their top side by Pt. Host rock-to-varnish and varnish-to-Pt boundaries are marked by white, dashed lines.

types differ from this field concerning several elements. Some element mass fractions, such as for Ce, are even more than ten times lower for some varnishes. Concerning Ba, none of the rock varnishes besides Type I and II plot within the gray shaded range. This is also expressed in Fig. 5, showing that most Type I varnish measurements plot on the x-axis (Mn/Ba) at lower values than the majority of the other varnishes. Our results show that different rock varnish types can be separated from each other based on their chemical composition (Figs. 2–5), and only Type I and II varnishes are not easily distinguishable.

Of the rock varnishes plotted in Fig. 4, only Type II varnish has equally high Ce mass fractions as Type I. This can be explained with Fig. 6 a, where Mn is plotted versus Ce. A clear positive correlation between Mn and Ce can be observed for all Type I and II varnishes. However, the correlation is less pronounced and scatters considerably for Type II. All other rock varnishes (Type III, IV, and V) show no significant correlation between the mass fractions of Mn and Ce and are generally low in Ce. Of all rock varnishes, only Type IV shows extremely high Pb concentrations (0.2–1.4%; Fig. 6 b). No correlation between the Mn and Pb mass fraction can be observed. The Pb concentrations reflect its abundance in urban areas, since Pb gets readily incorporated into Mn oxyhydroxides (Feng et al., 2007).

Fig. 7 shows an REE plot for all rock varnish types. A clear discrimination can be made between Type I and II varnish and the other rock varnishes by the combination of Ce enrichment (arid: $Ce/Ce^* = 1.5–3.8$), enrichment in light REE (arid: $La_N/Yb_N = 10.4–12.9$), the negative Eu anomaly (arid: $Eu/Eu^* = 0.6–0.7$), and the overall REE mass fraction (arid: 3200–11,200 $\mu g\ g^{-1}$).

We also investigated dust collected adjacent to the varnish samples,

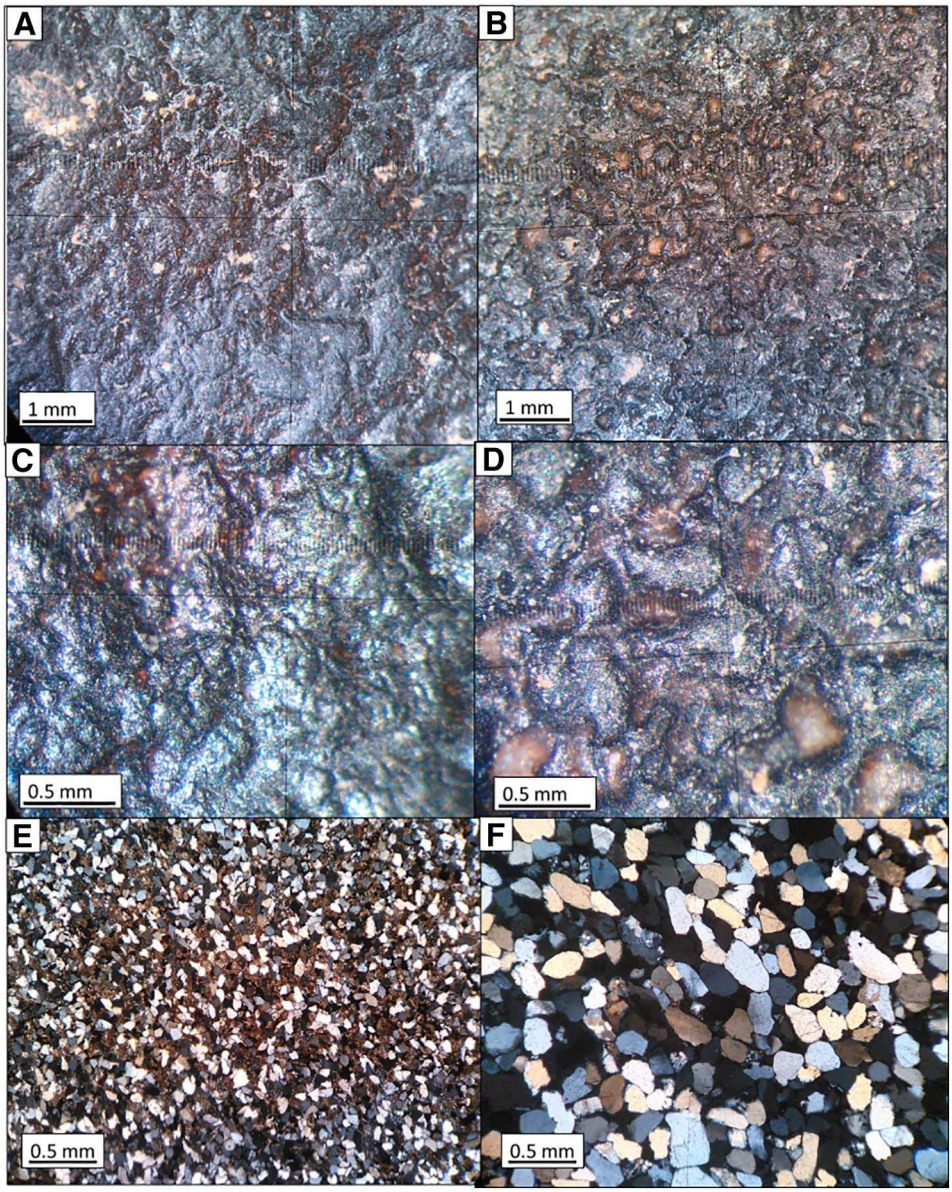

Fig. 3. Microscope images of two Saudi Arabian varnishes. A), C), E): Type I varnish from Jebel Yatib (AR14 Y1), B), D), F): Type I varnish from Jubbah (AR14 J1). Images A), B), C), and D) were taken as reflected light images from the surfaces of the varnishes with a conventional binocular microscope, images E), F) are transmission light polarization microscope images of the host rocks (sandstones) made of thin sections (25–30 μm).

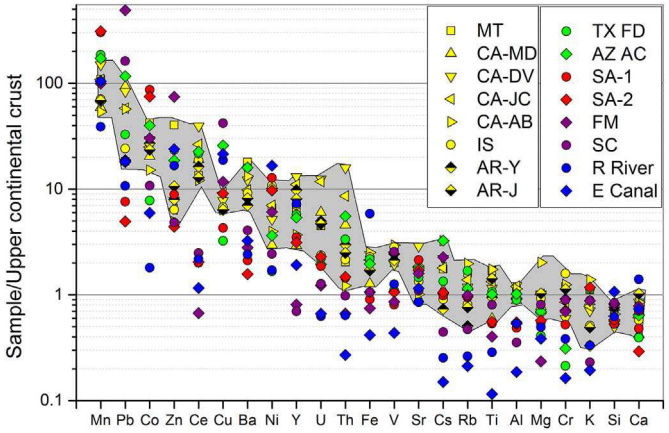

Fig. 4. Chemical composition of different varnishes from different regions, sorted by their average mass fractions. The gray shaded area is the plotting area of Type I varnish. All Type I varnishes plot within this relatively narrow field, while none of the other varnishes falls within this field for all elements. Only Type II varnish matches Type I varnish for most elements (exceptions are the transition metals Co, Cu, and Cr). Color code: Yellow: Type I varnish; green: Type II varnish; red: Type III varnish; purple: Type IV varnish; blue: Type V varnish. (For interpretation of the references to color in this figure legend, the reader is referred to the web version of this article.)

since this dust is thought to be the major source for the enriched elements. Detailed studies on the dust component are to be published by Otter et al. (in preparation). The REE patterns (Fig. C in the Appendix) show that Type I varnish is strongly enriched compared to the adjacent, fine grained dust, even though the fine grained dust is already more than two times enriched compared to the coarse grained (> 50 μm) dust (Otter et al., in preparation). The dust does not show a positive Ce anomaly, but the La_N/Yb_N ratio is similar for all dust samples, and similar to that of the varnishes. There is almost no enrichment in REEs in varnish SA-2 compared to the adjacent dust, but a small positive Ce anomaly can still be observed in the varnish.

Comparing varnish and dust ratios shows that a fractionation factor exists, which is identical for all Type I varnishes. It matches the fine fraction (< 50 μm) of arid desert mineral dust to the associated rock varnish (Fig. D in the Appendix). This factor is 9 for the Mn/Ba ratio and 0.2 for the Al/Ni ratio. It is not possible to match all coarse-grained arid desert dusts to the corresponding rock varnishes using the same factor for all samples. This is not surprising, since it is likely that only the fine-grained particles are responsible for the varnish accumulation. However, mineral dust from the semi-arid desert cannot be matched to the corresponding Type III varnish using the same factor. To match the fine fraction to the varnish for this rock varnish type, a factor of about 16 for the Mn/Ba ratio and 0.06 for the Al/Ni ratio is needed.

4.3. Matrix material investigations by electron paramagnetic resonance spectroscopy

We investigated rock varnishes of Type I and III from five locations (SA10 #9a, CA14 JC1, IS13 V2, AR14 Y1, CA13 AB2-2; Fig. 8) and compared the results to EPR measurements from a Type IV varnish from the Smithsonian Castle measured and published recently (Livingston et al., 2016). Fig. 8 shows RT and 90 K measurements at low (0.22–0.23 mW) power settings. Spectra at high power setting (209–225 mW) are plotted in Fig. E of the Appendix. All samples show similar resonance peaks. They exhibit the Fe^{3+} resonance at about 1500 G, which became more pronounced at lower temperatures. The typical peak related to Mn oxyhydroxide appears at about 3300 G. The broad linewidth of the signal can be attributed to the spin-spin interaction due to the high concentrations of paramagnetic centers in local domains that give rise to a strong exchange interaction, as described by Kim et al. (2011). The signal was slightly broader for the lower temperature (90 K) measurements, indicating the absence of Mn^{2+}-Mn^{2+} isolated pairs (Kim et al., 2011). The fine six-line patterns due to highly dispersed Mn^{2+} at low concentrations (Kim et al., 2011) appeared in the low-power spectra of the IS, CA-AB, CA-JC, and SA-2 samples at 90 K on the main resonance peak flank (Fig. 8 B). The measured spectra resemble the spectrum of the Type IV rock varnish presented by Livingston et al. (2016) and measured at 77 K, 10 mW, and 9.38 GHz, close to the settings for the spectra plotted in Fig. 8 B.

All samples fall into the category of intermediate linewidths (about 800–1100 G) and are therefore indicators for an aged Mn bio-oxide or partially transformed hexagonal birnessite. However, there are several differences between them. Sample CA-AB shows an initial rise of the signal, similar to that of all other samples, followed by a strong decline with increasing magnetic field. Also sample SA-2 shows a much broader peak shoulder and a lower peak amplitude at RT than the samples IS and CA. This pattern changes with decreasing temperature settings, resulting in a similar spectrum at 90 K, compared to the other samples. These phenomena could be attributed to the presence of domains with ferrimagnetic or antiferromagnetic properties that induce a complex behavior in response to the application of an external magnetic field and to the temperature change.

4.4. Element distribution maps by scanning transmission X-ray microscopy

The element distribution maps at the nm scale were obtained by STXM-NEXAFS. These measurements were additionally used for oxidation state determinations ($Fe^{2+/3+}$, $Mn^{2+/3+/4+}$), and for the determination of functional groups and moieties of carbon. In this work, only STXM-NEXAFS maps of Mn, Fe, and Ca are shown, emphasizing the presence or absence of layered structures in varnishes from different environments. Figs. 7, 8, 9, and 10 show the different varnish types. Only the typical Type I varnish sample reveals continuous and horizontal Mn-, Fe-, and Ca-rich layers. Calcium occurring together with Mn in rock varnish was previously described by Raymond et al. (1993), an observation that is confirmed by our data. Calcium often shows sharper features in all varnishes than Mn. In contrast to Mn, Ca and Fe are also present at higher amounts in mineral dust particles. While Type I, III, and V varnishes show Fe-rich layers, Type II and IV varnishes show only Fe-rich minerals and areas instead of layers. Type III varnish can be subdivided into two appearance groups: a) dense, homogenous varnish without cavities (Fig. 11-1), and b) cavity-rich varnish, which shows some botryoidal, cauliflower-like Mn-sheets, interspersed by areas containing nests of larger mineral particles (Fig. 11-2). Type II varnish shows areas that are Fe-rich and Mn-poor, but no layering is observable. Large, rounded mineral grains and elongated clay minerals are integrated into the varnish matrix (Fig. 10-1). Manganese and Ca are especially enriched at the contacts between mineral grains and matrix and along the rims of cavities (Fig. 10-2). Type IV varnish FM (Fig. 12-2) shows Fe-rich particles almost exclusively at the host rock - varnish boundary, where they might have acted as nucleation particles for Mn oxyhydroxide mineral growth (Burns and Brown, 1972).

5. Discussion

5.1. Element distribution, element composition, absorption properties, and structures

5.1.1. Dust contribution

Our results show that the chemistry of different rock varnishes is quite diverse. However, the element composition of Type I varnish does not vary significantly among the worldwide sampling locations. The similar element mass fractions might be interpreted as the result of dust sources of similar element compositions. However, this would be surprising, given that the samples were collected on several different continents with presumably different dust compositions. On the other hand, the widely differing plotting clusters for the disparate rock

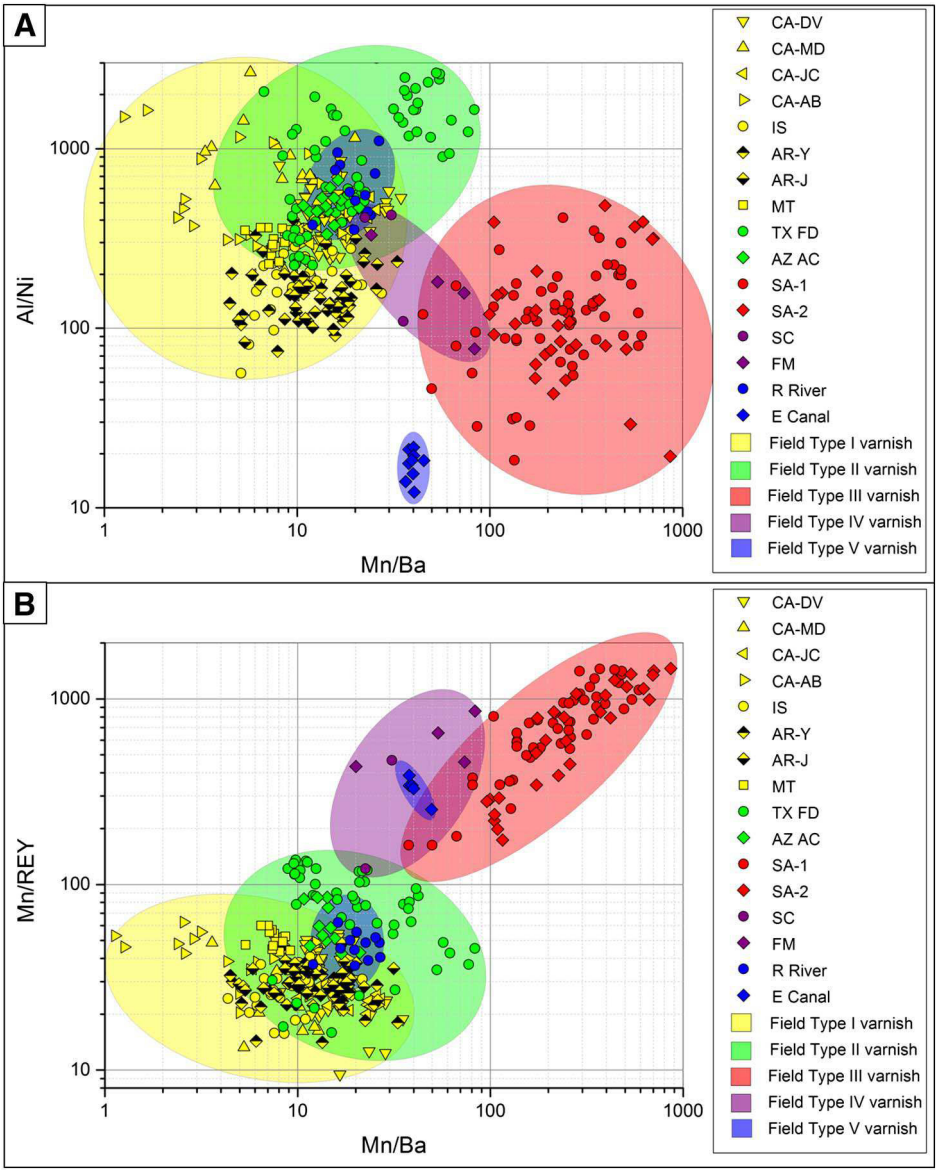

Fig. 5. a) Al/Ni vs. Mn/Ba ratio plot and b) Mn/REY vs. Mn/Ba ratio plot for all measured varnish samples. Fields, in which one type of varnish plots, are colored in the according color codes. Type I, and III varnishes plot significantly apart from each other. The Type II varnish field overlaps significantly with the Type I varnish field. Type V varnish plots in two different fields for samples from two different rivers. This indicates that river water is the main element source for Type V varnish. Type IV varnish intercepts Type II, III, and V varnish fields. Color code: Yellow: Type I varnish; green: Type II varnish; red: Type III varnish; purple: Type IV varnish; blue: Type V varnish. (For interpretation of the references to color in this figure legend, the reader is referred to the web version of this article.)

varnish types cannot be explained only by varying dust compositions, since these show much smaller differences, as shown in Fig. D in the Appendix. Rather, it is probable that different formation processes are responsible or that different Mn oxyhydroxides are present.

5.1.2. Ba, Ni, and Pb

A likely explanation for the observed similarities and dissimilarities is the existence of similar or different Mn oxyhydroxide crystal structures or growth conditions, such as the pH ranges. For Mn oxyhydroxides with different crystallographic structures, the surface chemical properties, such as the adsorption and desorption capacity of heavy metals, differ significantly from each other (Feng et al., 2007; Li et al., 2004; Pan et al., 2004). This can result in the preferred sorption of certain positively charged elements such as e.g., Ni^{2+} or Ba^{2+}. These two elements are of particular interest, since their incorporation into Mn oxyhydroxides is different. While Ba is a large ion (diameter $Ba^{2+} \sim 2.5$ Å) that can only occupy large vacant positions, such as intra-tunnel sites, the transition metal, Ni (diameter $Ni^{2+} \sim 1.49$ Å), can be incorporated in tunnels, between sheets, or even as substitute for Mn (diameter $Mn^{2+/4+} \sim 1.6/1.4$ Å).

Large atoms, such as Ba and Pb, are thought to destroy sheet structures and stabilize or promote tunnel structures (Tebo et al., 2004). The high amount of large cations observed in arid desert varnish indicates that pure birnessite is not the prevalent Mn oxyhydroxide phase, but that either partially aged and transformed (e.g., sheet structure to tunnel structure) minerals such as hollandite ($Ba_x(Mn^{4+}, Mn^{3+})_8O_{16}$) are abundant as well, which is also in agreement with our EPR investigations. Another explanation could be that an initial mixture of birnessite with other tunnel Mn oxides existed, as suggested by McKeown and Post (2001). Fig. 5 shows that the Ba mass fraction is strongly enriched only in Type I and II varnishes, while the enrichment for Pb, also a large cation (diameter $Pb^{2+} \sim 2.4$ Å), is highest in Type IV varnishes (Fig. 6 b). A reason for this behavior might be the differences in Pb availability in the surrounding environment, since Pb is highly abundant in urban areas and along roadsides (Lytle et al., 1995), as reflected in the high enrichment in the urban varnishes

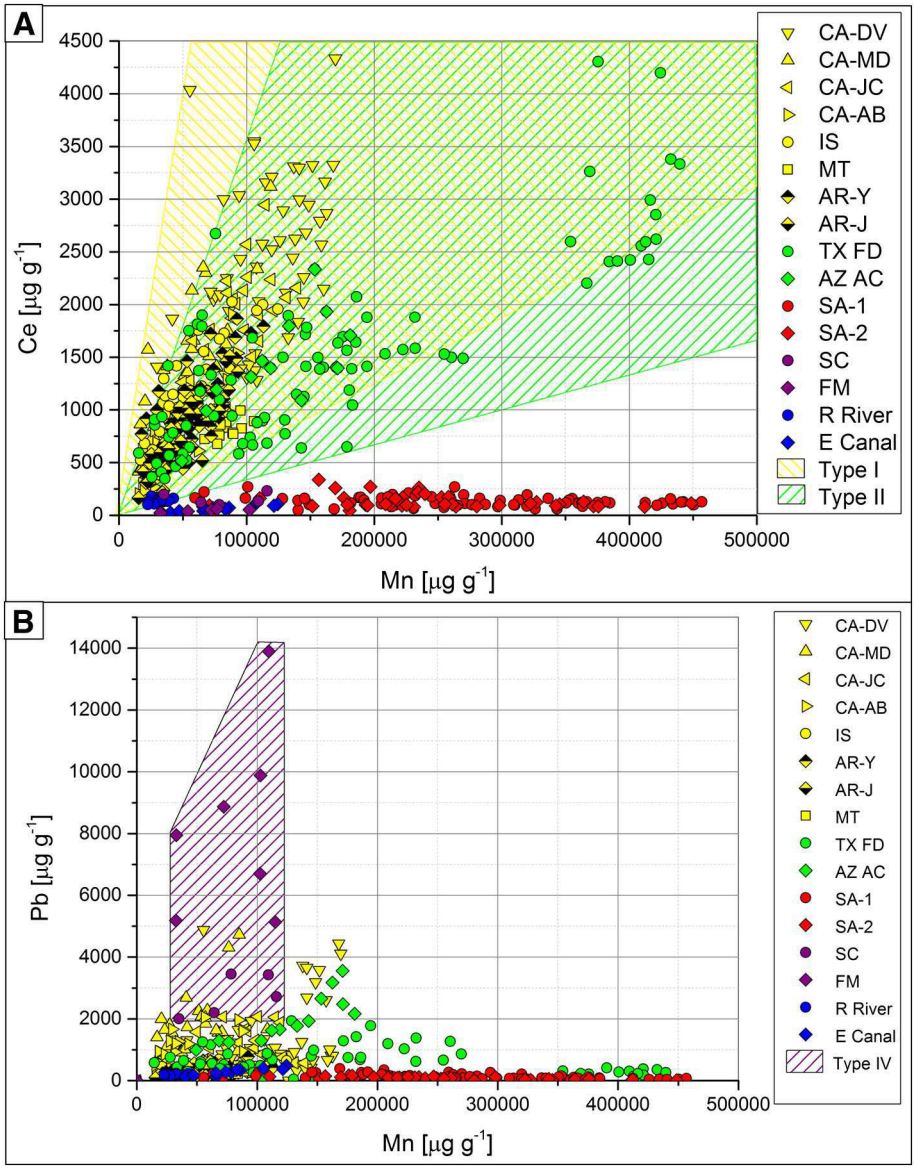

Fig. 6. a) Ce vs. Mn plot for all measured varnish samples. A significant correlation between Mn and Ce is only observable for all Type I and II varnishes. All other varnishes show no significant correlation. b) Pb vs. Mn plot for all measured varnish samples. Only Type IV varnish shows a significant enrichment of Pb, independent of the Mn mass fraction, of 0.2–1.4% Pb. Color code: Yellow: Type I varnish; green: Type II varnish; red: Type III varnish; purple: Type IV varnish; blue: Type V varnish. (For interpretation of the references to color in this figure legend, the reader is referred to the web version of this article.)

(Figs. 2 and 4b). Lead is the element most readily incorporated into Mn oxyhydroxides over a wide range of pH conditions (Feng et al., 2007).

Further factors accounting for the large differences between Pb enrichments of different varnish types might be different pH conditions or ligand abundances. Lead also forms more stable and larger complexes in the presence of ligands of longer hydrocarbon chains. This decreases the adsorption potential, since the complexes are too large to be introduced into interlayer sites (Abollino et al., 2003). Lead can be bound as hydroxy complex on the external basic surfaces of clay minerals (Rybicka et al., 1995) or Mn oxyhydroxides (Feng et al., 2007). It competes with H^+ ions with decreasing pH, since H^+ can rapidly exchange for the Pb ion (Rybicka et al., 1995), as well as for other ions.

5.1.3. Trace element enrichment behavior

As shown in Fig. 4, many cations, such as Pb, Co, Ce, Ba, Y, Ni, U, Th, Fe, and Sr, are highly enriched in rock varnish. Fig. 4 also shows that Type I and II varnishes have much higher adsorption potentials than the other varnishes. The different adsorption behavior might be an indicator for another mode of origin, since, for example, biogenic and non-biogenic Mn oxides differ in their sorption behavior. Bio-oxides have structurally less Mn^{3+}, since they are generated by two one-electron transfers from Mn^{2+} over Mn^{3+} to Mn^{4+}, where Mn^{3+} is a non-solid intermediate and exists only in solution (Tebo et al., 2004). Available Mn^{3+} will be generated secondarily when the Mn oxyhydroxide functions as electron acceptor, i.e., as oxidant. The sorption of Mn bio-oxides occurs primarily at vacancies, which are common in the usually poorly crystalline Mn bio-oxides, or on biofilms or bacterial sheaths, which are produced by the organisms during the precipitation (Tebo et al., 2004). Furthermore, biogenic oxides are usually actively growing in the presence of contaminant metal ions (Tebo et al., 2004) and therefore the cation enrichment is often higher in bio-oxides than in abiogenic Mn oxyhydroxides. However, the clay mineral fraction in rock varnish, deposited and incorporated earlier, might also contribute to the element sorption of, e.g., Pb, Cd, Cu, Ni, and Zn (Rybicka et al., 1995). Type II varnish element enrichments are very similar to those of Type I varnishes. The exceptions, Co, Cu, and Cr, might be results of either different growth mechanisms, but more likely reflect sources

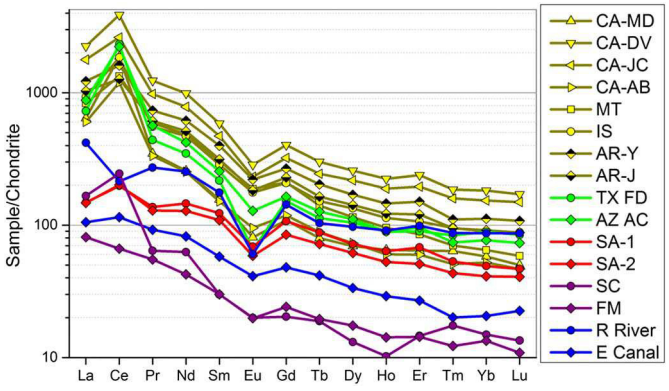

Fig. 7. Rare earth element patterns normalized to a chondritic composition (Evensen et al., 1978). All Type I, II, and III varnishes show a positive Ce anomaly. All Type I and II varnishes show a significant enrichment of light REEs (LREEs) relative to heavy REEs (HREEs). Type V and IV varnish show all the possibilities: positive, negative, and no Ce enrichment. Color code: Yellow: Type I varnish; green: Type II varnish; red: Type III varnish; purple: Type IV varnish; blue: Type V varnish. (For interpretation of the references to color in this figure legend, the reader is referred to the web version of this article.)

with different transition metal contents.

5.1.4. Rare earth elements

The high positive Ce anomaly shown in Fig. 7 might be an indicator for the growth rate of the varnishes (Bau et al., 2014). Cerium, dissimilar to the other REEs whose highest oxidation state is REE^{+3}, is the only REE that can also be found at a higher positive valence state (Ce^{4+}). Manganese oxides are one of the strongest naturally occurring oxidants and participate in a wide range of redox reactions. Manganese oxyhydroxides function for instance as electron acceptors for the oxidation of Ce:

$$Ce^{3+}_{(aq)} + MnO_{2(s)} + 2H_2O_{(l)} = CeO_{2(s)} + MnO(OH)_{(s)} + 3H^{+}_{(aq)}$$

(Ohta and Kawabe, 2001) or

$$2Ce^{3+}_{(aq)} + MnO_{2(s)} + 2H_2O_{(l)} = 2CeO_{2(s)} + Mn^{2+}_{(aq)} + 4H^{+}_{(aq)}$$

(Ohta and Kawabe, 2001).

By this process, the Mn oxyhydroxide gains additional negative charge, which can be balanced by further adsorption of cations. The generated Ce^{4+} can precipitate as insoluble cerium dioxide (CeO_2), explaining the enrichment of Ce compared to the other REEs, which are only enriched by the process of sorption, where they are in competition with other ions.

The plot Ce vs. Mn (Fig. 6 a) shows the increase of Ce for different Mn mass fractions for Type I and II varnish. The faster the varnish grows, the less Ce can be precipitated on the uppermost layer, since the Ce accumulation depends on the Ce availability over a certain time period (Bau et al., 2014). The Ce anomaly is of specific interest, since it can be compared to the enrichment of the other REEs, which are not enriched by the same process. Since we do not understand the genesis of rock varnishes, we do not know how much enrichment to expect for other elements relative to, e.g., the dust component. However, for Ce, the REE pattern can be used for direct comparison. Fig. 6 a) thus indicates a higher growth rate for most of the Type II varnishes compared to Type I varnish. Furthermore, while Type I varnishes are highly enriched in REEs relative to their dust sources, Type III varnishes seem to have only a very low enrichment in comparison to the adjacent mineral dust (Fig. D in the Appendix). This observation is in agreement with the lack of an increase of Ce for higher Mn mass fractions (Fig. 6 a).

5.1.5. Al/Ni vs Mn/Ba ratios

Since Al is distributed fairly homogeneously in rock varnish (Goldsmith et al., 2014) and Ba occurs together with Mn (Raymond et al., 1993), we chose a plot of the Al/Ni vs the Mn/Ba ratios for a comparison of the different varnish types (Fig. 5 a). Additionally, we chose Mn/REY (REEs and Y) vs. Mn/Ba since we can express the enrichment of the elements Ba and the REY independent of the Mn mass fractions (Fig. 5 b). All these elements are mainly enriched within the Mn-rich phase. Fig. 5 shows that the varnishes from similar environments plot together in discrete fields, distinguishing the various varnish types. Only the two Type V varnish samples plot apart from one another, even though they were collected from a similar environment (river splash) and from locations not far apart. This can be explained if their primary ion source is river water with significantly differing ion abundances, rather than mineral dust with a composition close to the UCC. The cation availability is presumably different for the large natural Adirondack River and the small man-made Erie Canal. The Type I and III varnishes plot in well-separated fields, while Type IV varnish intercepts other varnish fields. It can be separated by its Pb content (Fig. 6 b). Type I and II varnish show considerable overlap in this plot, while they differ in other features, such as crust thickness and the absence of layering.

5.1.6. Manganese-rich mineral matrix

To investigate the role of the crystal structures of the Mn oxyhydroxides in the matrix material of Type I and III varnish, we studied EPR spectra of several rock varnish samples. The spectra were also compared to a spectrum of sample SC (Livingston et al., 2016), a Type IV varnish, and they were all considered in the context of the biogenic-abiogenic plot published by Kim et al. (2011). We found that all investigated samples fall within the range of materials formed originally as Mn bio-oxides, based on the interpretation by Kim et al. (2011). Beyond this overall finding, we observed some differences between samples. The varnishes investigated can be subdivided into three categories: Type I varnish samples CA-JC, IS, and AR-Y show an EPR pattern similar to that of sample SC, which is a Type IV varnish. One Type I varnish, sample CA-AB, shows a lower absorption peak. It is unclear if this is the result of a different composition and mineralogy, or if other factors are involved, such as more host rock material within the varnish powder, due to rock abrasion during the sample preparation. Type III varnish reveals a significantly different absorption peak shape, comparing high and low T absorption (Fig. 8). This is typical for a saturated sample. It is therefore conceivable, that this sample has a higher abundance of layer site vacancies, and therefore a lower number of close neighbors, which suggests a higher fraction of hexagonal birnessite, or a more recent genesis with less time for transformation processes. This observation is also true, but less distinct, for sample CA-AB, a Type I varnish. Large numbers of abundant layer site vacancies, small particle sizes, and the absence or lack (0–5%) of Mn^{3+} might account for a higher probability for a biogenic origin, but hexagonal birnessite might also have formed abiotically.

5.1.7. Manganese- and iron-layering

The observations by STXM-NEXAFS give new insights into the application of rock varnish as local paleoclimate archive. The absence of parallel continuous layers of Fe and Mn in varnishes other than Type I exclude them from becoming a paleoclimate archive using the established method of Mn-, Ba-, and Fe-layer correlation (Dorn, 1984). This paleoclimate reconstruction technique is based on the assumption that Mn- and Ba-rich layers represent wet climates and Fe-rich layers dry climates (Broecker and Liu, 2001).

The reason for the lack of layers in the arid desert varnish sample AR-J is most probably the loose, $CaCO_3$-rich cement of the underlying rock in combination with the relatively large quartz grains. These prevent a fully closed varnish coating due to superelevation of the topography and may also cause further movement, disordering, and rearrangement of possibly former existing layers. Therefore, the full cover of the host rock by varnish, as well as the type of underlying rock, have to be considered when searching for potential paleoclimate archives.

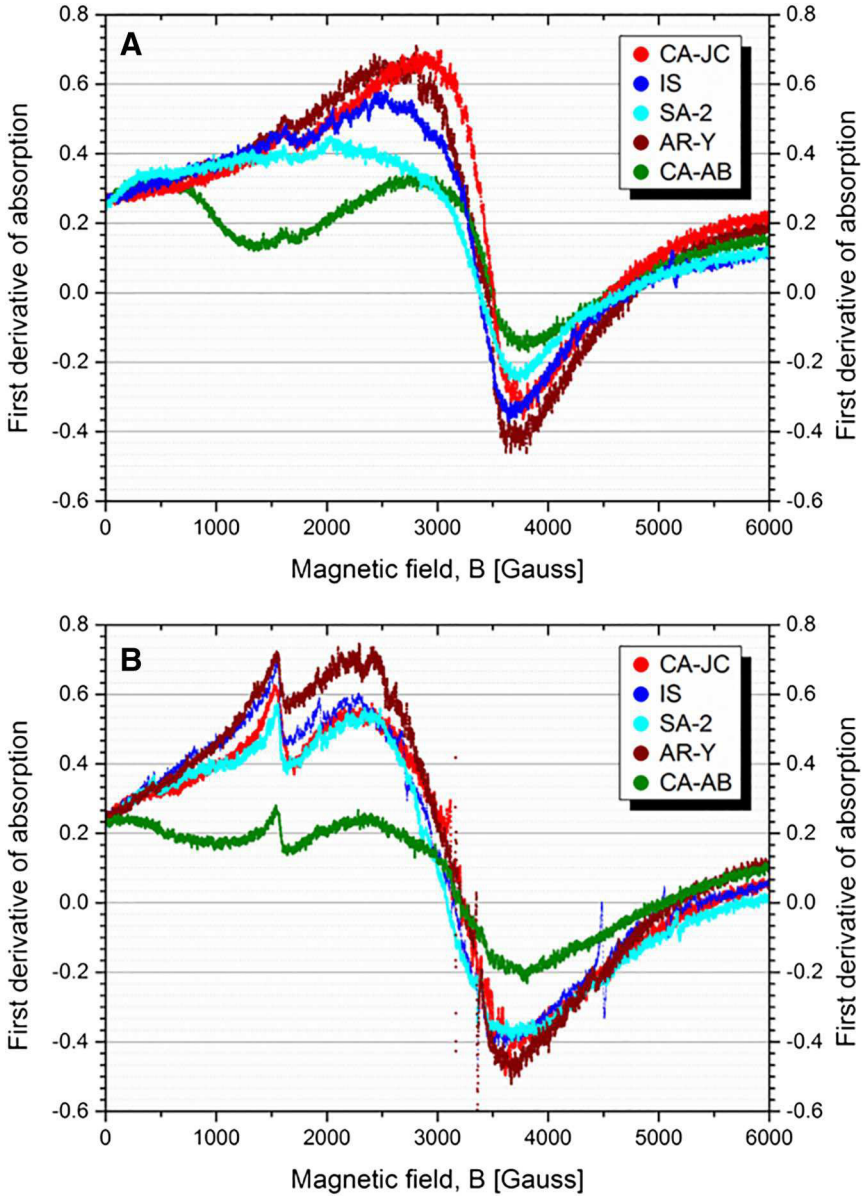

Fig. 8. Electron paramagnetic resonance spectra of five rock varnish samples (SA10 #9a, CA14 JC1, IS13 V2, AR14 Y1, CA13 AB2-2). A) spectra measured at room temperature (about 293 K) and with 0.23 mW. B) spectra measured at 90 K and with 0.22 mW. In all spectra, a Fe^{3+} peak can be observed at about 1500 G on the flank of the relatively narrow (560–1200 G) Mn absorption peak.

5.1.8. Calcium

In all rock varnishes investigated, Ca occurs together with Mn, probably due to the ability of Mn oxyhydroxides to adsorb and incorporate Ca. This was suggested by Raymond et al. (1993), who had come to this conclusion on the basis of a positive correlation between Mn and Ca in their bulk varnish samples. Our microanalytical techniques allowed us to demonstrate this relationship more specifically by showing a high abundance of Mn and Ca at the same sites within the samples. The STXM-NEXAFS element maps proved that Ca and Mn are distributed similarly in the varnish, and that Ca is incorporated into the Mn-rich matrix and does not occur as separate mineral phases. Calcium can be adsorbed into inter-tunnel and inter-sheet sites, it can replace Mn in octahedral sites, or fill vacant octahedral sites in Mn oxyhydroxides. Therefore, in addition to the option of applying Mn/Fe and Ba/Fe as paleoclimate proxies, Ca/Fe layering within Type I varnishes might be suitable as well, since the Ca-layers seem to be more pronounced than the Mn-layers, based on the STXM-NEXAFS observations in this work (Figs. 9, 10, 11, and 12).

5.1.9. Stromatolitic features

Manganese stromatolites were described from a cave in Spain by Lozano and Rossi (2012) and Rossi et al. (2010). A commonality of some of the varnishes investigated here with these cave Mn stromatolites are the structures observed, such as dendritic layers that branch upward and outward (Rossi et al., 2010). This description is especially applicable to Fig. 2 F, and was also observed in Type II varnish. However, the cave stromatolites had dimensions in the cm range, with lamination thicknesses of 1–5 μm (Rossi et al., 2010), while in our samples the structures have an overall thickness of only a few micrometers. Type I varnish reveals laminated and stromatolitic features. This combination resembles the so-called Taylor stromatolites described by McLoughlin et al. (2008), who produced these structures non-biogenically. They form by the accretion of colloids in a turbulent air flow (McLoughlin et al., 2008).

5.2. Different types of rock varnish

Based on microanalytical studies, our study shows that the term

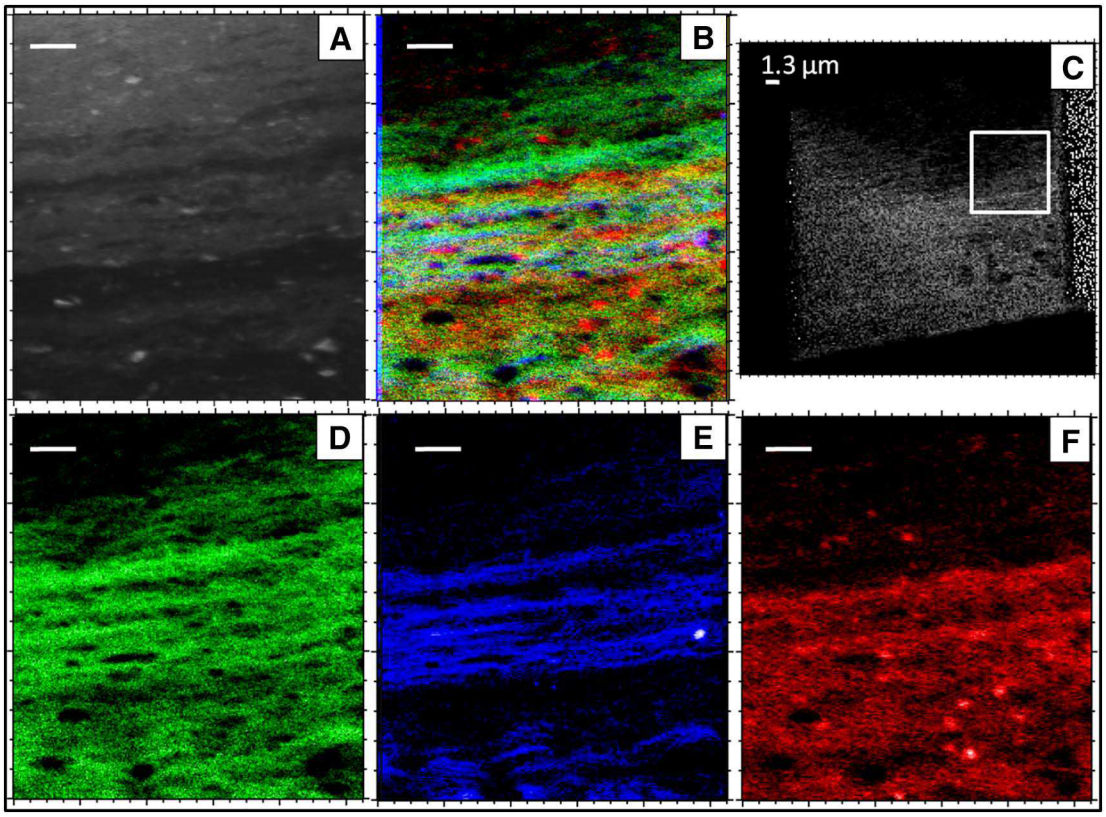

Fig. 9. Element distribution maps obtained by scanning transmission X-ray microscopy. Maps and images of Type I varnish, sample CA14 JC-8. Scale bar represents 1.3 µm, image a) was taken at 293 eV, b) is an overlay of Fe (red), Mn (green), and Ca (blue), c) is an overview image, d) a Mn map, e) a Ca map, and f) a Fe map. (For interpretation of the references to color in this figure legend, the reader is referred to the web version of this article.)

"rock varnish" requires further classification into different types, related to their formation environment, microstructure, and chemical composition (Table 5). We propose to subdivide rock varnish into Types I-V. Typical characteristics of each type are provided in Table 5, and additional images of each type and environmental surrounding can be found in Fig. F of the Appendix.

5.2.1. Type I varnish

Type I varnish can be found in arid deserts and usually shows fine-grained laminated structures (Fig. 2 A, B), with small (1–10 nm) mineral dust particles. Some crusts reveal additional cauliflower-like structures. Superelevated structures within the host rock surface hamper the formation of layers (Fig. 2 E). Alternating Mn- and Fe-rich layers, continuous and parallel to the host rock surface, might reflect paleoclimate fluctuations. These layers were only clearly observable in Type I varnish (Fig. 9). The thickest varnish and best-defined layerings are observable in microbasins, i.e., small depressions on horizontal rock surfaces. Next to Mn-rich layers, a second layering can be observed, which seems to result from varying amounts of mineral grains with different element compositions. These layers probably represent different dust fluxes and sources. Type I varnish has a distinct element composition, with high REE (Ce/Ce* = 1.5–3.8, La_N/Yb_N = 10.4–12.9, Eu/Eu* = 0.6–0.7, total REE mass fraction 3200–11,200 µg g^{-1}) and high Ba mass fractions. Cerium mass fractions are positively correlated with Mn mass fractions (Fig. 6 a), and all samples show a positive Ce anomaly (Fig. 7). Type I varnish shows EPR spectra that indicate the abundance of hexagonal birnessite, which aged and transformed with time (Fig. 8). The varnish coating is highly enriched in REEs compared to mineral dust collected nearby (Fig. C, Appendix).

5.2.2. Type II varnish

Type II varnishes, collected in semi-arid deserts, have larger Fe-rich areas and large, rounded mineral particles (Fig. 2 I). They often show upwards and outwards branching structures on the µm scale within the profile, and no Mn layering is detectable at the 100 nm to µm scale. The surfaces of these varnishes often reveal nodules grown on top of the exceptionally thick crusts (up to 500 µm thick Mn-rich crusts). Manganese, Fe, and Ca form rims around grains and cavities (Fig. 10-2). Rims lining cavities might be an evidence for either mineralization from a fluid, or dissolution and re-precipitation around a former feature, such as a microbial cell. The element composition of Type II varnish is close to that of Type I varnish (Fig. 4), but diverges for some elements, such as Co, Cu, and Cr. A strong positive correlation exists between Ce and Mn (Fig. 6 a), Ce is highly enriched (Fig. 4), and a positive Ce anomaly was found in all samples (Fig. 7). The Ce vs Mn plot scatters more than that of Type I varnish, and the Ce enrichment is lower for many samples. This indicates a higher growth rate for some Type II varnishes than for Type I varnishes. A fast growth is also indicated by the large particles within the matrix (Fig. 2 I).

5.2.3. Type III varnish

Type III varnish, found in a semi-arid desert, shows cavities and large (1–3 µm) angular mineral grains within a Mn-rich matrix (Fig. 2 C, D). Iron is abundant in mineral grains (Fig. 11), in some cases also contributing to the matrix composition, showing features following the botryoidal Mn-layers. Type III varnish shows two distinct internal structures: The first kind of Type III varnish contains large amounts of ellipsoidal cavities within the varnish matrix (Fig. 11-2). Wavy layering of the Mn-rich matrix can be observed, interspersed by chaotic structures with large minerals, mineral grain "nests", and cavities (Fig. 2 C, D). The second kind has a dense Mn-rich matrix, lacking features such as layers or cavities (Fig. 11-1). These two different kinds of varnish features, both found within the same type of varnish, seem to correlate with their position in the sampling site. Structureless, dense

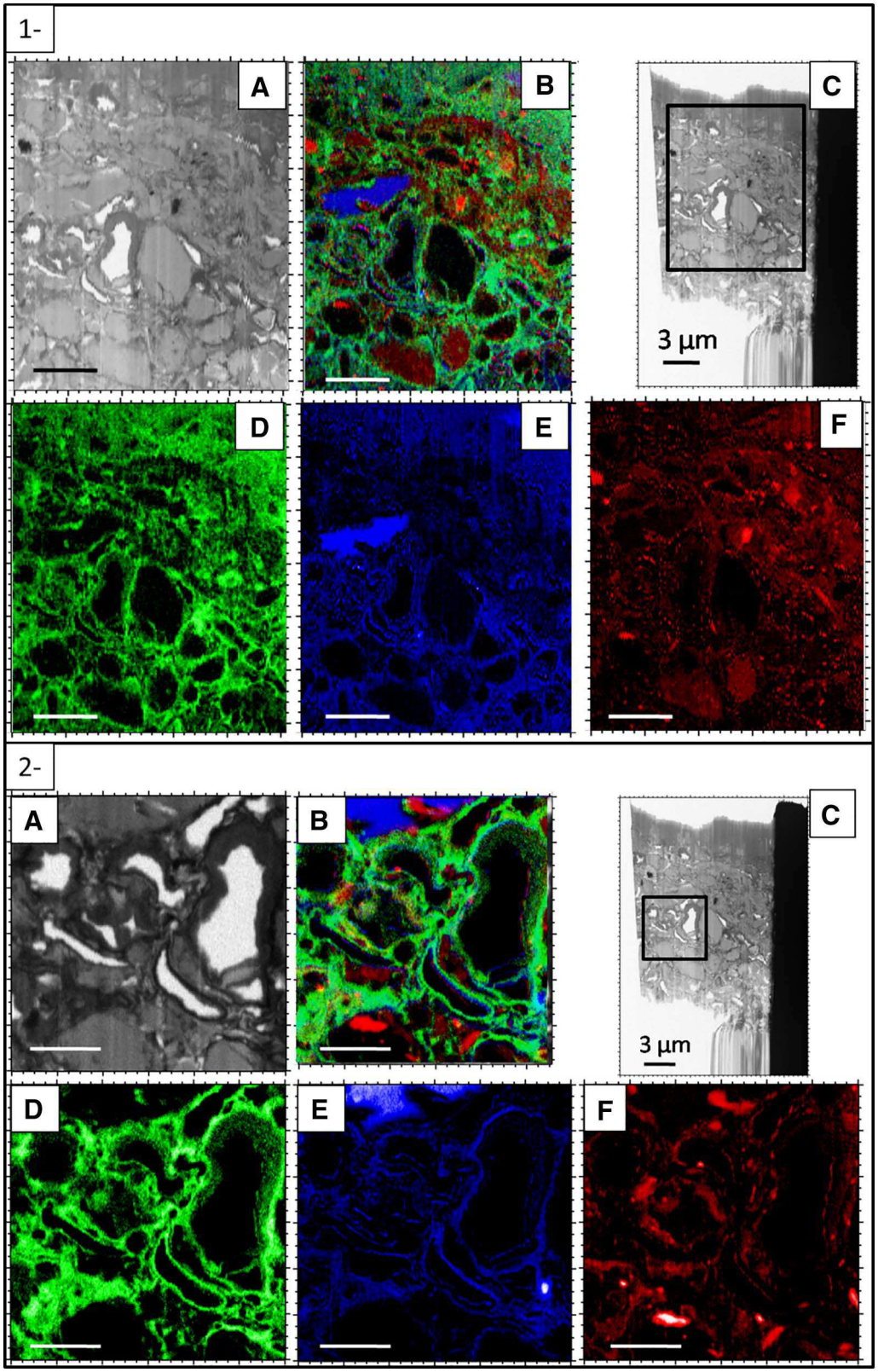

Fig. 10. Element distribution maps obtained by scanning transmission X-ray microscopy. Maps and images of Type II varnish. All images were obtained from sample TX FD 1. Scale bar represents 3 µm, Fig. 10-1 are overview images, Fig. 10-2 are close-up maps. Image a) of Fig. 10-1 was taken at 530.5 eV, b) is an overlay of Fe (red), Mn (green), and Ca (blue), c) is an overview image, d) a Mn map, e) a Ca map, and f) a Fe map. Image a) of Fig. 10-2 was taken at 642 eV, b) is an overlay of Fe (red), Mn (green), and Ca (blue), c) is an overview image, d) a Mn map, e) a Ca map, and f) a Fe map. (For interpretation of the references to color in this figure legend, the reader is referred to the web version of this article.)

varnish coatings were found on pebbles in the middle of varnish patches. They are shiny black in appearance, with a strong luster. The cavity-rich varnishes, showing botryoidal mats of Mn- and Ca-rich material, were collected on pebbles at the edges of the varnish patches. It is likely that the difference in appearance is an aging phenomenon, and that the structures change over time. This interpretation is in

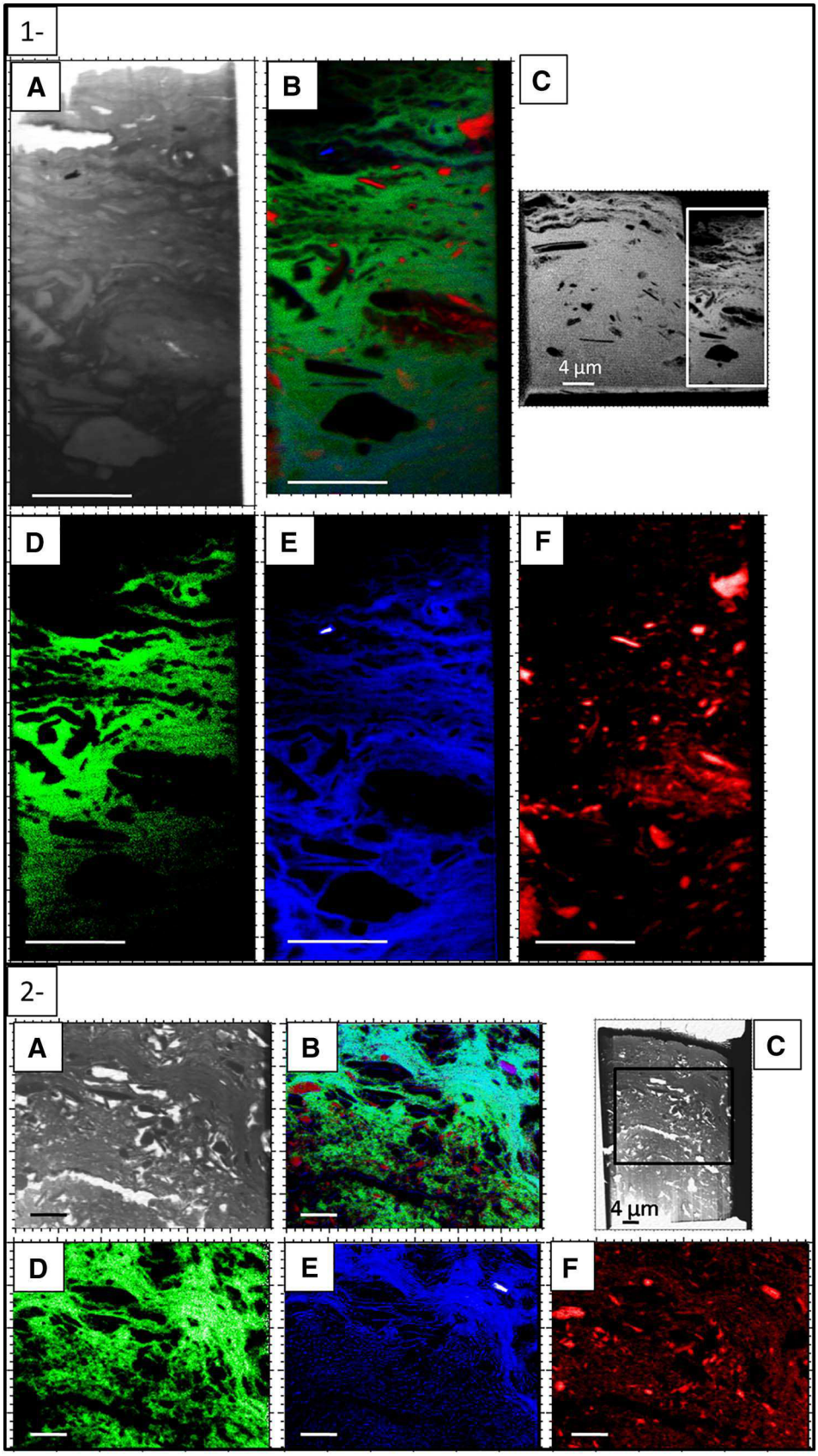

Fig. 11. Element distribution maps obtained by scanning transmission X-ray microscopy. Maps and images of Type III varnishes. Images of Fig. 11-1 show sample SA 14 09a, images of Fig. 11-2 sample SA13 mM-f. Fig. 11-1: Scale bar represents 4 µm, image a) was taken at 349 eV, b) is an overlay of Fe (red), Mn (green), and Ca (blue), c) is an overview image, d) a Mn map, e) a Ca map, and f) a Fe map. Fig. 11-2: Scale bar represents 4 µm, image a) was taken at 342 eV, b) is an overlay of Fe (red), Mn (green), and Ca (blue), c) is an overview image, d) a Mn map, e) a Ca map, and f) a Fe map. (For interpretation of the references to color in this figure legend, the reader is referred to the web version of this article.)

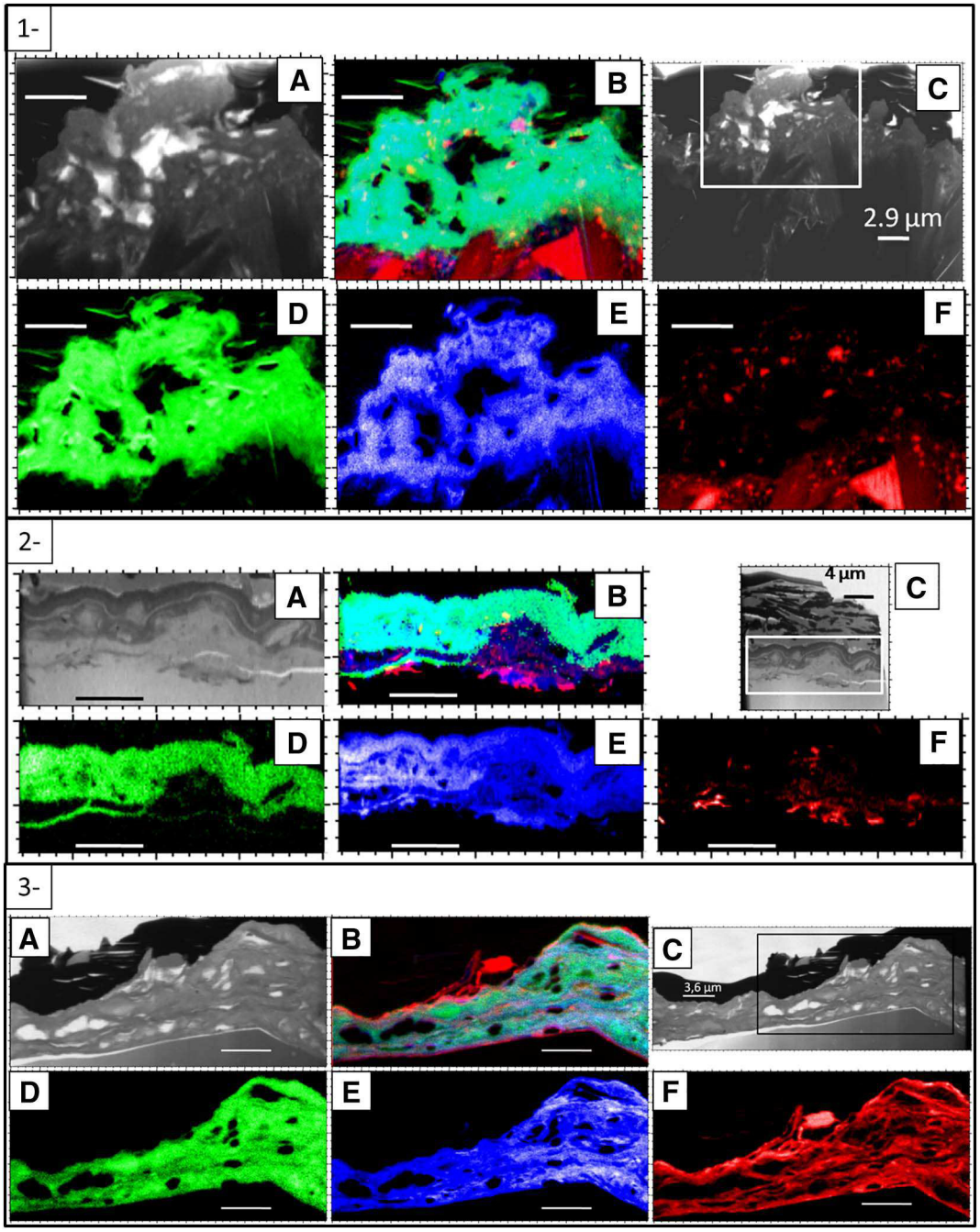

Fig. 12. Element distribution maps obtained by scanning transmission X-ray microscopy. Images and maps of Type IV and V varnishes. Images of Fig. 12-1 show sample SC (Type IV), images of Fig. 12-2 sample FM (Type IV), images of Fig. 12-3 show sample E Canal (Type V). Fig. 12-1: Scale bar represents 2.9 µm, image a) was taken at 637 eV, b) is an overlay of Fe (red), Mn (green), and Ca (blue), c) is an overview image, d) a Mn map, e) a Ca map, and f) a Fe map. Fig. 12-2: Scale bar represents 4 µm, image a) was taken at 530.5 eV, b) is an overlay of Fe (red), Mn (green), and Ca (blue), c) is an overview image, d) a Mn map, e) a Ca map, and f) a Fe map. Fig. 12-3: Scale bar represents 3.6 µm, image a) was taken at 525 eV, b) is an overlay of Fe (red), Mn (green), and Ca (blue), c) is an overview image, d) a Mn map, e) a Ca map, and f) a Fe map. (For interpretation of the references to color in this figure legend, the reader is referred to the web version of this article.)

Table 5
Categorization of varnish types by structures and chemical composition.

	Environment	Structures	Ce	Ba	Mn	Pb	Ce/Ce*	La_N/Yb_N	Total REEs
Type I	Arid deserts	Mat-like layers, intermitted by mineral nests	+ + +	+ + +	+ +	+ +	+ + +	+ + +	+ + +
Type II	Semi-arid to arid deserts	No layers	+ + +	+ + +	+ + +	+ +	+ + +	+ + +	+ + +
Type III	Semi-arid deserts	No layers	+	+	+ + +	−	+	−	+
Type IV	Urban areas	No layers	−	+	+	+ + +	−	+	−
Type V	River splash zones	Discontinuous layers	−	+	−	−	−	−	+

agreement with the increase of cavities within the matrix from the varnish-rock contact up to the top of the aged varnish crusts (Fig. 11-1). Type III varnish has very high Mn mass fractions (about 40%) and very low Ba and Pb values. It can be distinguished from Type I, II, and V by its Al/Ni vs. Mn/Ba plotting field, and from Type IV by the Pb vs. Mn diagram (Fig. 6 b). The varnish grows from the soil-atmosphere-rock contact upwards and downwards on the pebbles, and grows therefore partially subsoil. All samples show a positive Ce anomaly. This varnish has very low enrichment of REEs relative to mineral dust from the adjacent soil, the highest enrichment was observed for Ce (Fig. C, Appendix). Based on EPR measurements, a high fraction of hexagonal birnessite was found, which might indicate an originally biological genesis for this varnish type, with a more recent formation than for Type I varnish (Fig. 8).

5.2.4. Type IV varnish

Type IV varnish collected from urban building facades shows structures differing from all other varnish types, and differing for the two samples within this one type. The two samples investigated seem to have similar fast growth rates (μm per a few decades), environmental surroundings (city areas), and host rock substrates (sandstone). They both appear as patches on building facades. However, the structures observed within ultra-thin sections are dissimilar. In the sample from the Freiburger Münster (FM, Fig. 2 H) we observed thick, round features that are encased by the Mn-rich matrix, resulting in a botryoidal structure. A layering was observed in SEM images of this sample (FM), but the layers are not based on differences in the Mn abundance (Fig. 12-2). The other sample (Smithsonian Castle (SC), Fig. 2 F) showed a structureless matrix with a high abundance of small, angular mineral grains and cavities, and finger-like upwards branching nodes building the upper varnish surface. Type IV varnishes show Fe enrichment only in mineral grains (Fig. 10-1, 10-2). Even though their structures differ significantly, the chemical composition of both samples show very high Pb (0.2–1.4%) and very low Fe mass fractions. Type IV can be distinguished from Type I and II by the Ce vs. Mn diagram (Fig. 6 a), and from Type III and V by the Pb vs. Mn plot (Fig. 6 b). The samples showed a mixture of positive, absent, and negative Ce anomalies (Fig. 7).

5.2.5. Type V varnish

Type V varnish, formed in river splash zones and first described by von Humboldt, can be black or dull brown in color. Discontinuous layers of Mn, Fe, and Ca are observable, however, they are not parallel to the rock surface (Fig. 12-3). No major amounts of mineral particles were observed in this type, in contrast to all other types of rock varnishes. The element source of Type V varnish is presumably river water, based on different plotting fields of samples collected at river sites not far apart (Fig. 5). Due to this source, much lower Th, Cs, Rb, and Ti mass fractions were observed compared to other varnishes. Furthermore, major elements are significantly depleted relative to the UCC (Fig. 4). The samples showed a mixture of positive, absent, and negative Ce anomalies (Fig. 7). Type V varnishes have low Mn mass fractions (3–8%) and grow rapidly (tens to hundreds of years to thicknesses of about 5 μm) within river splash zones. They can be distinguished from Type I, II, and III varnishes by the Al/Ni vs. Mn/Ba plotting field (Fig. 5 a), and from Type IV by the Pb vs. Mn diagram (Fig. 6 b).

5.2.6. Importance of categorization

Since a large number of publications used rock varnishes as paleoclimate archives (Baied and Somonte, 2013; Dorn, 1988; Liu and Broecker, 2007, 2008a, 2008b, 2013; Liu et al., 2013; Liu, 2003; Liu et al., 2000; Zerboni, 2008), it is important to understand that only Type I varnish is suitable to this task. However, Type I varnish cannot only be used as paleoclimate archives based on element composition changes between layers, it can also be used to macroscopically detect age differences between different petroglyph and geoglyph engravings (Bednarik, 2009; Black et al., 2017; Eisenberg-Degen and Rosen, 2013; Whitley et al., 1984), to reconstruct desert pavement evolution (McFadden et al., 1989), or to retrace geomorphic processes in arid landscapes by remote sensing (Farr and Chadwick, 1996; Gillespie et al., 1984). Likewise, other rock varnish types might be utilized applying these relative age controls, but more information about formation rates and coloring needs to be collected beforehand for these varnishes. Nevertheless, they can already provide other important information. Type IV varnish, for example, might be an appropriate tool to monitor heavy metal air pollution in urban areas, while Type V varnish might inform about heavy metal pollution in river systems.

6. Conclusions

Based on microanalytical studies, we show that the term “rock varnish” needs to be subdivided into more specific categories. Here, we propose to subdivide rock varnish into five types. The combination of “fingerprint” ratios (Mn/Ba, Al/Ni, Mn/REY, Mn/Ce, Mn/Pb, La_N/Yb_N, and Ce/Ce*), total REE contents, internal features, element distribution, and element composition can be used to distinguish the potential paleoclimate archive Type I varnish from other rock varnishes (Table 5). An original composition of hexagonal birnessite is suggested for all Type I, III, and IV varnishes, based on EPR measurements, with a higher fraction of birnessite, or a lower amount of transformations by aging, for Type III varnish.

A high Ce/Ce* ratio and high REE enrichments are good indicators for slowly growing varnishes that had a long accumulation time and are therefore likely to be good paleoclimate archives representing long time periods (Bau et al., 2014). We found these varnishes only in arid and semi-arid deserts so far. However, not all varnishes falling into the category Type I can be used as potential paleoclimate archive, as samples showing steep topographies of the host rock surface are inapplicable. It is clear from Alexander von Humboldt's description that the first rock varnish recorded in the literature > 200 years ago was a river splash varnish, presumably of Type V, and therefore quite different from the dry rock varnishes that became the focus of later studies. The differing chemical composition and structures suggest different geneses for the different varnish types. This would also explain the mystery of the large reported differences in growth rate and thickness of rock varnishes described in the literature, as well as the dissent about the biogenic or abiotic origin of rock varnishes.

Acknowledgements

This work was supported by the Max Planck Graduate Center with the Johannes Gutenberg University Mainz (MPGC), the Max Planck Society, and King Saud University. The ALS is supported by the Director, Office of Science, Office of Basic Energy Sciences, of the US Department of Energy under Contract DE-AC02-05CH11231. We thank the.

Helmholtz-Zentrum Berlin for the allocation of the synchrotron radiation beamtime at BESSY II. Sampling of desert varnish in Israel was conducted during a funded ExpeER project. We want to thank B. Macholdt for collecting the Mauritanian rock varnish, R. Livingston for providing the urban varnish from the Smithsonian Castle, B. E. DiGregorio for providing all river splash zone varnishes, and T. Liu for providing a rock varnish sample collected in Death Valley. The help of Hosam Tuffah, Mohammed Al-Huraish, and Ayed Al-Harthy during the field campaign in Saudi Arabia is gratefully acknowledged. We furthermore thank T. Laubscher for enabling and assisting sample taking at the Freiburger Münster, Maik Biegler who prepared the varnish thin- and thick-sections, and L. M. Otter for the dust sieving. Furthermore, we want to thank Jan Leitner and Antje Sorowka for conducting the SEM element maps.

Appendix A

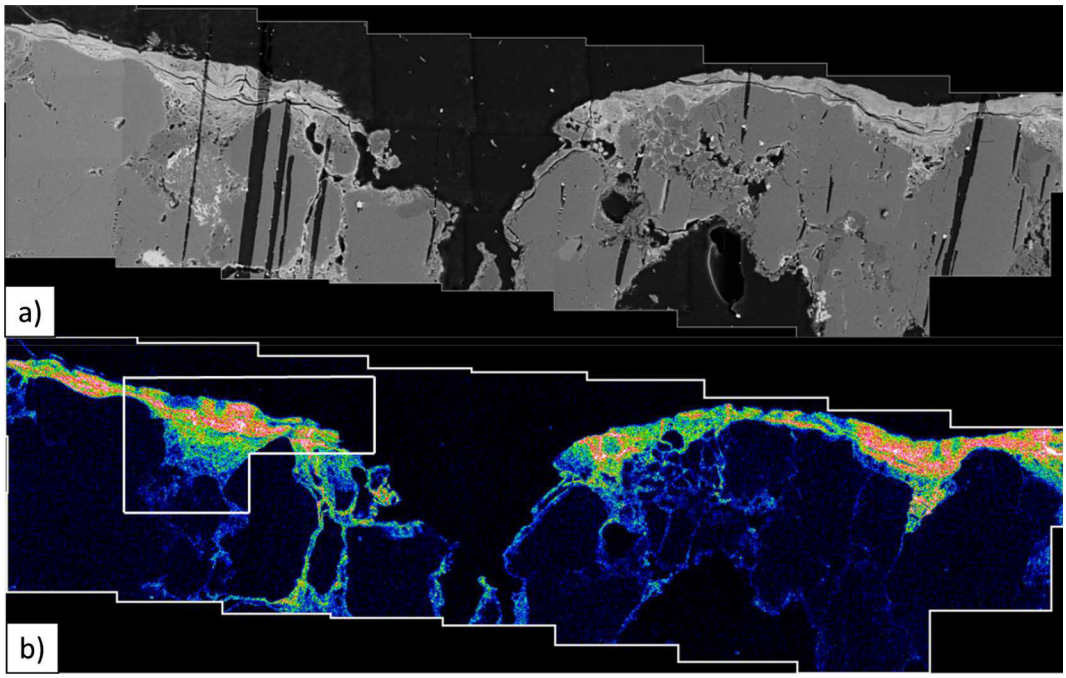

Fig. A. Secondary electron microscopy (SEM) images of a varnish sample from Saudi Arabia, Yatib, collected from an almost vertical surface. Fig. C a) is an backscattered electron image, Fig. C b) is an EDX mapping of the element Mn. Layers are observable in both images.

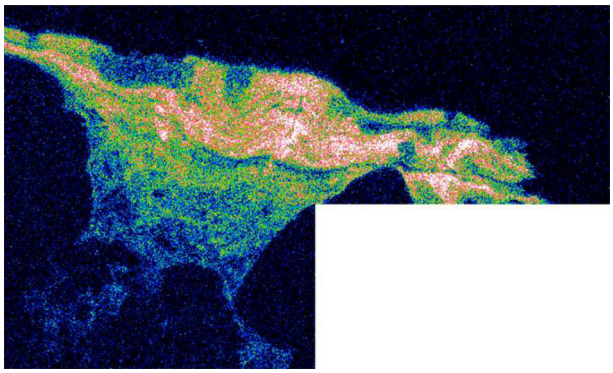

Fig. B. Close up of marked area in Fig. C b).

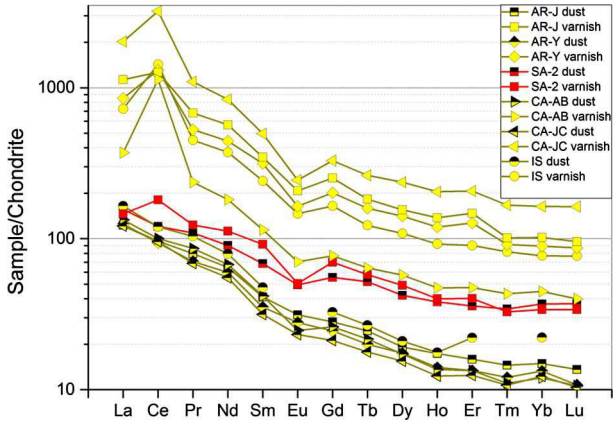

Fig. C. CI chondrite normalized rare earth element patterns of varnish and fine sieved (< 50 μm) dust samples. Type I varnishes (yellow) show a significant enrichment of REEs relative to adjacent collected dust. Type III varnish (red) shows only a very small enrichment.

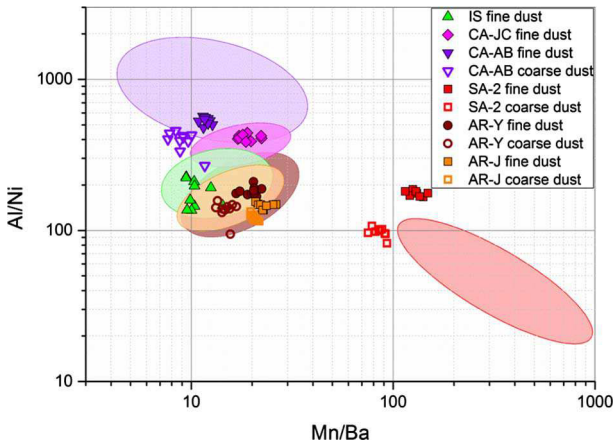

Fig. D. Al/Ni vs. Mn/Ba ratio plot for dust fine fractions (< 50 μm) and dust coarse fractions (≥ 50 μm, milled) from dust collected adjacent to varnish. Al/Ni and Mn/Ba dust ratios were multiplied by fractionation factors of 0.2, and 9, respectively. The colored fields are the ranges where the corresponding rock varnishes plot for each equally colored dust sample. Purple, pink, green, orange, and brown fields: Type I varnishes; red colored field: Type III varnish.

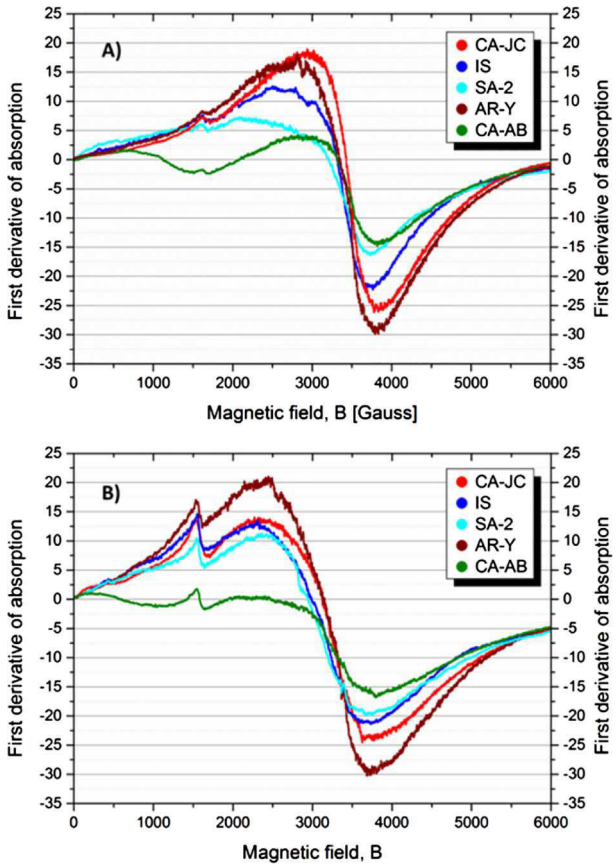

Fig. E. Electron paramagnetic resonance spectra of five rock varnish samples. A) spectra measured at RT (293 K) and with 210 mW. B) spectra measured at 90 K and with 224 mW. In all spectra, a Fe^{3+} peak can be observed at about 1500 G on the flank of the relatively narrow (560–1200 G) Mn absorption peak.

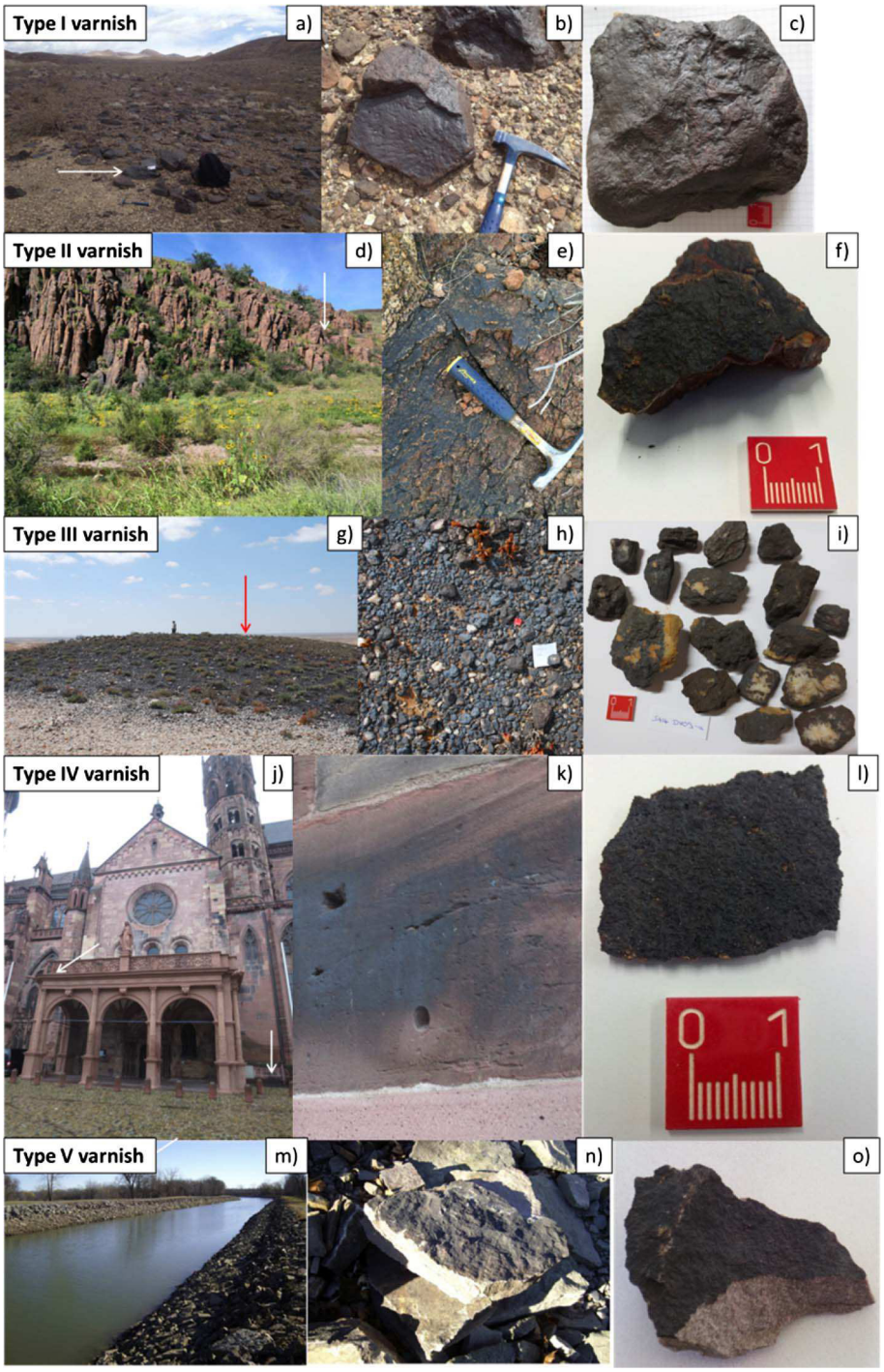

Fig. F. Different varnish types from a collection site at a distance to close-up images. Images a, b, and c represent Type I varnish, images d, e, and f Type II varnish, images g, h, and i Type III varnish, images j, k, and l Type IV varnish, and images m, n, and o Type V varnish. Images m and n were taken from the publication by Krinsley et al. (2012), from whom the samples were obtained. Image a, d, g, j, and m show the geomorphic context, images b, e, h, k, and n were taken at about 1 m distance, and images c, f, i, l, and o are close-up views of individual samples. All images are only representatives for a certain Type. The Type I varnishes shown are samples from the Mojave Desert, Type II varnishes are represented by Texan samples, Type III varnishes are South African samples (SA-2), Type IV varnishes are shown on the example of the Freiburger Münster, Germany, and the Type V varnishes shown are samples from the Erie Barge Canal region. All Type V varnish samples were provided by Barry E. DiGregorio.

Table 1
fs ICP-MS results of all samples, including the relative standard deviation (RSD).

Element	Isotope used	CA-DV						CA-JC							
		CA14 DV10		CA14 DV11		CA14 DV12		CA14 JC1		CA14 JC4		CA14 JC9		CA14 JC8	
		[µg g^{-1}]	RSD [%]	[µg g^{-1}]	RSD [%]	[µg g^{-1}]	RSD [%]	[µg g^{-1}]	RSD [%]	[µg g^{-1}]	RSD [%]	[µg g^{-1}]	RSD [%]	[µg g^{-1}]	RSD [%]

Na	Na^{23}	3996	9	6251	53	12,626	33	3279	23	4912	47	11,871	40	874	39
Mg	Mg^{25}	12,833	19	15,117	31	12,913	24	19,636	24	14,493	29	10,978	20	15,085	22
Al	Al^{27}	99,401	12	101,653	9	90,414	12	111,806	5	90,491	18	111,871	10	78,465	17
Si	Si^{29}	154,146	10	149,495	12	172,347	16	167,231	17	195,085	16	198,256	10	223,625	14
P	P^{31}	7720	24	19,627	26	12,977	18	7693	28	6237	17	5354	23	13,065	27
K	K^{39}	20,263	29	16,500	14	17,214	29	19,360	24	13,369	39	29,317	32	10,641	20
Ca	Ca^{43}	11,573	24	22,460	37	37,534	25	13,695	26	10,519	21	7769	15	30,748	36
Ti	Ti^{47}	3712	33	5423	24	3435	18	6166	40	3054	38	4208	35	7039	44
V	V^{51}	227	18	180	17	157	32	208	11	165	19	157	15	454	38
Cr	Cr^{53}	66	38	59	33	40	26	78	21	59	30	58	9	118	16
Mn	Mn^{55}	141,238	26	123,935	24	120,168	26	88,468	41	95,997	16	83,034	30	69,117	21
Fe	Fe^{57}	91,031	29	92,667	14	71,724	20	99,729	20	82,939	23	73,501	15	79,626	11
Co	Co^{59}	684	24	404	18	444	16	394	30	435	22	330	22	567	24
Ni	Ni^{60}	372	23	225	32	214	16	328	20	250	22	223	8	523	21
Cu	Cu^{63}	370	32	141	26	145	21	267	27	229	16	239	43	299	17
Zn	Zn^{67}	761	36	440	23	368	23	367	23	311	23	233	8	819	25
Rb	Rb^{85}	124	20	103	27	99	17	134	21	88	36	182	42	61	14
Sr	Sr^{88}	732	30	745	24	1391	17	543	42	666	29	392	27	745	34
Y	Y^{89}	518	30	162	21	154	25	253	26	237	20	236	36	203	22
Zr	Zr^{90}	290	17	356	15	299	24	286	14	273	35	224	29	243	8
Cs	Cs^{133}	14	27	11	35	9.1	27	13	14	8.6	30.5	9.1	35	4.2	11.2
Ba	Ba^{138}	9826	30	7265	28	9953	20	8072	49	5369	34	3653	30	7334	18
La	La^{139}	1089	29	305	30	317	28	491	28	495	18	445	28	309	24
Ce	Ce^{140}	3297	18	2010	34	1856	27	1751	28	2048	25	1817	23	1064	21
Pr	Pr^{141}	224	26	72	32	73	31	104	28	106	20	94	33	73	22
Nd	Nd^{143}	891	26	276	30	282	31	404	28	396	19	380	28	305	22
Sm	Sm^{147}	172	24	54	29	52	30	78	28	76	22	75	26	60	21
Eu	Eu^{151}	32	24	10	27	10	25	14	27	14	23	13	29	13	20
Gd	Gd^{157}	164	26	47	26	47	27	70	27	67	24	71	28	55	22
Tb	Tb^{159}	22	21	6.7	25	6.4	29	10	27	10	24	10	36	7.7	20.8
Dy	Dy^{161}	124	22	39	23	38	26	59	27	60	26	57	34	46	22
Ho	Ho^{165}	25	25	7.7	24	6.9	23	12	24	12	26	11	21	8.6	20.2
Er	Er^{167}	71	23	23	23	21	28	34	22	34	25	35	22	27	22
Tm	Tm^{169}	8.9	19	2.9	23	2.7	30	4.7	23	4.3	29.6	4.4	23	3.0	23.2
Yb	Yb^{173}	58	16	17	22	17	28	28	22	27	25	28	26	18	21
Lu	Lu^{175}	8.2	16	2.6	21	2.6	27	4.4	19	4.1	25.0	4.0	28	2.7	22.1
Pb	Pb^{208}	3651	22	761	23	463	33	558	24	1342	36	1781	16	278	20
Th	Th^{232}	281	36	120	25	107	25	80	33	128	28	121	38	34	30
U	U^{238}	36	22	25	20	17	27	38	24	53	34	23	12	13	22

Element	Isotope used	CA-AB						IS		SA-1			
		CA13 ABD-2		CA13 ABD-3		CA13 ABD-5		IS13 V3		SA10 #10		SA10 #11	
		[μg g^{-1}]	RSD [%]	[μg g^{-1}]	RSD [%]	[μg g^{-1}]	RSD [%]	[μg g^{-1}]	RSD [%]	[μg g^{-1}]	RSD [%]	[μg g^{-1}]	RSD [%]
Na	Na^{23}	2149	41	593	52	937	35	2857	18	11,940	44	5049	14
Mg	Mg^{25}	17,303	24	43,533	45	29,954	35	15,895	20	7442	30	9087	14
Al	Al^{27}	84,668	21	109,732	26	84,811	21	96,228	16	37,580	18	33,637	14
Si	Si^{29}	222,301	17	195,011	18	196,353	5	211,422	19	182,893	32	142,189	20
P	P^{31}	6021	31	789	24	4276	22	2920	23	3174	27	2878	17
K	K^{39}	13,193	50	71,939	10	11,671	35	13,060	15	18,728	35	24,969	15
Ca	Ca^{43}	23,241	36	3134	28	39,192	44	17,387	14	17,590	18	14,417	6
Ti	Ti^{47}	5239	51	10,343	45	4433	24	4936	23	1770	41	2007	24
V	V^{51}	146	41	309	36	400	14	275	12	84	25	73	14
Cr	Cr^{53}	8.2	53.8	197	56	140	36	146	12	44	32	51	15
Mn	Mn^{55}	31,187	37	21,823	19	71,898	34	83,123	31	202,776	42	309,039	12
Fe	Fe^{57}	96,513	33	98,189	43	100,235	16	90,403	14	35,077	31	28,462	22
Co	Co^{59}	276	41	115	28	395	32	699	23	1308	47	1596	19
Ni	Ni^{60}	113	42	175	40	274	22	513	30	268	32	286	24
Cu	Cu^{63}	120	26	93	20	325	32	189	25	151	28	90	22
Zn	Zn^{67}	256	31	283	39	449	35	429	13	533	29	659	19
Rb	Rb^{85}	77	39	350	34	70	28	78	14	76	20	97	12
Sr	Sr^{88}	265	40	225	30	478	33	574	23	946	30	611	29

Y	Y^{89}	61	32	13	23	158	28	171	21	108	31	79	18
Zr	Zr^{90}	60	47	29	32	85	19	270	13	92	22	67	20
Cs	Cs^{133}	7.1	42.4	33	34	7.3	24	4.6	17	3.8	21	6.0	35
Ba	Ba^{138}	2721	31	12,806	34	9290	39	8986	26	1379	36	861	34
La	La^{139}	94	31	74	31	274	33	235	21	45	25	25	21
Ce	Ce^{140}	900	47	273	20	1118	46	1608	23	109	31	79	20
Pr	Pr^{141}	25	38	12	34	60	27	62	20	17	18	12	30
Nd	Nd^{143}	93	39	35	32	232	26	253	21	87	11	68	28
Sm	Sm^{147}	18	34	6.7	35.2	45	25	54	20	25	14	20	28
Eu	Eu^{151}	4.1	33.7	2.0	22.0	10	24	12	21	5.4	21	4.6	27
Gd	Gd^{157}	16	33	7.0	34.4	50	26	51	20	30	26	23	21
Tb	Tb^{159}	2.8	42.8	0.9	28.8	6.3	24	7.0	20	4.9	26	3.4	20
Dy	Dy^{161}	15	34	4.7	30.1	36	24	42	22	26	28	19	22
Ho	Ho^{165}	2.7	34.1	0.91	24.97	6.6	26	7.9	19	5.3	30	3.8	21
Er	Er^{167}	10	40	2.3	31.4	18	26	23	20	17	35	11	20
Tm	Tm^{169}	1.2	43.4	0.33	36.32	2.3	23	3.0	20	1.9	32	1.4	22
Yb	Yb^{173}	8.6	39.3	1.9	31.5	15	18	18	19	12	31	8.3	23
Lu	Lu^{175}	1.1	29.7	0.29	38.00	2.2	23	2.7	19	1.9	28	1.2	25
Pb	Pb^{208}	1075	41	582	33	1252	41	491	32	103	36	55	32
Th	Th^{232}	8.3	39.3	6.2	29.5	24	26	27	25	16	31	13	33
U	U^{238}	14	39	3.3	32.3	22	34	5.7	15	5.3	33	4.7	20

Element	Isotope used	SC		FM		MT		SA-2							
		Livingston		FM965		MT		SA14 DV05a		SA14 DV05b		SA14 DV09a		SA14 DV09b	
		[$\mu g\ g^{-1}$]	RSD [%]	[$\mu g\ g^{-1}$]	RSD [%]	[$\mu g\ g^{-1}$]	RSD [%]	[$\mu g\ g^{-1}$]	RSD [%]	[$\mu g\ g^{-1}$]	RSD [%]	[$\mu g\ g^{-1}$]	RSD [%]	[$\mu g\ g^{-1}$]	RSD [%]
Na	Na^{23}	3197	69	1839	42	717	37	1311	15	1146	18	1632	16	1104	32
Mg	Mg^{25}	12,070	20	3515	34	14,025	7	4451	33	10,082	18	7190	32	12,428	17
Al	Al^{27}	28,811	31	43,563	26	93,871	5	24,936	21	57,552	21	47,351	28	49,493	25
Si	Si^{29}	261,636	26	252,571	18	204,608	5	168,961	40	193,074	21	212,219	33	149,422	29
P	P^{31}	357	20	25,868	50	6798	21	3729	33	4154	19	4410	38	2939	11
K	K^{39}	5339	21	20,445	26	25,800	6	28,141	38	31,064	21	23,034	32	27,144	15
Ca	Ca^{43}	18,030	40	20,114	28	20,985	14	5295	33	5573	25	6514	28	12,644	17
Ti	Ti^{47}	3077	41	1545	23	6465	11	881	27	3052	32	1340	44	3260	45
V	V^{51}	248	38	83	37	194	6	66	23	129	20	109	41	107	26
Cr	Cr^{53}	82	38	64	22	110	10	33	20	75	24	80	39	74	28
Mn	Mn^{55}	80,650	41	77,108	39	84,442	11	286,141	32	195,456	28	219,989	25	259,669	32
Fe	Fe^{57}	41,345	39	29,124	30	84,010	10	18,290	20	48,982	19	55,637	33	43,414	25
Co	Co^{59}	187	17	525	71	731	14	1993	35	1471	18	991	23	733	17
Ni	Ni^{60}	114	33	286	39	311	15	80	33	451	32	381	29	921	27
Cu	Cu^{63}	1177	55	328	28	178	8	91	31	271	31	305	39	350	41
Zn	Zn^{67}	326	43	5000	36	2697	14	87	38	286	29	228	17	582	24
Rb	Rb^{85}	40	31	83	31	134	7	49	16	122	28	68	26	82	20
Sr	Sr^{88}	349	36	510	28	560	22	430	25	447	28	603	50	706	17
Y	Y^{89}	15	17	17	28	133	13	44	22	142	21	33	35	43	17
Zr	Zr^{90}	36	26	35	38	168	18	34	28	137	27	90	31	91	34
Cs	Cs^{133}	2.2	28	11	23	8.5	7	2.8	19	7.5	28	5.1	24	5.3	26
Ba	Ba^{138}	2537	28	1747	27	11,245	19	634	32	1473	35	832	53	987	25
La	La^{139}	41	42	20	51	204	15	25	16	62	33	21	31	36	34
Ce	Ce^{140}	157	35	42	33	851	12	102	15	214	32	83	26	115	30
Pr	Pr^{141}	6.2	44	5.3	48	57	13	9	16	20	27	8	39	12	26
Nd	Nd^{143}	30	42	20	41	230	15	45	21	107	27	37	38	53	25
Sm	Sm^{147}	4.6	22	4.6	36	47	12	12	24	31	29	10	34	14	23
Eu	Eu^{151}	1.2	54	1.1	28	11	14	2.4	26	6.1	26	2.2	35	2.9	19
Gd	Gd^{157}	4.2	27	4.9	23	43	14	12	24	31	24	12	21	14	20
Tb	Tb^{159}	0.70	34	0.73	37	5.3	12	1.9	29	5.1	25	1.6	20	2.2	21
Dy	Dy^{161}	3.3	39	4.4	37	29	10	10	29	30	23	10	36	12	20
Ho	Ho^{165}	0.58	41	0.81	31	5.4	9	2.0	26	5.8	21	1.9	32	2.3	21
Er	Er^{167}	2.4	38	2.4	30	14	10	5.1	23	17	20	5.4	30	6.7	21
Tm	Tm^{169}	0.45	45	0.31	29	1.8	11	0.70	24	2.2	22	0.73	36	0.84	27
Yb	Yb^{173}	2.5	33	2.2	39	11	9	3.9	24	13	24	4.8	25	5.6	19
Lu	Lu^{175}	0.34	42	0.28	39	1.5	10	0.60	17	2.0	19	0.68	20	0.86	28

Pb	Pb^{208}	2762	24	8299	30	312	25	36	50	105	38	107	38	88	30
Th	Th^{232}	10	45	7.0	34	21	19	7.3	22	22	25	16	28	17	28
U	U^{238}	3.4	47	3.3	23	12	11	2.6	32	7.1	25	10	37	5.1	24

		AR-Y											
Element	Isotope used	AR14 Y5-3		AR14 Y4a		AR14 Y3		AR14 Y2b		AR14 Y2a		AR14 Y1	
		[μg g^{-1}]	RSD [%]	[μg g^{-1}]	RSD [%]	[μg g^{-1}]	RSD [%]	[μg g^{-1}]	RSD [%]	[μg g^{-1}]	RSD [%]	[μg g^{-1}]	RSD [%]
Na	Na^{23}	374	24	381	59	485	41	482	21	590	25	198	33
Mg	Mg^{25}	18,441	19	7597	39	8887	40	12,180	35	5588	36	7950	48
Al	Al^{27}	101,429	9	47,063	25	83,164	35	69,475	25	63,915	43	80,198	29
Si	Si^{29}	193,070	10	278,634	12	245,347	21	258,207	26	293,946	19	275,291	19
P	P^{31}	8050	11	7931	29	21,096	44	6550	29	6310	35	9638	36
K	K^{39}	12,648	17	5726	31	5862	46	9922	33	5084	41	6843	44
Ca	Ca^{43}	13,979	24	20,745	25	33,491	47	11,437	37	9202	26	10,965	35
Ti	Ti^{47}	7052	23	3243	45	2725	30	3706	27	2204	36	2856	54
V	V^{51}	267	11	189	33	170	37	235	34	208	35	169	33
Cr	Cr^{53}	134	13	62	36	65	37	108	29	67	43	66	44
Mn	Mn^{55}	80,700	21	49,700	64	50,234	42	41,654	19	47,755	43	43,227	49
Fe	Fe^{57}	104,729	12	60,066	35	52,641	37	70,527	22	53,060	32	56,718	44
Co	Co^{59}	625	20	579	5	267	26	377	38	433	43	528	42
Ni	Ni^{60}	801	18	313	48	484	46	400	44	362	32	375	36
Cu	Cu^{63}	285	12	214	39	156	41	147	42	138	35	132	31
Zn	Zn^{67}	1143	13	540	42	781	41	288	43	217	34	226	16
Rb	Rb^{85}	73	19	30	38	32	47	55	33	29	42	37	45
Sr	Sr^{88}	586	21	908	19	685	31	332	44	435	45	308	44
Y	Y^{89}	319	15	183	29	250	36	158	29	151	35	172	29
Zr	Zr^{90}	333	18	258	22	163	34	226	24	196	26	216	21
Cs	Cs^{133}	6.4	19	2.8	32	2.5	42	3.9	27	2.5	42	3.5	32
Ba	Ba^{138}	4787	21	8683	39	6231	38	2229	35	2290	46	2078	41
La	La^{139}	472	14	372	20	324	25	209	35	207	36	208	29
Ce	Ce^{140}	1401	22	1433	28	702	26	990	23	677	38	968	35
Pr	Pr^{141}	110	15	86	24	73	25	52	33	50	32	53	28
Nd	Nd^{143}	449	16	354	23	307	26	213	32	208	31	223	28
Sm	Sm^{147}	90	16	70	26	60	24	48	30	49	35	51	36
Eu	Eu^{151}	19	15	14	22	14	26	9	33	10	34	11	27
Gd	Gd^{157}	82	15	61	18	59	26	40	25	42	34	45	30
Tb	Tb^{159}	11	15	8.3	24	7.9	27	5.4	26	6.4	34	6.4	31
Dy	Dy^{161}	67	15	37	47	45	29	34	30	37	31	38	28
Ho	Ho^{165}	13	16	7.1	37	9.0	27	6.7	28	6.8	32	6.9	24
Er	Er^{167}	35	14	18	35	32	34	18	25	23	35	23	29
Tm	Tm^{169}	4.7	16	2.4	22	3.1	33	2.2	19	2.5	31	2.1	25
Yb	Yb^{173}	30	14	18	24	19	32	15	23	15	33	14	27
Lu	Lu^{175}	4.4	17	2.9	21	2.6	26	2.1	25	2.3	31	2.1	24
Pb	Pb^{208}	312	25	626	23	312	43	250	29	228	33	191	36
Th	Th^{232}	43	17	38	48	21	40	25	28	27	23	34	25
U	U^{238}	21	16	7.1	41	17	34	11	22	12	31	13	33

		AR-J											
Element	Isotope used	AR14J2-4		AR14 J2-3		AR14 J2-2		AR14 J2		AR14 J1		AR14 J1a	
		[μg g^{-1}]	RSD [%]	[μg g^{-1}]	RSD [%]	[μg g^{-1}]	RSD [%]	[μg g^{-1}]	RSD [%]	[μg g^{-1}]	RSD [%]	[μg g^{-1}]	RSD [%]
Na	Na^{23}	443	20	499	24	734	47	846	39	273	38	408	32
Mg	Mg^{25}	13,627	29	17,878	27	16,365	32	14,947	22	11,022	35	18,689	21
Al	Al^{27}	66,167	46	87,870	19	64,398	22	78,201	17	68,222	32	90,252	25
Si	Si^{29}	186,855	5	227,918	18	249,522	22	228,107	14	268,399	19	266,314	17
P	P^{31}	24,537	1	14,349	38	14,676	51	12,608	27	15,274	39	8554	28
K	K^{39}	11,263	4	12,410	25	10,566	32	10,351	20	10,375	40	13,415	32

Ca	Ca^{43}	40,814	16	33,798	37	26,332	35	29,809	36	18,317	37	8257	45
Ti	Ti^{47}	5631	13	5571	32	3938	31	6637	44	4381	37	6677	24
V	V^{51}	186	55	233	19	209	25	435	38	193	29	163	25
Cr	Cr^{53}	88	46	113	24	99	19	117	16	93	37	116	28
Mn	Mn^{55}	67,552	54	54,303	15	49,295	37	67,731	21	48,351	46	33,916	29
Fe	Fe^{57}	63,960	52	74,003	17	61,379	28	77,730	11	58,363	31	66,414	23
Co	Co^{59}	524	48	383	16	381	16	563	24	341	47	251	42
Ni	Ni^{60}	588	39	610	34	438	36	489	21	427	30	321	34
Cu	Cu^{63}	136	56	187	16	180	32	279	17	129	44	168	31
Zn	Zn^{67}	1006	26	774	35	653	34	793	25	588	47	474	25
Rb	Rb^{85}	57	53	76	27	63	29	60	14	60	35	69	32
Sr	Sr^{88}	687	39	734	20	700	36	749	34	460	35	234	33
Y	Y^{89}	192	49	189	16	167	28	200	22	157	25	114	30
Zr	Zr^{90}	182	55	221	19	216	31	242	8	202	38	180	24
Cs	Cs^{133}	4.5	47	6.5	32	5.1	29	4.2	11	4.3	32	5.6	21
Ba	Ba^{138}	6535	48	3958	29	5862	44	7482	18	4920	57	1931	30
La	La^{139}	327	42	277	15	260	29	304	24	217	25	128	30
Ce	Ce^{140}	1134	42	808	17	778	16	1066	21	691	30	387	48
Pr	Pr^{141}	78	45	65	14	58	32	72	22	50	30	31	34
Nd	Nd^{143}	313	46	270	13	239	32	300	22	206	29	131	32
Sm	Sm^{147}	62	45	53	12	46	33	59	21	41	30	28	31
Eu	Eu^{151}	14	45	12	11	10	30	13	20	8.8	29	6.3	33
Gd	Gd^{157}	64	44	51	11	45	30	55	22	39	29	27	33
Tb	Tb^{159}	7.9	50	6.8	11	5.7	33	7.6	21	5.1	30	3.8	36
Dy	Dy^{161}	46	50	39	13	34	31	45	22	30	32	23	33
Ho	Ho^{165}	8.2	51	7.8	10	6.5	32	8.5	20	5.9	28	4.7	33
Er	Er^{167}	21	51	25	10	20	31	26	22	15	28	13	32
Tm	Tm^{169}	3.0	47	2.6	15	2.3	34	3.0	23	2.0	32	1.7	31
Yb	Yb^{173}	18	51	17	14	14	32	17	21	13	30	11	31
Lu	Lu^{175}	2.6	41	2.4	17	2.0	34	2.7	22	2.0	33	1.6	33
Pb	Pb^{208}	478	4	376	25	434	34	291	20	156	19	102	48
Th	Th^{232}	37	31	22	24	24	39	35	30	21	40	19	25
U	U^{238}	11	38	16	23	13	18	13	22	12	15	11	33

Element	Isotope used	TX FD													
		TX FD 1		TX FD 2		TX FD 3		TX FD 4		TX FD 5		TX FD 6		TX FD 7	
		[μg g^{-1}]	RSD [%]	[μg g^{-1}]	RSD [%]	[μg g^{-1}]	RSD [%]	[μg g^{-1}]	RSD [%]	[μg g^{-1}]	RSD [%]	[μg g^{-1}]	RSD [%]	[μg g^{-1}]	RSD [%]
Na	Na^{23}	3668	36	1059	26	403	16	1962	39	5039	23	5776	45	4198	36
Mg	Mg^{25}	6408	26	8978	26	8034	17	6532	32	2720	40	6775	45	3447	47
Al	Al^{27}	80,849	18	40,675	19	89,833	11	69,058	30	75,923	9	72,262	29	82,208	17
Si	Si^{29}	200,653	14	62,855	17	120,040	12	171,717	11	244,737	13	230,105	18	241,112	22
P	P^{31}	4821	43	2953	7	9608	21	6571	30	4611	40	2212	48	5563	39
K	K^{39}	32,085	17	10,344	23	15,091	12	27,352	26	40,288	20	25,638	32	32,824	37
Ca	Ca^{43}	13,090	30	17,731	21	12,370	20	9003	24	4601	32	10,248	40	3732	31
Ti	Ti^{47}	3224	37	1155	27	5250	23	4879	39	5613	52	5145	29	3486	35
V	V^{51}	24	35	352	11	123	16	50	46	36	39	114	33	52	43
Cr	Cr^{53}	7.5	37	4.7	36	45	18	33	29	5	67	23	37	19	37
Mn	Mn^{55}	109,688	32	402,117	6	203,053	20	145,729	17	48,148	34	43,269	50	57,031	49
Fe	Fe^{57}	65,938	43	38,903	15	99,958	20	114,244	23	76,479	26	135,430	45	65,987	34
Co	Co^{59}	77	36	50	24	469	17	28	51	76	43	118	54	129	44
Ni	Ni^{60}	48	32	132	22	176	18	59	35	48	46	59	39	27	13
Cu	Cu^{63}	47	42	231	14	124	21	90	22	35	33	63	39	44	34
Zn	Zn^{67}	4364	23	741	15	2144	28	728	42	914	18	1148	40	933	45
Rb	Rb^{85}	178	15	30	21	94	15	188	22	152	13	174	33	174	32
Sr	Sr^{88}	375	29	1797	23	431	21	315	22	91	25	127	45	137	38
Y	Y^{89}	159	26	62	13	105	10	95	42	154	22	145	24	123	42
Zr	Zr^{90}	308	47	1161	29	379	22	1076	53	2193	46	1359	34	536	48
Cs	Cs^{133}	4.3	29	3	26	10	15	12	17	4	31	6	40	5.8	40
Ba	Ba^{138}	2711	32	39,724	11	10,419	21	9884	23	1141	52	3907	43	1804	57
La	La^{139}	132	22	208	12	185	13	112	43	206	29	234	38	159	37
Ce	Ce^{140}	1229	32	2910	22	1622	12	993	31	593	30	1419	49	799	29

Pr	Pr^{141}	31	25	43	14	48	11	27	46	43	29	53	36	39	33
Nd	Nd^{143}	118	28	168	12	193	12	122	42	179	29	204	33	149	34
Sm	Sm^{147}	25	25	35	13	41	16	27	44	37	36	40	35	29	29
Eu	Eu^{151}	2.5	29	1.7	15	6.2	13	2.7	45	3.4	35	3.3	38	2.6	44
Gd	Gd^{157}	26	27	27	14	36	20	34	26	34	21	33	33	29	36
Tb	Tb^{159}	3.9	24	3.4	20	4.9	15	3.6	39	4.6	21	4.8	30	4.2	37
Dy	Dy^{161}	26	23	21	22	29	19	23	43	30	26	32	24	28	40
Ho	Ho^{165}	5.1	23	3.5	13	5.4	21	4.2	42	6.0	25	6.3	23	5.7	40
Er	Er^{167}	16	28	8	10	14	12	14	24	20	24	20	21	16	36
Tm	Tm^{169}	2.4	33	1.2	10	2.1	11	2.2	41	3.0	30	3.0	31	2.2	33
Yb	Yb^{173}	17	38	8	8	14	21	15	46	16	25	21	23	15	31
Lu	Lu^{175}	2.3	40	1.3	15	2.0	21	2.2	44	2.5	13	3.0	24	2.4	31
Pb	Pb^{208}	505	33	242	42	1133	36	40	49	259	32	1019	34	706	41
Th	Th^{232}	29	37	13	40	66	16	24	38	32	37	38	30	44	31
U	U^{238}	4.8	36	5.4	11	7.3	23	4.9	40	4.4	32	6.1	26	8.8	32

Element	Isotope used	R River		E Canal		AZ AC	
		R River		E Canal		AZ AC	
		[μg g^{-1}]	RSD [%]	[μg g^{-1}]	RSD [%]	[μg g^{-1}]	RSD [%]
Na	Na^{23}	2217	33	183	26	2771	28
Mg	Mg^{25}	7381	25	5748	32	10,360	19
Al	Al^{27}	43,671	11	15,203	31	83,323	15
Si	Si^{29}	193,715	11	332,471	14	176,003	18
P	P^{31}	11,946	23	3284	24	20,120	20
K	K^{39}	7718	27	4509	33	20,368	24
Ca	Ca^{43}	36,012	26	18,895	31	16,400	26
Ti	Ti^{47}	1098	23	444	35	3868	24
V	V^{51}	122	20	42	32	104	19
Cr	Cr^{53}	35	16	15	34	29	24
Mn	Mn^{55}	30,078	18	81,067	34	133,323	33
Fe	Fe^{57}	229,473	10	16,306	31	76,860	22
Co	Co^{59}	31	18	103	33	690	27
Ni	Ni^{60}	80	32	782	34	171	24
Cu	Cu^{63}	526	37	600	27	724	31
Zn	Zn^{67}	1114	22	1603	23	1249	33
Rb	Rb^{85}	22	23	18	34	96	23
Sr	Sr^{88}	272	36	369	28	571	23
Y	Y^{89}	153	13	40	24	113	20
Zr	Zr^{90}	26	24	34	22	235	26
Cs	Cs^{133}	1.2	34	0.74	28	16	26
Ba	Ba^{138}	1500	31	2021	36	9973	34
La	La^{139}	103	13	26	27	215	26
Ce	Ce^{140}	137	15	73	39	1425	32
Pr	Pr^{141}	26	13	8.9	34	55	25
Nd	Nd^{143}	120	14	39	33	200	25
Sm	Sm^{147}	27	15	8.9	27	39	21
Eu	Eu^{151}	3.5	14	2.4	33	7.5	21.6
Gd	Gd^{157}	29	15	10	27	34	22
Tb	Tb^{159}	3.9	14	1.6	32	4.8	22
Dy	Dy^{161}	25	13	8.5	29	28	23
Ho	Ho^{165}	5.2	13	1.6	27	5.1	21
Er	Er^{167}	16	14	4.5	36	16	21
Tm	Tm^{169}	2.2	13	0.51	22	1.9	22
Yb	Yb^{173}	14	16	3.4	24	13	23
Lu	Lu^{175}	2.2	17	0.57	27	1.9	22
Pb	Pb^{208}	182	17	311	42	1988	39
Th	Th^{232}	6.7	15	2.8	29	58	30
U	U^{238}	1.7	27	1.8	30	5.2	28

References

Abollino, O., Aceto, M., Malandrino, M., Sarzanini, C., Mentasti, E., 2003. Adsorption of heavy metals on Na-montmorillonite. Effect of pH and organic substances. Water Res. 37, 1619–1627.

Baied, C.A., Somonte, C., 2013. Mid-Holocene geochronology, palaeoenvironments, and occupational dynamics at Quebrada de Amaicha, Tucuman, Argentina. Quat. Int. 299, 80–89.

Bau, M., Schmidt, K., Koschinsky, A., Hein, J., Kuhn, T., Usui, A., 2014. Discriminating between different genetic types of marine ferro-manganese crusts and nodules based on rare earth elements and yttrium. Chem. Geol. 381, 1–9.

Bednarik, R.G., 2009. Experimental colorimetric analysis of petroglyphs. Rock ART Res. 26, 55.

Black, J.L., MacLeod, I.D., Smith, B.W., 2017. Theoretical effects of industrial emissions on colour change at rock art sites on Burrup Peninsula, Western Australia. J. Archaeol. Sci. Rep. 12, 457–462.

Broecker, W.S., Liu, T., 2001. Rock varnish: record of desert wetness? GSA Today (August), 4–10.

Burns, R.G., Brown, B.A., 1972. Nucleation and mineralogical controls on the composition of manganese nodules. In: Ferromanganese Deposits on the Ocean Floor, pp. 51–61.

DiGregorio, B.E., 2001. Rock varnish as a habitat for extant life on Mars. In: Hoover, R.B., Levin, G.V., Paepe, R.R., Rozanov, A.Y. (Eds.), Instruments, Methods, and Missions for Astrobiology IV, pp. 120–130.

Dorn, R.I., 1984. Cause and implications of rock varnish microchemical laminations. Nature 310, 767–770.

Dorn, R.I., 1988. A rock varnish interpretation of alluvial-fan development in Death Valley, California. Natl. Geogr. Res. 4, 56–73.

Dorn, R.I., 2008. In: Nash, D.J., McLaren, S.J. (Eds.), Rock Varnish in Geochemical Sediments and Landscapes. Blackwell Publishing Ltd, Oxford, UK Chapter 8, pp. 246–297.

Dorn, R.I., 2009. Desert rock coatings. In: Parsons, A.J., Abrahams, A.D. (Eds.), Geomorphology of Desert Environments. Springer, Amsterdam, pp. 153–186.

Dorn, R.I., Krinsley, D.H., Liu, T.Z., Anderson, S., Clark, J., Cahill, T.A., Gill, T.E., 1992. Manganese-rich rock varnish does occur in Antarctica. Chem. Geol. 99, 289–298.

Eisenberg-Degen, D., Rosen, S.A., 2013. Chronological Trends in Negev Rock Art: the Har Michia Petroglyphs as a Test Case, Arts. Multidisciplinary Digital Publishing Institutepp. 225–252.

Engel, C.G., Sharp, R.P., 1958. Chemical data on desert varnish. Geol. Soc. Am. Bull. 69, 487–518.

Evensen, N., Hamilton, P.J., O'nions, R., 1978. Rare-earth abundances in chondritic meteorites. Geochim. Cosmochim. Acta 42, 1199–1212.

Farr, T.G., Chadwick, O.A., 1996. Geomorphic processes and remote sensing signatures of alluvial fans in the Kun Lun Mountains, China. J. Geophys. Res. Planets 101, 23091–23100.

Feng, X.H., Zhai, L.M., Tan, W.F., Liu, F., He, J.Z., 2007. Adsorption and redox reactions of heavy metals on synthesized Mn oxide minerals. Environ. Pollut. 147, 366–373.

Follath, R., Schmidt, J.S., Weigand, M., Fauth, K., 2010. The X-ray microscopy beamline UE46-PGM2 at BESSY. In: Garrett, R., Gentle, I., Nugent, K., Wilkins, S. (Eds.), Sri 2009: The 10th International Conference on Synchrotron Radiation Instrumentation, pp. 323–326.

Gillespie, A.R., Kahle, A.B., Palluconi, F.D., 1984. Mapping alluvial fans in Death Valley, California, using multichannel thermal infrared images. Geophys. Res. Lett. 11, 1153–1156.

Goldsmith, Y., Stein, M., Enzel, Y., 2014. From dust to varnish: Geochemical constraints on rock varnish formation in the Negev Desert, Israel. Geochim. Cosmochim. Acta 126, 97–111.

Hodge, V.F., Farmer, D.E., Diaz, T., Orndorff, R.L., 2005. Prompt detection of alpha particles from Po-210: another clue to the origin of rock varnish? J. Environ. Radioact. 78, 331–342.

Jochum, K.P., Stoll, B., Weis, U., Jacob, D.E., Mertz-Kraus, R., Andreae, M.O., 2014. Non-matrix-matched calibration for the multi-element analysis of geological and environmental samples using 200 nm femtosecond LA-ICP-MS: a comparison with nanosecond lasers. Geostand. Geoanal. Res. 38, 265–292.

Jochum, K., Wilson, S., Becker, H., Garbe-Schönberg, D., Groschopf, N., Kadlag, Y., Macholdt, D., Mertz-Kraus, R., Otter, L., Stoll, B., 2016. FeMnOx-1: A new microanalytical reference material for the investigation of Mn–Fe rich geological samples. Chem. Geol. 432, 34–40.

Kijlstra, W.S., Poels, E.K., Bliek, A., Weckhuysen, B.M., Schoonheydt, R.A., 1997. Characterization of Al2O3-supported manganese oxides by electron spin resonance and diffuse reflectance spectroscopy. J. Phys. Chem. B 101, 309–316.

Kilcoyne, A.L.D., Tyliszczak, T., Steele, W.F., Fakra, S., Hitchcock, P., Franck, K., Anderson, E., Harteneck, B., Rightor, E.G., Mitchell, G.E., Hitchcock, A.P., Yang, L., Warwick, T., Ade, H., 2003. Interferometer-controlled scanning transmission X-ray microscopes at the advanced light source. J. Synchrotron Radiat. 10, 125–136.

Kim, S.S., Bargar, J.R., Nealson, K.H., Flood, B.E., Kirschvink, J.L., Raub, T.D., Tebo, B.M., Villalobos, M., 2011. Searching for biosignatures using electron paramagnetic resonance (EPR) analysis of manganese oxides. Astrobiology 11, 775–786.

Kohl, L., Laganière, J., Edwards, K.A., Billings, S.A., Morrill, P.L., Van Biesen, G., Ziegler, S.E., 2015. Distinct fungal and bacterial $\delta^{13}C$ signatures as potential drivers of increasing $\delta^{13}C$ of soil organic matter with depth. Biogeochemistry 124, 13–26.

Krinsley, D.H., Dorn, R.I., DiGregorio, B.E., Langworthy, K.A., Ditto, J., 2012. Rock varnish in New York: an accelerated snapshot of accretionary processes. Geomorphology 138, 339–351.

Krinsley, D., Ditto, J., Langworthy, K., Dorn, R.I., Thompson, T., 2013. Varnish microlaminations: new insights from focused ion beam preparation. Phys. Geogr. 34, 159–173.

Lanza, N.L., Clegg, S.M., Wiens, R.C., McInroy, R.E., Newsom, H.E., Deans, M.D., 2012. Examining natural rock varnish and weathering rinds with laser-induced breakdown spectroscopy for application to ChemCam on Mars. Appl. Opt. 51, B74–B82.

Lee, M.R., Bland, P.A., 2003. Dating climatic change in hot deserts using desert varnish on meteorite finds. Earth Planet. Sci. Lett. 206, 187–198.

Li, X., Pan, G., Qin, Y., Hu, T., Wu, Z., Xie, Y., 2004. EXAFS studies on adsorption–desorption reversibility at manganese oxide–water interfaces: II. Reversible adsorption of zinc on δ-MnO_2. J. Colloid Interface Sci. 271, 35–40.

Liu, T.Z., 2003. Blind testing of rock varnish microstratigraphy as a chronometric indicator: results on late quaternary lava flows in the Mojave Desert, California. Geomorphology 53, 209–234.

Liu, T.H., Broecker, W.S., 2000. How fast does rock varnish grow? Geology 28, 183–186.

Liu, T., Broecker, W.S., 2007. Holocene rock varnish microstratigraphy and its chronometric application in the drylands of western USA. Geomorphology 84, 1–21.

Liu, T., Broecker, W.S., 2008a. Rock varnish evidence for latest Pleistocene millennial-scale wet events in the drylands of western United States. Geology 36, 403–406.

Liu, T., Broecker, W.S., 2008b. Rock varnish microlamination dating of late quaternary geomorphic features in the drylands of western USA. Geomorphology 93, 501–523.

Liu, T., Broecker, W.S., 2013. Millennial-scale varnish microlamination dating of late Pleistocene geomorphic features in the drylands of western USA. Geomorphology 187, 38–60.

Liu, T.Z., Broecker, W.S., Bell, J.W., Mandeville, C.W., 2000. Terminal pleistocene wet event recorded in rock varnish from Las Vegas Valley, southern Nevada. Palaeogeogr. Palaeoclimatol. Palaeoecol. 161, 423–433.

Liu, T., Broecker, W.S., Stein, M., 2013. Rock varnish evidence for a younger Dryas wet period in the Dead Sea basin. Geophys. Res. Lett. 40, 2229–2235.

Livingston, R., Grissom, C.A., Vicenzi, E.P., Weldon-Yochim, Z.A., Little, N.C., Douglas, J.G., Fowler, A.J., Santelli, C.M., Macholdt, D.S., Ortiz-Montalvo, D.L., Watson, S.S., 2016. Investigation of urban rock varnish on the sandstone of the Smithsonian Castle. In: Science and Art: A Future for Stone. 399.

Lozano, R.P., Rossi, C., 2012. Exceptional preservation of Mn-oxidizing microbes in cave stromatolites (El Soplao, Spain). Sediment. Geol. 255, 42–55.

Lytle, C., Smith, B., McKinnon, C., 1995. Manganese accumulation along Utah roadways: a possible indication of motor vehicle exhaust pollution. Sci. Total Environ. 162, 105–109.

Macholdt, D.S., Jochum, K.P., Stoll, B., Weis, U., Andreae, M.O., 2014. A new technique to determine element amounts down to femtograms in dust using femtosecond laser ablation-inductively coupled plasma-mass spectrometry. Chem. Geol. 383, 123–131.

Macholdt, D., Jochum, K., Pöhlker, C., Stoll, B., Weis, U., Weber, B., Müller, M., Kappl, M., Buhre, S., Kilcoyne, A., 2015. Microanalytical methods for in-situ high-resolution analysis of rock varnish at the micrometer to nanometer scale. Chem. Geol. 411, 57–68.

Macholdt, D.S., Jochum, K.P., Wilson, S.A., Otter, L.M., Stoll, B., Weis, U., Andreae, M.O., 2016. Suitability of Mn-and Fe-Rich Reference Materials for Microanalytical Research. Geostand. Geoanal. Res. 40, 493–504. http://dx.doi.org/10.1111/ggr.12119.

McFadden, L.D., Ritter, J.B., Wells, S.G., 1989. Use of multiparameter relative-age methods for age estimation and correlation of alluvial fan surfaces on a desert piedmont, eastern Mojave Desert, California. Quat. Res. 32, 276–290.

McKeown, D.A., Post, J.E., 2001. Characterization of manganese oxide mineralogy in rock varnish and dendrites using X-ray absorption spectroscopy. Am. Mineral. 86, 701–713.

McLoughlin, N., Wilson, L., Brasier, M., 2008. Growth of synthetic stromatolites and wrinkle structures in the absence of microbes–implications for the early fossil record. Geobiology 6, 95–105.

Northup, D.E., Snider, J.R., Spilde, M.N., Porter, M.L., van de Kamp, J.L., Boston, P.J., Nyberg, A.M., Bargar, J.R., 2010. Diversity of rock varnish bacterial communities from Black Canyon, New Mexico. J. Geophys. Res. Biogeosci. 115.

Nowinski, P., Hodge, V.F., Gerstenberger, S., Cizdziel, J.V., 2013. Analysis of mercury in rock varnish samples in areas impacted by coal-fired power plants. Environ. Pollut. 179, 132–137.

Ohta, A., Kawabe, I., 2001. REE(III) adsorption onto Mn dioxide (delta-MnO2) and Fe oxyhydroxide: Ce(III) oxidation by delta-MnO2. Geochim. Cosmochim. Acta 65, 695–703.

Otter, L.M., Macholdt, D.S., Jochum, K.P., Stoll, B., Weis, U., Weber, B., Al-Amrid, A.M., Haug, G.H., Andreae, M.O., 2017. Relationship between Rock Varnish and Adjacent Mineral Dust. (in preparation).

Pan, G., Qin, Y., Li, X., Hu, T., Wu, Z., Xie, Y., 2004. EXAFS studies on adsorption–desorption reversibility at manganese oxides–water interfaces: I. Irreversible adsorption of zinc onto manganite (γ-MnOOH). J. Colloid Interface Sci. 271, 28–34.

Perry, R.S., Kolb, V.M., 2004. Biological and organic constituents of desert varnish: review and new hypotheses. In: Hoover, R.B., Rozanov, A.Y. (Eds.), Instruments, Methods, and Missions for Astrobiology VII, pp. 202–217.

Perry, R.S., Sephton, M.A., 2006. Desert varnish: an environmental recorder for Mars. Astron. Geophys. 47, 34–35.

Perry, R.S., Dodsworth, J., Staley, J.T., Engel, M.H., 2004. Bacterial diversity in desert varnish. In: Harris, R.A., Ouwehand, L. (Eds.), Proceedings of the Iii European Workshop on Exo-Astrobiology: Mars: the Search for Life, pp. 259–260.

Perry, R.S., Kolb, V.M., Lynne, B.Y., Sephton, M.A., McLoughlin, N., Engel, M.H., Olendzenski, L., Brasier, M., Staley, J.T., 2005. In: How desert varnish forms? Proceedings of the SPIE - the International Society for Optical Engineering 5906, 59060V-59061-59012. .

Potter, R.M., Rossman, G.R., 1979. The manganese- and iron-oxide mineralogy of desert varnish. Chem. Geol. 25, 79–94.

Raymond, R., Guthrie, G., Bish, D., Reneau, S., Chipera, S., 1993. Biomineralization of manganese in rock varnish. Catena Suppl. 21, 321.
Reneau, S.L., Raymond, R., Harrington, C.D., 1992. Elemental relationships in rock varnish stratigraphic layers, Cima Volcanic Field, California - implications for varnish development and the interpretation of varnish chemistry. Am. J. Sci. 292, 684–723.
Rossi, C., Lozano, R.P., Isanta, N., Hellstrom, J., 2010. Manganese stromatolites in caves: El Soplao (Cantabria, Spain). Geology 38, 1119–1122.
Rudnick, R.L., Gao, S., 2003. 3.01 - Composition of the Continental Crust. Treatise on Geochemistry. Vol. 3. Elsevier Ltdpp. 1–64.
Rybicka, E.H., Calmano, W., Breeger, A., 1995. Heavy metals sorption/desorption on competing clay minerals; an experimental study. Appl. Clay Sci. 9, 369–381.
Spilde, M.N., Boston, P., Northrup, D., 2002. Subterranean manganese deposits in caves: analogies to rock varnish. In: Geological Society of American Abstracts with Programs, . http://gsa.confex.com/gsa/2002AM/finalprogram/abstract46060.htm.
Spilde, M.N., Melim, L.A., Northup, D.E., Boston, P.J., 2013. Anthropogenic lead as a tracer of rock varnish growth: implications for rates of formation. Geology 41, 263–266.
Tebo, B.M., Bargar, J.R., Clement, B.G., Dick, G.J., Murray, K.J., Parker, D., Verity, R., Webb, S.M., 2004. Biogenic manganese oxides: properties and mechanisms of formation. Annu. Rev. Earth Planet. Sci. 32, 287–328.
Tebo, B.M., Johnson, H.A., McCarthy, J.K., Templeton, A.S., 2005. Geomicrobiology of manganese (II) oxidation. Trends Microbiol. 13, 421–428.
Thiagarajan, N., Lee, C.T.A., 2004. Trace-element evidence for the origin of desert varnish by direct aqueous atmospheric deposition. Earth Planet. Sci. Lett. 224, 131–141.
Vicenzi, E.P., Grissom, C.A., Livingston, R.A., Weldon-Yochim, Z., 2016. Rock varnish on architectural stone: microscopy and analysis of nanoscale manganese oxide deposits on the Smithsonian Castle, Washington, DC. Annu. Rev. Earth Planet. Sci. 4.
Von Humboldt, A., Bonpland, A., 1819. Voyage aux Régions Équinoxiales du Nouveau Continent. II. pp. 299–304.
Watchman, A., 2000. A review of the history of dating rock varnishes. Earth Sci. Rev. 49, 261–277.
Whitley, D.S., Baird, J., Bennett, J., Tuck Jr., R.G., 1984. The use of relative repatination in the chronological ordering of petroglyph assemblages. J. New World Archaeol. 6, 19–25.
Zerboni, A., 2008. Holocene rock varnish on the Messak plateau (Libyan Sahara): Chronology of weathering processes. Geomorphology 102, 640–651.

B.5

Macholdt et al., submitted

Investigations of black manganese-rich crusts on a cathedral

Dorothea S. Macholdt[a,b], Siegfried Herrmann[b], Klaus Peter Jochum[b], A. L. David Kilcoyne[c], Thomas Laubscher[d], Jonas H. K. Pfisterer[e], Christopher Pöhlker[a], Beate Schwager[b], Bettina Weber[f], Markus Weigand[g], Katrin F. Domke[e], and Meinrat O. Andreae[a,h]

a Biogeochemistry Department, Max Planck Institute for Chemistry, Mainz, Germany.
b Climate Geochemistry Department, Max Planck Institute for Chemistry, Mainz, Germany.
c Lawrence Berkeley National Laboratory, Berkeley, CA, United States.
d Freiburger Münster Münsterbauverein, Freiburg, Germany.
e Molecular Spectroscopy Department, Max Planck Institute for Polymer Research, Mainz, Germany.
f Multiphase Chemistry Department, Max Planck Institute for Chemistry, Mainz, Germany.
g Modern Magnetic Systems Department, Max Planck Institute for Intelligent Systems, Stuttgart, Germany.
h Geology and Geophysics Department, King Saud University, Riyadh, Saudi Arabia.

Submitted to Atmospheric Environment

Investigations of black manganese-rich crusts on a cathedral

Dorothea S. Macholdt[a,b], Siegfried Herrmann[b], Klaus Peter Jochum[b], A. L. David Kilcoyne[c], Thomas Laubscher[d], Jonas H. K. Pfisterer[e], Christopher Pöhlker[a], Beate Schwager[b], Bettina Weber[f], Markus Weigand[g], Katrin F. Domke[e], and Meinrat O. Andreae[a,h]

a Biogeochemistry Department, Max Planck Institute for Chemistry, Mainz, Germany.

b Climate Geochemistry Department, Max Planck Institute for Chemistry, Mainz, Germany.

c Lawrence Berkeley National Laboratory, Berkeley, CA, United States.

d Freiburger Münster Münsterbauverein, Freiburg, Germany.

e Molecular Spectroscopy Department, Max Planck Institute for Polymer Research, Mainz, Germany.

f Multiphase Chemistry Department, Max Planck Institute for Chemistry, Mainz, Germany.

g Modern Magnetic Systems Department, Max Planck Institute for Intelligent Systems, Stuttgart, Germany.

h Geology and Geophysics Department, King Saud University, Riyadh, Saudi Arabia.

Prepared for the Journal Atmospheric Environment

Abstract

Black manganese-rich crusts show a worldwide abundance on façades of historical buildings. In this study they were exemplarily studied on the façade of the Freiburger Münster (Freiburg Minster), Germany, and measured in-situ by portable X-ray fluorescence (XRF). The XRF was calibrated to allow the conversion from apparent mass fractions to Mn surface density (Mn amount per area), since portable XRF mass fraction measurements from thin layers violate the assumption of a homogeneous measurement volume. Additionally, 200 nm femtosecond laser ablation-inductively coupled plasma-mass spectrometry (fs LA-ICP-MS) measurements, scanning transmission X-ray microscopy-near edge X-ray absorption fine structure spectroscopy (STXM-NEXAFS), Raman spectroscopy, and imaging by light microscopy were conducted to obtain further insight into the crust material, such as biogenic contributions, element distributions, trace element compositions, and available functional groups.

Crusts appear as black patches distributed in many places on the minster's facade, but Mn-rich crusts (with a Mn surface density >150 µg cm^{-2}) are restricted to a maximum height of about 7 m. The only exceptions are those developed on the Renaissance-Vorhalle (Renaissance portico) at a height of about 7.7 m, a part of the façade, which had been cleaned and painted with a silicon resin as recently as 2003. These crusts thus accumulated over a period of only 12 years. Yet, they are exceptionally Mn-rich with a surface density of 1360 µg cm^{-2}, and therefore require an accumulation rate of about 100 µg cm^{-2} Mn per year.

Trace element analyses support the theory that vehicle emissions are responsible for most of the Mn supply. Lead, barium, and zinc correlate with manganese, indicating element sources such as tire material, brake pads, and resuspended road dust. Microscopical investigations show no organisms on the Mn-rich crusts. In contrast, Mn-free black crusts sampled at greater heights (>8 m) exhibited fungal and cyanobacterial encrustation. Carbon-rich spots were found by STXM-NEXAFS underneath one of the Mn-rich crusts. However, these carbon occurrences originate from soot and polycyclic aromatic hydrocarbons (PAHs) deposited on top of the crust, rather than from organisms responsible for the crusts formation, as shown by STXM-NEXAFS and Raman spectroscopic measurements. Our results suggest that the crusts develop abiogenically, with vehicle emissions as dominant element sources.

Keywords:

manganese crusts; portable XRF; Freiburger Münster; rock varnish; vehicle emission; manganese deposition mechanisms

1. Introduction

Historic buildings and monuments in urban areas often show extensive dark or black discolorations, which affect their aesthetic appeal and whose restauration can have considerable economic implications (Newby et al., 1991). Up to recently, most of these blackened areas were thought to be formed by the accumulation of soot, which on carbonate building materials is often incorporated into a matrix of gypsum. The main source of the soot can be traced back to fossil fuel combustion, which depending on the time and place concerned may be dominated by coal burning, diesel engines, and other activities (Bonazza et al., 2007a; Bonazza et al., 2005; Brimblecombe and Grossi, 2009; De Oliveira et al., 2011; Grossi and Brimblecombe, 2002; Grossi and Brimblecombe, 2008; Pio et al., 1998; Ruffolo et al., 2015; Sáiz-Jiménez and Hermosin, 2004).

Figure 1: The Freiburger Münster (Freiburg Minster), Freiburg, Germany. The minster, which was built from around 1200 to 1513, is a well-known cathedral belonging to the Freiburg archdiocese. (Image credit: Von Oberth, CC BY-SA 3.0, https://commons.wikimedia.org/w/index.php?curid=1158443)

The gypsum layer develops due to the sulfur dioxide (SO_2) released in the course of fossil fuel combustion, which can either react directly with the carbonate material or after its oxidation to sulfuric acid in the atmosphere (Bonazza et al., 2005; Brimblecombe and Grossi, 2009; Grossi and Brimblecombe, 2002; Ruffolo et al., 2015). Colored organic compounds incorporated into the coatings can result in brownish or yellowish discolorations (Bonazza et al., 2007a; Brimblecombe and Grossi, 2009; Grossi and Brimblecombe, 2008). More recently, the growth of cyanobacteria (Bonazza et al., 2007b; Uchida et al., 2016), bacteria (Miller et al., 2012), and fungi (De Oliveira et al., 2011; Gorbushina et al., 1993; Saiz-Jimenez et al., 2012; Viles and Gorbushina, 2003) was also implicated in the discoloration of exposed stone materials.

However, in the last few years it was found that some black crusts are actually Mn-rich coatings (Grissom et al., 2014; Grüner, 2011; Livingston et al., 2016; Uchida et al., 2016; Vicenzi, 2016) with an as yet unknown genesis. These black crusts in urban open areas lack identifiable biogenic structures (Grissom et al., 2014; Livingston et al., 2016; Vicenzi, 2016) and are thus dissimilar to Mn-rich crusts found in cave environments, which were often found to be of biogenic origin (Frierdich et al., 2011; Miller et al., 2012; Saiz-Jimenez et al., 2012; White et al., 2009). Manganese-rich coatings on facades of buildings of historical interest are often found on siliceous stones, such as quartz-based sandstones, in contrast to the soot-rich crusts on limestones, marbles, or calcareous sandstones (Bonazza et al., 2007a; Bonazza et al., 2005; Brimblecombe and Grossi, 2009; Grossi and Brimblecombe, 2002; Grossi and Brimblecombe, 2008). Grossi and Brimblecombe (2002) report that quartz-

based sandstones behave differently from limestones and marbles, since they are resistant to sulfur-based acids in the air and they “tend to become dirtier in rain-washed areas than in sheltered areas”.

Such Mn-rich coatings were described for the Freiburger Münster, Freiburg, Germany (Fig. 1) by Grüner (2011). They had also been observed on several other buildings of historical interest, such as at the church in Stödtlen, Germany (Grüner, 2011), the Smithsonian Institute in Washington D.C., USA (Grissom et al., 2014; Livingston et al., 2016; Vicenzi, 2016), and the Khmer temples in Cambodia (Uchida et al., 2016), indicating the worldwide abundance of these crusts. Manganese-rich crusts on historical buildings are not only found on sandstone building blocks, but also on laterites and bricks (Uchida et al., 2016). No systematic association has been observed between the surface roughness of the building blocks and crust development, neither on the Freiburger Münster, nor on the Smithsonian Castle (Vicenzi, 2016). Furthermore, the patches are most abundant on the building blocks themselves, and only to a lesser extent on the mortar between them. The crusts seem to start growing on the sandstone and only cover the mortar in cases when the crusts span several blocks, an observation also made at the Smithsonian Institute (Vicenzi, 2016).

As these patches disfigure the appearance of the buildings, attempts were sometimes made to seal and protect the building blocks by painting them with various coatings or sealants. At the Freiburger Münster, especially manganese-rich crusts have been found on the Renaissance-Vorhalle which was built in 1620. This addition to the minster was painted with a hydrophobic, diffusion-open silicon resin paint during restauration work in 2003 (Grüner, 2011), which might have created conditions particularly suitable for Mn-crust growth. Another part of the minster, the Schöpfungsportal (creation portal), was painted with a pore-closing silicic acid ester on several areas. Black crusts grew at these locations within only about four years. The Schöpfungsportal is of specific interest because of existing photographic documentation spanning the last 100 years. It appears that the applied coatings have actually facilitated the growth of the black crusts, hence it is of importance to understand their genesis and formation mechanisms before considering further restoration measures.

This study aims to investigate the chemical composition of these coatings, their distribution on the cathedral surfaces, their formation mechanisms, and the source of the Mn at the example of the Freiburger Münster. The minster, which was built from around 1200 until 1513, is a well-known cathedral belonging to the Freiburg archdiocese. Black crusts at the minster were investigated and mapped up to a height of about 30 m. Their chemical composition was obtained using a portable XRF, a non-destructive technique very suitable for historic buildings and artefacts. In addition, we investigated two samples by optical microscopy, 200 nm fs LA-ICP-MS, Raman spectroscopy, and STXM-NEXAFS, to obtain major and trace element compositions, reveal structures, determine the presence of organisms, and investigate carbon functional groups and carbon abundances within the crusts.

2. Material and methods

The Freiburger Münster was investigated at different sites and heights (Fig. 2). Measurements were taken at the Joch 12 S at the Chor (0.5 m height), at the Sterngalerie-Nische south-side (1.5 m height), below the Renaissance-Vorhalle (no silicone resin paint, about 1.5 m height), and at the Schöpfungsportal north-side (2 m height), at the south/east Facade of the “Sterngalerie am Hauptturm” (1.5 m height), at the pillar 2/3 north-side Sockelbereich (1.5 m height), at the Strebepfeiler 13/14 S (7 m height), at the Renaissance-Vorhalle (south-side) on the gallery (about 7.7 m height), at the Strebepfeiler 14/15 S (5 m, 7 m, 11 m, 15 m, 17 m, 19 m, and 21 m height), at the Joch 15 N on the Kapellenpfeiler (13 m height), at the Hochchorpfeiler 11/12 N (13 m height), at the Strebepfeiler 10/11 N (13 m height), at the Hochchorwand Joch 13 (13 m and 25 m height), at

the southern Hahnenturm (28 m height), at the Sterngalerie east-side (28 m height), and at the Hauptturm (30 m height).

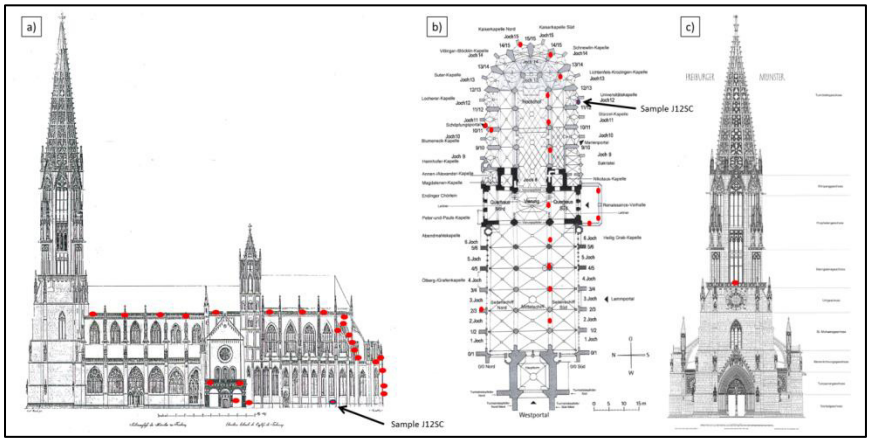

Figure 2: The South Facade of the Freiburger Münster (a), a cross section (b), and the Haupttum (c). Marked in red are the main locations where measurements were conducted. (Image credits: Freiburger Münsterbauverein)

Additionally, the building stones were investigated using samples of clean, unexposed rocks to obtain their Mn content (Table 1). The materials from different quarries used as building block resources were Lorettoberger, Heimbacher/Tannenbacher, Schweinstätter, Pfinztäler, Pfaffenweiler, Neckartäler, Fischbacher, and Almendsberger sandstone (Fig. 3, Table 1). The sources of some sandstones are not known, one of them a reference sample called AA1, as well as the sandstone used to build “Chor Nord” and “Turm S-W” (Table 1).

Table 1: Portable XRF measurements of the building blocks from several different quarries. The numbers in the first column correspond to the numbers in Fig. 2.

# on image	Quarries and descriptions	MnO [%]
1	AA1	<0.015
2	Above Schöpfungsportal 0-4.1	0.088
3 (a)	Lorettoberger 0-1.3 light colored side	0.042
3 (b)	Lorettoberger 0-1.3 dark red side	<0.015
3 (c)	Lorettoberger 0-1.3 brown vein	0.041
4	Lorettoberger 0-1.5	<0.015
5	Lorettoberger 0-1.9	<0.015
6	Heimbacher/Tannenbacher 0-3.2	<0.015
7	Heimbacher/Tannenbacher 0-3.1	<0.015
8	Heimbacher/Tannenbacher 0-2.2	<0.015
9	Heimbacher/Tannenbacher 0-2.1	<0.015
10	Schweinstätter	0.074
11	Pfinztäler S 1.1	<0.015
12	Pfaffenweiler 0-5.1	0.047
13 (a)	Neckartäler A 12.2	<0.015
13 (b)	Neckartäler A 12.1 on clay filled puddle	0.134
14	Fischbacher 0-7.1	0.035
15	Almensberger A 2.3	<0.015
16	Chor Nord	<0.015
17	Turm S-W	<0.015

18	Yellow Tennenbacher, medieval	0.032

Figure 3: Sandstone samples from the different quarries that were used as sources for the building materials for the Freiburger Münster during its construction and restoration. The numbers correspond to the measurement results in Table 1.

A portable XRF (Thermo Fisher Scientific Niton XL3) was used to investigate the black patches on the Freiburger Münster, especially for the MnO content and the patch distribution. Similar instruments have been used previously for this type of measurements because of their portability and non-destructive operation (Livingston et al., 2016; Uchida et al., 2016; Vicenzi, 2016). Measurements were conducted in the "mining" mode, and measurements with each filter were integrated for 20 s. The instrument is equipped with an X-ray source with an energy of 50 keV, a silver anode, and has a spot size of 8 mm. For quality control, the reference material TILL-4 (GeoReM database http://georem.mpch-mainz.gwdg.de) was measured before and after each XRF measurement sequence, as well as between each sample for the calibration curve measurements. A total of one hundred measurements were made on various parts of the Freiburger Münster. The results directly derived from the measurements on the uncoated sandstones are valid as measure of the Mn concentration in the rock, since sandstones are relatively homogeneous. However, the measurements on the black crusts had to be calibrated differently, since X-rays are produced and scattered back from different depths. Many authors provide the measurement results of thin layers as they were read directly from their portable XRF instrument (Livingston et al., 2016; Uchida et al., 2016). Nevertheless, these authors also state that their numbers are not actual concentrations, but provide relative estimates suitable for comparison only (Uchida et al., 2016; Vicenzi, 2016). The depth from which information can be retrieved depends on the atomic number of the element of interest, as well as on the composition of the matrix material, which is in this case the crust and a certain depth of the rock behind it.

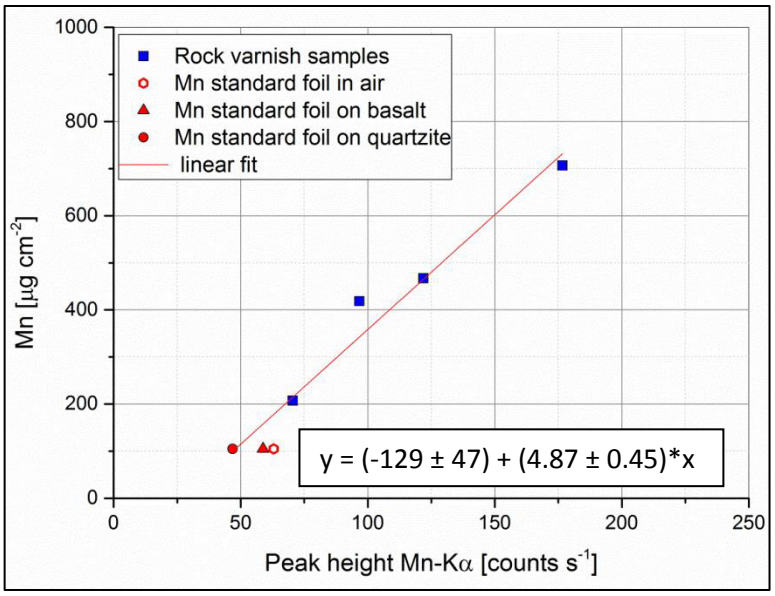

Figure 4: Calibration curve produced by linear fit to obtain Mn surface densities (masses per area) from measurements by portable XRF. The four blue squares are measurements from leaching experiments using rock varnish crusts. The red symbols represent the measurements obtained from a Mn standard foil produced by Micromatter™ in air (hexagon), with a quartzitic background material (circle), and with a basaltic background material (triangle). The measurement of the foil in air was excluded from the fit since it does not represent the conditions of a Mn-crust on a host rock.

To obtain a calibration curve appropriate for the Mn coatings, we used four Mn-covered rock samples (rock varnishes from California). Squares cut from these rocks were used to obtain crust-covered surfaces between 4.38 and 6.25 cm². The exact surface areas were determined utilizing the software ImageJ. The Mn-rich crusts were measured by portable XRF on 21 different spots on each rock used for calibration, since the thickness of the crust varies across the rock surface. An average value was taken for the calibration. Additionally, the underlying rocks on the backside of the squares were measured to obtain the MnO contents of the host rocks.

The crusts were dissolved off the rock surface by treatment with 0.02 M hydroxylamine hydrochloride at a pH of 2.5 and a temperature of 70°C. The solution was evaporated and the procedure repeated several times until XRF measurements on the formerly MnO-covered surface gave values similar to those of the host rock. The solution was heated until the dissolved crust material precipitated, the precipitate was weighed and dissolved in 2% HNO_3. This solution was measured by ICP-MS (Agilent 7900 ICP-MS) for its Mn content, with Rh as internal standard element. The reference materials BHVO-2 and BCR-2 (GeoReM database http://georem.mpch-mainz.gwdg.de) were additionally measured for quality control. The Mn surface density (i.e., the amount of Mn per surface area) was calculated using the sample surface area and mass of Mn in the sample obtained from the dilution factor and the Mn mass fractions measured by ICP-MS. In addition to the calibration values derived by this method, we also used a standard foil from Micromatter™ with a Mn loading of 104.7 µg cm^{-2}. The Mn K-α count rate (peak height) obtained by the XRF from this standard foil, showed significant differences depending on whether it was measured in air or with a rock slice (basalt or quartzite) behind it (Fig. 4). We consider the values obtained with the rock backings as the most appropriate for our measurements on Mn crusts. Plotting the Mn surface density against the Mn K-α count rate of the four rock varnish samples and the standard foil with the rock backings, we obtained a calibration curve (Fig. 4). Our results are in accordance with previously published numbers of 150-300 µg cm^{-2} Mn on varnish crusts measured by Reneau (1993).

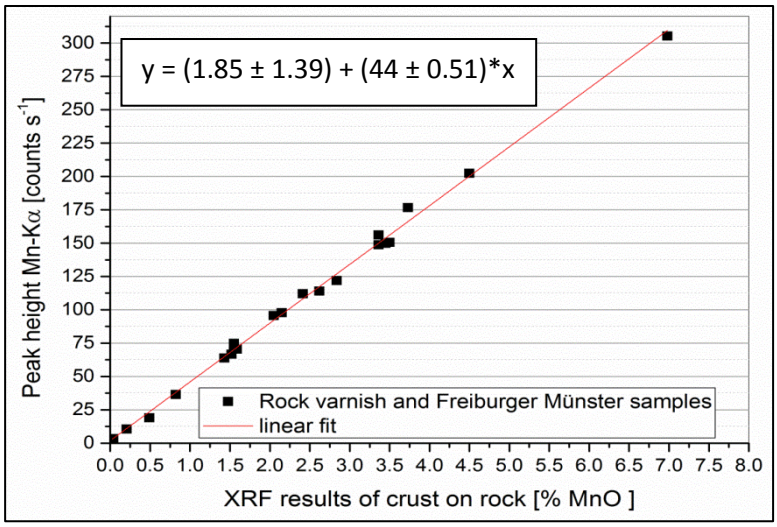

Figure 5: Plot of the peak height of Mn K-α versus the apparent Mn concentration reported by the portable XRF.

Since the portable XRF reports its results in the form of an apparent concentration rather than as count rates, we evaluated the relationship between count rate and reported concentration (Fig. 5). We found that as long as long as the host rock matrix is more or less the same (sandstone in our case), the correlation is excellent, and the apparent concentrations can be used for convenience to convert the XRF measurements into surface densities. On the other hand, our measurements with the standard foil indicated a significant influence of the host rock matrix. Calibrations using host rocks similar to the samples, and use of the count rates obtained from the spectra, are required for accurate results.

In one sample, J12SC, taken from Joch 12S at the Chor at 0.5 m height, 39 elements were measured by a 200 nm fs LA-ICP-MS (a ThermoFisher Element 2 single-collector sector-field ICP-mass spectrometer combined with an ESI 200 nm fs laser ablation system NWRFemto) to obtain accurate mass fractions of major and trace elements with low detection limits. As reference materials, GSE-1G and NIST 610 (GeoReM database http://georem.mpch-mainz.gwdg.de) were chosen. Laser ablation was conducted in a New Wave Large Format Cell in a He atmosphere. All measurements were conducted in medium mass resolution mode (2000) with flat-top peaks. The sample was introduced as thick-section (70 µm) of the cross section of the crust. After pre-ablation the sample was scanned via line scans along a profile from the underlying rock through the varnish into the embedding resin. To normalize the data, the oxides of the major elements (Na_2O, MgO, Al_2O_3, SiO_2, P_2O_5, K_2O, CaO, TiO_2, MnO_2, and Fe_2O_3) were assumed to add up to 98 %. By this method, the procedure is reproducible and easily recalculated if future measurements are able to provide the exact amount of water and organics within the crusts.

Furthermore, sample J12SC and reference compounds were investigated by STXM-NEXAFS with the X-ray microscope at beamline 5.3.2.2 at the synchrotron Advanced Light Source (ALS), Berkeley, CA, USA, and with the MAXYMUS microscope at the synchrotron BESSY II, Helmholtz-Zentrum Berlin, Germany, to obtain element distribution maps and to study the functional groups of the carbon distributed within the sample. A description of the STXM-NEXAFS technique can be found in Moffet (2011). Since STXM-NEXAFS is a transmission light method and requires samples of a thickness of about 100 nm, focused ion beam (FIB) sputtering (milling) was performed at the Max Planck Institute for Polymer Research (Mainz, Germany) using a Nova600Nanolab FIB dual-beam instrument of FEI to prepare an ultra-thin section of the sample (50 µm x 30 µm x 150 nm). Details

on the X-ray microscopes can be found in Kilcoyne et al. (2003) as well as Weigand (2014) and Follath et al. (2010). The STXM measurement and sample handling techniques are described in Pöhlker et al. (2012).

The same sample was used to conduct conventional Raman spectroscopy. Raman spectra were obtained using a Bruker Senterra Instrument at the Max Planck Institute for Polymer Research (Mainz, Germany). The measurements were made with a 785 nm laser and an objective of 50x magnification. The spot size was about 2 µm, 2 acquisitions were chosen, and an aperture of 5 x 1000 µm. The spectral range from 0-3500 cm^{-1} was measured with a resolution of 3-5 cm^{-1}. The power was increased from 1 mW, over 10 mW, up to 25 mW, and exposure times between 90 and 180 s were chosen, using the settings published by Sadezky et al. (2005) for orientation. Since the sample was very thin (100-200 nm), the high power settings eventually destroyed the sample. To validate the data, additional measurements were conducted on an unprocessed piece of sample J12SC, with 10 mW, an objective of 20x magnification, and a spot size of about 4 µm. The same bands were detected at the same wavenumbers, indicating that the bands were not produced by degradation of the sample material by the laser. Baseline correction was performed with the software OPUS 7.5 Senterra E. A concave rubberband correction with 10 iterations for 64 baseline points was conducted. Uncorrected raw spectra are provided in Fig. A of the appendix.

3. Results and discussion

3.1.Sandstones as possible source of Mn

Measurements were conducted to obtain an overview over the Mn abundances in the materials used for the construction of the minster (sandstones) (Table 1) and the presence of Mn in the crusts on the minster's facade (Table 2). Several bare sandstones were measured at the facade, as well as freshly-cut sandstone surfaces from several quarries that had been used as sources for the sandstone blocks of the minster. The sandstone matrix measurements revealed MnO mass fractions between <0.015% (below the detection limit) and 0.088%. Small clay lenses (up to 1 cm in diameter) within one sandstone sample had MnO mass fractions up to 0.134% Mn.

Table 2: Portable XRF measurements of the Freiburger Münster facade. Several measurements were taken at each location, only the highest values are given.

Location	maximal XRF percentages received (% MnO)	peak height Mn-Kα	Mn per area [µg cm^{-2}]	height above ground [m]
J12SC, Joch 12 S-Chor	3.36	148.76	595	0.5
S-E Facade Sterngalerie am Hauptturm	<0.015	n.d.	n.a.	1.5
Pillar 2/3 north-side Sockelbereich	3.36	156.19	631	1.5
Sterngalerie niche, south-side	0.027	2.88	n.a.	1.5
Below the Renaissance Vorhalle	3.45	149.91	600	1.5
Schöpfungsportal north-side	2.62	114	425	2
Strebepfeiler 14/15 S	1.43	63.73	180	5
Strebepfeiler 14/15 S	1.52	66.77	195	7
Strebpfeiler 13/14 S	1.55	74.81	234	7
Rennaissance-Vorhalle	6.98	305.3	1357	7.7
Strebepfeiler 14/15 S	<0.015	n.d.	n.a.	11
Joch 15 N, Kapellpfeiler	<0.015	n.d.	n.a.	13
Hochchorpfeiler 11/12 N	<0.015	n.d.	n.a.	13

Strebepfeiler 10/11 N	<0.015	n.d.	n.a.	13
Strebepfeiler 14/15 S	<0.015	n.d.	n.a.	15
Strebepfeiler 14/15 S, west-side of column	<0.015	n.d.	n.a.	15
Strebepfeiler 14/15 S, east-side of column	<0.015	n.d.	n.a.	17
Top of the Strebepfeiler 14/15 S	<0.015	n.d.	n.a.	19
Strebepfeiler 14/15 S towards Hochchor	<0.015	n.d.	n.a.	21
Hochchorwand, Joch 13	0.821	36.48	48	23
Hochchorwand, Joch 13	0.206	10.52	n.a.	25
Along the facade of the Münster	<0.015	n.d.	n.a.	28
Southern Hahnenturm inner side	0.028	3.46	n.a.	28
Southern Hahnenturm outer side	<0.015	n.d.	n.a.	28
Sterngalerie east-side	0.038	3.4	n.a.	28
Hauptturm	<0.015	n.d.	n.a.	30

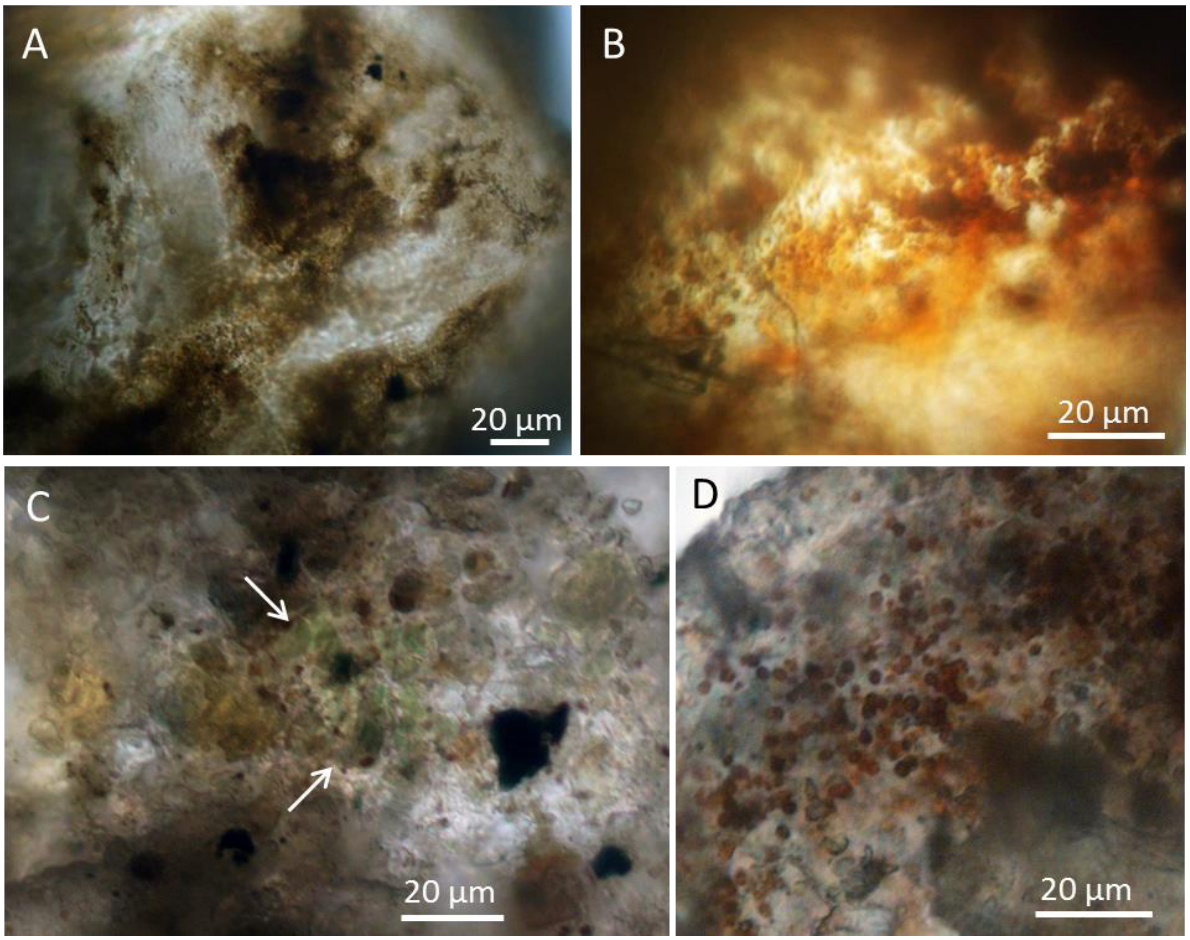

Figure 6: Light microscopy of material from the Freiburger Münster. A) dark brown to black stains on rocks originating from soot, Mn-, and Fe accumulation (631 µg cm^{-2} Mn); no fungal hyphae or cellular pigments are visible. B) orange, carotenoid-like and brown pigments within cell-like structures on the same sample. Images A and B were taken from a sample from Joch 12 S am Chor (J12SC), at 0.5 m height (Fig. 7 d, Table 3). C) cyanobacteria (arrow) on rocks originating from the "Sterngalerie" (Mn amount below the detection limit). D) brown fungal cells and hyphae originating from the "Sterngalerie".

The black patches at the minster's facade were measured from 0.5 m to about 30 m height. Manganese-rich patches (≥ 150 µg cm^{-2}) were only found up to a height of 7 m. The exception were especially Mn-rich patches at the Renaissance-Vorhalle (Renaissance portico) at a height of about 7.7 m, a supplement to the

minster, which had been painted during restauration work (2003) with a silicon resin. Visually similar black patches were found at greater heights, but they all lacked high Mn mass fractions. They either showed elevated amounts of CaO (~20%) and S (~6%), or biological encrustations. While high Ca and S mass fractions of black patches indicate a gypsum crust ($CaSO_4*2H_2O$) which captured soot particles, the organisms found were identified as black fungi and cyanobacteria (Fig. 6 C-D). Black fungi (De Oliveira et al., 2011; Gorbushina et al., 1993; Saiz-Jimenez et al., 2012; Viles and Gorbushina, 2003), cyanobacteria (Bonazza et al., 2007b; Uchida et al., 2016), and black gypsum crusts (Bonazza et al., 2005; Brimblecombe and Grossi, 2009; Grossi and Brimblecombe, 2002; Ruffolo et al., 2015) have been previously observed forming black crusts on rock surfaces. It cannot be distinguished by macroscopic features if the black patches are soot, fungi, or Mn-rich crust, but they do clearly show different chemical compositions (Fig. 7).

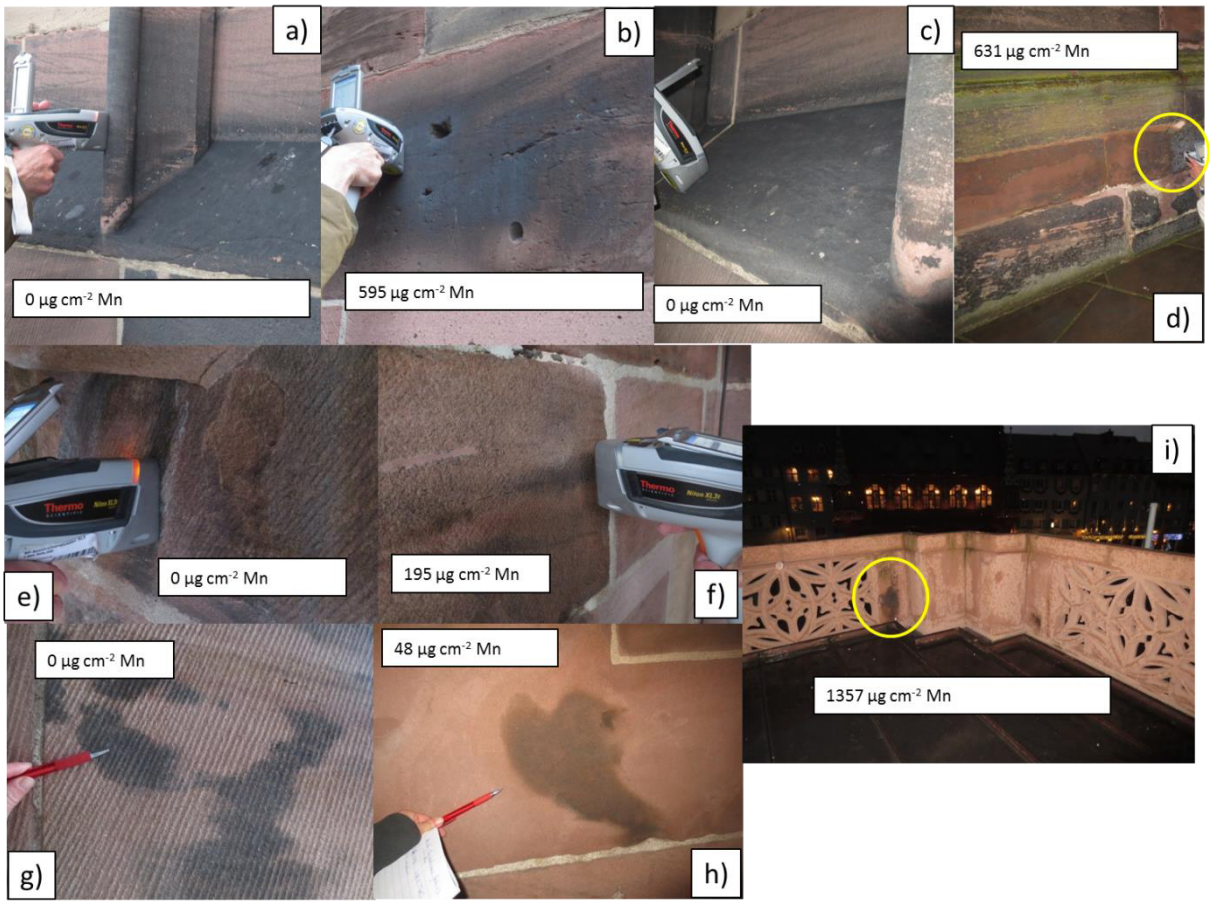

Figure 7: Measurement spots and measured Mn surface densities. One cannot distinguish visually if the black patches are soot, fungi, or Mn-rich crusts. Sample J12SC was taken from the area shown in d).

Previous authors had discussed whether the Mn-rich crusts on facades might obtain their elements by leaching of the underlying sandstone, transport through the sandstones pore systems, and deposition at the surface (Grüner, 2011). Most sandstones used to build the minster have MnO amounts below the detection limit of the portable XRF used (0.015% MnO). Thus, to obtain enough Mn to form a crust of 3.36% MnO (J12SC) from a sandstone with <0.015% MnO, transport of all available Mn present in the sandstone from a depth of at least 5 cm to the surface would be necessary. This depth is indeed in the range where capillary rise can occur in porous sandstones (Tsunazawa et al., 2016). However, no Mn-lined fissures are observable in cross sections and the crusts seem to be continuous layers and not predominantly abundant close to pore systems or intruding the rock surface similar to weathering crusts (Fig. 8 a, j). The patch distribution could be explained by proximity to areas with higher porosity, however, the height limitation of Mn-rich patches to below 7 m, the leach-

ing process within the sandstones, and the preferred accumulation of Mn^{4+} over Fe^{3+} could not be explained. It is not clear how Mn should be mobilized within the sandstones, which would require low pH or reducing conditions, and which processes would allow the precipitation and oxidation of Mn^{2+} to immobile Mn^{4+} at the rock surface. Another good indicator that this process is probably not the main driving force behind the development of the crusts is the fast and preferential growth on top of sealing paints that had been applied on the sandstone surfaces.

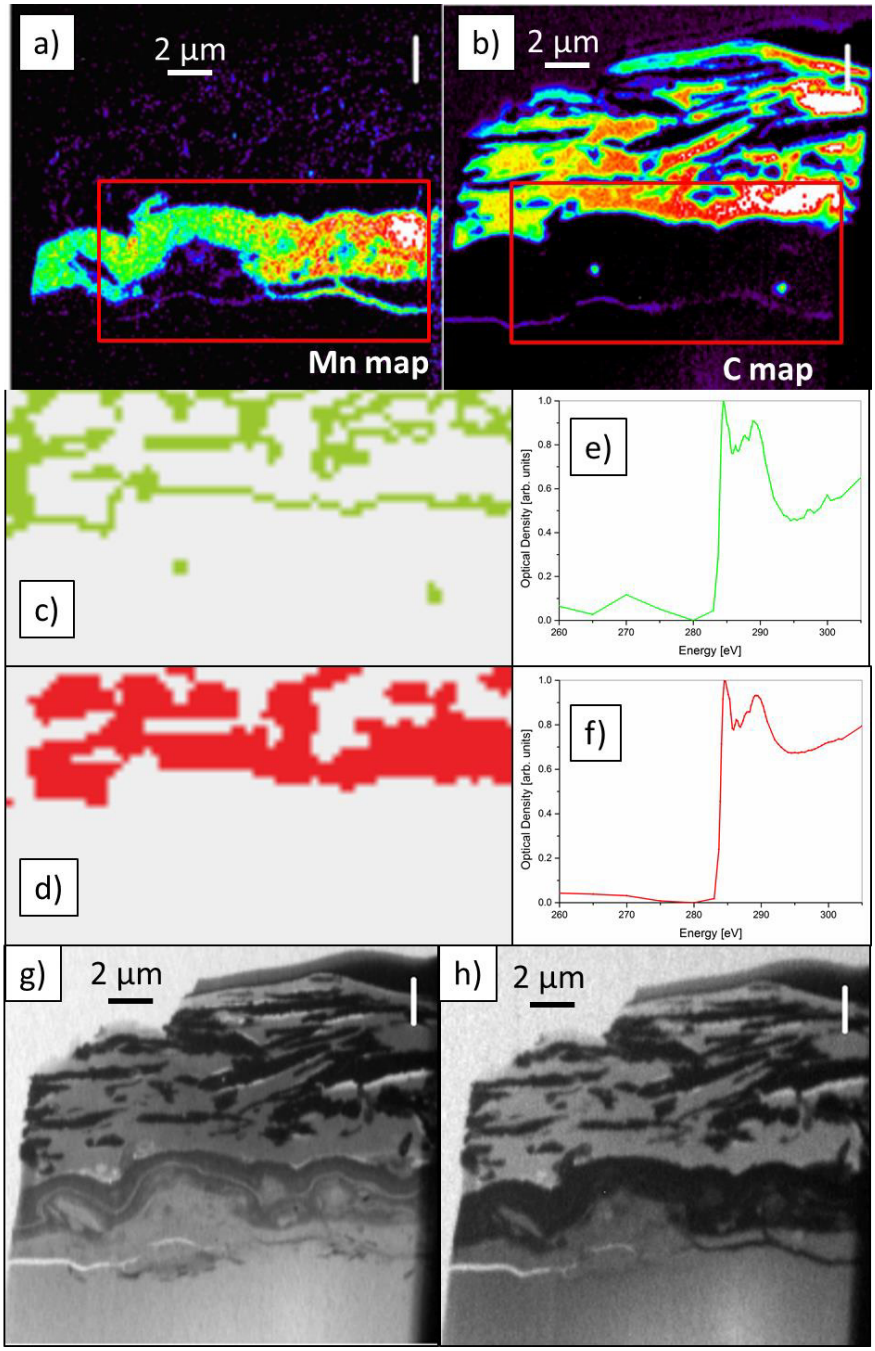

Figure 8: Element maps of Mn (a) and C (b) obtained by STXM—NEXAFS measurements. Cluster analyses of the range of energy in which carbon absorbs (260-305 eV) show two C-rich clusters (c, d), with strong absorption bands (e, f) indicating the presence of soot. These two clusters show that the carbon from underneath the Mn-rich crust shows the same functional groups as the carbon deposited on top of the crust and might therefore only be introduced below the Mn-layer through cavities. The carbon clustering was conducted for the area marked by a red box in (a, b). Fig. 7 (g) is a structure overview image at the Mn pre-edge (530.5 eV) and (h) an overview at the absorption energy of Mn (641 eV).

3.2.Vehicle emissions as potential sources of Mn

Another possible source of Mn is pollution by traffic or similar sources, which could explain the acceleration of crust growth in recent times. Motor vehicles are known to be a major source of particulate matter and contribute strongly to the distribution of metal-containing particles in urban air (Schauer et al., 2006). The abundance of Mn in air masses in larger German cities is about 20 ng m^{-3}, based on Vallero (2014) and Martin Shafer (personal communications, 2016). Since the addition of Mn to gasoline was restricted in Germany to 6

mg l^{-1} by January 2011, and to 2 mg l^{-1} by January 2014, according to § 3 (5) of the Kraftstoffverordnung 2012, Mn gasoline additives are not a significant source of Mn to air in Germany. However, other traffic related sources are relevant. An average car produces 10-200 µg km^{-1} Mn per km driven (particles <10 µm), most of which is released by wearing down and evaporation of brake material (0.1-0.17 % of the dust produced by brake material <10 µm is Mn), to a lesser extent from resuspended road dust (up to 700 µg g^{-1} of the resuspended road dust is Mn), and only marginally from tailpipe emissions (22-74 µg g^{-1} of the tailpipe emission is Mn) (Schauer et al., 2006). Regarding the particle size distribution, information diverges. While Schauer et al. (2006) state that Mn-rich particles are most abundant in the size range between 1-10 µm, with the highest mass abundance between 1-1.8 µm, Birmili et al. (2006) found during their studies that particles <0.5 µm and >1.5 µm are the main Mn contributors in the fine and coarse particulate matter (PM) size ranges. They interpret the observed spread across all size ranges as indicator for the existence of several different source mechanisms.

Since mechanically generated particles are relatively coarse in size, normal grinding of brake material cannot be the sole mechanism of brake wear emission (Schauer et al., 2006). Since brake pads are made of organometallic material (Rogge et al., 1993), friction-heated surfaces of brake pads and rotors are most likely to also contribute to the PM production by volatilization and condensation of the material (Garg et al., 2000; Sanders et al., 2002). Tire material does not contribute to Mn emissions, but it releases Zn in relatively large amounts (Schauer et al., 2006). The high Zn mass fractions (5000 µg g^{-1}) in the crusts measured on the Freiburger Münster are thus an additional indicator for vehicles as PM sources (Table 3). Other traffic-related elements of high abundance in the crusts on the Freiburger Münster are Pb (8300 µg g^{-1}) and Ba (1750 µg g^{-1}) (Table 3).

Table 3: Results from 200 nm fs LA-ICP-MS measurements of sample J12SC (taken from Joch 12 S at the Chor at 0.5 m height; Fig. 4 d, Table 3).

Element	Isotope used	Sample J12SC		Element	Isotope used	Sample J12SC	
		[µg g^{-1}]	RSD [%]			[µg g^{-1}]	RSD [%]
Na	Na^{23}	1840	42	Cs	Cs^{133}	11	23
Mg	Mg^{25}	3520	34	Ba	Ba^{138}	1750	27
Al	Al^{27}	43563	26	La	La^{139}	20	51
Si	Si^{29}	253000	18	Ce	Ce^{140}	42	33
P	P^{31}	25900	50	Pr	Pr^{141}	5.3	48
K	K^{39}	20400	26	Nd	Nd^{143}	20	41
Ca	Ca^{43}	20100	28	Sm	Sm^{147}	4.6	36
Ti	Ti^{47}	1550	23	Eu	Eu^{151}	1.1	28
V	V^{51}	83	37	Gd	Gd^{157}	4.9	23
Cr	Cr^{53}	64	22	Tb	Tb^{159}	0.73	37
Mn	Mn^{55}	77100	39	Dy	Dy^{161}	4.4	37
Fe	Fe^{57}	29100	30	Ho	Ho^{165}	0.81	31
Co	Co^{59}	525	71	Er	Er^{167}	2.4	30
Ni	Ni^{60}	286	39	Tm	Tm^{169}	0.31	29
Cu	Cu^{63}	328	28	Yb	Yb^{173}	2.2	39
Zn	Zn^{67}	5000	36	Lu	Lu^{175}	0.28	39
Rb	Rb^{85}	83	31	Pb	Pb^{208}	8300	30
Sr	Sr^{88}	510	28	Th	Th^{232}	7	34
Y	Y^{89}	17	28	U	U^{238}	3.3	23
Zr	Zr^{90}	35	38				

Brake pad wear is also the dominant contributor to Ba in urban air, since barium sulfate is a major component of them. Barium sulfate is used as stable filler that accounts for up to 40% of the brake pad weight (Blau, 2001). Unlike U.S. American and Japanese vehicles, European vehicles' brake linings are usually low-steel or NAO materials due to higher performance requirements (Birmili et al., 2006). They consist of steel (0-20 %), Cu (16%-22%), Al_2O_3 (0-2.5%), Fe_2O_3 (0-10%), ZnS (5-6%), $BaSO_4$ (10%-16%), and organic binding materials, according to the "Bremsenhandbuch" (brake handbook) (Breuer and Bill, 2006). The largest Ba mass fractions can be found in PM >10 µm, since they form by mechanical abrasion (Schauer et al., 2006). Barium was found to have an abundance of about 3.5-17.1 ng m^{-3} in urban air (Schauer et al., 2006).

Lead can be emitted from several sources, including fuel and motor oil combustion, brake wear, and resuspension of enriched road dust (Cadle et al., 1997; Garg et al., 2000; Young et al., 2002), among which resuspended road dust predominates (Schauer et al., 2006). A major fraction of the Pb in road dust still has its source in industrial and tailpipe emissions from the time before the phase-out of leaded gasoline, but also from Pb wheel weights that are lost from vehicle wheels and get pulverized by traffic (Root, 2000). Since tetraethyl lead, the former organometallic additive to gasoline, tended to oxidize and damage valves, spark plugs, and combustion chambers, brominated and chlorinated organics were added as scavengers (Robert, 1984). These compounds convert Pb oxides to volatile halide salts which exit through the tailpipe (Nriagu, 1990). Since these compounds are resistant to degradation, they are still common in the environment despite the lead phase-out (Oudijk, 2010). Nowadays, Pb concentrations of 1-9 ng m^{-3} were measured in urban air in Milwaukee and Waukesha, WI, USA and Denver, CO, USA (Schauer et al., 2006). The agreement of the main inorganic particulate matter released by vehicles and the main enrichments of elements within the crusts suggests that vehicle emissions are indeed good candidates for the sources of the Mn, Ba, Pb, and Zn observed on the Freiburger Münster.

3.3.Manganese leaching and distribution

Manganese produced and released through the processes described above has an average leachable fraction of 90% (at 37°C, pH ~7.4, and leaching for 8 h) (Schauer et al., 2006). For comparison, Fe has only a leachable fraction of 10-25%, which is in agreement with the enrichment of Mn over Fe in the minster's crusts, even though the elements generally behave quite similar. Barium and Pb have a leachable fraction of about 25%, and Cu, Zn, and Sb 50-60% (Schauer et al., 2006). While Janssen et al. (1997) also found a solubility of 91% for Mn in a weak acidic solution, Espinosa et al. (2002) and Birmili et al. (2006) determined a solubility of 10-40 % in a pH-neutral water solution. However, since rain tends to be slightly acidic, it is likely that most of the Mn in aerosols is soluble in urban environments. Leaching and redeposition of aerosol Mn is thus a plausible mechanism for the enrichment of Mn on the facade of the Freiburger Münster. An explanation for the decrease of Mn with height can be the vertical distribution of vehicle emissions. The highest exhaust fume amounts are reported close to the ground, rapidly decreasing at greater heights (DePaul and Sheih, 1985). The exact height up to which vehicle movements influence the flow and turbulence of air masses, and by this the distribution of vehicle emissions, depends on the width and height of the street canyons within a city, as well as on wind speed, tree density, and other factors. Turbulent air masses, responsible for the distribution of the vehicle emissions, are reported to reach up to 7 to 12 m (DePaul and Sheih, 1985; Qin and Kot, 1993). This relation between the concentration of heavy metals in black crusts and the distribution height of vehicular traffic emissions was observed before by Ruffolo et al. (2015).

The limitation of the Mn-rich patches to sandstone buildings, while not affecting houses that are close by, has puzzled authors before (Vicenzi, 2016). One possible explanation is the availability of alkali and alkaline earth metal containing minerals within sandstones, which increase the pH value. The rough surface, which

prevents water from draining and has a tendency to remain cold and delay evaporation or even initiate condensation of water, could also contribute. The discolorations on the facade of the Freiburger Münster show a patchy shape, often starting in the middle of the sandstone blocks. This is in agreement with the observation that during warmer days, condensation can occur preferentially in the middle of the sandstone blocks where the material is surrounded by rock in five of six directions. Rock surfaces are known to be favorable sites for condensation from the atmosphere (Duvdevani, 1949; Duvdevani, 1953), providing an additional water source that is not available to the rest of the sandstone block. Furthermore, clay layers are abundant within sandstones, containing minerals that store water in their interlayer sites. The water film deposited on the rock surface will initially have slightly to strongly acidic pH values, similar to the pH value of rain or fog in urban areas. Upon deposition, the pH value of the water film increases due to the exposition to alkali and alkaline earth metal containing minerals within the sandstone. Furthermore, protons can be absorbed by clay minerals, releasing cations to the water film, increasing the pH value of the solution.

A Pourbaix diagram (E_h-pH diagram) can be utilized to determine the conditions needed for the oxidation from Mn^{2+} to Mn^{4+}. Increasing the pH value from 6 (rain water) to about 8-9 (addition of alkaline paint, alkaline catalysts from paint, or alkali and alkaline earth oxides or carbonates) shifts the system from the stability field of mobile dissolved Mn^{2+} into the stability field of immobile solid γ-MnOOH(s) or δ-MnO_2(s) (Brookins, 2012; Takeno, 2005). Thus, a phase boundary is crossed in the Pourbaix diagram and the immobile Mn^{4+} phase is thermodynamically favored. However, Mn^{2+} can persist metastably in solution for years in the absence of catalysts or biogenic oxidation. Nevertheless, when water evaporates, the Mn activity increases and the solid Mn stability field, or range of conditions where Mn^{4+} is stable, shifts towards lower pH and E_h conditions (Hem, 1963). Thus, the transformation from Mn^{2+} to Mn^{4+}, even in the absence of a catalyst, becomes more likely (Martin, 2005). Manganese^{4+} can then precipitate and form stable, immobile Mn oxyhydroxide phases. Since each sandstone block at the minster is different concerning its mineral distribution and content, this could result in the observed, seemingly randomly distributed, crust-free and crust-covered rock surfaces. To confirm this assumption, chemical and mineralogical analyses of the sandstones themselves need to be made.

The oxidation might not only take place as homogeneous oxidation, as described above, but also as heterogeneous oxidation, e.g., when it is catalyzed by a metal oxide surface. These surfaces can either be those of foreign minerals, but in the case of manganese, autocatalysis can also contribute significantly, e.g., Mn^{2+} can produce additional MnOOH on an MnOOH surface (Martin, 2005). The system catalyzes itself, the reaction rate increases as the reaction proceeds, and the occurrence of Mn as patches can become explainable by this process. Manganese oxidation can also be catalyzed by bacteria, fungi, and other organisms; however, microorganisms (fungi and cyanobacteria) were only found in Mn-poor regions at the Freiburger Münster (Fig. 6 C-D). No microorganisms could be verified on the Mn-rich patches (Fig. 6 A-B). Most Mn-rich crusts developed in areas that have a high water throughput. This indicates that water, or rather particles dissolved or leached in water, are a probable source for the Mn mass fractions, a theory also proposed by Livingston et al. (2016) for urban Mn crusts. However, the patches observed below the Renaissance-Vorhalle can only obtain splash water or condensed water as sources, since they are not directly exposed to rain, indicating the importance of splash and condensation water deposition.

3.4.Wet vs. dry deposition mechanisms

Air pollutants are deposited or transferred to materials surfaces through two mechanisms referred to as “wet” and “dry” deposition (Everett et al., 1988). Wet deposition occurs when pollutants are brought down dissolved in rainwater, whereas dry deposition refers to processes through which a pollutant deposits directly on surfaces (Grossi and Brimblecombe, 2002). Dry deposition happens all the time, while wet deposition is due

to precipitation and consequently is an intermittent event with both spatial and temporal variations (Grossi and Brimblecombe, 2002). To calculate the dry deposition rate of Mn at the Freiburger Münster, the absolute abundance of Mn in air masses around Freiburg is of importance. This Mn abundance was reported to be about 20 ng m^{-3} in larger German cities, based on Vallero (2014) and Martin Shafer (personal communications, 2016). The dry deposition rate also depends on the dry deposition velocity, which depends on the particle size, shape, aggregation, density, the Reynolds number of the flow, and the surface roughness of the deposition material (Pesava et al., 1999; Sehmel, 1980). Since the minster's walls are highly structured by blocks of stone, ornaments, and sculptures, the flow over these surfaces does not form a simple turbulent boundary layer (Pesava et al., 1999). To understand dry deposition velocities on sandstone facades, one has to consider the rough surface with complex geometry creating a separated boundary layer (Pesava et al., 1999). The dry deposition is higher for rough sandstone surfaces than for smooth surfaces (Pesava et al., 1999; Sehmel, 1980), and the deposition velocity depends on the orientation, structure, and location of the surface. Edges and corners have higher deposition rates than surfaces in the middle of the building. On average, the deposition rate of particles with about 0.6 – 0.8 µm mean diameters on cubic sandstone features with 0.2 mm roughness height are in the range of 0.03-0.14 cm s^{-1} with an average of about 0.05 cm s^{-1} (Pesava et al., 1999). Flat surfaces produce significantly lower deposition velocities (about 0.005 cm s^{-1}) and the deposition speed increases rapidly for a surface roughness of >0.15 mm (Pesava et al., 1999). Using these values and an average Mn concentration of 20 ng m^{-3}, the dry deposition rate for Mn at the Freiburger Münster can be calculated to be in the range of 19 - 88 ng cm^{-2} a^{-1}, depending on the exact position of the sandstone square. However, these values were calculated for particle sizes in the range between 0.1 and 1 µm, where the deposition velocity is lowest and only a weak function of the particle size (Guha, 1997). Since Mn-rich particles released by vehicular traffic are up to 1.8 µm in size, these numbers are probably underestimations of the actual deposition velocity. Still, using the values above, it would take about 1360 - 6300 years to grow a crust of 120 µg cm^{-2} solely by dry deposition, indicating that wet deposition must play an important role.

To obtain the wet deposition rate, we use the wet scavenging ratio of about 10^6 for Ca (concentration in rain divided by the concentration in air) (Hicks (2005) and the average annual precipitation in Germany (about 1000 mm). This provides wet deposition rates of about 2 µg cm^{-2} a^{-1} and the crust's accumulation would thus take about 60 years. This calculated value is significantly higher than the Mn wet deposition value calculated by Conko et al. (2004) for Reston, Virginia, USA. They found Mn wet deposition rates of 0.2 µg cm^{-2} a^{-1}. However, these values were calculated based on measurements in Reston in 1998, a suburb of Washington D.C. The reported Mn abundance at the Washington monument (city center of Washington D.C.) was only about 2 ng m^{-3} in 1992 and 2.5 ng m^{-3} in 1993 (Wallace and Slonecker, 1997), about a ten times lower than the Mn abundance in air reported from large German cities. The calculated wet deposition rate of about 2 µg cm^{-2} a^{-1} in Freiburg can hence be considered as reasonable.

However, even wet deposition values are almost too low to explain the crust accumulation at the minster, requiring some 60 years for the buildup of a crust with 120 µg cm^{-2} of Mn. Since both wet and dry deposition take place in parallel, the deposition rates can be added up, and additional condensed water on sandstones and clay mineral incorporations in the sandstone can slightly increase the dry deposition rates. Deposition of soluble materials occurs more readily on moist surfaces (Grossi and Brimblecombe, 2002), and clay minerals are able to fix relatively large amounts of Mn, depending on the pH and Eh conditions (Reddy and Perkins, 1974). It seems very likely that manganese oxides are mainly absorbed as external coatings onto typical clay minerals such as illite and bentonite (Potter and Rossman, 1977). Therefore, autocatalysis, in combination with wet and dry deposition, the abundance of clay minerals, and regular condensation of water at the stone surfaces, are factors that can contribute to explaining the crust's accumulation.

3.5. Trace elements and organics in the crusts

The LA-ICP-MS results revealed that elements easily scavenged by Mn oxyhydroxides are enriched in the black crusts (Table 3). Their composition is similar to that of common rock varnish, but reveals several differences, e.g., lower Ce and Fe mass fractions and significantly higher Mn values. Especially interesting is the lack of the positive Ce anomaly that is usually associated with Mn oxyhydroxides, such as rock varnish. Since Ce is the only rare earth element (REE) that can be oxidized from Ce^{3+} to Ce^{4+}, it is often found enriched in Mn-rich crusts, resulting in a positive Ce anomaly (Ohta and Kawabe, 2001; Thiagarajan and Lee, 2004). Measurements of urban air in Madrid, Spain (0.76 ng m^{-3} Ce) revealed positive Ce anomalies (Ce*=1.27) (Moreno et al., 2013). Cerium is thought to be enriched in air due to vehicle emissions from catalytic converters (Moreno et al., 2013) and from cerium oxide-based diesel fuel additives (Park et al., 2008). However, if Ce is abundant in PM in its oxidized form (CeO_2), it is insoluble and will not become enriched by scavenging processes of Mn oxyhydroxides. The lack of a positive Ce anomaly in the crusts at the minster might thus be due to the rapid accumulation of the crusts in addition to the PM containing primarily insoluble Ce^{4+}.

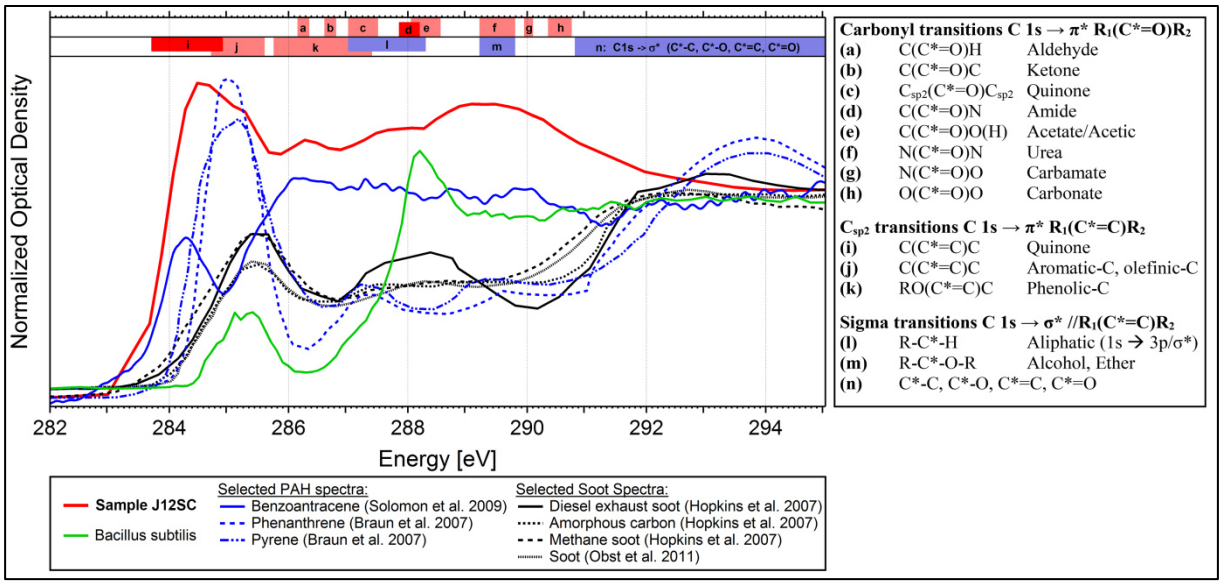

Figure 9: Scanning transmission X-ray microscopy-NEXAFS spectra of sample J12SC. The spectrum of the sample (red) corresponds well with a mixture of soot and PAH, based on literature data. The bacillus subtilis spectrum (green), measured in addition, does not agree with the spectrum obtained from the minster's wall.

Element maps of Mn obtained by STXM—NEXAFS measurements (Fig. 8 a) show that the black crust has an additional coating of a carbon- and nitrogen-rich substance, presumably organic matter (Fig. 8 b). Underneath the Mn-coating, two additional spots of C-rich material can be observed (Fig. 8 b). The carbon underneath the crust has no direct contact to the Mn crust, and the spots are too small to possibly be bacterial cells (<< 1 µm). Cluster analysis of the STXM-NEXAFS energy stack scans was conducted. It was used to determine if the carbon material underneath the crusts is similar to the organic layer on top of the crust. The results show two similar C-rich clusters (Fig. 8 c, d) with sharp and strong absorption edges of several different functional groups (Fig. 8 e, f). These two clusters reveal that the carbon from underneath the Mn-rich crust has the same functional groups as the carbon on top of the crust (Fig. 8 d, f) and the two C-rich spots could thus have been introduced into the Mn-layer through an open cavity system. Resonance peaks of carbon were found at 284.7 eV (quinones), 285.4 eV (aromatic carbon), 286.3 eV (aryl, vinyl-keto), 287.65 eV (aliphatic group), and 288.85 (carboxyl group), showing the broad range of different moieties within the material (Cody et al., 2008; Lehmann et al., 2005). One spectrum of bacillus subtilis was plotted in addition in Fig. 9, to illustrate that the spectrum does not agree with those of bacteria. Additionally plotted are soot (Hopkins et al., 2007; Obst et al., 2011) and polycyclic aromatic hydrocarbon (Braun et al., 2007; Solomon et al., 2009) spectra for comparison, which indicate

that the carbon fraction of sample J12SC is a mixture of soot and different polyaromatic compounds (Fig. 9). The presence of bacteria or fungi, which could be responsible for the growth, can thus be excluded. Raman spectroscopic measurements of the material also indicate the substance to be a soot-like material (bands at 1314 cm^{-1} and 1586 cm^{-1}), and also exclude the abundance of bacteria or fungi (Fig. 10). The C-rich crust on the FIB-prepared sample J12SC shows distinct soot bands (Patel et al., 2012; Sadezky et al., 2005; Sahoo and Kandasubramanian, 2014), which increase with increasing power settings. The additionally measured unprocessed sample J12SC shows a mixture of soot and birnessite bands (Freitas et al., 2013; Gui et al., 2015; Julien and Massot, 2002). Birnessite is a Mn oxyhydroxide phase that is typical of terrestrial Mn-rich crusts, and thus not unexpected in this context. The mixture of both materials results from the measurements perpendicular to the surface, probing into both the C-rich and Mn-rich layer. We hence conclude that this carbon is not directly involved in the crusts genesis, and that no indicator for a biogenic genesis was found. Whether the Mn-rich layer is still growing under the thick carbon-rich crust cannot be clarified.

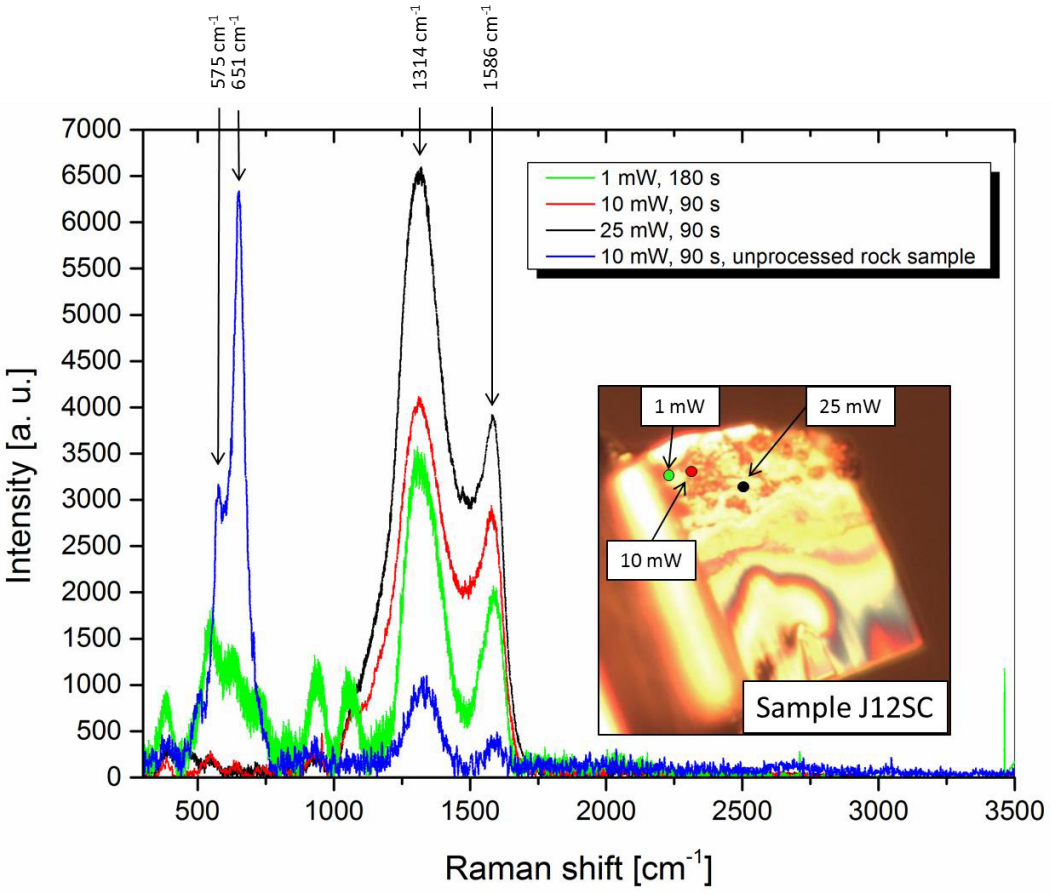

Figure 10: Raman spectra of sample J12SC measured with different power settings. The power was increased from 1 mW up to 25 mW. To confirm that the spectrum was not produced by degradation of the thin sample (thickness of 100-200 nm), a spectrum of the unprocessed rock surface was taken. This spectrum shows the same soot-like bands (1314 cm^{-1}, 1586 cm^{-1}), as well as additional dominating birnessite bands (577 cm^{-1}, 649 cm^{-1}) of the Mn-crust underneath the C-rich crust.

3.6.Renaissance-Vorhalle

At the Freiburger Münster, manganese-rich (> 150 µg cm^{-2}) patches are only found up to a height of about 7 m, with decreasing amounts at higher elevations. This makes the Renaissance-Vorhalle an exception, with

exceptionally high Mn mass fractions at a height of about 7.7 m. One difference between the Renaissance-Vorhalle and the rest of the Münster is that it was painted with a hydrophobic, diffusion-open silicon resin

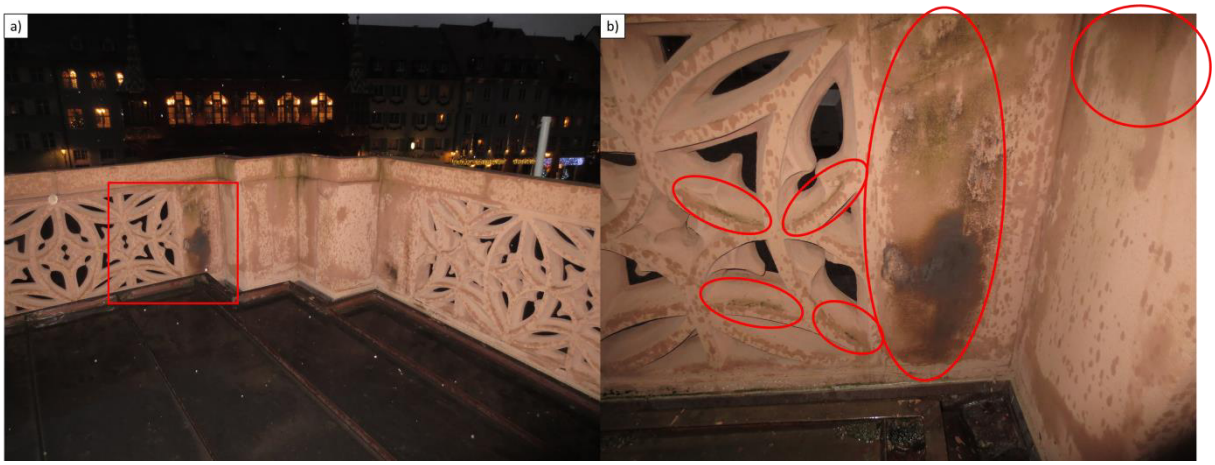

Figure 11: The Renaissance-Vorhalle during a rain-event (a) and a close-up view of a Mn-rich crust (b). Black crusts and biogenic material develop at surfaces which get wet and remain wet in spite of the hydrophobic silicon resin paint. One can presume that the paint is too thin on these surfaces, or that fissures or cracks allow water to intrude between the paint and the rock.

paint (Fa. Remmers) during its restauration in 2003. This paint permits diffusion of water through the paint to the air/paint surface, where it can slowly evaporate. When this paint develops fissures or cracks, water can intrude between the paint and the sandstone. The approximate locations of fissures and cracks can be detected by observing the rocks after a rain event (Fig. 11). The rocks under and around these cracks stay wet, while other surfaces dry quickly, due to the hydrophobic character of this paint. It can be observed that the Mn-rich crusts, as well as organic growth, develop preferentially on top of these wet surfaces (Fig. 11). Since the paint has a pH value of about 8-9, Mn^{2+}, which is mobile and stable under slightly acidic conditions such as in rain within urban areas, might start precipitating under oxic conditions. If surfaces that are supplied with water (by diffusion of rainwater through the paint), have an alkaline pH value, and get an additional supply of Mn^{2+} from atmospheric aerosols, the precipitation of Mn oxyhydroxide crusts could start. The steady supply of small amounts of water over a long time period through a diffusion-open paint could explain the faster accumulation of the crusts even at these high elevations. Since the water underneath the paint moves around structures protruding out on vertical surfaces, these structures remain initially uncovered by the crusts (Fig. 12 a) until the crust is too thick elsewhere to allow diffusion. As a consequence, the paint covering the protruding structures gets subsequently activated and crusts can start to develop on these surfaces as well (Fig. 12 b). Crusts can continue growing by autocatalysis, even if the water supply by the paint is stopped due to sealing by a crust, until the crusted areas start to exfoliate from the rock together with the paint itself (Fig. 12 c). Crusts with 1360 µg cm^{-2} Mn were measured on top of the silicon resin, which had grown in the period between 2003 and 2015. This suggests an accumulation rate of about 100 µg cm^{-2} a^{-1}. These high Mn accumulation rates are not explainable by usual dry or wet deposition and condensation, being about 50 times higher than expected. Even a faster and more frequent precipitation, as described above, does not satisfactorily solve the question about the Mn source for this high accumulation rate, and we can offer no explanation for the mechanism producing these extremely fast-growing crusts.

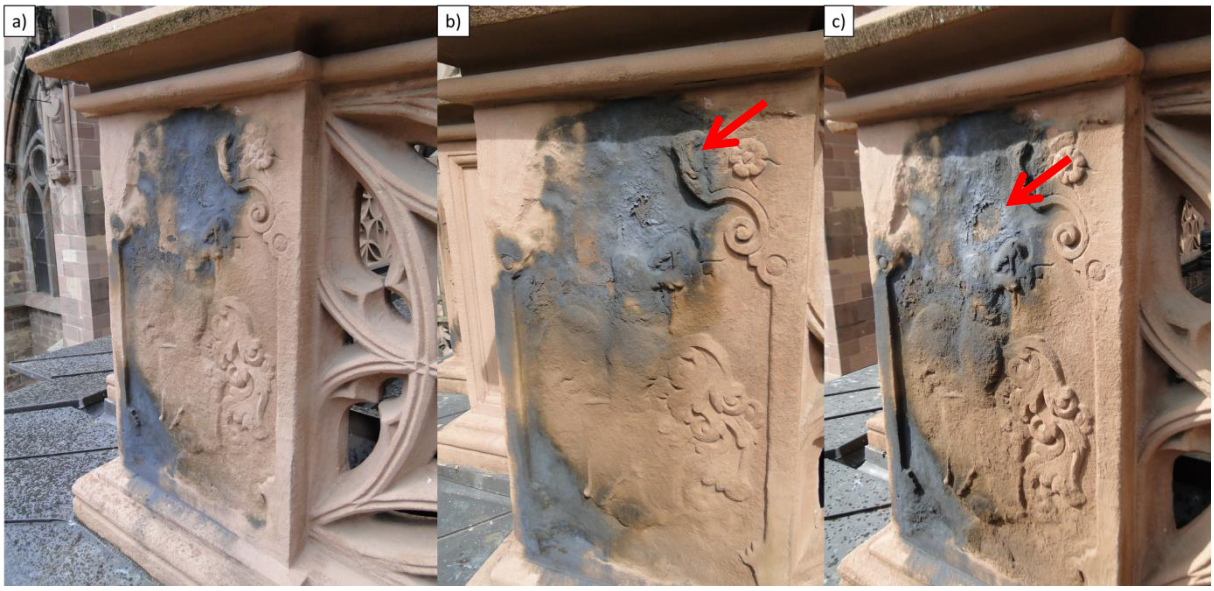

Figure 12: Stone carving at the Renaissance-Vorhalle photographically documented over a time period of three years, a) 2012, b) 2015, c) 2016. The crust develops rapidly with time, overgrowing higher elevated structures (marked in b). When the crust becomes too thick, exfoliation follows (marked in c). (Image credits: Freiburger Münsterbauverein)

3.7.Schöpfungsportal

Of interest is also the Schöpfungsportal (Fig. 13) because of an existing photographic documentation spanning the last 100 years (Fig. 13). One black patch (lower yellow circle on the left side of the Portal, Fig. 13 g) developed in a time period of ≤ 100 years, between about 1913 and 2007. Two additional black crusts at the Schöpfungsportal (upper yellow circles on the left side of the Portal, Fig. 13 e and f) developed within no more than four years (between 2007 and 2011). This observation indicates that the development of these patches is very fast as well. An explanation for the two new patches could be the painting of the Schöpfungsportal between 2005 and 2007 during the restauration. In contrast to the paint used for the Renaissance-Vorhalle, which is hydrophobic and diffusion-open, this coating was used to seal pore systems and is intended to be closed to water diffusion. A silicic acid ester ($Si(OR)_4$) was applied to the surface to preserve it ($Si(OC_2H_5)_4 + 4\ H_2O \rightarrow SiO_2 \cdot n\ H_2O + 4\ C_2H_5OH$). However, to allow the reaction from the intermediate SiOH-HOSi to an amorphous silica gel consisting of SiO_2 and water to proceed fast enough, an alkaline catalyst is added to initiate the hydrolysis. When the vapors produced by the reactions exit the system, the volume of the paint changes. At areas where the coating is exceptionally thick, a system of fissures evolves. This is the area where rainwater can enter and remain for a longer time period. This Mn-enriched rainwater in combination with the alkaline catalyst can result in the oxidation of Mn by alkalization of the system and precipitation of Mn oxyhydroxides. The final product can be the rapid development of the two new patches observed at the Schöpfungsportal.

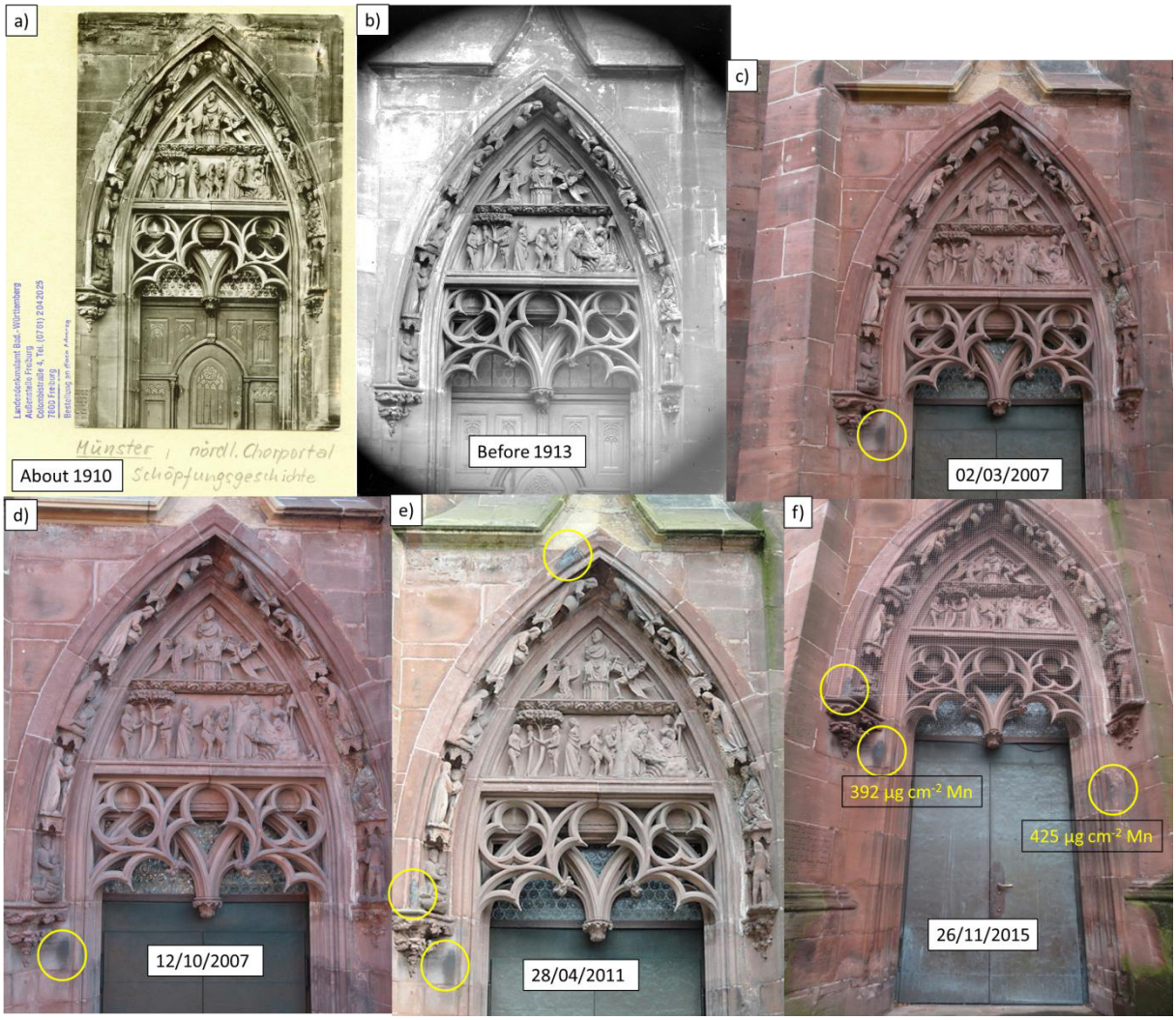

Figure 13: The Schöpfungsportal of the Freiburger Münster, photographed over a period of more than 100 years: The development of black crusts can be monitored. Black crusts are marked by yellow circles. In Fig. 13 f, measured Mn surface densities are also shown. (Image credit Fig. 13 a: Landesamt fuer Denkmalpflege im RP Stuttgart; image credit Fig. 13 b: Münsterbauverein Freiburg; image credits Figs. 13 c and d: J. Quatmann, restorer)

4. Conclusion

Most of the patches found at the facade of the Freiburger Münster at a height of >7 m are Mn-free. They seem to originate more likely from soot or biopigments of black fungi (Fig. 6) than from Mn accumulation. In contrast, almost all black patches at heights up to 7 m revealed high mass fractions of Mn. The enrichment within the patches with high Mn amounts is unlikely to originate from the sandstone building blocks and atmospheric deposition of Mn is favored as possible element source of Mn. Vehicle emissions with their high Mn, Pb, Zn, and Ba mass fractions are very likely the metal sources for the airborne particles. This is in agreement with the high amounts of the trace elements Pb, Ba, and Zn found within the crusts.

We used a portable XRF to obtain Mn surface densities in µg cm^{-2}. Thus, an approximate growth rate can be calculated for the crusts on the minster. Calculations strongly indicate wet deposition as major Mn deposition mechanism, in combination with dry deposition, condensed water, and clay mineral interaction. Manganese from vehicle sources has a leachable fraction of about 90%, allowing the high Mn enrichment found within the crusts. The oxidation from mobile Mn^{2+} to immobile Mn^{4+} appears to happen abiogenically, via pH shifts from acidic rain to alkaline conditions caused by the alkali and earth alkaline containing minerals and clay min-

erals in sandstones. Biogenic oxidation can be excluded as factor in the Mn precipitation at the Freiburger Münster. No evidence for organisms was found, neither by light microscopy nor in the course of the search for functional groups and remains of bacterial structures by X-ray microspectroscopy. Raman spectroscopic investigations support the finding of a soot-like material as only present form of organics in the crust.

The height limitation to about 7 m of Mn-rich crusts might be due to the height up to which vehicle emissions and movements dominate the pollutant levels, and to the flow and turbulence of air masses. The element composition of the minster's crusts is similar to that of common rock varnishes, however, the source materials and formation mechanism seem to differ. While rock varnish has a major contribution to its formation by deposition and leaching of mineral dust, the minster's crusts seem to be dominated by anthropogenic emissions and, if at all, only marginally influenced by natural dust minerals.

On the Schöpfungsportal and the Renaissance-Vorhalle, the crusts are especially thick. Since the crusts on the Renaissance-Vorhalle grew on top of a resin applied in 2003, an accumulation rate of more than 100 µg cm^{-2} a^{-1} can be estimated, assuming a uniform growth from 2003 until 2015. Alkaline additives to coloring and pore-space-sealing agents might have contributed to this phenomenon, but we cannot satisfactorily explain these extremely high Mn growth rates on this part of the building.

In conclusion, black patches on building facades, until to now usually interpreted as soot or biopigments, seem to be often Mn-rich deposits. Three different kinds of Mn-rich patches were observed on the Freiburger Münster: 1) thin Mn-rich crusts on vertical surfaces, 2) relatively thick crusts, which grew rapidly, on the Schöpfungsportal, and 3) especially fast growing and thick crusts, which show exfoliation due to the underlying silicon resin layer, at the Renaissance-Vorhalle. Black, Mn-rich crusts have been found on several buildings tested for such patches at locations distributed worldwide. This indicates that the phenomenon is more common than expected until recently, and further investigations are of scientific interest as well as of great importance for monument conservation and restoration.

5. Acknowledgments

This work was supported by the Max Planck Graduate Center with the Johannes Gutenberg University Mainz (MPGC) and the Max Planck Society. We want to thank Maik Biegler for the sample preparation for the LA-ICP-MS measurements and the Münsterbauverein Freiburg, Luzius Kürten, and Uwe Zäh for making it possible to conduct this research. We would like to thank Petya Yordanova for assistance during microscopy and R. Livingston for bringing up the idea to investigate urban varnish. Furthermore, we would like to thank the Münsterbauverein Freiburg, Johanna Quatmann, and the Landesamt fuer Denkmalpflege in Rheinland-Pfalz Stuttgart for providing images. We thank J. J. Schauer and M. M. Shafer for sharing their unpublished data on Mn in European aerosols. This work was supported by the Max Planck Graduate Center with the Johannes Gutenberg University Mainz (MPGC), the Max Planck Society, and King Saud University. The ALS is supported by the Director, Office of Science, Office of Basic Energy Sciences, of the US Department of Energy under Contract DE-AC02-05CH11231. We thank the Helmholtz-Zentrum Berlin for the allocation of the synchrotron radiation beamtime at BESSY II.

6. References

Birmili, W., Allen, A.G., Bary, F., Harrison, R.M., 2006. Trace metal concentrations and water solubility in size-fractionated atmospheric particles and influence of road traffic. Environmental science & technology, 40(4): 1144-1153.

Blau, P.J., 2001. Compositions, functions, and testing of friction brake materials and their additives, Oak Ridge National Lab., TN (US).

Bonazza, A., Brimblecombe, P., Grossi, C.M., Sabbioni, C., 2007a. Carbon in black crusts from the Tower of London. Environmental science & technology, 41(12): 4199-4204.
Bonazza, A., Sabbioni, C., Ghedini, N., 2005. Quantitative data on carbon fractions in interpretation of black crusts and soiling on European built heritage. Atmospheric Environment, 39(14): 2607-2618.
Bonazza, A. et al., 2007b. Did smoke from the Kuwait oil well fires affect Iranian archaeological heritage? Environmental science & technology, 41(7): 2378-2386.
Braun, A., Mun, B.S., Huggins, F.E., Huffman, G.P., 2007. Carbon speciation of diesel exhaust and urban particulate matter NIST standard reference materials with C (1s) NEXAFS spectroscopy. Environmental science & technology, 41(1): 173-178.
Breuer, B., Bill, K.H., 2006. Bremsenhandbuch: Grundlagen, Komponenten, Systeme, Fahrdynamik. Springer-Verlag.
Brimblecombe, P., Grossi, C.M., 2009. Millennium-long damage to building materials in London. Science of the Total Environment, 407(4): 1354-1361.
Brookins, D.G., 2012. Eh-pH diagrams for geochemistry. Springer Science & Business Media.
Cadle, S.H. et al., 1997. Particulate emission rates from in-use high-emitting vehicles recruited in Orange County, California. Environmental Science & Technology, 31(12): 3405-3412.
Cody, G.D. et al., 2008. Quantitative organic and light-element analysis of comet 81P/Wild 2 particles using C-, N-, and O-μ-XANES. Meteoritics & Planetary Science, 43(1-2): 353-365.
Conko, K.M., Rice, K.C., Kennedy, M.M., 2004. Atmospheric wet deposition of trace elements to a suburban environment, Reston, Virginia, USA. Atmospheric Environment, 38(24): 4025-4033.
De Oliveira, B.P. et al., 2011. An integrated approach to assess the origins of black films on a granite monument. Environmental Earth Sciences, 63(7-8): 1677-1690.
DePaul, F., Sheih, C., 1985. A tracer study of dispersion in an urban street canyon. Atmospheric Environment (1967), 19(4): 555-559.
Duvdevani, S., 1949. Dew observations and their significance—new methods in dew estimation, Proc. UN Sci. Conf. Conserv. Utilization of Resources, pp. 45-47.
Duvdevani, S., 1953. Dew gradients in relation to climate, soil and topography, Desert Research Symposium, Jerusalem, pp. 136-52.
Espinosa, A.J.F., Rodríguez, M.T., de la Rosa, F.J.B., Sánchez, J.C.J., 2002. A chemical speciation of trace metals for fine urban particles. Atmospheric Environment, 36(5): 773-780.
Everett, L. et al., 1988. The effects of acid deposition on buildings and building materials in the United Kingdom. Building Effects Review Group. Department of the Environment.
Follath, R., Schmidt, J.S., Weigand, M., Fauth, K., 2010. The X-ray microscopy beamline UE46-PGM2 at BESSY. Sri 2009: The 10th International Conference on Synchrotron Radiation Instrumentation. Eds: R. Garrett, I. Gentle, K. Nugent, S. Wilkins(AIP Conference Proceedings): 323-326.
Freitas, R.M., Perilli, T.A., Ladeira, A.C.Q., 2013. Oxidative precipitation of manganese from acid mine drainage by potassium permanganate. Journal of Chemistry, 2013.
Frierdich, A.J., Hasenmueller, E.A., Catalano, J.G., 2011. Composition and structure of nanocrystalline Fe and Mn oxide cave deposits: Implications for trace element mobility in karst systems. Chemical Geology, 284(1): 82-96.
Garg, B.D. et al., 2000. Brake wear particulate matter emissions. Environmental Science & Technology, 34(21): 4463-4469.
Gorbushina, A. et al., 1993. Role of black fungi in color change and biodeterioration of antique marbles. Geomicrobiology Journal, 11(3-4): 205-221.
Grissom, C.A. et al., 2014. Manganese in black crusts on Seneca sandstone. Microscopy and Microanalysis, 20(S3): 2044-2045.
Grossi, C., Brimblecombe, P., 2002. The effect of atmospheric pollution on building materials, Journal de Physique IV (Proceedings). EDP sciences, pp. 197-210.
Grossi, C., Brimblecombe, P., 2008. Past and future colouring patterns of historic stone buildings. Materiales de Construcción, 58(289-290): 143-160.

Grüner, F.W., Otto; Kürten, Luzius; Riemann, Jennifer 2011. Verschwärzung von Sandsteinoberflächen durch Eisen-/Manganoxide, neue Ergebnisse zu Ursache und restauratorischer Behandlung mittels Kompressen. Natursteinsanierung Stuttgart 2011. Neue Natursteinsanierungsergebnisse und messtechnische Erfassungen sowie Sanierungsbeispiele, Conference: 7-21.

Guha, A., 1997. A unified Eulerian theory of turbulent deposition to smooth and rough surfaces. Journal of Aerosol Science, 28(8): 1517-1537.

Gui, Z. et al., 2015. Co-electrodeposition of RuO 2–MnO 2 nanowires and the contribution of RuO 2 to the capacitance increase. Physical Chemistry Chemical Physics, 17(23): 15173-15180.

Hem, J.D., 1963. Chemical equilibria and rates of manganese oxidation, USGPO.

Hicks, B.B., 2005. A climatology of wet deposition scavenging ratios for the United States. Atmospheric Environment, 39(9): 1585-1596.

Hopkins, R.J., Tivanski, A.V., Marten, B.D., Gilles, M.K., 2007. Chemical bonding and structure of black carbon reference materials and individual carbonaceous atmospheric aerosols. Journal of Aerosol Science, 38(6): 573-591.

Janssen, N.A., Van Mansom, D.F., Van Der Jagt, K., Harssema, H., Hoek, G., 1997. Mass concentration and elemental composition of airborne particulate matter at street and background locations. Atmospheric Environment, 31(8): 1185-1193.

Julien, C., Massot, M., 2002. Spectroscopic studies of the local structure in positive electrodes for lithium batteries. Physical Chemistry Chemical Physics, 4(17): 4226-4235.

Kilcoyne, A.L.D. et al., 2003. Interferometer-controlled scanning transmission X-ray microscopes at the Advanced Light Source. Journal of Synchrotron Radiation, 10: 125-136.

Lehmann, J. et al., 2005. Near-edge X-ray absorption fine structure (NEXAFS) spectroscopy for mapping nano-scale distribution of organic carbon forms in soil: Application to black carbon particles. Global Biogeochemical Cycles, 19(1).

Livingston, R. et al., 2016. Investigation of urban rock varnish on the sandstone of the Smithsonian Castle. Science and Art: A Future for Stone: 399.

Martin, S.T., 2005. Precipitation and dissolution of iron and manganese oxides. Environmental Catalysis: 61-81.

Miller, A. et al., 2012. Biogenic Mn oxide minerals coating in a subsurface granite environment. Chemical Geology, 322: 181-191.

Moffet, R.C., 2011. Scanning transmission X-ray microscopy: Applications in atmospheric aerosol research. Lawrence Berkeley National Laboratory.

Moreno, T. et al., 2013. Daily and hourly sourcing of metallic and mineral dust in urban air contaminated by traffic and coal-burning emissions. Atmospheric Environment, 68: 33-44.

Nriagu, J.O., 1990. The rise and fall of leaded gasoline. Science of the total environment, 92: 13-28.

Obst, M. et al., 2011. Quantitative high-resolution mapping of phenanthrene sorption to black carbon particles. Environmental science & technology, 45(17): 7314-7322.

Ohta, A., Kawabe, I., 2001. REE(III) adsorption onto Mn dioxide (delta-MnO2) and Fe oxyhydroxide: Ce(III) oxidation by delta-MnO2. Geochimica Et Cosmochimica Acta, 65(5): 695-703.

Oudijk, G., 2010. The rise and fall of organometallic additives in automotive gasoline. Environmental Forensics, 11(1-2): 17-49.

Park, B. et al., 2008. Hazard and risk assessment of a nanoparticulate cerium oxide-based diesel fuel additive—a case study. Inhalation toxicology, 20(6): 547-566.

Patel, M., Ricardo, C.L.A., Scardi, P., Aswath, P.B., 2012. Morphology, structure and chemistry of extracted diesel soot—Part I: Transmission electron microscopy, Raman spectroscopy, X-ray photoelectron spectroscopy and synchrotron X-ray diffraction study. Tribology International, 52: 29-39.

Pesava, P., Aksu, R., Toprak, S., Horvath, H., Seidl, S., 1999. Dry deposition of particles to building surfaces and soiling. Science of the total environment, 235(1): 25-35.

Pio, C.A., Ramos, M.M., Duarte, A.C., 1998. Atmospheric aerosol and soiling of external surfaces in an urban environment. Atmospheric Environment, 32(11): 1979-1989.

Pöhlker, C. et al., 2012. Biogenic potassium salt particles as seeds for secondary organic aerosol in the Amazon. Science, 337(6098): 1075-1078.
Potter, R.M., Rossman, G.R., 1977. Desert varnish: the importance of clay minerals. Science, 196(4297): 1446-1448.
Qin, Y., Kot, S., 1993. Dispersion of vehicular emission in street canyons, Guangzhou City, South China (PRC). Atmospheric Environment. Part B. Urban Atmosphere, 27(3): 283-291.
Reddy, M., Perkins, H., 1974. Fixation of zinc by clay minerals. Soil Science Society of America Journal, 38(2): 229-231.
Reneau, S.L., 1993. Manganese accumulation in rock-varnish on a desert piedmont, Mojave Desert, California, and application to evaluating varnish development. Quaternary Research, 40(3): 309-317.
Robert, J.C., 1984. Ethyl: a history of the corporation and the people who made it. University Press of Virginia.
Rogge, W.F., Hildemann, L.M., Mazurek, M.A., Cass, G.R., Simoneit, B.R., 1993. Sources of fine organic aerosol. 3. Road dust, tire debris, and organometallic brake lining dust: roads as sources and sinks. Environmental Science & Technology, 27(9): 1892-1904.
Root, R.A., 2000. Lead loading of urban streets by motor vehicle wheel weights. Environmental Health Perspectives, 108(10): 937.
Ruffolo, S.A. et al., 2015. An analysis of the black crusts from the Seville Cathedral: A challenge to deepen the understanding of the relationships among microstructure, microchemical features and pollution sources. Science of the Total Environment, 502: 157-166.
Sadezky, A., Muckenhuber, H., Grothe, H., Niessner, R., Pöschl, U., 2005. Raman microspectroscopy of soot and related carbonaceous materials: spectral analysis and structural information. Carbon, 43(8): 1731-1742.
Sahoo, B.N., Kandasubramanian, B., 2014. Photoluminescent carbon soot particles derived from controlled combustion of camphor for superhydrophobic applications. RSC Advances, 4(22): 11331-11342.
Sáiz-Jiménez, C., Hermosin, B., 2004. Black crusts in the European built environment. Corros Rev, 22(5-6): 381-393.
Saiz-Jimenez, C., Miller, A.Z., Martin-Sanchez, P.M., Hernandez-Marine, M., 2012. Uncovering the origin of the black stains in Lascaux Cave in France. Environmental microbiology, 14(12): 3220-3231.
Sanders, P.G., Dalka, T., Xu, N., Maricq, M.M., Basch, R., 2002. Brake dynamometer measurement of airborne brake wear debris. 0148-7191, SAE Technical Paper.
Schauer, J.J. et al., 2006. Characterization of metals emitted from motor vehicles. Research report (Health Effects Institute)(133): 1-76; discussion 77-88.
Sehmel, G.A., 1980. Particle and gas dry deposition: a review. Atmospheric Environment (1967), 14(9): 983-1011.
Solomon, D. et al., 2009. Carbon (1s) NEXAFS spectroscopy of biogeochemically relevant reference organic compounds. Soil Science Society of America Journal, 73(6): 1817-1830.
Takeno, N., 2005. Atlas of Eh-pH diagrams. Geological survey of Japan open file report, 419: 102.
Thiagarajan, N., Lee, C.T.A., 2004. Trace-element evidence for the origin of desert varnish by direct aqueous atmospheric deposition. Earth and Planetary Science Letters, 224(1-2): 131-141.
Tsunazawa, Y., Yokoyama, T., Nishiyama, N., 2016. An experimental study on the rate and mechanism of capillary rise in sandstone. Progress in Earth and Planetary Science, 3(1): 1-10.
Uchida, E., Watanabe, R., Osawa, S., 2016. Precipitation of manganese oxides on the surface of construction materials in the Khmer temples, Cambodia. Heritage Science, 4(1): 1.
Vallero, D., 2014. Fundamentals of air pollution. Academic press.
Vicenzi, E.P., Grissom, C.A., Livingston, R.A., Weldon-Yochim, Z., 2016. Rock varnish on architectural stone: microscopy and analysis of nanoscale manganese oxide deposits on the Smithsonian Castle, Washington, DC. Heritage Science, 4(26).
Viles, H.A., Gorbushina, A.A., 2003. Soiling and microbial colonisation on urban roadside limestone: a three year study in Oxford, England. Building and Environment, 38(9): 1217-1224.

Wallace, L., Slonecker, T., 1997. Ambient Air Concentrations of Fine (PM25) Manganese in US National Parks and in California and Canadian Cities: The Possible Impact of Adding MMT to Unleaded Gasoline. Journal of the Air & Waste Management Association, 47(6): 642-652.
Weigand, M., 2014. Realization of a New Magnetic Scanning X-ray Microscope and Investigation of Landau Structures Under Pulsed Field Excitation, Universität Stuttgart Stuttgart (und Cuvillier Verlag, Göttingen).
White, W.B., Vito, C., Scheetz, B.E., 2009. The mineralogy and trace element chemistry of black manganese oxide deposits from caves. Journal of Cave and Karst Studies, 71(2): 136-143.
Young, T.M., Heeraman, D.A., Sirin, G., Ashbaugh, L.L., 2002. Resuspension of soil as a source of airborne lead near industrial facilities and highways. Environmental science & technology, 36(11): 2484-2490.

Appendix

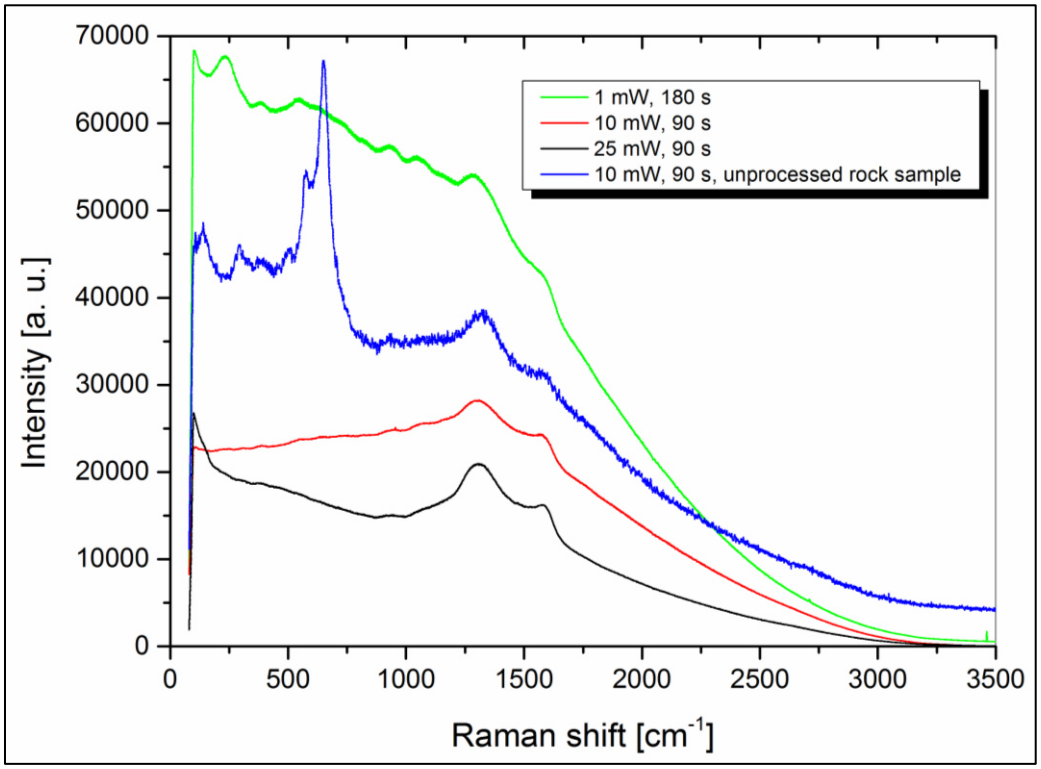

Figure A: Raw spectra of all Raman measurements plotted in Fig. 10. For the baseline correction, the spectra from 80- 300 cm^{-1} were cut in order to allow a reasonable background subtraction.